

The hydrocarbon-pool chemistry of methanol conversions in zeolite catalysts

Liu, Chuncheng

DOI

[10.4233/uuid:3762e136-0fbf-4e7a-b701-36399a3c2cd0](https://doi.org/10.4233/uuid:3762e136-0fbf-4e7a-b701-36399a3c2cd0)

Publication date

2022

Document Version

Final published version

Citation (APA)

Liu, C. (2022). *The hydrocarbon-pool chemistry of methanol conversions in zeolite catalysts*. [Dissertation (TU Delft), Delft University of Technology]. <https://doi.org/10.4233/uuid:3762e136-0fbf-4e7a-b701-36399a3c2cd0>

Important note

To cite this publication, please use the final published version (if applicable). Please check the document version above.

Copyright

Other than for strictly personal use, it is not permitted to download, forward or distribute the text or part of it, without the consent of the author(s) and/or copyright holder(s), unless the work is under an open content license such as Creative Commons.

Takedown policy

Please contact us and provide details if you believe this document breaches copyrights. We will remove access to the work immediately and investigate your claim.

The hydrocarbon-pool chemistry of methanol conversions in zeolite catalysts

Dissertation

for the purpose of obtaining the degree of doctor

at Delft University of Technology

by the authority of the Rector Magnificus,

Prof.dr.ir T.H.J.J van der Hagen,

chair of the Board of Doctorates

to be defended publicly on

Monday, 31 October 2022 at 17:30 o'clock

by

Chuncheng LIU

Master of Science in Energy Engineering,

Politecnico di Milano, Italy

born in Shandong, China

This dissertation has been approved by the promotor.

Composition of the doctoral committee:

Rector Magnificus	chairman
Prof.dr. E.A. Pidko	Delft University of Technology, promotor
Prof.dr. F. Kapteijn	Delft University of Technology, promotor
Dr. E.A. Uslamin	Delft University of Technology, copromotor

Independent members:

Prof.dr.ir. A. Urakawa	Delft University of Technology
Prof.dr. U. Olsbye	University of Oslo, Norway
Prof.dr.ir. L. Lefferts	University of Twente
Prof.dr.ir. J.R. van Ommen	Delft University of Technology
Prof.dr. A.J. Houtepen	Delft University of Technology, reserve member

To my family

Chuncheng LIU

The hydrocarbon-pool chemistry of methanol conversions in zeolite catalysts

About this work

The research described in this thesis has been conducted at the Catalysis Engineering and Inorganic Systems Engineering sections of the Chemical Engineering Department, Faculty of Applied Sciences (TNW), Delft University of Technology. This work is part of the Advanced Research Center for Chemical Building Blocks, ARC CBBC, which is co-founded and co-financed by the Dutch Research Council (NWO) and the Netherlands Ministry of Economic Affairs and Climate Policy under the project “Exploration of Non-commodity Zeolite Frameworks for Small Molecule Activation: Acidity, Reactivity and Coke Formation”, project nr. 2016.007.TUD.



Cover by: Chuncheng LIU

Printed by: Proefschriftspecialist

Copyright © 2022 by Chuncheng Liu

ISBN 978-94-6384-379-9

An electronic version of this dissertation is available at

<https://repository.tudelft.nl/>

Table of Contents

Chapter 1	General introduction	1
Chapter 2	An integrated approach to the key parameters in MTO reaction catalyzed by MFI/MEL zeolite materials	35
Chapter 3	Direct discerning reaction pathways in MTH reactions by transient operation - FASPA	81
Chapter 4	Revealing main reaction paths to olefins and aromatics in the MTH process over H-ZSM-5	133
Chapter 5	High stability of MTA process over bimetallic Ca,Ga-modified ZSM-5	159
	Summary and outlook	205
	Samenvatting en vooruitzichten	215
	Acknowledgements	225
	List of publications	229
	Curriculum Vitae	231

Chapter 1. General introduction

In this chapter, a general introduction of the methanol-to-hydrocarbons process has been given guiding the readers through the history of its development, fundamental concepts, and current challenges in the mechanistic understanding and the process optimization.

1.1 MeOH economy

Fossil fuels have enabled an unprecedented era of affluence for human development in the last two centuries, beginning with coal and progressing through petroleum oil and natural gas. Besides the energy supply, petroleum industry refines more than 90% of the chemical products (namely, petrochemicals), which are widely used in many fields, such as packaging, clothing, painting, and the pharmaceutical industry. The central role of non-renewable fossil feedstocks in our economy has led to the drastic increase and continuous emissions of carbon dioxide into the atmosphere. The harmful effect of CO₂ on the global climate is widely acknowledged as one of the most critical issues for humankind. The global transition to renewable feedstocks and the direct CO₂ recycling and utilization is the only way to control the temperature rise down to 1.5 °C according to the newly signed international Glasgow Climate Pact^[1]. One of the attractive strategies for the future sustainable chemical industry is the so-called methanol (MeOH) economy, proposed by Georgy Olah in 2008, that introduces a comprehensive interconnected technological scheme (**Figure 1.1**) involving the production, transport, and utilization of MeOH as the primary industrial vector connecting the existing fossil-based and future circular industry fully based on renewable energy and feedstock.^[2] MeOH can be efficiently produced from various carbon sources, including the currently dominating fossil fuels (coal, oil, natural gas, etc.), as well as alternative feedstocks including municipal and industrial wastes and various types of biomass. Ideally, MeOH can be directly produced from CO₂ via hydrogenation using renewable H₂^[3, 4] or electroreduction^[5], followed by its further conversion into various value-added chemicals such as olefins, aromatics, *etc.*^[6]

This thesis is devoted to the investigation of the fundamental aspects of the latter part of the overall conversion scheme. Specifically, the focus was on understanding the role of various factors on the selectivity and catalyst stability in the MeOH conversions as well as developing new methodological tools to get a deeper mechanistic insight into the underlying complex chemistry taking place inside the zeolite micropores. In the next section, I will present a concise overview of the state-of-the-art and current understanding of the field, followed by a summary of the key objectives of this study and a thesis outline.

Sustainable chemistry within the methanol economy

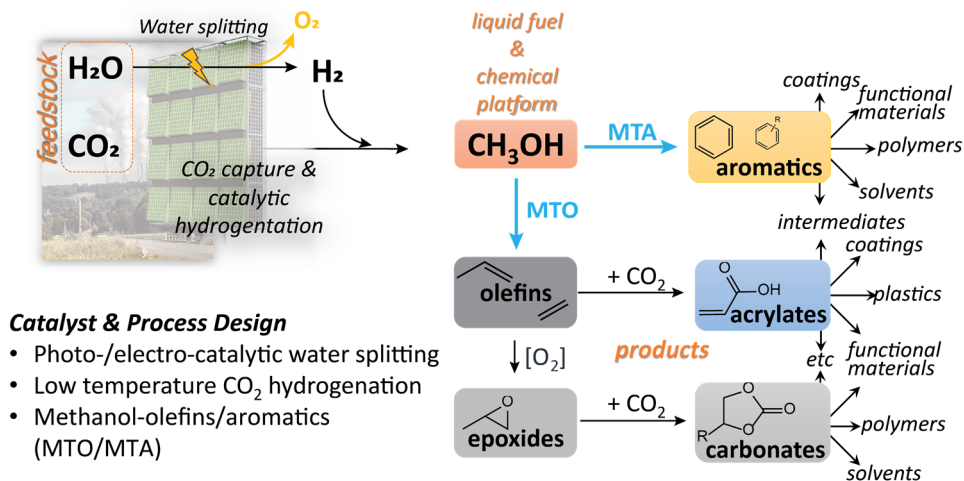


Figure 1.1. A schematic overview of a future fully renewable MeOH-centered chemical industry for the sustainable production and transformation of key chemical building blocks and chemical products.

1.2 Olefins and aromatics in chemical industry

Olefins and aromatics are among the most important chemical building blocks with a wide range of downstream products. Olefins (alkenes) are hydrocarbons having unsaturated C=C double bonds with a general formula of C_nH_{2n} . Light olefins containing 2, 3, and 4 carbon atoms, namely ethylene, propylene, and *iso/normal*-butylene, respectively, are in gaseous form under ambient conditions. Light olefins are key platform molecules to produce vital synthetic materials in a variety of industries. These chemicals represent key intermediates in the process schemes connecting the MeOH vector with value-added chemical products (**Figure 1.1**).

For example, polyethylene, produced by the polymerization of ethylene, is the most widely used plastic today due to its low weight and excellent impact and corrosion resistance. Butadiene (two C=C double bonds), made from butylenes by dehydrogenation, is the principal precursor of polybutadiene, also called synthetic rubber, which is widely utilized in tire manufacturing. Besides the direct polymerization, oxidization, halogenation, and alkylation of olefins also produce many chemical precursors to a multitude of chemical products such as polyvinyl chloride, polyethylene terephthalate, and polystyrene.

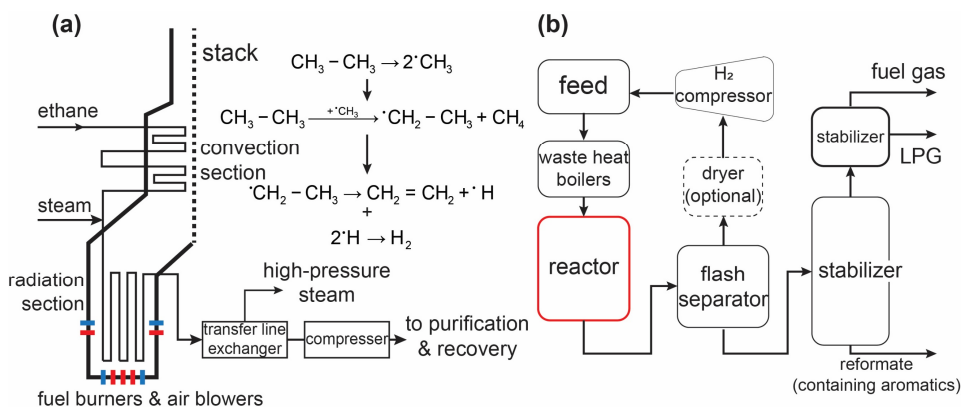


Figure 1.2. Half plan slice of a steam cracking furnace and radical reaction mechanism of ethane pyrolysis to ethylene (a) and the general flow scheme of a commercial catalytic reformer unit for aromatics production (b).^[7]

Steam cracking of gaseous or liquid hydrocarbon feeds like ethane or naphtha remains the dominant industrial method to produce ethylene and propylene. The steam cracking reaction is a non-catalytic process and proceeds via a radical reaction mechanism.^[8] **Figure 1.2(a)** presents a schematic overview of the steam cracking process in a steam cracking furnace. The process operates with ethane or liquid hydrocarbon feed, such as naphtha or LPG (liquefied petroleum gas), that is diluted with steam and heated in an oxygen-free furnace. The cracking in the radiation part occurs quickly after preheating and reaching the reaction temperature (850 °C). The reacting effluent flow is then immediately quenched to increase the selectivity to desired products. They are then sent to transfer line exchangers followed by multi-level fractional distillation columns, where desirable products are purified. Diluted steam not only pre-heats the hydrocarbon feed but also lowers the hydrocarbon partial pressure, reducing coke-forming processes and preventing carbonaceous coke build-up on the heating pipes.

When using ethane as feed, the reaction is initiated by cleavage of the C–C bond forming two methyl radicals (**Figure 1.2(a)**). In the subsequent propagation steps, a hydrogen atom is first abstracted resulting in the formation of a methane molecule and an ethyl radical. The formed ethyl radical goes through the hydrogen transfer reaction forming an ethylene molecule and a hydrogen radical, while the latter meets another hydrogen radical forming hydrogen. The methyl radical can also attack ethylene leading to the formation of propylene, while the longer olefins are obtained through analogous propagation steps.

Depending on the hydrocarbon feedstocks, propylene, butylenes, and light aromatics may also be generated and separated from the distillation process. Nowadays, steam cracking produces practically all ethylene and 64% of propylene, whereas propane dehydrogenation and fluid catalytic cracking (FCC) of LPG create 32% and 2% of propylene, respectively.^[9]

Similar to light olefins, aromatics also play a key role in the current petrochemical as well as the future renewable chemical industries (**Figure 1.1**). Aromatics (formula C_nH_{2n-6}) are compounds that contain at least one benzene ring having a resonance-stabilized unsaturated cycle structure. “Light aromatics” referring to benzene, toluene, ethylbenzene, and *o*-/*p*-/*m*-xylene (BTEX) with only one benzene ring, are considered the basic building blocks in the petrochemical industry. Aromatics and their derivatives are vital for the production of dyes, aramid fibers, solvents, and other functional materials. Since the first evolution by IARC (The International Agency for Research on Cancer) in 1974^[10], benzene and most aromatics have been found to be carcinogenic to humans.^[11] Fortunately, these are never the final consumer products. The conventional supply of aromatics heavily hinges on the catalytic cracking and reforming of naphtha (C_6 - C_{12}) providing more than 80% of the global BTEX production volume. Catalytic reforming is usually carried out by first feeding a naphtha and hydrogen mixture into a furnace, where the mixture is heated before entering into reactors (in series). The cracking of naphtha results in the formation of aromatics and other side products like hydrogen, which is separated and then recycled in the downstream distillation processes (**Figure 1.2(b)**). Next to the catalytic reforming, steam cracking of gasoline in ethylene manufacturing also accounts for one of the primary sources of benzene production. In fact, due to the higher value of aromatics than ethylene, one of the optimization objectives for the steam cracking process is to increase the selectivity to light aromatics as much as possible.

The demand for light olefins and BTEX is expected to rise steadily in the future, whereas the transition to a renewable and circular economy requires the rapid replacement of the current oil-based production processes with alternative more efficient and versatile technologies based on renewable resources. The catalytic conversion of MeOH to hydrocarbons (MTH) represents an attractive approach to achieving this goal.

1.3 History and development of the MTH process

As early as in 1880, scientists discovered that MeOH and other alcohols could be converted into hexamethylbenzene and olefins over a fused ZnCl₂ catalyst at high temperatures.^[12] However this reaction did not receive much attention from the scientific community until the second half of the 20th century.^[12] The modern version of the MTH process was discovered in the 1970s by two teams from Mobil simultaneously. Mobil Chemical in Edison, New Jersey, was trying to convert MeOH to ethylene oxide, while Mobil Oil's Central Research Laboratory in Princeton was trying to methylate isobutene using MeOH to produce 2,2-dimethylpropane. When a mixture of MeOH and isobutene was fed through H-ZSM-5, MeOH was unexpectedly fully converted into a wide range of hydrocarbons including aromatics. Following the two oil crises in 1973 and 1978, the world's first fixed-bed MeOH-to-gasoline (MTG)^[13-15] facility was built in New Zealand ten years after this discovery. By 1986, the start-up phase was completed, resulting in the commercial production of 570 kt of gasoline per year.

Although these technological concepts have been around for more than 40 years, the real industrialization of these techniques has been through several highs and lows, mainly influenced by the international oil price and supply-demand relationships. **Figure 1.3** presents an overview of the key milestones and the associated patent and peer-review publication activities in the development of MTH catalytic science and technology. The first patent surge happened immediately after the discovery of the MTH process. Although paper publishing shows a certain delay, the number of publications started increasing in the 1990s at a time when the world started looking for alternative sources of fossil fuels. Interestingly, the patenting process tends to stagnate in the last decade of the 20th century. Concurrently, Dahl and Kolboe introduced an essential mechanistic concept, the hydrocarbon pool mechanism^[16], which has been substantially developed during the last two decades^[17, 18], representing and leading to a continuous increase in the publication output. Early research and development of MTH were undertaken by ExxonMobil (merger of Exxon and Mobil)^[21, 22], UOP^[23-25], Lurgi^[26], and Japanese research institutes^[27]. After entering the 21st century, some of these parties have managed to successfully develop and implement MeOH-to-olefins (MTO) plants, most of which are in China. In Nanjing, for example, UOP and Wison developed and placed into operation an MTO facility in 2013 with an annual capacity of 295 kt of olefins.

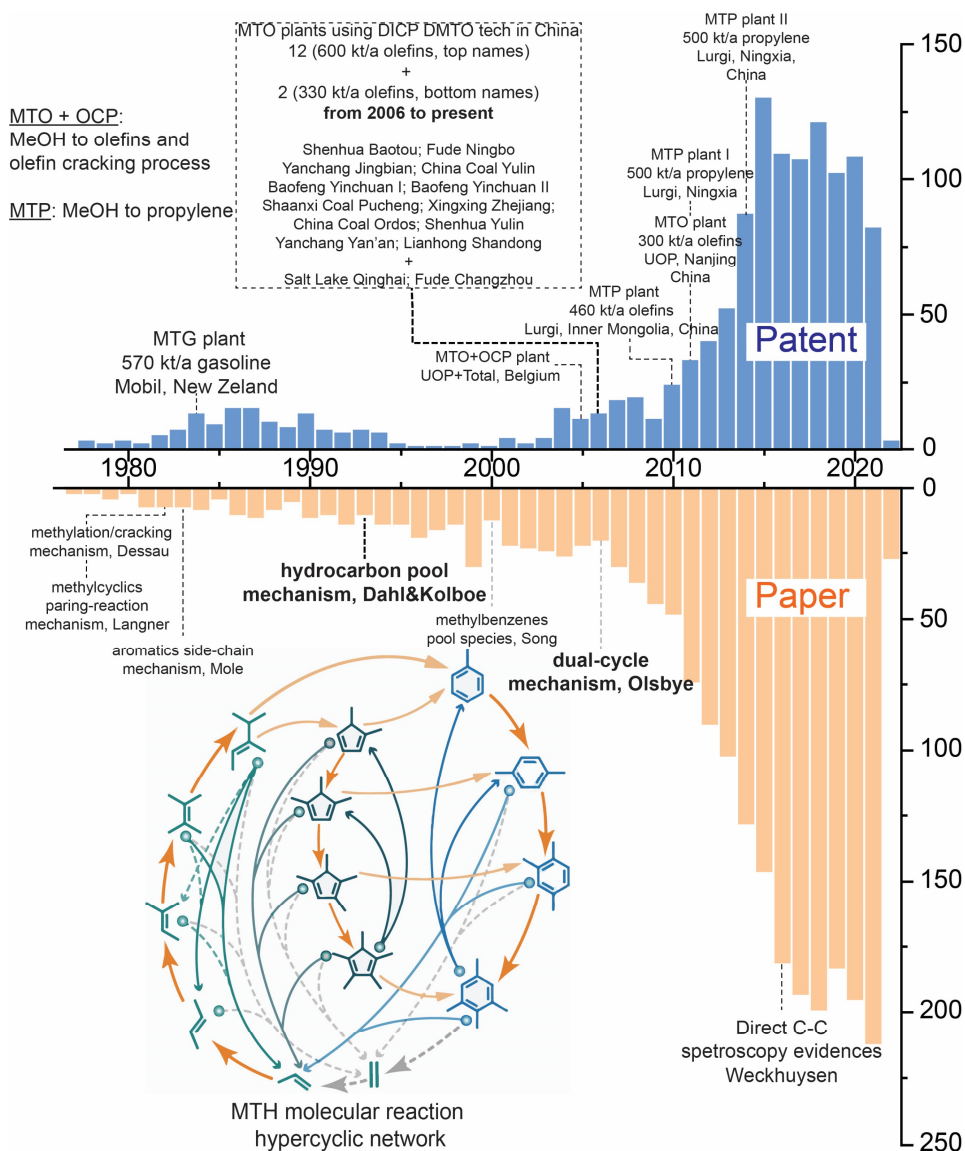


Figure 1.3. The industrialization and mechanistic finding milestones of the MTH process.^[19, 20] Publication results were collected from all available databases via Web of Science within 1977-present.

Three MeOH-to-propylene (MTP) industrial plants have been built and put into operation at Shenhua Ningxia Coal Group Company by Lurgi, a German company dedicated to the development of MTP technology. Nowadays, the application and rapid development of these processes mainly take place in China, which is closely related to its coal-rich characteristics and the fact as the major

petroleum-importing country. It is worth mentioning that MTO technology in China has progressed rapidly since the 1980s mainly undertaken by research institutes including Dalian Institute of Chemical Physics (DICP), Sinopec, and Tsinghua University. The large-scale commercial MTO facility was built-up and put into operation in Baotou, China, in 2006, which for the first time gives the annual capacity of 600 kt of olefins. To date, 24 MTO units have been built (or are under construction) in China, with a total capacity of 13.6 million tons of olefins per year.^[28] The successful industrial application of MTO technology has also boosted a continued explosion of peer-reviewed papers and a second burst of patents (**Figure 1.3**).

Depending on the target products, MTH (MeOH-to-hydrocarbons) is categorized as: MTG (MeOH-to-gasoline), MTO (MeOH-to-olefins), MTP (MeOH-to-propylene), and MTA (MeOH-to-aromatics). The MTA process is considered as the emerging route to produce aromatics, which currently fully relies on the petrochemical refinery. However, due to the technical issues including rapid deactivation and limited selectivity to light aromatics, the current MTA development is still on the laboratory scale or at the pilot stage.^[29] The introduction and investigation of the MTA process will be given separately in **Chapter 5**.

1.4 MTH mechanism

MeOH can be readily dehydrated into dimethyl ether (DME) over solid catalysts such as Al_2O_3 or $\text{Al}_2\text{O}_3\text{-SiO}_2$ with acid sites. However, the selectivity to olefins over these amorphous catalysts is limited. Thus, the use of molecular sieves as catalysts ensures the success of MTH technology. Molecular sieve crystals, or called zeolites, not only provide the active sites for MTH reactions, but also display a regular pore structure, and these molecular-sized pores play an important role in regulating the reaction pathway and enhancing the transformation into light olefins. The subsequent reactions of these olefins generate alkanes and aromatics.

The scientific community has conducted extensive fundamental research on the MTH process. A consensus has been reached so far that the underlying mechanism is extremely complicated: the transformation of MeOH into the final products goes through multiple reaction pathways; a variety of reaction intermediates are involved following different mechanisms; various zeolites with different pore structures are being used, leading to different interactions between

acid sites and reaction intermediates. The tremendous complexity of the MTH reaction mechanism inevitably hindered early mechanistic studies.

1.4.1 The first C–C bond formation

Today's rapidly advancing technology has led to an increasing number of research papers that use advanced characterization tools to answer the two most important (but-not-least) questions that exist in the field of MTH, namely, (1) how is the first C–C bond formed? and (2) how are final hydrocarbon products generated?

Initially, the production of olefins was postulated to be a result of a direct C–C formation from a consecutive coupling of MeOH (or DME). Up to now, researchers have proposed at least 20 different direct first C–C bond formation mechanisms named after involved intermediates, *e.g.* methyl carbonium ion^[30, 31], methane-formaldehyde^[32], carbene^[6, 33], oxonium ylid^[34], methoxymethyl cation^[35], CO-mediated methyl acetate^[36, 37], *etc.* **Figure 1.4** presents a schematic overview of these different proposed reaction schemes.

However, these proposed mechanisms have been questioned for a long time. For example, the mechanism with the formation of a methyl carbonium ion as the key intermediate (**Figure 1.4(a)**) was proposed in analogy to the well-known alkane monomolecular cracking mechanism catalysed by superacids.^[38, 39] However, direct evidence of the presence of the methoxyl ethyl cation in zeolite catalysts has never been presented. Alternatively, a carbene-insertion mechanism (**Figure 1.4(c)**) proposed by Chang and Silvestri suggests that carbene can be formed via α -elimination of surface methoxy species, followed by the insertion of the carbene into the C–O bond of MeOH to form the first C–C bond.^[6] However, this mechanism suffers from the exceptionally high activation energy barrier (>200 kJ/mol^[40]) for C–H cleavage in the surface methoxy species for carbene formation.^[41] Similarly, the oxonium-ylid mechanism (**Figure 1.4(d)**) was also debated due to the plausible but energetically unfavorable formation of ylides via the deprotonation of the oxonium ion.^[34, 42]

In recent years, the wide utilization of advanced characterization tools, especially *in situ* solid-state NMR spectroscopy with ¹³C-isotope labeled MeOH feed, has provided more concrete experimental evidence for the presence of key intermediates. As an alternative to mechanism **(d)**, the trimethyl oxonium ion, instead of being transformed into ylides, directly assists the activation of C–H of MeOH or DME on the neighboring adjacent framework oxygen to form the surface ethoxy species leading to the primary formation of ethylene.^[43, 44]

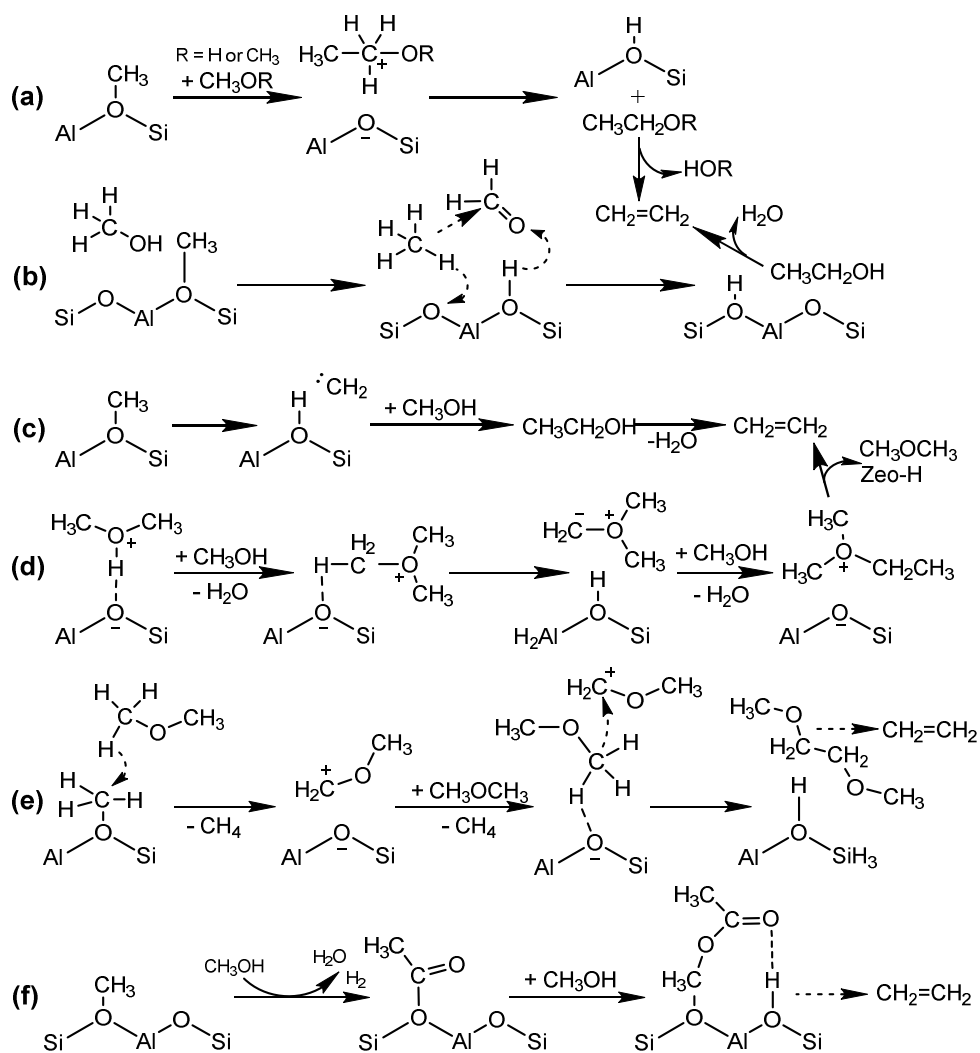


Figure 1.4. Scheme of selected first C–C formation mechanisms in MTH process over zeolite catalysts.

Although many experimental results provide evidence against the formation of gas phase carbene species from MeOH^[45, 46], more results from IR (infrared) spectroscopy^[47, 48] and NMR (nuclear magnetic resonance) spectroscopy measurements, on the other hand, indicate the existence of a surface carbene as a product of the polarization of the C–H bond of surface methoxy species by surrounding framework oxygens. In 2016, a C–C bond formation mechanism via the Koch-type carbonylation of surface methoxy species by CO (**Figure 1.4(f)**) was proposed by independent studies of Weckhuysen^[36] and Lercher^[37]. CO, H₂,

and methane can be readily formed in the MeOH dehydrogenation or disproportionation reactions. Experimental evidence was presented in support of the presence of surface formate and acetate species in the zeolite catalyst. Another spectroscopic study combined with a computational approach indicates that extraframework Al, as the Lewis acid sites in the acidic zeolites, can readily activate dimethyl ether to form ethylene, methane, and surface formate species via the hydrogen transfer between surface methoxy species and coordinated MeOH on the adjacent extraframework Al site.^[49] It is worth noting that recently proposed C–C formation mechanisms always involve methane as the side product generated by the MeOH disproportionation and decomposition. The methane formation study during the early stage of the MTH process might provide an indirect way to explore the subsequent C–C formation reactions in the zeolite catalysts.

Based on the theoretical and computational studies and growing spectroscopic evidence of the existence of key intermediates in all reported mechanisms, it is reasonable to speculate that the MeOH activation and the first C–C bond formation can take place through a variety of direct mechanisms. Although the high energy barrier for the first bond formation leads to a low conversion rate of MeOH, it is well recognized that after a short incubation period, also called the induction period, the MeOH transformation proceeds via an autocatalysis process, where the primary olefins contribute significantly to the conversion rate of MeOH. Subsequently, the hydrocarbon pool process dominates the formation of final products including olefins and aromatics.

1.4.2 Hydrocarbon pool mechanism

Next to the first C–C bond formation, the reaction route from MeOH to final products is another key question to be answered. The proposal of the hydrocarbon pool mechanism^[16] was actually inspired by the ‘S’-shaped (or sigmoid) conversion curve of MeOH along time, which is typical for autocatalysis in reaction kinetics. Early experimental studies found that upon co-feeding trace amounts of hydrocarbons like cyclohexene (readily formed from cyclohexanol dehydration^[50]) or toluene^[51] with MeOH, just like adding a spark to a barrel of gunpowder, the MeOH conversion is enormously increased quickly reaching 100%. Therefore, the primary ethylene or propylene formed from the first C–C formation contributes negligibly to the final products. Alternatively, they behave as the organo-catalyst promoting the methylation by MeOH leading to a continuous methylation/cracking reaction in the MTH process. The subsequent

reactions, including hydrogen transfer, cyclization, aromatization, and aromatic disproportionation, are categorized into the secondary reactions, which are responsible for the production of aromatics. Since the hydrocarbon pool concept was proposed in 1993^[15], most of the related research has been directed at two core research topics into this mechanism driving its refinement and further development.

The first topic is to identify the active species involved in the hydrocarbon pool. As early as in 1982, based on the carbene mechanism and the experimental ¹³C-MeOH co-feeding results, Dessau and Lapierre discussed a propagation mechanism, in which olefins are the products of consecutive methylation of intermediates in the form of (CH₂)_n.^[52] Along with the proposal of the hydrocarbon pool concept, Dahl and Kolboe found that MeOH hardly reacts with ethylene and propylene in a SAPO-34 zeolite catalyst and concluded that these light olefins cannot be the reactive pool species.^[17, 18] However, the non-reactivity of propylene with MeOH might be attributed to the suppressed diffusion rate of propylene and butylenes (as methylation products) through the narrow 8-membered ring window of SAPO-34. In a later study, Kolboe and co-workers found that ethylene and propylene contain >50% of ¹³C directly from ¹³C-MeOH when co-feeding with ¹²C-toluene over H-ZSM-5, which is a 10-membered ring zeolite with a larger pore size than H-SAPO-34.^[53] Meanwhile, they noticed the pronounced isotopic incorporation in polymethylbenzenes, implying their reactivity in the pool mechanism. This triggered many following studies on the identification of aromatic pool species and corresponding reactions to final products in different zeolites. Haw and co-workers developed a pulse-quench *in situ* NMR experiment^[54, 55], which enables it to probe the retained organic species on the zeolite surface readily quenched after MeOH pulses. A clear time delay before the observation of the first hydrocarbon was assigned to the kinetic induction period for initiating the autocatalysis process. ¹³C CP/MAS solid-state NMR spectra show that most organic species are 1,3-dimethylpentenyl ions after ¹³C-ethylene pulsing to a fresh H-ZSM-5 catalyst.^[55] Other methylpentenyl ions like 1,2,3-trimethylpentenyl ions^[56] and 1,3,4-trimethylpentenyl ions^[56] and even pentamethylbenzenium ions^[56, 57], were also found in H-ZSM-5 under various MeOH conversion conditions. Depending on the zeolite topology (pore size) and corresponding acidic strength, in the large pores of H-Beta the heptamethylbenzenium ions are readily formed^[58], whereas the formation of such species in H-SAPO-34 did not occur, attributed to its weaker acid sites unable to prevent the deprotonation of these ions. Accordingly, Haw concluded that the

neutral methylbenzenes are the organic pool species in the MTH mechanism for H-SAPO-34. A later *in situ* NMR study by Liu and co-workers revealed the presence of methylpentenyl ions and methylbenzenium ions at mild reaction temperatures (<400 °C) inside the pores of H-SSZ-13 - another CHA-type zeolite but exhibiting stronger acid sites than H-SAPO-34.^[59]

However, we should notice that some of these findings were reported by using either co-feeding hydrocarbons with MeOH or non-MeOH like ethylene feedings at various reaction conditions. The direct observations of these carbenium ions over typical MTH zeolites (MFI-type H-ZSM-5 or CHA-type H-SSZ-13 and H-SAPO-34) in an MTH experiment under industrially relevant conditions are still limited. The origin of these species is widely accepted as a result of methylation-oligomerization-cyclization from MeOH and primary ethylene. It is important to note that the topology of the zeolite catalyst and its acidity control the structure of retained species and thus may affect the subsequent reaction pathway. This so-called structure-activity relationship in the zeolite-catalyzed MTH reactions will be described in more detail in the next section.

The other core topic in the hydrocarbon pool mechanism comprises the reaction pathways to final products. To explain the acceleration by aromatic hydrocarbons of MeOH conversion^[51], researchers proposed the cycle-type reactions on aromatic core species, including the successive ring expansion/contraction and sidechain growing/split-off, which are called the paring mechanism and the side-chain mechanism (**Figure 1.5**), respectively. In the former mechanism proposed by Sullivan in 1961^[60], the contraction of an aromatic ring generates methylated cyclopentenyl species, which then go through the cracking reactions to form light olefins. The final step is methylation of cyclopentenyl species followed by ring expansion eventually closing the cycle. In the side-chain mechanism, the core hydrocarbon pool intermediates, the heptamethylbenzenium ions, generate a C=C double bond on the side alkyl groups. The further methylation followed by the dealkylation produces ethylene, whereas a multi-methylation/dealkylation produces longer olefins.

Obviously, the distinction between these two mechanisms is whether the benzene ring is opened, and the key question is which mechanism prevails in the MTH process. To answer this question, the viability of these reaction mechanisms was evaluated based on the energy barriers for key reactions. Liu and co-workers reported that in the paring mechanism, the formation of pentamethylpentenyl ions

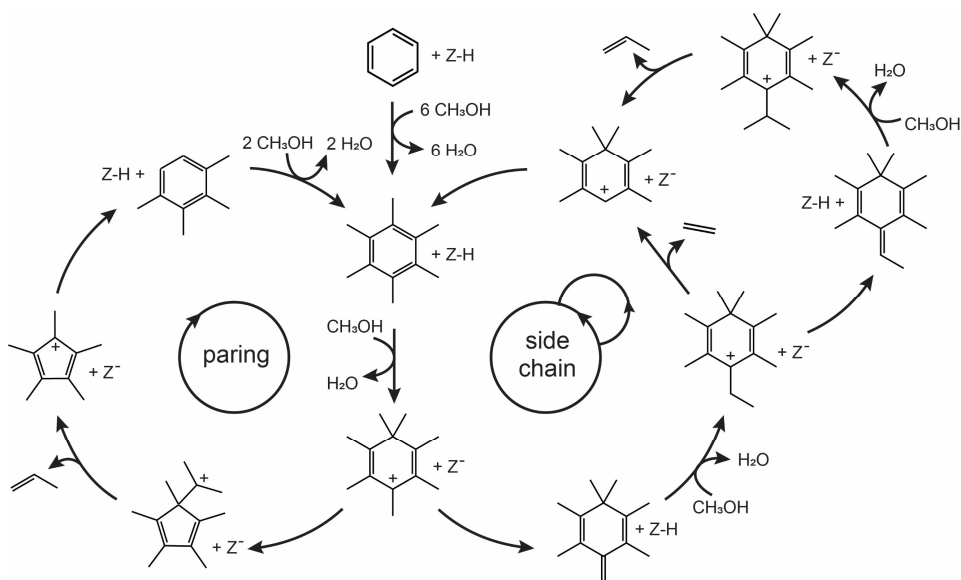


Figure 1.5. Representation of the paring and side-chain mechanisms in MTH catalysis.^[61]

with cleavage of propyl groups (forming propylene) in CHA-type zeolites needs to overcome a relatively high energy barrier of 153 kJ/mol.^[59] The cleavage of an ethyl group is even more difficult due to an even higher energy barrier.^[60] To compare, the energy barrier in the side-chain mechanism is ~40 kJ/mol less than in the paring mechanism, implying that the side-chain mechanism, in which polymethylbenzenes are the core pool species without ring contraction/expansion, is more energetically favored in CHA-type zeolite catalyst. A similar theoretical/computational effort was reported by Lesthaeghe and Speybroeck for ZSM-5 - an MFI-type zeolite with less space in the channel intersections.^[61] After investigating three potential pathways for ethylene elimination in the side-chain mechanism, they found that all energy barriers are around 200 kJ/mol, significantly higher than comparable reactions splitting off butylene in the paring mechanism in ZSM-5 zeolites (although different olefins are taken into account here).^[62] This further implies that rather than the side-chain mechanism, the paring mechanism prevails in H-ZSM-5 zeolites leading to olefins formation via the ring contraction/expansion reaction pathway.

Although theoretical calculations have provided fundamental guidance for the determination of the dominant reaction paths in MTH catalysis, neither the paring mechanism nor the side-chain mechanism was able to fully explain all product distributions of MTH reactions, especially in H-ZSM-5 showing a wide product range (C₁-C₁₂ aliphatics and aromatics in the gas phase product stream).

In 2006, Olsbye and co-workers compared the ^{13}C incorporation rates in different products of MeOH conversion in H-ZSM-5 catalyst using ^{12}C -/ ^{13}C -MeOH switching experiments. The time evolution of the ^{13}C content in the effluent after switching from ^{12}C -MeOH to ^{13}C -MeOH flow showed that C_3 - C_6 alkenes had a very similar ^{13}C content, whereas ethylene and aromatics, had less but equal ^{13}C content and showed a slower ^{13}C incorporation along time on stream (**Figure 1.6(a)**). Since the highly substituted methylbenzenes like heptamethylbenzenes as observed in H-Beta or H-SSZ-13 cannot be formed in H-ZSM-5 due to the limited space in the channel intersections, the light aromatics like trimethylbenzenes and xylenes behave as hydrocarbon pool species.^[52]

Based on the lower ^{13}C -incorporation rate of ethylene and aromatics relative to that of other light alkenes, an aromatic cycle was built up dominating the production of light aromatics and exclusive formation of ethylene via dealkylation/split-off of aromatics through the side-chain mechanism. In parallel with the aromatic cycle, an olefinic cycle was proposed, in which olefinic intermediates have a higher reactivity resulting in a faster formation of propylene and higher olefinic products. The connection between these two cycles can be hydrogen transfer, cyclization, and aromatization reactions with alkanes as side products (**Figure 1.6(b)**). The difference between the olefinic cycle and Dessau's methylation/cracking propagation mechanism is that, in the dual-cycle mechanism, the formation of ethylene is excluded from the methylation/cracking reactions of olefins, which might sound too absolute. In fact, the lower ^{13}C content in aromatics from the first GC analysis at 0.5 min (**Figure 1.6(a)**) can be affected by other processes during the switch, which will be discussed in **Chapter 4**.

The dual-cycle mechanism provides the opportunity for researchers to achieve the coveted control of the MTO process. Optimizing the process favoring one cycle over the other could provide a means to increase the selectivity of the preferred product. Additionally, suppressing the aromatic cycle could also prevent coke formation and delay ultimate deactivation since fewer diffusion-limiting aromatics are formed in the pore.

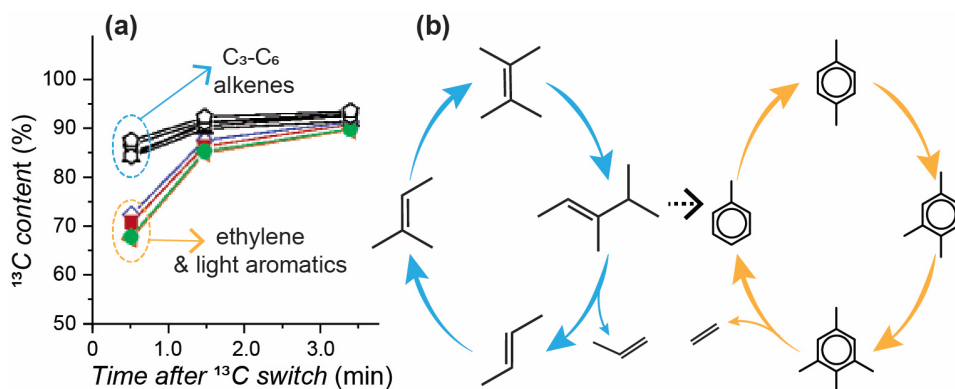


Figure 1.6. Time evolution of ^{13}C content in gas phase hydrocarbon products after switching from ^{12}C -MeOH to ^{13}C -MeOH stream into an H-ZSM-5 zeolite catalyst at $350\text{ }^\circ\text{C}$ (a) and simplified dual-cycle mechanism in H-ZSM-5 (b), proposed by Olsbye and co-workers.^[63]

1.4.3 MTH deactivation

Like other acid site-catalyzed hydrocarbon reactions, the MTH catalyst deactivation is inevitable due to the inert hydrocarbon accumulation along with the desired hydrocarbon formation. However, deactivation mechanisms in H-ZSM-5 and H-SAPO-34, as two mostly used catalysts in the industrialized MTH plant, are entirely different. For CHA-type H-SAPO-34 catalyst, the large cage ensures the confinement and stabilization of highly methylated benzenes as the hydrocarbon pool intermediates, while the narrow windows only allow the light olefins like ethylene and propylene to pass through. Its deactivation mainly stems from the fact that methylated benzenes, the hydrocarbon pool intermediates, are quickly transformed into condensed naphthalene and even phenanthrene. The formed polyaromatics showing much lower reactivity than methylated benzenes in the process occupy the cage and gradually accumulate in the micropore. This process slows down or blocks the diffusion of reactant and reduces the total amount of accessible active sites (Brønsted acid sites), eventually causing the deactivation.^[64, 65]

For example, MFI-type H-ZSM-5 catalyst shows a lower selectivity to coke (0.3 C% at $380\text{ }^\circ\text{C}$ ^[66]) than SAPO-34 (> 10 C% at $400\text{ }^\circ\text{C}$ ^[67]). Unlike the polyaromatics blocking the pore in SAPO-34, researchers conclude that coke can only be formed on external surfaces of ZSM-5 because the channel intersections (0.9–1.0 nm) cannot accommodate the bulky unsaturated compounds, which can be readily dealkylated.^[66] Meanwhile, more evidence is provided for the initial

formation of the coke in the channels and later on the external surface.^[68-70] The application of *in situ* microscopy of the MTH reactions within large crystals helps to directly monitor the formation of coke during the MTH process in a time- and spatial-resolved manner.^[70, 71] It was found that for H-ZSM-5, graphitic-like coke layers preferably deposit at the crystal edge where straight channel openings directly reach the external crystal surface. Nevertheless, these initial coke deposits hardly block the acid sites, and therefore their impact on deactivation is probably negligible.^[72] With time-on-stream, a polyaromatic-type coke front moves towards the crystal center from the crystal edge, blocking the active sites and leading to catalyst deactivation. For CHA-type H-SAPO-34, polyaromatics immediately start being formed at the corners of the H-SAPO-34 crystals. These surface coke species reduce the diffusion of reactants into the crystal center, thereby causing further coke deposition inside the large SAPO-34 crystal.^[64, 65] A later study by Sanchez and Lercher confirms that in a back-mixed CSTR reactor and in a homogeneous MeOH atmosphere, H-ZSM-5 deactivates first rapidly and then at a much slower rate, indicating two different reaction pathways lead to the deactivation and coke formation along time on stream.^[68] In the early stage, the oxygen-containing coke species are potentially formed via CO- and formaldehyde-mediated reactions with MeOH^[73], which quickly occupy the active sites slowing down the MTH reactions. However, these initially formed coke species can still further react with MeOH and primary formed olefins, forming gas phase products and alkylated benzenes (this process is called “reanimation” in ref^[66]), while the accumulation of the polyaromatic species results in the slow deactivation process.

The zeolite deactivation is affected by operating conditions in the MTH process and zeolite structural parameters:

Reaction temperature. The hydrocarbon pool mechanism shows a cycle-type reaction network composed of “chain growing and split off” reactions over more than one intermediate involving long-chain olefins and methylated benzenes in the respective olefinic cycle and aromatic cycle. The catalyst deactivation can be interpreted as that these active cycle intermediates go through the undesired reaction path to bulky products like highly methylated benzenes or even polyaromatics, which are relatively inert and strongly adsorbed at active sites under operating conditions. Schulz found that changing the operating conditions like reaction temperature can re-activate these retained matters, which are initially inert at lower operating temperature (<300 °C) thereby blocking the pore.

After elevating temperature up to 400 °C and higher, the dealkylation rate of these retained unsaturated matters is accelerated, splitting off light olefins and reactivating the aromatic cycle. Afterwards, coke species start growing slowly on the external surface of H-ZSM-5. Therefore, at temperatures below 300 °C H-ZSM-5 deactivates fast resulting in a higher coke content (> 10 wt%), whereas at temperatures above 400 °C the lifetime (defined by total MeOH throughput before its conversion drops below a predefined level) of the same H-ZSM-5 can be extended by more than 10 times accompanying with a much smaller coke content (<0.3 wt%).^[66] For CHA-type zeolites, owing to the larger cavity the coke species are mainly polyaromatics like naphthalene or phenalene in the micropores, while their formation is also determined by operating temperatures. In a temperature-programmed MTH test over an H-SAPO-34 catalyst in a fluidized bed reactor, Liu and co-workers found a transition of retained species from (methyl)adamantanes to (methyl) naphthalene, further to phenalene and even pyrene. At temperature below 300 °C, the content of retained matters, which are mainly (methyl)adamantanes in the H-SAPO-34 catalyst, rapidly reaches 16 wt% causing the quick deactivation. When temperature increases to 400 °C, the content of retained hydrocarbons drops to 6 wt% while the catalyst shows the longest lifetime. Further increase of temperature significantly shortens the catalyst lifetime but the coke content stabilizes at ~9 wt%. Based on these observations, a transition process of coke species over H-SAPO-34 at the function of operating conditions is proposed (**Figure 1.7**).^[74]

Zeolite topology and zeolite acidity. Nowadays, CHA-type zeolites are widely used as MTO catalysts attributed to the narrow window in the framework significantly hindering the selectivity to C₃₊ products. However, these CHA-type zeolites like H-SAPO-34 suffer from fast deactivation due to the rapid formation of polyaromatics like naphthalene in the large cage (diameter > 1 nm). (Methyl)naphthalene or even pyrenes in the cage show very limited reactivity with MeOH, thereby blocking the pore and causing the catalyst deactivation. On the contrary, MFI-type zeolites with a 3D intersecting channel system have a smaller channel intersection space (~0.9 nm) than the space in the CHA cage. The formation of polyaromatics with more than one benzene ring is strongly suppressed, resulting in the long lifetime of H-ZSM-5 in the MTH process compared to H-SAPO-34. Other zeolite parameters including acid site concentration, strength, and their spatial distribution in the zeolite framework, are also key to the catalyst deactivation in the MTH process. Their roles in the deactivation mainly stem from the impact on the polyaromatization step, the key

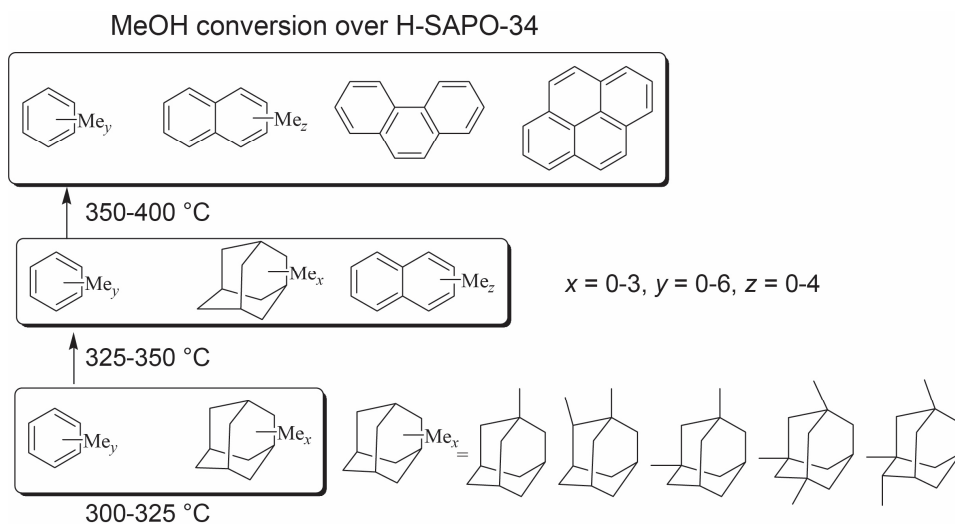


Figure 1.7. Coke species evolution in the temperature-programmed MeOH conversion over H-SAPO-34.^[74]

transition from active hydrocarbon pool intermediates to inert coke. As demonstrated in the hydrocarbon pool mechanism, the highly methylated benzenes are commonly regarded as the core intermediate for the formation of olefins and aromatics. However, these intermediates are also coke precursors towards the inert polyaromatic species blocking the active sites or reducing their accessibility, although a detailed kinetic investigation on this transformation is still limited. A previous study reveals that a higher concentration of acid sites (more active sites along the diffusion path) can accelerate the deactivation rate by increasing the probability of the consecutive polyaromatization reaction proceeding in the crystal.^[75] On the other side, the higher reaction rate of polyaromatization and the longer residence time of coke precursors at the stronger acid sites also contribute to the fast accumulation of polyaromatics in the micropore.^[70, 76] Recent studies focus more on the spatial distribution of acid sites (Brønsted acid sites) in the crystal to disclose the correlation with their MTH performance. A so-called Al-pair describing two proximate Al sites in the framework exhibiting the synergy effect (similarly enhancing the strength of the acid sites) promote the catalysed reactions such as the polyaromatization also leading to a faster deactivation.

Crystal size. The decent shape selectivity property of zeolite makes it the best catalyst candidate in many reactions including MTH. However, it is worth noting that the zeolite channels of molecular size can also introduce a strong

inhibition of the diffusion of reactant and the exit of products in the effluent flow, hindering the complete utilization of all active sites, causing rapid pore blocking and possibly hampering the kinetic investigation of MTH reactions (diffusion control versus kinetic control).^[65, 77] Researchers found that reducing the crystal size or synthesizing the nano-size zeolite crystal^[78-81] and preparing the hierarchical/mesoporous zeolite catalysts^[80, 82] are good strategies to improve the diffusive property in the zeolite catalysts. Accordingly, the stability of the zeolite in the MTH process is greatly enhanced. In principle, the shape-selectivity of the zeolite micropore system should be fully preserved after reducing the crystal size.^[83] Therefore, the product distribution in the MTH process should be independent of the crystal size. However, primarily formed olefins quickly diffuse out of the smaller crystal, preventing the propagation of the following secondary reactions forming aromatics and subsequently the aromatic-based reactions. This might explain the observed lower selectivity to ethylene and aromatics within nano-size zeolite catalysts, e.g., H-ZSM-5.^[84]

1.5 Towards the optimal MTH performance

The proposed hydrocarbon pool mechanism demonstrates the general reactions network starting from MeOH or dimethyl ether to the final products including olefins and aromatics. As introduced in the previous section, the nature (amount and type) of the hydrocarbon pool species ultimately determines the reactions in the MTH process accounting for different product distributions. Among all control parameters for the formation of hydrocarbon pool species, the zeolite topology and the acid site in the framework are of vital importance. Therefore, their roles in the MTH mechanism and the following process optimization will be discussed here.

Zeolites are crystalline aluminosilicates. Zeolite framework is composed of very regular channels and cavities of molecular (nanometre) size (therefore also called molecular sieves), providing a high specific surface area. The uniform micropores of the zeolite catalyst ensure a decent product shape selectivity, which means that the formation of larger products will be inhibited by the pore size (**Figure 1.8(a)**).^[85, 86] Meanwhile, the transition state selectivity would determine whether a certain transition state can be formed and stabilized in the confined location leading to specific products (routes **b-c** in **Figure 1.8**).^[86]

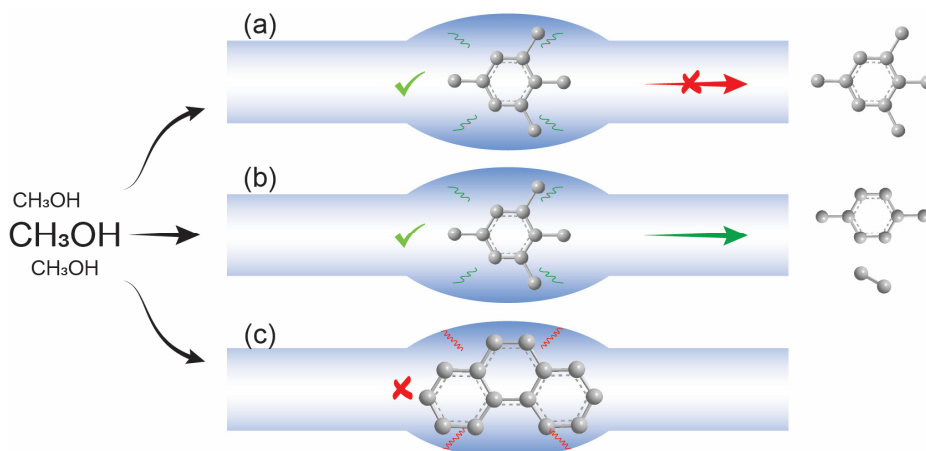


Figure 1.8. Basic mechanisms of product shape selectivity (a-b) and transition-state shape selectivity (c) in the MTH process.

There are more than 250 natural existing or synthesized zeolite topologies in the database.^[87] However, almost all zeolite-catalyzed reaction processes are based on a limited number of frameworks, the so-called Big Five (FAU, MFI, FER, MOR, and BEA). After the discovery of the MTH process over MFI-type H-ZSM-5 zeolite catalysts, CHA-type zeolites such as SAPO-34 and SSZ-13 became important catalysts for the MTO process attributed to their large cage and narrow windows leading to a narrower product distribution than H-ZSM-5. Nowadays, more zeolites of different topologies have been synthesized. The evaluation of their performance in the MTH process becomes a probe of guest-host interactions between organic molecules and the zeolite framework.

The basic structure of the zeolite framework unit is composed of silicon or aluminum tetrahedral coordinated by oxygens. If a cation like proton is to compensate for the negative charge from the trivalent aluminum in the framework, then a so-called Brønsted acid site is formed. Although the MeOH conversion proceeds via the indirect reaction mechanism, in which organic intermediates behave as the active sites to produce the final hydrocarbons, the formation and stabilization of primary olefins and bulky hydrocarbon pool intermediates, isomerization, cracking, and dealkylation reactions still occur over the Brønsted acid sites. Researchers found that the MTH catalytic performance may be completely different, although the tested zeolites possess the same topology but are synthesized under different conditions.^[88, 89] This occurrence clearly demonstrates that, in addition to the zeolite topology, other structural parameters like the concentration, strength, and more interestingly, the spatial distribution of

the Brønsted acid sites in the zeolite also determine the MTH catalytic performance. By increasing the Brønsted acid sites (lattice Al) concentration, the chance of interaction between guest substrates and Brønsted acid sites simultaneously increases, promoting the propagation reactions in the aromatic cycle and increasing aromatics and ethylene formation.^[75, 90] Besides the concentration, acid strength also has a significant effect on the MTH performance, which was initially investigated by Yuen^[91] and Olsbye^[92, 93], who separately compared the MTH performance over aluminosilicate and silicoaluminophosphate versions of CHA-type (H-SSZ-13 versus H-SAPO-34) and AFI-type (H-SSZ-24 versus H-SAPO-5) zeolites. Results showed that the aluminosilicate version of CHA-type and AFI-type, H-SSZ-13 and H-SSZ-24, respectively, enhances the MTH reaction rate in general resulting in a lower temperature of operation to reach the optimal performance (the highest MeOH throughput before deactivation). In the AFI-type zeolite composed of large-size (12-member ring) 1D pores, the more acidic H-SSZ-24 produces more aromatics in comparison with the moderately acidic H-SAPO-5. Furthermore, the higher deactivation rate over aluminosilicates (H-SSZ-13 and H-SSZ-24) creates more coke making them less stable than their silicoaluminophosphate counterparts. Moreover, zeolites with the same Brønsted acid sites density and strength can still exhibit a substantially different MTO performance, which is ascribed to the heterogeneous distribution of Al within the crystal.^[94] The presence of strong Brønsted acid sites on the external surface of zeolite crystallites was shown to promote coking and decreases the catalyst lifetime.^[95] At a high Al content when Al ions are in close vicinity, separated by two or more silicon tetrahedra, the so-called Al_{pair} is formed. The cooperation of the Brønsted acid sites associated with such Al_{pair} decreases the energy barrier for the formation of aromatic intermediates^[96] eventually increasing the selectivity to aromatic products at the expense of the selectivity to propylene. Zeolite morphology is another parameter mainly associated with deactivation; its impact has been discussed in the section on MTH deactivation.

To achieve a highly selective MTH process over a rather stable catalyst, more strategies after determining the zeolite topology have been reported based on the abovementioned structure-performance relationships:

Al distribution. Obviously, the product distribution and catalyst stability can be improved by reducing the concentration of Brønsted acid sites via decreasing the use of Al precursors (*e.g.*, sodium aluminate) during the zeolite synthesis.

Here, the concern is to tailor the spatial distribution of Brønsted acid sites in the zeolite framework via selectively introducing the Al into the structure. Researchers found that the Al siting is controlled by the thermodynamic property and kinetic factors. The theoretical results support that Al atoms at particular lattice T sites in the zeolite framework are more energetically favored, although the real Al distribution is strongly affected by many parameters during the synthesis including Si/Al sources, used structure-directing agents, charge-balance cations, and heteroatoms. Readers are referred to ref^[97] for an in-depth discussion of these influences on Al siting. The impact of lattice Al location, *e.g.*, in the channels or the channel intersections in the ZSM-5 in the MTH process, arises from the void space these sites are facing in the zeolite framework, resulting in different steric constraints (confinement effect) on the transition state of hydrocarbon pool intermediates. As an example, the Al located in the channel intersections in H-ZSM-5 facing a larger void space can accommodate bulkier hydrocarbon pool species like aromatics and accordingly promote the production of light aromatics and ethylene.^[89, 98] Nowadays, because of the wide application of more characterization tools, including ²⁷Al solid state NMR (nuclear magnetic resonance) spectroscopy^[89], UV/vis (ultraviolet/visible) spectroscopy of Co(II)-ion exchanged zeolites^[99], FT-IR (fourier transform-infrared) spectroscopy^[100], EPR (electron paramagnetic resonance) spectroscopy of Zn-exchanged zeolites^[101], probe reactions^[89] and advanced atom probe tomography^[102], the supramolecular view on the correlation between Al sitting and MTH performance becomes possible and draws more attention in the rational MTH catalyst design.

Phosphorus incorporation. The post-modification of zeolites with P-containing precursor is well known as a promotor in many zeolite-catalyzed reactions including fluid catalytic cracking^[103, 104] and the MTH process^[105]. As a promoter in the former process, phosphorus incorporation sufficiently increases the hydrothermal stability of the zeolite structure.^[106] Meanwhile, the addition of P into the micropore of zeolites also reduces the concentration and, more importantly, the strength of the Brønsted acid sites after interacting with Al, forming different types of aluminum phosphates.^[107-109] These new Al configurations after P incorporation are mostly attributed to the tetra-coordinated, but also to penta- or hexa-coordinated aluminums, which might distort the zeolite structure and reduce the crystallinity.^[110-112] About the impact of post-modification of P on different zeolite structures, readers are referred to a thorough review of Van der Bij and Weckhuysen.^[110] As a result of the reduced concentration and strength of Brønsted acid sites, the selectivity to light olefins

like propylene in the MTH process is significantly improved. Meanwhile, the catalyst lifetime (total throughput of MeOH before the deactivation) is prolonged.^[105, 111, 113, 114]

Metal modifications. Metal addition is also one of the main strategies in the acid site engineering. There are two distinct ways to introduce metal sites into the zeolites at different locations. One is called the direct or one-pot synthesis method, in which the metal species are encapsulated or located directly in the framework positions during zeolite crystallization. The other is the post-synthesis approach, where the metal species are generated on the extraframework (ion-exchanged) positions in a pre-existing zeolite. For the details of these preparation strategies, readers are referred to the review of Opanasenko and Martinez.^[115] Alkaline earth metals like Mg^[116-119], Ca^[116, 117, 119-121], Sr^[116, 117, 119], Ba^[117, 122] and transition metals like Ni and Co^[123] are incorporated to increase the selectivity to light olefins. An early study supports that the loss of Brønsted acid sites once exchanged with metal sites and optimized shape selectivity upon metal encapsulation in the micropores are the main reasons for the improved product selectivity to light olefins and extended lifetime in the MTO process. Besides the exchanging with Brønsted acid sites, the newly incorporated acid sites, the so-called Lewis acid sites from the newly added metal, may introduce new reaction paths or changes the kinetics of a certain elementary step resulting in the different product distribution.^[124] To meet the ever-increasing demand for light aromatics, the MTA process is a promising route to produce these basic building blocks from non-fossil fuel resources. To increase the selectivity to light aromatics from MeOH, metals like Ag^[125], Zn^[126], and Ga^[126] are added to catalyze the dehydrogenation reaction towards light aromatics in H-ZSM-5. However, due to the enhanced reactions towards aromatics, the consecutive polyaromatization is inevitably promoted causing the faster catalyst deactivation.

Process conditions optimization. Besides optimizing the operating conditions, *e.g.* temperature^[127], the most straightforward strategy to enhance the yield of target products is to co-feed either olefins or aromatics with MeOH aiming at the propagation of the olefin cycle or aromatic cycle, respectively.^[128] Interestingly, co-feeding olefins or aromatics (preferably ¹³C-labeled) with MeOH has been initially used as the tool to investigate the MTH mechanism and the hydrocarbon pool concept. Lercher and co-workers found that co-feeding olefins or aromatics with MeOH can shorten the initiation phase, corresponding to the induction period for the hydrocarbon pool build-up. However, other than

facilitating the olefin methylation, co-feeding olefins like 1-pentene does not alter the product distribution at the MeOH conversion higher than 70%. On the contrary, co-feeding light aromatics like benzene, toluene or xylenes can promote the aromatic cycle reactions resulting in a higher yield of ethylene and aromatics.^[129] Besides co-feeding olefins and aromatics, co-feeding high-pressure water^[130-132] or hydrogen^[132, 133] can greatly extend the lifetime of the MTH process. Although an irreversible hydrolysis of P-O-Al bond by water in SAPO-34 can be found after a long-term MTO running^[130], the presence of co-fed water can significantly increase the single-run stability of the catalyst against deactivation. Possible reasons are the competing adsorption of water and highly methylated benzenes as coke precursors, suppressing the consecutive reactions towards the polyaromatics.^[134] The addition of hydrogen enhances the catalytic hydrogenation ability of zeolites against the dehydrogenation process from MeOH and light olefins to highly unsaturated polyaromatics. Furthermore, co-feeding high-pressure water and hydrogen exhibits a synergy effect, which further extends the lifetime of the MTO process compared to co-feeding MeOH with only pure water or hydrogen.^[132]

Morphology modification. As discussed in “MTH deactivation”, on the one hand, the zeolite's molecular-size channels enable precise shape selectivity, whereas on the other hand, they may induce mass-transport issues, notably in the MTH process, where bulky polyaromatics, as inert coking species, are the major cause of catalyst deactivation. Therefore, much effort has been put into the synthesis of nano-sized zeolite crystals or creating hierarchical structures in the as-prepared zeolite materials to achieve a long lifetime in the MTH process. Multiple strategies include varying synthesis temperature^[135, 136], seed-assisted synthesis^[137], surfactant addition^[79], and post-modifications such as steaming^[138] and base/acid leaching^[139, 140] have been developed. Readers are referred to refs^[141, 142] for the detailed synthesis of nano-sized or mesoporous zeolites.

After more than 30 years of research, the MTH process remains one of the most popular topics of research in catalysis chemistry, engineering and technology. The extreme complexity of the MTH process, in which many parameters play a role, not only brings challenges for process optimization, but also hinders the kinetic study for in-depth understanding of the hydrocarbon pool mechanism and molecular-level structure-performance relationship. The topic must be revisited to answer multiple questions: “what is the major descriptor directing the selectivity of products?”; “what is the exact effect of metal

modification? How does metal affect the reaction pathways?"; "What is exactly the hydrocarbon pool? how does MeOH react with the pool forming the final product?". Answering these questions will give us further insight in the mechanism and opens the door to process optimization.

1.6 Outline of this thesis

The main challenges in the industrialized MTH process are to raise the MeOH selectivity to favor olefins or aromatics rather than alkanes and to increase the MeOH conversion capacity, which can be only achieved by a deep understanding of the complex reaction network, and the hydrocarbon pool mechanism.

Outstanding questions in this thesis are (i) among all introduced morphological and acidic properties of zeolite catalysts, what is/are the key performance indicators controlling the MeOH selectivity and catalyst stability? (ii) the nature of the hydrocarbon pool under the reaction conditions and how does MeOH react with pool species forming final products (iii) how to modify the acidity via metal incorporations to tune the selectivity and to improve the stability simultaneously?

Chapter 2 focuses on the application of 10-membered ring zeolites in the MTO process. A thorough analysis of zeolite physicochemical properties (topology, crystal size, and acidity) is performed and linked to the catalytic performance. Special attention is put to the Al (active sites) distribution within the crystal and zeolite framework by multiple characterizations including Co^{2+} ion exchange, ^{27}Al solid-state NMR, and 3-methylpentane cracking test. It is demonstrated that the enrichment of lattice Al in the channels is the primary key performance indicator controlling the selectivity to propylene in the MTO process, while the deactivation process appears to be a much more complex process depending on a wider range of zeolite properties.

Chapter 3 and **Chapter 4** are dedicated to the transient kinetic investigation of the hydrocarbon pool mechanism. In **Chapter 3**, a novel pulse-GC synchronization approach, called fast scanning-pulse analysis (FASPA), is applied to quantify the production in the transient operation. This FASPA technique allows the (sub-)second resolution of the full temporal products spectrum response upon a MeOH pulse providing direct and quantitative insight into the MTH reactions in those initial periods. Globally two consecutive reaction pathways can be discerned upon a MeOH pulse: a very fast primary product

formation in the presence of MeOH in a narrow active MTH reaction zone in the catalyst bed, followed by a slower formation of light aromatics, which is closely related to the decomposition and release of HCP species and secondary reactions in the absence of MeOH in the downstream part of the catalyst bed. In **Chapter 4**, the dynamics of the HCP mechanism in the medium-pore H-ZSM-5 zeolite catalyst is further investigated via ^{13}C -/ ^{12}C -MeOH/water switch experiments and the developed FASPA approach. Results confirm that a parallel olefin cycle route dominates the production of olefins and also aromatics via the subsequent cyclization and aromatization reactions in H-ZSM-5. In particular, the production routes of aromatics are directly discerned upon MeOH pulse injection involving the displacement, HCP reactions and secondary formations, demonstrating the dynamic feature of the HCP mechanism in the MTH process over H-ZSM-5. The role of water in the production of aromatics is addressed by competitive adsorption on the Brønsted acid sites.

Chapter 5 focuses on the bimetallic [Ca,Ga]/HZSM-5 in the MTA process. The MTA test showed that the high selectivity to aromatics and fast deactivation can be decoupled by the addition of a small amount of Ca to Ga-modified ZSM-5. A combined experimental and computational study revealed that the cooperation between the extraframework Ca and Ga ions inside the zeolite pores results in a hybrid structure with higher tolerance to water hydration and a higher energy barrier for C–H bond activation. All these observations explain the increased MTA lifetime for [Ca,Ga]/HZSM-5.

In the end, a summary of this thesis and corresponding outlook to the MTH catalysis are given. As a promising approach to producing the crucial hydrocarbon building blocks, MTH is recognized as one of the key ingredients within the MeOH economy contributing to green chemistry and CO₂ neutrality. This PhD thesis clearly demonstrates that a comprehensive structure-performance relationship is required to find out the key pulling strings to tune the product selectivity in the complex MTH process.

Note that all chapters have been written as individual publications and can be read independently. Because of this, some overlap may be present.

References

- (1) UNFCCC. *Glasgow Climate Pact, Decision -/CP. 26, advance unedited version*, **2021**, <https://unfccc.int/documents/310475>.
- (2) Olah, G. A.; Goeppert, A.; Prakash, G. S. *The Journal of Organic Chemistry* **2008**, *74* (2), 487-498.
- (3) Xu, X.; Moulijn, J. A. *Energy & Fuels* **1996**, *10* (2), 305-325.
- (4) W. Crabtree, G.; Mildred, S. D.; Michelle, V. B. *Physics Today* **2004**, *57* (12), 39-44.
- (5) Ayers, W. M. In *191. American Chemical Society national meeting, New York, NY (USA), 13-18 Apr 1986*, United States; **1988**.
- (6) Chang, C. D.; Silvestri, A. J. *Journal of Catalysis* **1977**, *47* (2), 249-259.
- (7) Rossi, F.; Rovaglio, M.; Manenti, F., in *Computer Aided Chemical Engineering, Vol. 45*, Elsevier, **2019**, pp. 873-897.
- (8) Rice, F. O.; Herzfeld, K. F. *Journal of the American Chemical Society* **1934**, *56* (2), 284-289.
- (9) Mokrani, T.; Scurrall, M. *Catalysis Reviews* **2009**, *51* (1), 1-145.
- (10) Cancer, I. A. f. R. o. *IARC Monographs on the Evaluation of the Carcinogenic Risk of Chemicals to Man, IARC Scientific Publications* **1974**, *7*, 111-140.
- (11) Goldstein, B. D.; Smith, M. T., in *Tumour Site Concordance and Mechanisms of Carcinogenesis*, International Agency for Research on Cancer, Lyon (FR), **2019**.
- (12) Le Bel, J. A.; Greene, W. H. *American Chemical Journal* **1880**, *2*, 6.
- (13) Chang, C. D.; Silvestri, A. J. *CHEMTECH* **1987**, *17:10*, 624-631.
- (14) Chang, C. D. *Catalysis Reviews* **1984**, *26* (3-4), 323-345.
- (15) Coughlin, R. W.; Verykios, X. E. *Journal of Catalysis* **1977**, *48* (1), 249-257.
- (16) Dahl, I. M.; Kolboe, S. *Catalysis Letters* **1993**, *20* (3), 329-336.
- (17) Dahl, I. M.; Kolboe, S. *Journal of Catalysis* **1994**, *149* (2), 458-464.
- (18) Dahl, I. M.; Kolboe, S. *Journal of Catalysis* **1996**, *161* (1), 304-309.
- (19) Ye, M.; Tian, P.; Liu, Z. *Engineering* **2021**, *7* (1), 17-21.
- (20) Lin, S.; Zhi, Y.; Chen, W.; Li, H.; Zhang, W.; Lou, C.; Wu, X.; Zeng, S.; Xu, S.; Xiao, J.; Zheng, A.; Wei, Y.; Liu, Z. *Journal of the American Chemical Society* **2021**, *143* (31), 12038-12052.
- (21) Sher, J.; Van Egmond, C. US 71700603 A, **2005**.
- (22) Cao, G.; Colle, T. H.; Martens, L. R. M.; Brown, S. H.; Xu, T. US 83754610 A, **2011**.
- (23) Bozzano, A. G.; Gregor, J. H.; Senetar, J. J. US 201113193805 A, **2014**.
- (24) Kalnes, T. N.; Voskoboynikov, T. V. US 3631205 A, **2008**.
- (25) Kalnes, T. N.; Wei, D. H.; Glover, B. K. US 94383304 A, **2008**.
- (26) Rothaemel, M.; Buchhold, H.; Koempel, H.; Glasmacher, A.; Ochs, A. EP 2006009076 W, **2007**.
- (27) Kumiai, S. W. K. G. K. *Progress in CI Chemistry in Japan*; Kodansha, **1989**.
- (28) Huang, G.; Hu, J.; Li, J.; Shi, X.; Ding, W.; Zhou, X. *Chemical Industry and Engineering Progress* **2020**, *39* (10), 3966-3974.
- (29) Li, T.; Shoinchorova, T.; Gascon, J.; Ruiz-Martínez, J. *ACS Catalysis* **2021**, *11* (13), 7780-7819.
- (30) Kagi, D. *Journal of Catalysis* **1981**, *69* (1), 242-243.
- (31) Ono, Y.; Mori, T. *Journal of the Chemical Society, Faraday Transactions 1: Physical Chemistry in Condensed Phases* **1981**, *77*, 2209-2221.

- (32) Tajima, N.; Tsuneda, T.; Toyama, F.; Hirao, K. *Journal of the American Chemical Society* **1998**, *120* (32), 8222-8229.
- (33) Chang, C. D. *Journal of Catalysis* **1981**, *69* (1), 244-245.
- (34) Lesthaeghe, D.; Van Speybroeck, V.; Marin, G. B.; Waroquier, M. *Chemical Physics Letters* **2006**, *417* (4), 309-315.
- (35) Li, J.; Wei, Z.; Chen, Y.; Jing, B.; He, Y.; Dong, M.; Jiao, H.; Li, X.; Qin, Z.; Wang, J.; Fan, W. *Journal of Catalysis* **2014**, *317*, 277-283.
- (36) Chowdhury, A. D.; Houben, K.; Whiting, G. T.; Mokhtar, M.; Asiri, A. M.; Al-Thabaiti, S. A.; Basahel, S. N.; Baldus, M.; Weckhuysen, B. M. *Angewandte Chemie International Edition* **2016**, *55* (51), 15840-15845.
- (37) Liu, Y.; Müller, S.; Berger, D.; Jelic, J.; Reuter, K.; Tonigold, M.; Sanchez-Sanchez, M.; Lercher, J. A. *Angewandte Chemie International Edition* **2016**, *55* (19), 5723-5726.
- (38) Olah, G. A.; Klopman, G.; Schlosberg, R. H. *Journal of the American Chemical Society* **1969**, *91* (12), 3261-3268.
- (39) Olah, G. A.; Demember, J. R.; Shen, J. *Journal of the American Chemical Society* **1973**, *95* (15), 4952-4956.
- (40) Sinclair, P. E.; Catlow, C. R. A. *The Journal of Physical Chemistry B* **1997**, *101* (3), 295-298.
- (41) Olah, G. A.; Prakash, G. K. S.; Ellis, R. W.; Olah, J. A. *Journal of the Chemical Society, Chemical Communications* **1986**, (1), 9-10.
- (42) Lesthaeghe, D.; Van Speybroeck, V.; Marin, G. B.; Waroquier, M. *Industrial & Engineering Chemistry Research* **2007**, *46* (26), 8832-8838.
- (43) Wu, X.; Xu, S.; Zhang, W.; Huang, J.; Li, J.; Yu, B.; Wei, Y.; Liu, Z. *Angewandte Chemie International Edition* **2017**, *56* (31), 9039-9043.
- (44) Sun, T.; Chen, W.; Xu, S.; Zheng, A.; Wu, X.; Zeng, S.; Wang, N.; Meng, X.; Wei, Y.; Liu, Z. *Chem* **2021**, *7* (9), 2415-2428.
- (45) Hutchings, G. J.; van Rensburg, L. J.; Pickl, W.; Hunter, R. *Journal of the Chemical Society, Faraday Transactions 1: Physical Chemistry in Condensed Phases* **1988**, *84* (5), 1311-1328.
- (46) Hunter, R.; Hutchings, G. J. *Journal of the Chemical Society, Chemical Communications* **1987**, (5), 377-379.
- (47) Yamazaki, H.; Shima, H.; Imai, H.; Yokoi, T.; Tatsumi, T.; Kondo, J. N. *Angewandte Chemie International Edition* **2011**, *50* (8), 1853-1856.
- (48) Yamazaki, H.; Shima, H.; Imai, H.; Yokoi, T.; Tatsumi, T.; Kondo, J. N. *The Journal of Physical Chemistry C* **2012**, *116* (45), 24091-24097.
- (49) Comas-Vives, A.; Valla, M.; Copéret, C.; Sautet, P. *ACS Central Science* **2015**, *1* (6), 313-319.
- (50) Langner, B. E. *Applied Catalysis* **1982**, *2* (4), 289-302.
- (51) Mole, T.; Bett, G.; Seddon, D. *Journal of Catalysis* **1983**, *84* (2), 435-445.
- (52) Dessau, R. M.; LaPierre, R. B. *Journal of Catalysis* **1982**, *78* (1), 136-141.
- (53) Mikkelsen, O.; Rønning, P. O.; Kolboe, S. *Microporous and Mesoporous Materials* **2000**, *40* (1), 95-113.
- (54) Haw, J. F.; Goguen, P. W.; Xu, T.; Skloss, T. W.; Song, W.; Wang, Z. *Angewandte Chemie International Edition* **1998**, *37* (7), 948-949.
- (55) Goguen, P. W.; Xu, T.; Barich, D. H.; Skloss, T. W.; Song, W.; Wang, Z.; Nicholas, J. B.; Haw, J. F. *Journal of the American Chemical Society* **1998**, *120* (11), 2650-2651.

- (56) Wang, C.; Chu, Y.; Zheng, A.; Xu, J.; Wang, Q.; Gao, P.; Qi, G.; Gong, Y.; Deng, F. *Chemistry – A European Journal* **2014**, *20* (39).
- (57) Xu, T.; Barich, D. H.; Goguen, P. W.; Song, W.; Wang, Z.; Nicholas, J. B.; Haw, J. F. *Journal of the American Chemical Society* **1998**, *120* (16), 4025-4026.
- (58) Song, W.; Nicholas, J. B.; Sassi, A.; Haw, J. F. *Catalysis Letters* **2002**, *81* (1), 49-53.
- (59) Xu, S.; Zheng, A.; Wei, Y.; Chen, J.; Li, J.; Chu, Y.; Zhang, M.; Wang, Q.; Zhou, Y.; Wang, J.; Deng, F.; Liu, Z. *Angewandte Chemie International Edition* **2013**, *52* (44), 11564-11568.
- (60) Sullivan, R. F.; Egan, C. J.; Langlois, G. E.; Sieg, R. P. *Journal of the American Chemical Society* **1961**, *83* (5), 1156-1160.
- (61) Lesthaeghe, D.; Horr , A.; Waroquier, M.; Marin, G. B.; Van Speybroeck, V. *Chemistry – A European Journal* **2009**, *15* (41), 10803-10808.
- (62) McCann, D. M.; Lesthaeghe, D.; Kletnieks, P. W.; Guenther, D. R.; Hayman, M. J.; Van Speybroeck, V.; Waroquier, M.; Haw, J. F. *Angewandte Chemie International Edition* **2008**, *47* (28), 5179-5182.
- (63) Svelle, S.; Joensen, F.; Nerlov, J.; Olsbye, U.; Lillerud, K.-P.; Kolboe, S.; Bj rgen, M. *Journal of the American Chemical Society* **2006**, *128* (46), 14770-14771.
- (64) Chen, D.; Rebo, H. P.; Holmen, A. *Chemical Engineering Science* **1999**, *54* (15), 3465-3473.
- (65) Chen, D.; Rebo, H. P.; Moljord, K.; Holmen, A. *Industrial & Engineering Chemistry Research* **1999**, *38* (11), 4241-4249.
- (66) Schulz, H. *Catalysis Today* **2010**, *154* (3), 183-194.
- (67) Gao, S.; Xu, S.; Wei, Y.; Qiao, Q.; Xu, Z.; Wu, X.; Zhang, M.; He, Y.; Xu, S.; Liu, Z. *Journal of Catalysis* **2018**, *367*, 306-314.
- (68) Bibby, D. M.; McLellan, G. D.; Howe, R. F., in *Studies in Surface Science and Catalysis, Vol. 34*, Elsevier, **1987**, pp. 651-658.
- (69) Bleken, F. L.; Barbera, K.; Bonino, F.; Olsbye, U.; Lillerud, K. P.; Bordiga, S.; Beato, P.; Janssens, T. V. W.; Svelle, S. *Journal of Catalysis* **2013**, *307*, 62-73.
- (70) Mores, D.; Stavitski, E.; Kox, M. H. F.; Kornatowski, J.; Olsbye, U.; Weckhuysen, B. M. *Chemistry – A European Journal* **2008**, *14* (36), 11320-11327.
- (71) Mores, D.; Kornatowski, J.; Olsbye, U.; Weckhuysen, B. M. *Chemistry – A European Journal* **2011**, *17* (10), 2874-2884.
- (72) M ller, S.; Liu, Y.; Vishnuvarthan, M.; Sun, X.; van Veen, A. C.; Haller, G. L.; Sanchez-Sanchez, M.; Lercher, J. A. *Journal of Catalysis* **2015**, *325*, 48-59.
- (73) Hutchings, G. J.; Gottschalk, F.; Hunter, R. *Industrial & Engineering Chemistry Research* **1987**, *26* (3), 635-637.
- (74) Yuan, C.; Wei, Y.; Li, J.; Xu, S.; Chen, J.; Zhou, Y.; Wang, Q.; Xu, L.; Liu, Z. *Chinese Journal of Catalysis* **2012**, *33* (2), 367-374.
- (75) Khare, R.; Liu, Z.; Han, Y.; Bhan, A. *Journal of Catalysis* **2017**, *348*, 300-305.
- (76) Schmidt, J. E.; Poplawsky, J. D.; Mazumder, B.; Attila,  .; Fu, D.; de Winter, D. A. M.; Meirer, F.; Bare, S. R.; Weckhuysen, B. M. *Angewandte Chemie International Edition* **2016**, *55* (37), 11173-11177.
- (77) Lee, S.; Choi, M. *Journal of Catalysis* **2019**, *375*, 183-192.
- (78) Hu, S.; Shan, J.; Zhang, Q.; Wang, Y.; Liu, Y.; Gong, Y.; Wu, Z.; Dou, T. *Applied Catalysis A: General* **2012**, *445-446*, 215-220.
- (79) Choi, M.; Na, K.; Kim, J.; Sakamoto, Y.; Terasaki, O.; Ryoo, R. *Nature* **2009**, *461*, 246.

- (80) Jeon, M. Y.; Kim, D.; Kumar, P.; Lee, P. S.; Rangnekar, N.; Bai, P.; Shete, M.; Elyassi, B.; Lee, H. S.; Narasimharao, K. *Nature* **2017**, *543* (7647), 690.
- (81) Wan, Z.; Li, G. K.; Wang, C.; Yang, H.; Zhang, D. *Applied Catalysis A: General* **2018**, *549*, 141-151.
- (82) Meng, L.; Zhu, X.; Wannapakdee, W.; Pestman, R.; Goesten, M. G.; Gao, L.; van Hoof, A. J. F.; Hensen, E. J. M. *Journal of Catalysis* **2018**, *361*, 135-142.
- (83) Sazama, P.; Pastvova, J.; Kaucky, D.; Moravkova, J.; Rathousky, J.; Jakubec, I.; Sadovska, G. *Journal of Catalysis* **2018**, *364*, 262-270.
- (84) Khare, R.; Millar, D.; Bhan, A. *Journal of Catalysis* **2015**, *321*, 23-31.
- (85) Hereijgers, B. P.; Bleken, F.; Nilsen, M. H.; Svelle, S.; Lillerud, K.-P.; Bjørgen, M.; Weckhuysen, B. M.; Olsbye, U. *Journal of Catalysis* **2009**, *264* (1), 77-87.
- (86) Smit, B.; Maesen, T. L. *Nature* **2008**, *451* (7179), 671-678.
- (87) Baerlocher, C.; McCusker, L. B. *Database of Zeolite Structures*, <http://www.iza-structure.org/databases/>.
- (88) Li, C.; Paris, C.; Martínez-Triguero, J.; Boronat, M.; Moliner, M.; Corma, A. *Nature Catalysis* **2018**, *1* (7), 547-554.
- (89) Yokoi, T.; Mochizuki, H.; Namba, S.; Kondo, J. N.; Tatsumi, T. *The Journal of Physical Chemistry C* **2015**, *119* (27), 15303-15315.
- (90) Wei, R.; Li, C.; Yang, C.; Shan, H. *Journal of Natural Gas Chemistry* **2011**, *20* (3), 261-265.
- (91) Yuen, L.-T.; Zones, S. I.; Harris, T. V.; Gallegos, E. J.; Auroux, A. *Microporous Materials* **1994**, *2* (2), 105-117.
- (92) Westgård Erichsen, M.; Svelle, S.; Olsbye, U. *Catalysis Today* **2013**, *215*, 216-223.
- (93) Bleken, F.; Bjørgen, M.; Palumbo, L.; Bordiga, S.; Svelle, S.; Lillerud, K.-P.; Olsbye, U. *Topics in Catalysis* **2009**, *52* (3), 218-228.
- (94) Yarulina, I.; Chowdhury, A. D.; Meirer, F.; Weckhuysen, B. M.; Gascon, J. *Nature Catalysis* **2018**, *1* (6), 398-411.
- (95) Danilina, N.; Krumeich, F.; Castelanelli, S. A.; van Bokhoven, J. A. *The Journal of Physical Chemistry C* **2010**, *114* (14), 6640-6645.
- (96) Pashkova, V.; Sklenak, S.; Klein, P.; Urbanova, M.; Dědeček, J. *Chemistry – A European Journal* **2016**, *22* (12), 3937-3941.
- (97) Wang, S.; He, Y.; Jiao, W.; Wang, J.; Fan, W. *Current Opinion in Chemical Engineering* **2019**, *23*, 146-154.
- (98) Liang, T.; Chen, J.; Qin, Z.; Li, J.; Wang, P.; Wang, S.; Wang, G.; Dong, M.; Fan, W.; Wang, J. *ACS Catalysis* **2016**, *6* (11), 7311-7325.
- (99) Dědeček, J.; Kaucký, D.; Wichterlová, B.; Gonsiorová, O. *Physical Chemistry Chemical Physics* **2002**, *4* (21), 5406-5413.
- (100) Potter, M. E.; Cholerton, M. E.; Kezina, J.; Bounds, R.; Carravetta, M.; Manzoli, M.; Gianotti, E.; Lefenfeld, M.; Raja, R. *ACS Catalysis* **2014**, *4* (11), 4161-4169.
- (101) Morra, E.; Berlier, G.; Borfecchia, E.; Bordiga, S.; Beato, P.; Chiesa, M. *The Journal of Physical Chemistry C* **2017**, *121* (26), 14238-14245.
- (102) Perea, D. E.; Arslan, I.; Liu, J.; Ristanović, Z.; Kovarik, L.; Arey, B. W.; Lercher, J. A.; Bare, S. R.; Weckhuysen, B. M. *Nature Communications* **2015**, *6* (1), 1-8.
- (103) Caeiro, G.; Magnoux, P.; Lopes, J. M.; Ribeiro, F. R.; Menezes, S. M. C.; Costa, A. F.; Cerqueira, H. S. *Applied Catalysis A: General* **2006**, *314* (2), 160-171.
- (104) Viswanathan, B.; Pulikottil, A. C. *Catalysis Letters* **1993**, *22* (4), 373-379.
- (105) Zhao, G.; Teng, J.; Xie, Z.; Jin, W.; Yang, W.; Chen, Q.; Tang, Y. *Journal of Catalysis* **2007**, *248* (1), 29-37.

- (106) Blasco, T.; Corma, A.; Martínez-Triguero, J. *Journal of Catalysis* **2006**, *237* (2), 267-277.
- (107) Kaeding, W. W.; Butter, S. A. *Journal of Catalysis* **1980**, *61* (1), 155-164.
- (108) Lercher, J. A.; Rimplmayr, G. *Applied Catalysis* **1986**, *25* (1), 215-222.
- (109) Xue, N.; Chen, X.; Nie, L.; Guo, X.; Ding, W.; Chen, Y.; Gu, M.; Xie, Z. *Journal of Catalysis* **2007**, *248* (1), 20-28.
- (110) van der Bij, H. E.; Weckhuysen, B. M. *Chemical Society Reviews* **2015**, *44* (20), 7406-7428.
- (111) Song, Y.; Zhang, L.-l.; Li, G.-d.; Shang, Y.-s.; Zhao, X.-m.; Ma, T.; Zhang, L.-m.; Zhai, Y.-l.; Gong, Y.-j.; Xu, J.; Deng, F. *Fuel Processing Technology* **2017**, *168*, 105-115.
- (112) Vu, D. V.; 廣田, 雄.; 西山, 憲.; 江頭, 靖.; 上山, 惟. *Journal of the Japan Petroleum Institute* **2010**, *53* (4), 232-238.
- (113) Li, P.; Zhang, W.; Han, X.; Bao, X. *Catalysis Letters* **2010**, *134* (1), 124-130.
- (114) Niu, X.; Wang, K.; Bai, Y.; Du, Y.-e.; Chen, Y.; Dong, M.; Fan, W. *Catalysts* **2020**, *10* (5), 484.
- (115) Shamzhy, M.; Opanasenko, M.; Concepción, P.; Martínez, A. *Chemical Society Reviews* **2019**, *48* (4), 1095-1149.
- (116) Okado, H.; Shoji, H.; Sano, T.; Ikai, S.; Hagiwara, H.; Takaya, H. *Applied Catalysis* **1988**, *41*, 121-135.
- (117) Goto, D.; Harada, Y.; Furumoto, Y.; Takahashi, A.; Fujitani, T.; Oumi, Y.; Sadakane, M.; Sano, T. *Applied Catalysis A: General* **2010**, *383* (1), 89-95.
- (118) Lévesque, P.; Bianchi, D.; Le Van Mao, R.; Pajonk, G. M. *Applied Catalysis* **1990**, *57* (1), 31-43.
- (119) Hideo, O.; Tsuneji, S.; Kunio, S.; Kiyomi, O.; Haruo, T. *Bulletin of the Chemical Society of Japan* **1988**, *61* (9), 3383-3385.
- (120) Suzuki, K.; Kiyozumi, Y.; Matsuzaki, K.; Ikai, S.; Shin, S. *Applied Catalysis* **1988**, *39*, 315-324.
- (121) Yarulina, I.; Bailleul, S.; Pustovarenko, A.; Martinez, J. R.; Wispelaere, K. D.; Hajek, J.; Weckhuysen, B. M.; Houben, K.; Baldus, M.; Van Speybroeck, V. *ChemCatChem* **2016**, *8* (19), 3057-3063.
- (122) Abdillahi, M. M.; El-Nafaty, U. A.; Al-Jarallah, A. M. *Applied Catalysis A: General* **1992**, *91* (1), 1-12.
- (123) Xu, L.; Liu, Z.; Du, A.; Wei, Y.; Sun, Z., in *Studies in Surface Science and Catalysis, Vol. 147*, Elsevier, **2004**, pp. 445-450.
- (124) Yarulina, I.; De Wispelaere, K.; Bailleul, S.; Goetze, J.; Radersma, M.; Abou-Hamad, E.; Vollmer, I.; Goesten, M.; Mezari, B.; Hensen, E. J. M.; Martínez-Espín, J. S.; Morten, M.; Mitchell, S.; Perez-Ramirez, J.; Olsbye, U.; Weckhuysen, B. M.; Van Speybroeck, V.; Kapteijn, F.; Gascon, J. *Nature Chemistry* **2018**, *10* (8), 804-812.
- (125) Inoue, Y.; Nakashiro, K.; Ono, Y. *Microporous Materials* **1995**, *4* (5), 379-383.
- (126) Ono, Y.; Adachi, H.; Senoda, Y. *Journal of the Chemical Society, Faraday Transactions 1: Physical Chemistry in Condensed Phases* **1988**, *84* (4), 1091-1099.
- (127) Chang, C. D.; Chu, C. T. W.; Socha, R. F. *Journal of Catalysis* **1984**, *86* (2), 289-296.
- (128) Ilias, S.; Bhan, A. *Journal of Catalysis* **2012**, *290*, 186-192.
- (129) Sun, X.; Mueller, S.; Shi, H.; Haller, G. L.; Sanchez-Sanchez, M.; van Veen, A. C.; Lercher, J. A. *Journal of Catalysis* **2014**, *314*, 21-31.

- (130) Liu, Y.; Wang, C.; Zhang, L.; Dai, W.; Chu, Y.; Xu, J.; Wu, G.; Gao, M.; Liu, W.; Xu, Z.; Wang, P.; Guan, N.; Dyballa, M.; Ye, M.; Deng, F.; Fan, W.; Li, L. *Nature Communications* **2021**, *12* (1), 4661.
- (131) Marchi, A. J.; Froment, G. F. *Applied Catalysis* **1991**, *71* (1), 139-152.
- (132) Zhao, X.; Li, J.; Tian, P.; Wang, L.; Li, X.; Lin, S.; Guo, X.; Liu, Z. *ACS Catalysis* **2019**, *9* (4), 3017-3025.
- (133) Arora, S. S.; Nieskens, D. L.; Malek, A.; Bhan, A. *Nature Catalysis* **2018**, *1* (9), 666-672.
- (134) De Wispelaere, K.; Wondergem, C. S.; Ensing, B.; Hemelsoet, K.; Meijer, E. J.; Weckhuysen, B. M.; Van Speybroeck, V.; Ruiz-Martínez, J. *ACS Catalysis* **2016**, *6* (3), 1991-2002.
- (135) Zhu, Z.; Xu, H.; Jiang, J.; Wu, H.; Wu, P. *ACS Applied Materials & Interfaces* **2017**, *9* (32), 27273-27283.
- (136) Mertens, M.; Strohmaier, K. G. US 99777801 A, **2005**.
- (137) Reding, G.; Mäurer, T.; Kraushaar-Czarnetzki, B. *Microporous and Mesoporous Materials* **2003**, *57* (1), 83-92.
- (138) Lago, R. M.; Haag, W. O.; Mikovsky, R. J.; Olson, D. H.; Hellring, S. D.; Schmitt, K. D.; Kerr, G. T., in *Studies in Surface Science and Catalysis, Vol. 28*, Elsevier, **1986**, pp. 677-684.
- (139) Morin, S.; Ayrault, P.; Gnep, N. S.; Guisnet, M. *Applied Catalysis A: General* **1998**, *166* (2), 281-292.
- (140) Masaru, O.; Shin-ya, S.; Junko, T.; Yasuto, N.; Eiichi, K.; Masahiko, M. *Chemistry Letters* **2000**, *29* (8), 882-883.
- (141) Tao, Y.; Kanoh, H.; Abrams, L.; Kaneko, K. *Chemical Reviews* **2006**, *106* (3), 896-910.
- (142) van Donk, S.; Janssen, A. H.; Bitter, J. H.; de Jong, K. P. *Catalysis Reviews* **2003**, *45* (2), 297-319.

Chapter 2. An integrated approach to the key parameters in MTO reaction catalyzed by MFI/MEL zeolite materials

Identification of the catalyst characteristics correlating with the key performance parameters including selectivity and stability is key to the rational catalyst design. In this chapter, the catalytic behaviour of MFI, MEL and their respective intergrowth zeolites was studied in detail to identify the property-performance relationship in the methanol-to-olefins process. The detailed material characterization reveals that both the high production of propylene and butylenes and the large methanol conversion capacity correlate with the enrichment of lattice Al sites in the channels of the pentasil structure as identified by ^{27}Al MAS NMR and 3-methylpentane cracking results. The lack of correlation between methanol-to-olefins performance and other catalyst characteristics, such as crystal size, presence of external Brønsted acid sites and Al pairing suggests their less pronounced role in defining the propylene selectivity. Catalyst deactivation is rather complex and is strongly affected by the enrichment of lattice Al in the intersections, the overall Al-content, and crystal size. The intergrowth of MFI and MEL phases accelerates the catalyst deactivation rate.

This Chapter has been published as:

Liu C, Uslamin EA, van Vreeswijk SH, Yarulina I, Ganapathy S, Weckhuysen BM, Kapteijn F, Pidko EA. Chinese Journal of Catalysis. **2022** Jul 1;43(7):1879-93.

2.1 Introduction

The methanol-to-olefins (MTO) technology has the potential to play a major role in the sustainable production of light olefins. It is recognized as one of the key ingredients within the methanol (MeOH) economy concept^[1, 2] enabling the production of the crucial hydrocarbon building blocks, such as light olefins, starting from CO₂ as the primary carbon source.^[3] Despite the worldwide industrialization of the MTO process^[4-6], intense research is still focusing on a better understanding of the underlying structure-performance relationship for the optimization of this catalytic process and the development of more selective and stable catalytic materials.^[7-14] In particular, the growing demand for renewable propylene emphasizes the importance of further optimization of the selectivity of the MTO catalysts towards propylene production.

The mechanism of the MTO process is highly complex. A multitude of parallel and consecutive chemical transformations of the substrates is catalyzed by Brønsted acid sites (BAS) resulting in a range of hydrocarbon products.^[15-19] After a rather short induction period, two catalytic cycles involving the interconversion of confined olefinic and aromatic intermediates promote simultaneously the MeOH conversion and the formation of longer-chain hydrocarbons.^[7, 20-22] The cracking of the olefinic intermediates in the so-called olefinic cycle is solely responsible for the formation of all olefinic products, with ethylene as an exception which is mainly produced via the dealkylation of larger aromatic intermediates within the aromatic cycle^[7, 23].

The concentration, location, and distribution of BAS are of primary importance to define the activity in the MTO process. By increasing the Al concentration, the chance of interaction between guest substrates and BAS simultaneously increases, eventually promoting the aromatic cycle, and increasing aromatics and ethylene formation.^[24, 25] Zeolites with the same BAS density can also exhibit a substantially different MTO performance, ascribed to the heterogeneous distribution of Al within the crystal.^[16] The presence of strong BAS on the external surface of zeolite crystallites was shown to promote coking and decreases the catalyst lifetime.^[26] At high Al content when Al ions are in close vicinity, separated by two or more silicon tetrahedra, the so-called Al_{pair} is formed. The cooperation of the BAS associated with such Al_{pair} decreases the energy barrier for the formation of aromatic intermediates^[27] eventually increasing the selectivity towards aromatic products at the expense of the selectivity towards propylene.

The relative rates of the two catalytic cycles also depend on the topological properties of the confined space, where the reaction takes place, and they determine the selectivity of the catalytic process. The uniform micropores of the zeolite catalyst ensure the efficient confinement and stabilization of the reaction intermediates (transition-state selectivity^[28]), while the pore diameter only allows the products that fit to pass through and escape the zeolite (product-selectivity^[28, 29]). Among more than 230 zeolite topologies, the 10-membered ring (10-MR) zeolites have attracted great interest in the MTO process.^[30-34] Particularly, 10-MR TON-type zeolites consisting of 1-dimensional channels exhibit high selectivity towards C₅₊ hydrocarbons with a negligible contribution of aromatics. Because of shape-selectivity the narrow channels (4.6 Å × 5.7 Å) host the key intermediates of the olefinic cycle, *e.g.* methylcyclopentenyl cations.^[34, 35] However, the application of TON-type zeolites in the MTO process is hindered by fast deactivation, which is probably due to the rapid coke deposition easily blocking the 1D channels^[31, 33, 34]. In this study, catalysts with zeolite topologies MFI (H-ZSM-5) and MEL (H-ZSM-11) of the pentasil family are investigated. These 10-MR zeolite topologies display 3-dimensional channel and intersection systems with very similar diameters. While MFI-type zeolite consists of straight (4.5 Å) and sinusoidal (4.7 Å) channels with intersection (6.4 Å), MEL-type consists of only straight channels (5.2 Å) with intersection (7.7 Å).^[36] These single topologies are further compared with mixed-topology zeolite catalysts consisting of intergrown MFI and MEL crystal phases, indicated by HZBM-10. A detailed skeletal description of how MFI and MEL phases mix at an atomic scale is given in ref^[37]. These 10-MR zeolites with 3-dimensional pores have been widely investigated because of the promising selectivity towards propylene and butylenes in MTO combined with the prolonged lifetime in comparison with 1-dimensional 10-MR zeolites.^[30-32]

The comparative MTO study of MFI-type, MEL-type and TON-type zeolites by Hunger and co-workers^[30] showed that under optimized conditions a comparable selectivity towards propylene (~50%) for MFI-type and MEL-type zeolites can be achieved at an optimal BAS density (~15 mmol/g), while the selectivity towards propylene is reduced to ~38% for TON-type zeolites (BAS ~30 mmol/g). The major conclusion was drawn that the BAS density is an important optimizing parameter for tuning the MTO selectivity, but did not provide insight in the relation with the structural properties of those zeolites. Fan and co-workers compared the MTO performance for MFI- and MEL-type zeolite catalysts and demonstrated that the MEL-type H-ZSM-11 is more selective in

producing light olefins.^[32] Furthermore, it was proposed that for the zeolites with a higher Si/Al ratio (>120), the lattice Al enrichment in the zeolite channels is the key factor that determines the MTO product selectivity. The use of materials featuring an intergrowth framework with mixing MFI and MEL topologies as an MTO catalyst was also shown to enhance the propylene selectivity in comparison with the pure MFI-based H-ZSM-5 catalysts.^[38] By varying the composition of MFI or MEL phases in the zeolite, the MeOH selectivity to propylene could be increased to ca. 46% from 27% for MFI. There is a general consensus in the research community that shape selectivity, ascribed to the subtle differences in the geometry and structure of the zeolite confined space, is one of the key factors that determines the MTO catalyst performance and, particularly, the selectivity towards propylene.^[39] However, the different synthesis methods for different zeolite topologies and various post-synthesis approaches inevitably introduced the variation in other parameters including crystal morphology, Si/Al ratio, Al distribution (at internal or external surface, in channels or intersections), and potentially other physicochemical properties, which all may also substantially affect the catalyst behavior. Therefore, an integrated approach for analyzing all these parameters is crucial to find out the key parameter(s) to control the catalytic performance. A thorough analysis of the possible correspondence thereafter will lead to a comprehensive structural-performance relationship.

In this study a systematic analysis of all the above-mentioned aspects is performed in an attempt to identify in a comprehensive approach the key descriptor(s) that intrinsically control(s) the MTO performance of the 10-MR zeolites under study, namely H-ZSM-5, H-ZSM-11 and an intergrowth phase H-ZBM-10. With this in mind, steady-state MTO tests combined with *operando* UV–vis spectroscopy measurements firstly emphasized the different catalytic behaviors with respect to selectivity, MTO stability, and various features on the surface of MEL-type, MFI-type, and the intergrowth zeolites. Through a wide range of characterization, spectroscopic measurements, and probe reactions, substantial differences were highlighted on the crystal size, BAS distribution over the crystal, Al_{pair} , and Al-siting of all tested zeolites. Combined with the MTO selectivity and stability, the correlation between each of the parameters and the catalytic performance was thoroughly evaluated and discussed. The significance of each parameter on the product selectivity and lifetime was eventually addressed.

2.2 Experimental methods

2.2.1 Chemicals

All reagents were of reagent grade and used without further purifications: sodium nitrate (NaNO_3 , Sigma Aldrich, ACS reagent, $\geq 99.0\%$), cobalt(II) nitrate hexahydrate (Alfa Aesar, ACS reagent, 98.0–102.0%), 1,3,5-triisopropylbenzene (1,3,5-TIPB, Sigma Aldrich, 95%), 3-methylpentane (3-MP, Alfa Aesar, 99+%), *n*-hexane (Sigma-Aldrich, 99%), 2,4-dimethylquinoline (2,4-DMQ, Alfa Aesar, 95%), MeOH (Sigma-Aldrich, for HPLC, $\geq 99.9\%$) and deionized water.

2.2.2 Zeolite materials

Zeolite samples with different topologies including MFI (ZSM-5), MEL (ZSM-11), and intergrowth MFI/MEL (ZBM-10) were obtained from commercial sources. ZSM-5 samples with different Si/Al ratio and crystal size including CBV5020E (Zeolyst Int., Si/Al=25), BASF1 (BASF, Si/Al = 25) and BASF2 (BASF, Si/Al = 50) are denoted by MFI-25-M, MFI-25-S and MFI-50-S, respectively (S and M indicate the respective small and medium crystal size based on scanning electron microscope (SEM) and X-ray powder diffraction (XRD) analysis). ZSM-11 samples were purchased from ACS Material (MZ110012, Si/Al = 25) denoted as MEL-25-S. Two intergrowth zeolite samples ZBM-10 featuring different crystal sizes were provided by BASF and named as MFI/MEL-25-S and MFI/MEL-50-L, where S and L represent samples with respective small and large crystal sizes. All the above-mentioned zeolite samples were calcined in air at 550 °C (2 °C/min) for 6 h to obtain the protonic form.

2.2.3 Chemical composition, structural and textural properties

The chemical composition of zeolite materials was assessed with ICP-AES (Inductively coupled plasma atomic emission spectroscopy) using a Perkin Elmer Optima 5300DV instrument (glass torch + saffire injector). Prior to measurement, 50 mg zeolite sample was digested in 4.5 mL 30% HCl + 1.5 mL 65% HNO_3 + 0.2 mL 40% HF using microwave heating for ca. 60 min. The resulting solutions were then diluted to 50 mL with deionized water.

X-ray powder diffraction (XRD) was performed in Bragg-Brentano geometry with a Bruker D8 Advance X-ray diffractometer using monochromatic $\text{Co } K\alpha$ ($\lambda = 1.788970 \text{ \AA}$) radiation between $2\theta = 5^\circ$ and 55° . The refinement and quantitative phase analysis were carried out using Topas software. The crystal size analysis was carried out by applying the Scherrer method:

$$D = \frac{K \times \lambda}{B \times \cos \theta} \quad (2.1)$$

where D represents the diameter of a spherical nanocrystal with $K = 0.89$, λ is the wavelength of X-ray, θ is the diffraction angle of the band at 9.2° , and B is the corrected half width of the observed half width considering the instrumental impact.

Microporous properties of each sample were assessed from N_2 physisorption isotherms at -196°C using Tristar II 3020. Prior to the measurements, samples were dried and degassed at 350°C for 6 h under constant N_2 flow.

X-ray Photoelectron Spectroscopy (XPS) was employed to determine the Si/Al ratio on the outer surface of the tested zeolites. XPS spectra were collected using a Thermo Scientific K-alpha spectrometer equipped with a monochromatic Al $K\alpha$ X-ray source and a 180° double-focusing hemispherical analyser with a 128-channel detector.

2.2.4 Acid site density and Al distribution

FT-IR pyridine adsorption

Transmission FT-IR spectroscopy of adsorbed pyridine as a probe molecule was used to quantify the acid site density of the catalytic materials (MFI-25-S as reference estimated from the formula: $H_nAl_nSi_{96-n}O_{192} \cdot 16H_2O$, $n = 3.7$). Samples (20 mg) were pressed in self-supported wafers with diameter 1.6 cm and then placed in an IR quartz cell. The spectra were collected at 2 cm^{-1} resolution using a Nicolet Nexus spectrometer equipped with an extended KBr beam splitting and an MCT detector. The amount of BAS and LAS was derived from the absorbance at 1545 and 1456 cm^{-1} using the integrated molar extinction coefficients of 0.73 and 1.11 , respectively.^[40] Assuming that one pyridine molecule is only adsorbed on one BAS/LAS, the following equations were used to estimate C_{BAS} and C_{LAS} :

$$C_{BAS} = 4.30 \times IA(BAS)R^2 / W \quad (2.2)$$

$$C_{LAS} = 2.83 \times IA(LAS)R^2 / W \quad (2.3)$$

where IA (BAS , LAS) represents the integrated absorbance of the band at 1545 and 1456 cm^{-1} , R is the radius of sample wafer (cm) and W is the weight of sample wafer (g).

FT-IR of adsorbed CO

To compare the strength of these acid sites, transmission FT-IR spectra with CO as probe was carried out at $-140\text{ }^{\circ}\text{C}$. 10 mg powder was pressed in a self-supported wafer with diameter 0.8 cm. After pre-treating at $400\text{ }^{\circ}\text{C}$ overnight under vacuum, IR spectra were collected at 2 cm^{-1} resolution using a Nicolet Nexus spectrometer within $400\text{--}4000\text{ cm}^{-1}$. During spectra collection, liquid nitrogen is used to maintain the IR cell temperature at ca. $-140\text{ }^{\circ}\text{C}$. The partial pressure of CO was stepwise increased (0.1 mbar per step) through a manifold connected to the specimen holder.

Solid state magic angle spinning (MAS) NMR measurements

Solid state MAS NMR measurements of fully hydrated samples were performed on a Bruker Ascend 500 magnet (11.7 T) equipped with a NEO console operating at a ^{27}Al resonance frequency of 130.32 MHz, using a Bruker 3.2 mm two channel MAS probe head. The MAS rate was set to 20 kHz for all measurements. To obtain the high-resolution ^{27}Al MAS NMR spectrum for quantitative analysis of Al distribution, the single pulse ^{27}Al MAS NMR measurements were recorded with a pulse length of 1.25 μs , a recycle delay of 0.5 s, and 10240 scans each.^[41] Two-dimensional (2D) multiple quantum magic-angle spinning (MQ MAS) NMR spectra were measured using a triple quantum z-filter pulse sequence. Excitation and conversion pulses of 3.4 μs and 1.1 μs and a selective soft pulse of 11 μs for the z-filter filtering were utilized. All 2D spectra consist of 100 transients, each transient incremented by 70 μs with a recycle delay of 0.2 s. Five characteristic peaks with the fixed width at 58 ppm, 56 ppm, 55 ppm, 53 ppm and 52 ppm were used for 1D ^{27}Al MAS NMR spectra deconvolution using the Voigt function^[42, 43] ($G/L = 0.5$ ^[44]).^[32, 41, 45]

Co(II) ion exchange and UV–vis diffuse reflectance spectra (UV–vis-DRS) measurements

To analyze the distribution of Al atoms (including Al_{pair} and $\text{Al}_{\text{single}}$) locations in the zeolite framework, UV–vis spectra of fully Co-exchanged zeolites were measured on a Perkin-Elmer Lambda 900 spectrophotometer equipped with an

integrating sphere (“Labsphere”) using BaSO₄ as a reference. Before measurement, the protonic zeolites were exchanged three times with 200 mL of 1M NaNO₃ solution per 1 g zeolite at 70 °C. After recovering by centrifugation, Co ion exchange was then performed with 100 mL 0.05M Co(NO₃)₂ solution per 1 g zeolite at room temperature under stirring for 24 h. The exchange was repeated three times with centrifugation between each repetition.^[46] Washed by deionized water after the third ion exchange, the obtained Co(II)-exchanged samples were then dried at room temperature under the dynamic vacuum and then dehydrated at 400 °C under constant N₂ flow for 7 h before being transferred to the self-sealing UV–vis sample holder in a moisture-free glovebox.^[47-49] The absorption intensity is expressed by the Schuster-Kubelka-Munk equation:

$$F(R_{\infty}) = (1 - R_{\infty})^2 / 2R_{\infty} \quad (2.4)$$

The distribution of Al atoms in the zeolite framework is categorized as Al_{pair} and Al_{single} as reported by Dědeček *et al.*^[46] Co(II) cations are selectively exchanged on Al_{pair} sites under the above-mentioned conditions.^[50] Combined with the amount of Na ions remaining in the framework after Co(II) ion exchange, the number of Al_{pair} and Al_{single} can be calculated as below:

$$Al_{single} = [Na] \quad (2.5)$$

$$Al_{pair} = 2 \times [Co] \quad (2.6)$$

$$Al_{framework} = [Na] + 2 \times [Co] \quad (2.7)$$

where [Co] and [Na] represent concentrations of Co²⁺ and Na⁺ in the sample determined by ICP-AES after Co ion exchange.

Cracking of 1,3,5-TIPB

To probe the external BAS, cracking of 1,3,5-TIPB was used as a probe reaction.^[51, 52] The catalytic tests were conducted in a fixed bed reactor. 20 mg catalyst (150–212 μm) was activated at 550 °C in 50 mL/min air before reaction at 200 °C. 1,3,5-TIPB in low concentration (0.3% v/v) was fed with 50 mL/min N₂ after passing through a saturator at 10 °C.

Cracking of 3-MP and *n*-hexane

To probe the Al-arrangement (channel versus intersection) in the zeolite framework^[32, 41], the cracking of 3-MP was used as a probe reaction conducted in a fixed bed reactor.^[53] In a typical experiment, 20 mg catalyst (150–212 μm) was activated at 550 °C in 50 mL/min air prior to reaction at 400 °C. 2,4-DMQ base was added to deactivate surface sites.^[51] To control total conversion below 10%, the partial pressure of 3-MP was adjusted at 3.8 kPa by passing 50 mL/min N_2 as carrier gas through a saturator at 5 °C. Hydrogen, methane and ethane are selectively formed through the monomolecular cracking of the pentacoordinate carbonium ion formed by the protonation of the 3-MP molecule on the BAS inside the zeolite crystals. In contrast, the energetically favorable bimolecular cracking^[54] via primary carbenium ions would require a more spacious space to hold the bulkier transition state of 3-MP and form hydrocarbons beyond C_3 . A previous study found that the bimolecular cracking can hardly occur on H-ZSM-22, which displays the 1-dimensional straight 10-MR channels without intersections.^[41] Thus, the selectivity towards the cracking products hydrogen, methane and ethane (moles / 100 mol cracked) is a good indicator of monomolecular cracking of 3-MP solely on BAS located in the straight or sinusoidal channels.

$$S_{H_2+CH_4+C_2H_6} = \frac{\phi_{CH_4} + \phi_{C_2H_6} + \phi_{H_2}}{\phi_{3-MP_{in}} - \phi_{3-MP_{out}}} \times 100\% \quad (2.8)$$

where ϕ_{C_n} and S represent the molar flow rate and selectivity in unit of moles per 100 mol 3-MP cracked, respectively.

Constraint index (CI) is used to evaluate the steric hindrance of a zeolite topology upon the reactant and represents the ratio of the (assumed) first-order rate constants of *n*-hexane and 3-MP cracking.^[55] To measure CI for studied materials, a 4 mm (ID) quartz tube reactor was filled with 20 mg sieved zeolite fraction (particle size 150–212 μm). *n*-Hexane and 3-MP were simultaneously fed into the reactor using 10 mL/min He as carrier passing through a saturator containing a mixture of *n*-hexane and 3-MP at 11 °C. The reaction was performed at 400 °C in the presence of 2,4-DMQ to deactivate surface sites.^[51] The CI value is calculated as:

$$CI = \frac{k_{n\text{-hexane}}}{k_{3\text{-MP}}} = \frac{\ln(1 - X_{n\text{-hexane}})}{\ln(1 - X_{3\text{-MP}})} \quad (2.9)$$

2.2.5 Catalytic performance testing

MTO reactions were performed at 450 °C using a fixed-bed reactor setup. The scheme of setup is given in **Figure A1**, Appendix A. A 4 mm (ID) quartz tube reactor was filled with 40 mg sieved zeolite fraction (particle size 150–212 μm). MeOH was fed into the reactor using a thermostated saturator with liquid MeOH and N₂ as a carrier gas. The reaction products were analysed with an online Thermo Trace GC equipped with a thermal conductivity detector (TCD) coupled with a PoraPLOT Q pre-column (2 m, 0.32 mm, 20 μm) and Molsieve 5A column (10 m, 0.32 mm) for analysis of permanent gases, a flame ionization detector (FID) equipped with RTX-1 column (2 m, 0.32 mm, 5.00 μm) and Al₂O₃/KCl column (15 m, 0.32 mm, 10 μm) for the analysis of C₁ to C₄ hydrocarbons and the other FID equipped with RTX-VMS column (30 m, 0.33 mm, 3.00 μm) for C₅₊ hydrocarbons.

Prior to reaction, the catalyst was activated in 50 mL/min air by heating up at 5 °C/min to 550 °C and then cooling down to the reaction temperature 450 °C. The partial pressure of MeOH in the flow was set at 5.2 kPa, corresponding with a weight hourly space velocity (WHSV) of 5.2 g_{MeOH}g_{cat}⁻¹h⁻¹. The reaction conversion, selectivity and yield were then calculated on a carbon molar basis as follows:

$$X = \frac{(\phi_{C,MeOH_{in}} - \phi_{C,MeOH_{out}} - 2\phi_{C,DME_{out}})}{\phi_{C,MeOH_{in}}} \times 100\% \quad (2.10)$$

$$S_{C_n} = \frac{n \cdot \phi_{C_n}}{(\phi_{C,MeOH_{in}} - \phi_{C,MeOH_{out}} - 2\phi_{C,DME_{out}})} \times 100\% \quad (2.11)$$

$$Y_{C_n} = \frac{X \times S_{C_n}}{100} \% \quad (2.12)$$

where X , ϕ_{C_n} , S_{C_n} and Y_{C_n} represent the carbon-based conversion of MeOH plus dimethyl ether (DME), molar flow rate and carbon selectivity to certain hydrocarbon product in the exhaust with carbon number equal to n and the corresponding carbon yield, respectively. To describe the catalyst deactivation, MeOH conversion capacity^[56] was estimated following:

$$R_0 = WHSV_{MeOH} \times t_{0.5} \quad (2.13)$$

here $WHSV_{\text{MeOH}}$ is the weight hourly space velocity of MeOH and $t_{0.5}$ is the catalyst lifetime when MeOH conversion is within 100–50%.

After catalytic tests, thermogravimetric analysis of the spent catalyst samples was performed on a Mettler Toledo TGA/SDTA 851e TGA analyzer. 20 mg Spent catalyst was first treated at 200 °C with 20 mL/min air for 1 h to remove water and other volatile species and then heated in the same air flow up to 800 °C at 5 °C/min while recording the sample mass.

2.2.6 *Operando* UV–vis diffuse reflectance spectroscopy

Operando UV–vis diffuse reflectance spectra were collected using 60 mg of sieved catalyst (particle size 212–355 μm) in a quartz, rectangular reactor. Details of the set-up can be found elsewhere.^[57–59] Prior to reaction and spectra collection, the catalyst was pre-treated at 550 °C in 10 mL/min O_2 for 1 h after which a He flow of 35 ml/min was used to get rid of the O_2 . The MTO reaction was carried out at 450 °C by flowing He as a carrier gas (25 mL/min) through a MeOH saturator kept at 21 °C, corresponding with a $WHSV$ of $\sim 5.4 \text{ g}_{\text{MeOH}}\text{g}_{\text{cat}}^{-1}\text{h}^{-1}$. During MeOH conversion, *operando* UV–Vis spectra were obtained using an AvaSpec 2048L spectrometer connected to a high-temperature UV–Vis optical fiber probe, which was used to collect spectra in reflection mode. Every minute a spectrum was saved with 100 accumulations of 80 ms exposure time.

2.3 Results

2.3.1 Physicochemical Properties

Figure 2.1 shows the representative XRD patterns for all zeolite materials together with Rietveld refinement and quantitative results in **Table 2.1**. XRD patterns of pure MFI samples and MEL-25-S show close agreements with the expected reflections of MFI and MEL phases, respectively.^[36] In comparison with MFI samples, the increasing ratio of intensity between the (0 1 3) reflection at 23.7° and the (2 4 1) reflection at 24.3° in MFI/MEL-25-S and MFI/MEL-50-L confirms the presence of the MEL in the intergrowth samples.^[38] The refinement in **Table 2.1** gives the unit cell parameters of all catalysts, which correspond well with the reported values.^[36] The XRD data indicate a high crystallinity of all the utilized materials. The crystallinity fraction shows that MFI/MEL-25-S contains 50%/50% of MFI and MEL phase, while MFI/MEL-50-L contains 63%/37% of MFI and MEL phase.

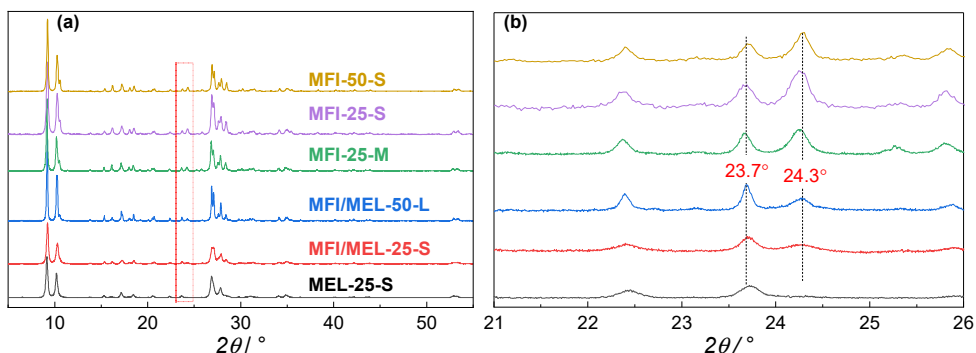


Figure 2.1. X-ray diffraction data comparing patterns for investigated samples (a), and a highlighted 21–26° range (b).

The textural and acidic characteristics of the zeolite catalysts are summarized in **Table 2.2**. The chemical compositions give the actual Si to Al ratio in agreement with that as provided. The SEM results (**Figure A2**, Appendix A) show that intergrowth MFI/MEL-50-L consists of the largest aggregates with a diameter of 2–5 μm while the other zeolites feature particle sizes below 1 μm . All samples have a similar micropore volume of 0.15–0.16 cm^3g^{-1} resulting in similar N_2 adsorption isotherms at $P/P^0 < 0.6$ (**Figure A3**). The smallest external surface area (27 m^2g^{-1}) is observed for the MFI/MEL-50-L featuring largest crystal size (830 \AA , **Table 2.2**). The steep uptake of N_2 from $P/P^0 > 0.7$ without an evident hysteresis loop on the samples with the ‘S’ suffix is in line with the developed external surface area of the smaller-crystallite materials. As a consequence, V_{total} , which is evaluated on the isotherm point at $P/P^0 = 0.95$ shows that samples with the small crystal size exhibit the larger amount of N_2 adsorbed of 0.28–0.31 cm^3g^{-1} than MFI-25-M (0.22 cm^3g^{-1}) and MFI/MEL-50-L (0.19 cm^3g^{-1}). These results together with the XRD data show that the crystal size varies as follows MFI/MEL-50-L > MFI-25-M > MFI-25-S \approx MFI-50-S \approx MEL-25-S \approx MFI/MEL-25-S.

Table 2.1. Unit-cell parameters and phase composition of all zeolites under study.

	Crystallinity (%)	a (Å)	b (Å)	c (Å)	MFI/MEL fraction (%)
MEL-25-S	93.2	20.0163	20.0163	13.379	-
MFI/MEL-25-S	96.5	20.0187/20.0039	19.8571/20.0039	13.3694/13.3620	50.3/49.7
MFI/MEL-50-L	95.1	20.0848/19.9790	19.9183/19.9790	13.3980/13.4087	63.5/36.5
MFI-25-S	93.3	19.9515	19.8526	13.3256	-
MFI-25-M	94.4	19.897	19.846	13.348	-
MFI-50-S	94.9	19.9365	19.8285	13.3481	-

Table 2.2. Summarized textural and acidic properties of studied catalysts.

	Si/Al ^a (mol mol ⁻¹)	size ^b (Å)	V _{total} ^c (cm ³ g ⁻¹)	V _{micro} ^c (cm ³ g ⁻¹)	S _{ext} ^c (m ² g ⁻¹)	S _{BET} ^d (m ² g ⁻¹)	BAS ^e (μmolg ⁻¹)	LAS ^e (μmolg ⁻¹)
MEL-25-S	27	419	0.31	0.14	85	439	543	90
MFI/MEL-25-S	25	463	0.31	0.15	81	448	556	139
MFI-25-M	26	613	0.22	0.17	56	414	575	94
MFI-25-S	25	428	0.27	0.16	67	453	530	74
MFI/MEL-50-L	48	830	0.19	0.16	27	423	376	72
MFI-50-S	50	428	0.29	0.16	77	471	338	91

^aMolar ratio determined by ICP-AES. ^bFrom crystal size analysis on the XRD pattern within 8.4–9.8° by applying the Scherrer equation. ^cFrom N₂ adsorption isotherms (**Figure A3**) using the t-plot method. ^dFrom N₂ adsorption isotherms using the BET method. ^eConcentrations of BAS and LAS derived from FT-IR spectroscopy analysis with pyridine as probe (**Figure A4**).

The acidic properties of the catalysts assessed by FT-IR spectroscopy of adsorbed pyridine confirm that the concentrations of BAS in the Si/Al = 25 and = 50 samples are consistent with their chemical compositions, while MFI/MEL-25-S contains a higher density of Lewis acid sites (LAS) than the others.

The strength of BAS was assessed by FT-IR of adsorbed CO. Upon interacting with CO, the downward shift in the OH stretching frequency and the upward shift in the CO vibrations are directly related to the strength of BAS.^[60] As shown in **Figure 2.2**, a similar $\Delta\nu(\text{OH})$ (310–314 cm⁻¹ in Si/Al = 25 and 313–317 cm⁻¹ in Si/Al = 50) is observed. Together with the similar C–O stretching shift (35–36 cm⁻¹ in Si/Al = 25 and 36–37 cm⁻¹ in Si/Al = 50), it indicates an almost identical strength of the BAS for all studied samples.^[60–63] BAS with slightly higher strength was characterized for MFI-50-S and MFI/MEL-50-L, which is ascribed to the lower Al concentration in those materials.^[64, 65]

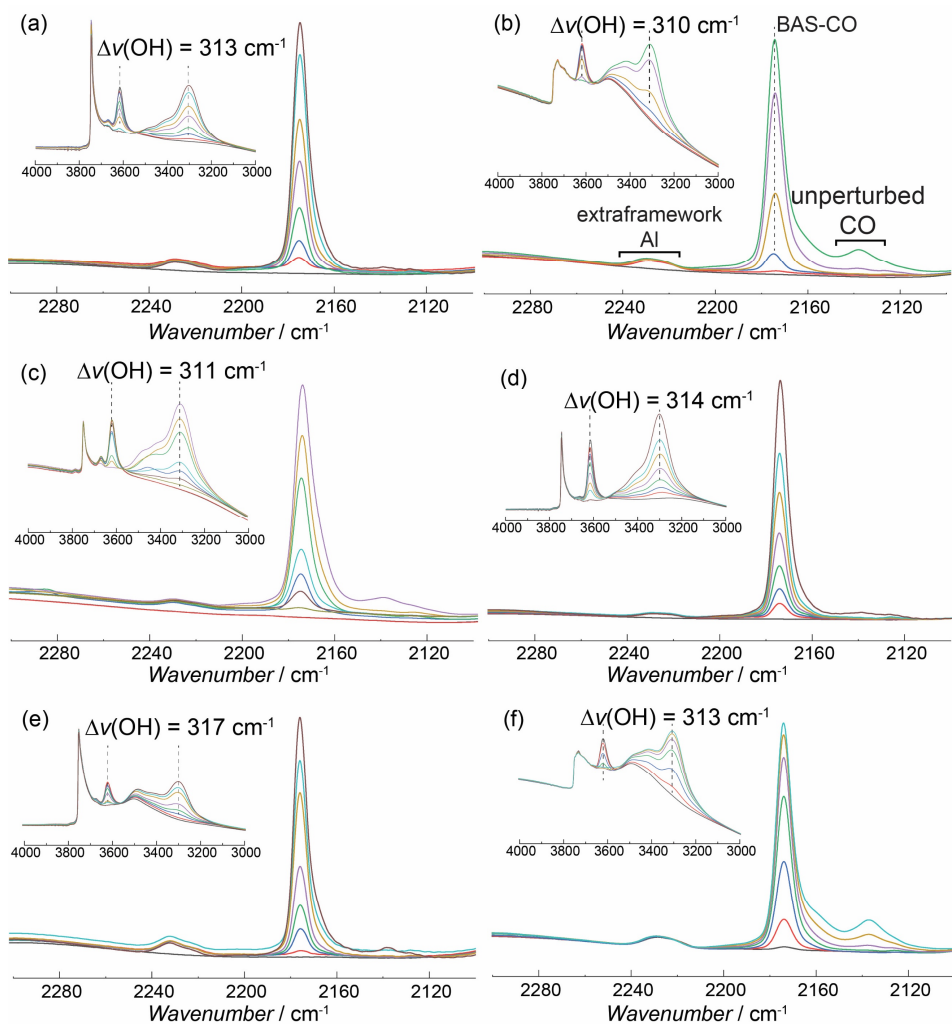


Figure 2.2. FT-IR spectrum of adsorbed CO within 4000–3000 cm^{-1} OH stretching range and 2250–2100 cm^{-1} CO stretching range on (a) MEL-25-S, (b) MFI/MEL-25-S, (c) MFI-25-M, (d) MFI-25-S, (e) MFI-50-S and (f) MFI/MEL-50-L. Broad bands between 2250–2200 cm^{-1} at low CO coverage represent CO adsorbed at extraframework Al-species with heterogeneous nuclei nature. H-bonded C–O stretching is observed at 2173–2175 cm^{-1} . Absorbance with increasing intensity at 2140 cm^{-1} with high CO loading is assigned to unperturbed C–O stretching. Each spectrum represents one CO dosing of less than 0.01 mbar.

2.3.2 Catalytic Testing

To evaluate the MTO catalytic performance at steady-state conditions, the overall MTO activity and deactivation as defined by cumulative production yields and MeOH conversion capacity^[56], for all materials are summarized in **Figure 2.3**.

For all catalysts, the main products are categorized into light olefins (ethylene $C_2^=$, propylene $C_3^=$ and butylenes $C_4^=$), C_1 - C_4 (methane, ethane, propane and butanes), BTEX (benzene, toluene, ethylbenzene and xylenes), and C_{5+} for undefined hydrocarbons with carbon number higher than 4.

At the initial stage of the reaction full MeOH conversion is achieved. With the increase in cumulative MeOH throughput all catalysts deactivate giving rise to a rapid decrease in conversion due to coke deposition blocking zeolite micropores and the active sites.^[66] For all catalysts, except for the shorter lived MFI/MEL-50-L, the propylene selectivity remains constant with TOS till MeOH conversion starts decreasing as shown in **Figure A5**. On the other hand, the selectivity to ethylene and to BTEX gradually decreases with TOS before MeOH conversion drops. The similar profiles of ethylene and aromatics (BTEX) within the 100% MeOH conversion range further support the mechanistic proposal by Olsbye *et al.* on the role of the aromatics-based cycle for ethylene production.^[7]

The MeOH conversion capacity of MFI-50-S is $14.1 \text{ mol}_{\text{carbon}}\text{mmol}_{\text{BAS}}^{-1}$, which is higher than $7.4 \text{ mol}_{\text{carbon}}\text{mmol}_{\text{BAS}}^{-1}$ obtained over MFI-25-S, emphasizing the positive impact of the lower Al concentration on the catalyst stability.^[15] Regarding the crystallite size, MFI-25-M with relatively larger crystal sizes exhibits a slightly lower conversion capacity ($6.6 \text{ mol}_{\text{carbon}}\text{mmol}_{\text{BAS}}^{-1}$) than its counterpart MFI-25-S ($7.4 \text{ mol}_{\text{carbon}}\text{mmol}_{\text{BAS}}^{-1}$). This is in line with previous observations that mesoporosity development, achieved by either synthesizing nano-sized zeolites or introducing a hierarchical structure, improves the catalyst stability in the MTO process.^[67-70] The intergrowth MFI/MEL-25-S and MFI/MEL-50-L catalysts show the lowest MeOH conversion capacity (ca. 5.8 and $6.1 \text{ mol}_{\text{carbon}}\text{mmol}_{\text{BAS}}^{-1}$, respectively) suggesting the intergrowth of the two zeolite phases increases the catalyst deactivation rate.

The product distributions in the MTO test are evaluated based on the cumulative yields (**Figure 2.3(b)**) and the carbon selectivity at varying MeOH conversion levels (**Figure 2.4**). Previous studies suggest the decrease in conversion in the later stage of the MTO test (gradual deactivation) can be regarded as the change in contact time due to the coke deposition particularly for MFI-type and TON-type zeolites.^[56, 71, 72]

For all catalysts, the cumulative yields of propylene and butylenes are higher than other products (**Figure 2.3(b)**), which suggests the olefinic cycle reactions prevail over all materials at studied MTO conditions. Similar to the trend in the MeOH conversion capacity, MEL-25-S has the higher cumulative yield of

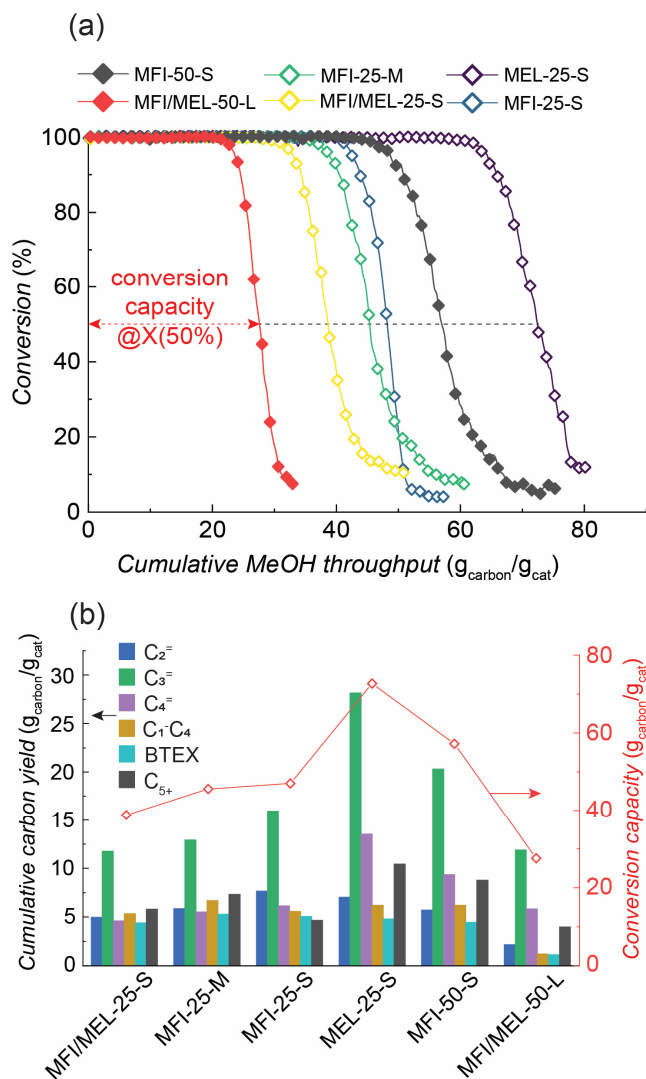


Figure 2.3. MeOH conversion as a function of cumulative MeOH throughput (a) and cumulative carbon yields of different hydrocarbons until MeOH conversion is at 50% (color bars) and estimated conversion capacity (symbols to right axis) (b) for all studied catalysts in MTO tests. Reaction conditions: $T = 450\text{ }^{\circ}\text{C}$, $m_{\text{cat}} = 40\text{ mg}$ (150–212 μm), 1 bar, $WHSV = 5.2\text{ g}_{\text{MeOH}}/\text{g}_{\text{cat}}\cdot\text{h}^{-1}$, carrier gas $\text{N}_2 = 50\text{ mL}/\text{min}$. The full picture of MeOH conversion and product selectivity curves as a function of time on stream (TOS) are presented in **Figure A5**.

propylene ($4.3\text{ mol}_{\text{carbon}}/\text{mmol}_{\text{BAS}}^{-1}$) than MFI-25-S, MFI-25-M and MFI/MEL-25-S (2.6, 1.9, and $1.8\text{ mol}_{\text{carbon}}/\text{mmol}_{\text{BAS}}^{-1}$, respectively) with Si/Al of 25. A similar trend was also observed for samples with Si/Al of 50 emphasizing the impact of catalyst stability on the cumulative yields in the MTO process.

Upon decreasing MeOH conversion, the selectivity to propylene and butylene decreases while that to ethylene gradually increases (**Figure 2.4**). The latter can be interpreted that more polyaromatic precursors present in the catalyst during the deactivation proceeds the dealkylation to give the ethylene formation. To note, the trends of selectivity towards propylene and ethylene are similar for all catalysts. Only the selectivity to ethylene over MFI-25-S, deviates from this general trend, showing no increase but a more constant level over a MeOH conversion of 80–20%. This correlates with the decreasing BTEX over that range in contrast to the more constant level for the other samples. Focusing on the comparison of product distribution over studied materials, the selectivity at MeOH conversion of 80% is chosen as reference in this study.

The selectivity to propylene is 27% and 38% for MFI/MEL-25-S and MFI/MEL-50-L, and 10% and 9% to ethylene, respectively. This is in line with earlier reports showing that a higher lattice Al concentration in MFI enhances the interaction of substituted benzene intermediates with BAS giving rise to the propagation of the aromatics-based cycle and, accordingly, an increased ethylene and BTEX selectivity in the MTO process.^[24] In a previous study the total light olefin selectivity in MTO was observed to monotonically increase with the crystal size, attributed to diffusion interference and a higher retention of methylbenzenes^[73]. This latter is in line with a higher selectivity to ethylene of MFI-25-M than MFI-25-S in our study. Overall, the observed differences in selectivity levels for the different samples point to the importance of other intrinsic catalyst characteristics that define the performance and selectivity of the MTO catalysts.

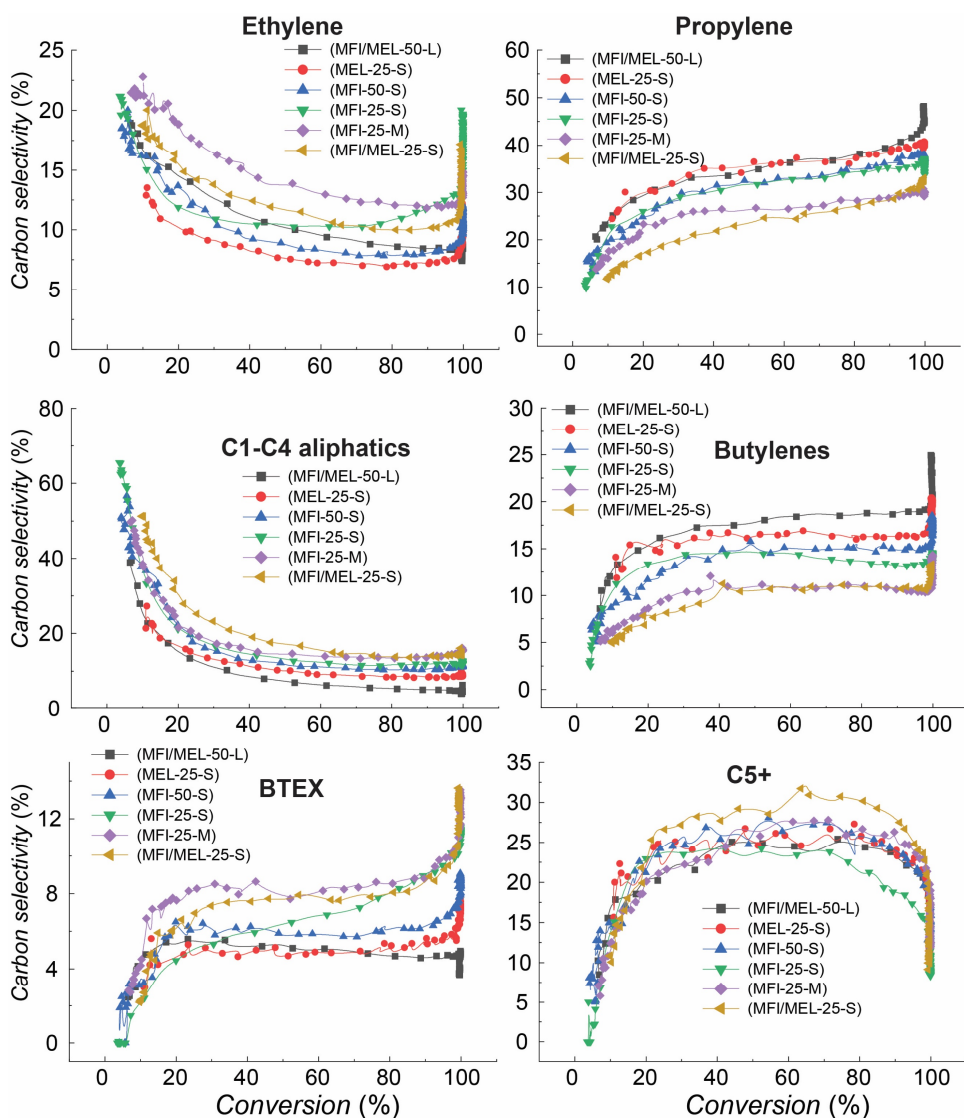


Figure 2.4. Carbon selectivity to different products as a function of MeOH conversion over studied materials. Reaction conditions: Reaction conditions: $T = 450\text{ }^{\circ}\text{C}$, $m_{\text{cat}} = 40\text{ mg}$ (150–212 μm), 1 bar, $WHSV = 5.2\text{ g}_{\text{MeOH}}\text{g}_{\text{cat}}^{-1}\text{h}^{-1}$, carrier gas $\text{N}_2 = 50\text{ mL/min}$.

2.3.3 Operando UV–vis Spectroscopy

The active hydrocarbons formed from MeOH and then retained in the zeolite frameworks are defined as the hydrocarbon pool intermediates.^[74, 75] During the MTO test, *operando* UV–vis spectra of the catalyst were recorded to follow the formation of the retained hydrocarbons. The results are displayed in **Figure 2.5**.

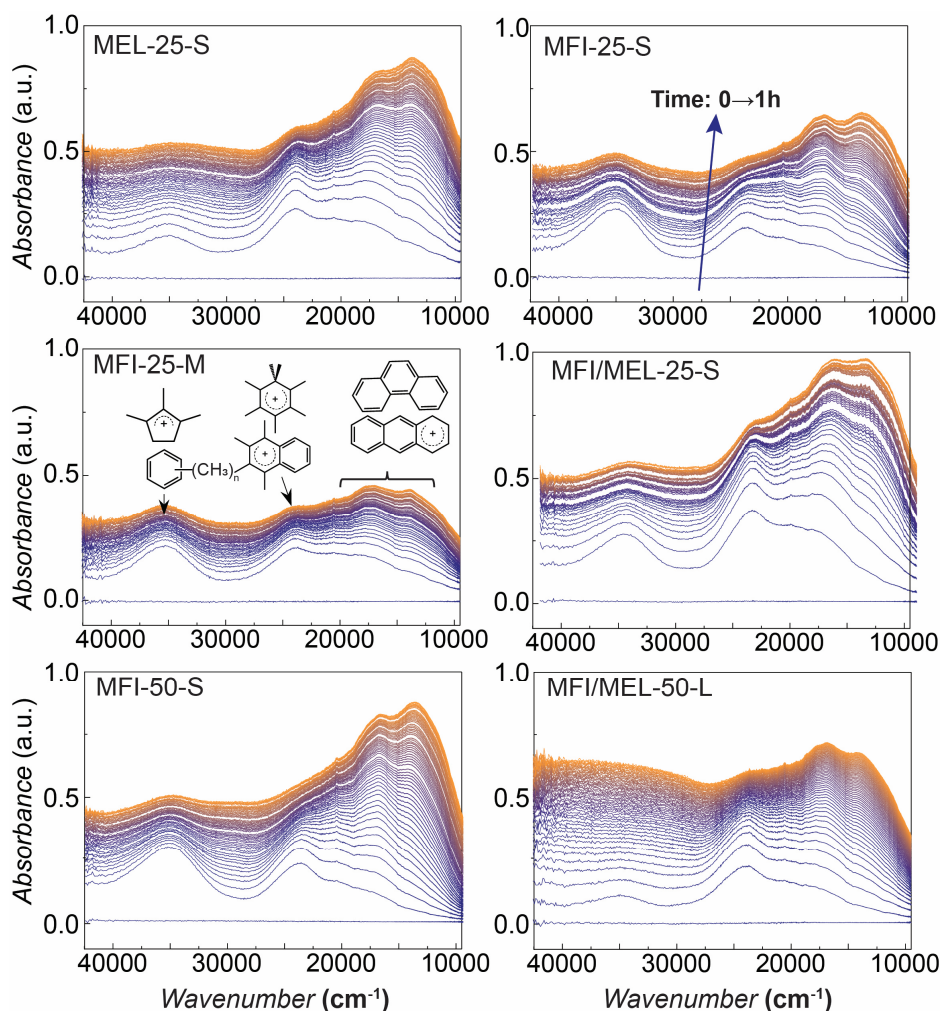


Figure 2.5. Time-resolved *operando* UV-vis spectra during MeOH conversion at 450 °C over studied catalysts. All spectra were collected during time-on-stream (TOS) within 0–1 h with 1 min interval. Band Assignments in the 40000–12500 cm^{-1} are displayed in UV-vis spectra for MFI-25-M.^[57, 58]

With *operando* UV-vis spectroscopy, aromatic intermediates in MTO can be determined as well as polyaromatic compounds which act as coke precursors and are thereby deactivating species.^[12, 18, 57, 58, 76] Only the UV-vis spectra of the first hour of the reaction are represented as after this contributions of broad coke features are increasing in intensity (**Figure A7**), which results in a more difficult comparison as the individual absorbance bands are less visible. On all catalysts, three main features including the absorbance bands at ca. 35000 cm^{-1} , 23000 cm^{-1} and a long tail in the 20000–12000 cm^{-1} are remarkable especially in the first 10

spectra corresponding to TOS up to 10 min. These absorbance bands are assigned, respectively, to neutral methylated benzenes/cyclopentenyl carbocations, methylated benzene/naphthalene carbocations, and (alkylated) polyaromatics. For the MFI-type catalysts, the methylated benzenes with a characteristic absorption band at 35000 cm^{-1} are widely accepted as the active species in the aromatic cycle towards the production of BTEX and ethylene^[7, 12, 76, 77], whereas, the polyaromatic species giving rise to the absorbance band in the specified range $20000\text{--}12000\text{ cm}^{-1}$ are attributed to coke species^[78, 79]. The shape of the UV–vis profiles along TOS differs greatly for all studied zeolites, clearly indicating the different features (e.g., density, structure, etc.) of the retained hydrocarbons present in MTO towards the steady-state MTO product distributions. After reacting for 1 h for all zeolites, the bands at 35000 cm^{-1} and 23000 cm^{-1} diminished in intensity while the UV–vis absorption in the broad range of $20000\text{--}12000\text{ cm}^{-1}$ continuously grew, which is related to the accumulation of polyaromatics, probably on the external surface hindering the UV–vis absorption of inner species.^[76] Compared with MFI-25-S and MFI/MEL-25-S, the relatively weak UV–vis absorption for methylated benzenes (35000 cm^{-1}) in MEL-25-S is well in line with its high propylene and low ethylene selectivity (**Figure 2.4**), confirming the higher contribution of the olefinic cycle in the dual-cycle mechanism. Additionally, the mediated contribution of methylbenzenes for MFI/MEL-25-S is ascribed to the combination of MFI and MEL structures.

A faster stabilization is observed of the UV–vis absorbance bands for MFI-25-M compared to MFI-25-S. The relatively higher contribution of polyaromatics ($20000\text{--}12000\text{ cm}^{-1}$) for MFI-25-M especially during the first 10 spectra might be related to its faster deactivation than MFI-25-S (**Figure 2.5**), and suggests blocking access to the larger crystallites of MFI-25-M and hence a lower coke deposition (**Figure A6**). When comparing zeolites with the different Si/Al ratios, MFI-50-S shows very similar UV–vis spectra as MFI-25-S, while MFI/MEL-50-L shows a much smaller band at 35000 cm^{-1} , very similar to MEL-25-S in the very early stage of the reaction. A low formation of less methylated benzenes and/or charged monoenyl/cyclopentenyl species (35000 cm^{-1}) compared to the other zeolites, indicates a less pronounced aromatic cycle resulting in a higher propylene selectivity over MFI/MEL-50-L.

2.3.4 Effect of external BAS

The external acid site was characterized by the 1,3,5-TIPB cracking as a probe reaction. The critical diameter of 1,3,5-TIPB ($> 8\text{ \AA}$) limits its diffusion into the

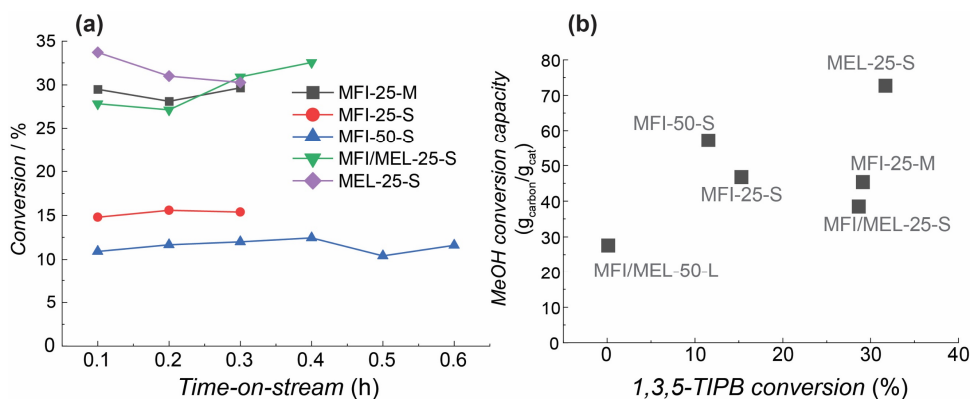


Figure 2.6. 1,3,5-TIPB conversion profiles with function of time-on-stream (a) and MeOH conversion capacity as a function of 1,3,5-TIPB conversion (b) over catalysts at 200 °C. Cracking conditions: $T = 200$ °C, $m_{\text{cat}} = 20$ mg (150–212 μm), 1 bar, $P_{1,3,5\text{-TIPB}} = 0.3$ kPa, carrier gas $\text{N}_2 = 50$ mL/min. Cracking conversion was averaged within TOS = 0.1–0.3 h.

micropores (< 6 Å) of the zeolites. Thus, the cracking of 1,3,5-TIPB selectively occurs at the external crystal surface. To investigate the effect of external acid sites on MTO stability, the 1,3,5-TIPB cracking results together with MeOH conversion capacity are plotted in **Figure 2.6**.

The 1,3,5-TIPB cracking conversion indicates the different external acid site concentrations for all catalysts. Among the studied catalysts, the negligible cracking activity of MFI/MEL-50-L at 200 °C correlates with its largest crystal size (smallest external surface) and an ultimately low external acid density in comparison with MFI-50-S. The latter is also evidenced by its higher Si/Al at the external surface than MFI-50-S (**Table 2.3**). On the contrary, the highest 1,3,5-TIPB conversion of MEL-25-S stands out and suggests the highest concentration of BAS on its external surface. XPS analysis in **Table 2.3** and **Figure A8**, however, indicates a lower Al content at the external surface of MEL-25-S than that of MFI-25-M and MFI/MEL-25-S. Mores *et al.* observed coke deposited on the external BAS in the MTO process blocks the pores for further access to the internal BAS, which causes the catalyst deactivation.^[80] However, our results do not present a clear correlation between the concentration of the external BAS and MeOH conversion capacity (**Figure 2.6**). MFI/MEL-50-L showing negligible cracking activity at the outer surface also converts the lowest amount of MeOH before deactivation in the MTO test. Further, the highest MeOH conversion capacity is observed for MEL-25-S, which also shows the highest 1,3,5-TIPB cracking conversion.

Table 2.3. Comparison of Si/Al ratio determined by XPS ($\text{Si}/\text{Al}_{\text{XPS}}$) and Si/Al ratio determined by ICP-AES analysis ($\text{Si}/\text{Al}_{\text{bulk}}$).

	$\text{Si}/\text{Al}_{\text{XPS}}$	$\text{Si}/\text{Al}_{\text{bulk}}$
MEL-25-S	36	27
MFI-25-S	38	25
MFI/MEL-25-S	23	26
MFI-25-M	26	25
MFI-50-S	32	48
MFI/MEL-50-L	43	50

2.3.5 Effect of Aluminium Location

Recent research shows that the isomorphous substitution of T-sites by Al in the zeolite framework is not random.^[81, 82] Also the BAS facing cavities or channels are associated with different catalytic activities, due to the confinement effects on the intermediates.^[45, 81, 83, 84] To probe the Al distribution in the zeolite catalysts and investigate its effect on the MTO performance, three techniques were applied, namely, the UV–vis analysis of Co-ion exchanged catalysts, ²⁷Al MAS NMR, and C₆ paraffin (3-MP and *n*-hexane) cracking tests.

Al pairing

The Al distribution in the zeolite catalysts was first quantified by combining Co(II) ion exchange and UV–vis spectroscopy analysis. Co(II) exchange allowed quantification of Al pairing and provided an insight into the Al distribution in the framework.^[48, 83] The comparison of the Al_{pair} fraction (derived from UV–vis spectrum deconvolution shown in **Figure A9**) and MTO performance (regarding selectivity towards propylene and the MeOH throughput) of all zeolites is presented in **Figure 2.7**.

The results in **Figure 2.7** and **Table A1** point to the very different Al pairing in the studied zeolites. MEL-25-S and intergrowth MFI/MEL-25-S have a large fraction of Al_{pair}, 47% and 46%, respectively. Two MFI-type catalysts, MFI-25-S and MFI-25-M show a similar fraction of Al_{pair}, 29%, and 30%, respectively. MFI-50-S with the lower Al contents has 42% of Al_{pair}, whereas MFI/MEL-50-L has only 13% of framework Al in paired configurations. The location of Al_{pair} sites was further analyzed by deconvoluting the UV–vis spectra of fully dehydrated Co-exchanged samples (**Figure A9**) following the procedures reported by Dědeček *et al.*^[47, 48] Most of Al_{pair} is located at the intersections, in line with the previous studies.^[47, 48] MEL-25-S and intergrowth MFI/MEL-25-S

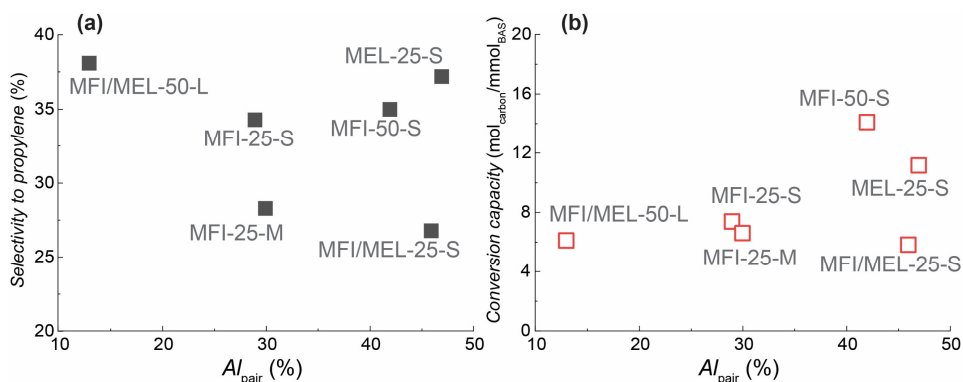


Figure 2.7. Selectivity to propylene (a) and MeOH conversion capacity (b) versus the proportion of Al_{pair} of tested samples. Al_{pair} is measured based on Co concentration determined by ICP-AES after Co ion exchange.

have the higher fraction of Al_{pair} (77%) at the channel intersection sites than 71–73% for MFI-25-S, MFI-25-M, and MFI-50-S. The MFI/MEL-50-L has 68% Al_{pair} at the channel intersections.

Previous research indicated that Al in pair (able to host the Co²⁺ hexa-aqua-complex during ion exchange) could cooperate during acid-catalyzed reactions such as MTO on BAS.^[46] From this perspective, hydrogen transfer and aromatization reactions that require higher activation energy should occur more easily over Al_{pair} leading to more aromatics products and lower selectivity towards propylene. However, such structure-performance correlation is not observed in this study. MEL-25-S containing the highest amount of Al_{pair} (47%) with 77% of them at intersections shows the highest selectivity to propylene, as the typical product from the olefinic cycle in the MTO process. Furthermore, results in **Figure 2.7(b)** suggest that the fraction of Al_{pair} also does not correlate with the MeOH conversion capacity. MEL-25-S and MFI/MEL-25-S both contain a relatively high fraction of Al in pair compared to other catalysts. However, MEL-25-S converts the largest amount of MeOH before deactivation, whereas MFI/MEL-25-S converts the smallest amount of MeOH and represents the least stable MTO catalyst in the group of Si/Al = 25.

Al location

NMR measurements were performed to provide a more general view of Al (no matter pairing or single) at different locations in the framework. **Figure 2.8** shows two dimensional (2D) ²⁷Al MQ/MAS NMR spectra with corresponding 1D ²⁷Al MAS NMR spectrum on the top in the 65–45 ppm range.

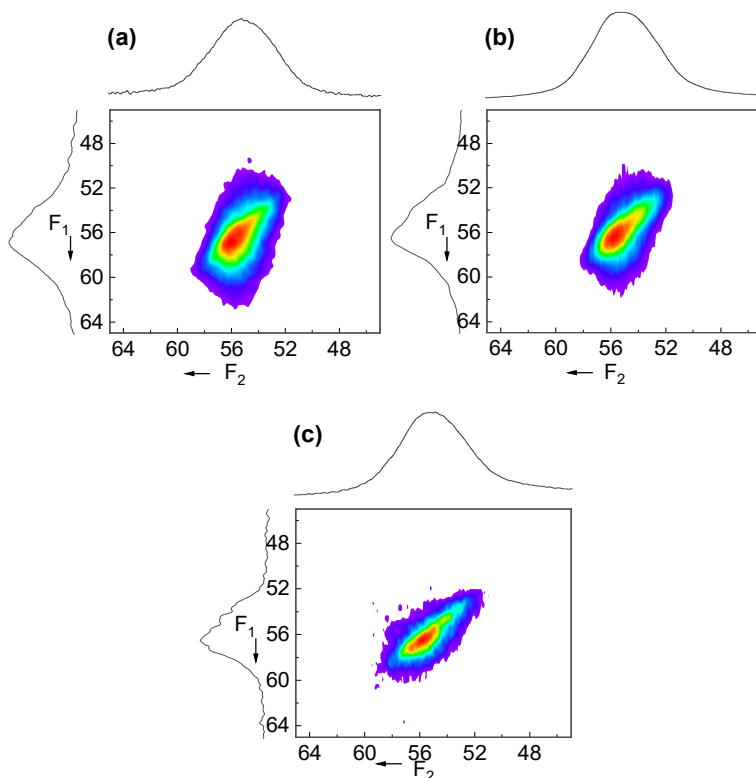


Figure 2.8. 2D ^{27}Al MQ MAS NMR spectrum of (a) MEL-25-S, (b) MFI-25-M, and (c) MFI/MEL-25-S together with the isotopic projection F1 spectrum at the left and the corresponding ^{27}Al MAS NMR spectrum at the top of the 2D contour profile.

All ^{27}Al MAS NMR spectra contain a broad peak at 65–45 ppm and a low-intensity peak at ~ 0 ppm, suggesting that most Al atoms are located at tetrahedral sites (T-sites) and few Al atoms at extraframework locations with octahedral coordination.^[63, 85] 2D ^{27}Al MQ MAS NMR spectrum reflects the isotropic chemical shift (δ_{iso}) accompanied by the second-order quadrupolar effect (S_Q) in F1 projection. The ellipsoidal 2D contour and asymmetrical F1 projection clearly show the presence of overlapping signals within 64–45 ppm, which reveals that Al is located at different T-sites in the zeolite unit cell.^[82] To distinguish these Al atoms, the broad signal at 65–45 ppm was deconvoluted into five peaks at 58 ppm, 56 ppm, 55 ppm, 54 ppm and 52 ppm. The results are presented in **Figure A10** and the numerical analysis results in **Table 2.4**. Significantly different proportions of the characteristic peaks were obtained for all zeolites, which indicate the diverging Al distribution over the different positions in the frameworks.

Table 2.4. The fraction of various peaks obtained from the ^{27}Al MAS NMR spectrum.

	$\text{Al}_{\text{intersection}}$ / %	$\text{Al}_{\text{channel}}$ / %	Characteristic peaks proportion / %				
			58±0.3 ppm	56±0.2 ppm	55±0.5 ppm	53±0.4 ppm	52±0.3 ppm
MEL-25-S	46.4	53.6	11.1	24.0	29.6	24.1	11.2
MFI-25-S	47.9	52.1	9.0	28.6	24.2	23.6	14.7
MFI/MEL- 25-S	48.7*	51.3*	14.2	25.0	28.6	24.1	8.2
MFI-25-M	49.3	50.7	11.7	25.5	24.8	25.3	12.7
MFI-50-S	47.0	53.0	8.0	26.9	25.5	26.1	13.5
MFI/MEL- 50-L	45.2*	54.8*	15.3	32.1	31.8	18.3	2.5

*: Al proportions for intergrowth samples were calculated based on the fraction of MFI and MEL phase in **Table 2.1**.

Based on the combination of the C_6 paraffin cracking and ^{27}Al MAS NMR deconvolution results, Yokoi *et al.* attributed the peak at 56 ppm and 53 to the T-sites facing the straight or sinusoidal channels, whereas the signal at 54–55 ppm was assigned to the T-sites of ZSM-5 intersections.^[41] A similar assignment for ZSM-11 zeolite was carried out on the basis of DFT calculations by Wang *et al.*^[32] Here, the peaks at 56 ppm and 55 ppm were assigned to T-sites facing the straight channels, while the other peaks in the ^{27}Al MAS NMR spectra to the intersection sites of ZSM-11. Following these assignments, our data (**Table 2.4**) reveal that in the group with Si/Al 25, MEL-25-S contains the highest fraction of Al in the straight channels. The related MFI-25-S shows a comparable Al distribution with only a slightly higher fraction of Al occupying the intersection sites. The preference for Al sitting at the intersection sites is most pronounced for MFI/MEL-25-S and MFI-25-M samples. At lower Al content, the fraction of Al in the channels slightly increases suggesting a better Al dispersion in the lattice.

The results in **Table 2.4** suggest that the $\text{Al}_{\text{channel}}$ fraction and selectivity to propylene and butylene correlate well for all studied catalysts. MEL-25-S and MFI/MEL-50-L show the highest selectivities of propylene (35–36%) and butylenes (16–18%) in line with their highest fraction of Al in the channels. However, in view of the typical $\pm 5\%$ uncertainty in the deconvolution of ^{27}Al MAS NMR spectra^[86], additional characterization of the Al distribution was carried out.

To further distinguish framework Al located in channels or intersections, 3-MP cracking at 400 °C was performed on all catalysts. The location of framework Al was based on the different product selectivity observed, originating from the different transition-state shape selectivity for intersection or channel. 3-MP

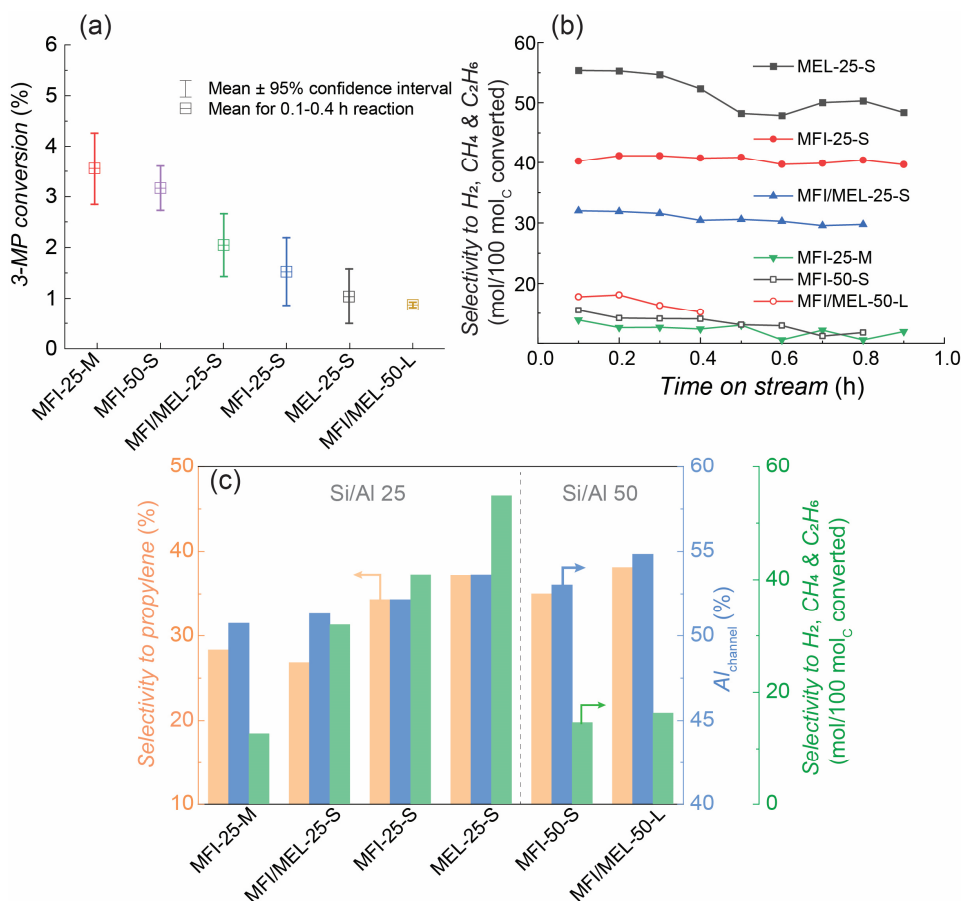


Figure 2.9. 3-MP cracking conversion (a) and selected production profiles with function of time-on-stream (b) over various samples; Carbon selectivity to propylene versus selectivity towards hydrogen, methane and ethane of 3-MP monomolecular cracking over samples with Si/Al of 25 and Si/Al of 50 (c). 3-MP cracking conditions: $T = 400$ °C, $m_{cat} = 20$ mg (150–212 μ m), 1 bar, carrier gas $N_2 = 50$ mL/min, 3-MP partial pressure = 3.8 kPa in the presence of 2,4-DMQ (<0.1 kPa).

monomolecular cracking selectively forms hydrogen, methane, and ethane, whereas the simultaneous bimolecular cracking forms larger carbenium ions and eventually aromatics via the classical hydrogen transfer and dehydrogenation reactions and hardly yields products below C_3 . Because bimolecular cracking via a bulky transition state is more restricted than monomolecular cracking in the narrow channels of ZSM-5 or ZSM-11, the production level of lower hydrocarbons (methane and ethane) and hydrogen from monomolecular cracking can be used to describe the proportion of Al in the channels.^[41, 87] 2,4-DMQ was added to avoid unselective cracking at the external crystallite surface.

The overall 3-MP conversion of <5% for all materials is well located in the differential regime, so activity and product selectivity can be directly compared.^[88] Accordingly, an excellent correlation between MTO selectivity to propylene and 3-MP cracking selectivity towards hydrogen, methane and ethane is observed for samples with the same Al content (Si/Al = 25 or 50, **Figure 2.9**).

MEL-25-S shows the highest selectivity towards hydrogen, methane and ethane (55%), whereas MFI-25-M the lowest selectivity (13%). Combined with **Table 2.4**, this means that the higher the fraction of Al in channels, the higher the selectivity towards propylene in MTO regardless of the zeolite structure except for MFI/MEL-25-S. Interestingly, an even better correlation between selectivity to propylene and Al fraction at channels is observed when the selectivity at steady-state conditions (MeOH conversion of 100% at TOS of 1 h in **Figure A5**) is chosen for all catalysts, in which MFI/MEL-25-S exhibits a higher selectivity to propylene than MFI-25-M.

The shape selectivity of different zeolite topologies for *n*-hexane and 3-MP cracking has also been quantified by the so-called constraint index (CI) presented in section 2.3.^[41, 89, 90] In our case, however, the studied materials possess a very similar channel/intersection structure and the sensitivity of this approach becomes less distinctive. Furthermore, the heterogeneous position distribution of lattice Al, shown by ²⁷Al MAS NMR, will affect the cracking mechanism of 3-MP leading to different 3-MP conversions and CI values.^[41] As example serves the CI test over MFI-25-S and MEL-25-S here. The *n*-hexane and 3-MP cracking (**Figure 2.10**) over MEL-25-S and MFI-25-S show that the CI (constraint index) value for MEL-25-S (1.2) is slightly larger than for MFI-25-S (1.0), and would suggest a larger steric hindrance in MEL-25-S than MFI-25-S.^[41, 89, 90] However, this observation is opposite to the fact that the pore size of MEL is slightly larger than MFI. Thus, in this study, CI serves more as a descriptor for a different lattice Al-distribution rather than a steric reactant hindrance of zeolite topology.

These results correlate well with the deconvolution results from ²⁷Al MAS NMR, which also indicates a higher fraction of Al in the channels on MEL-25-S than on MFI-25-M. An indicative trend between MTO propylene selectivity (activity of olefinic cycle) and Al location in the channel from NMR and from 3-MP cracking is also found for the samples with Si/Al of 50. With the lower Al content of MFI-50-S and MFI/MEL-50-L, the bimolecular cracking of 3-MP is a more dominant pathway because of the much lower activation energy^[53], resulting in selectivity towards methane, ethane and hydrogen below 17%. This also accounts for the higher total 3-MP conversion data for the samples with a

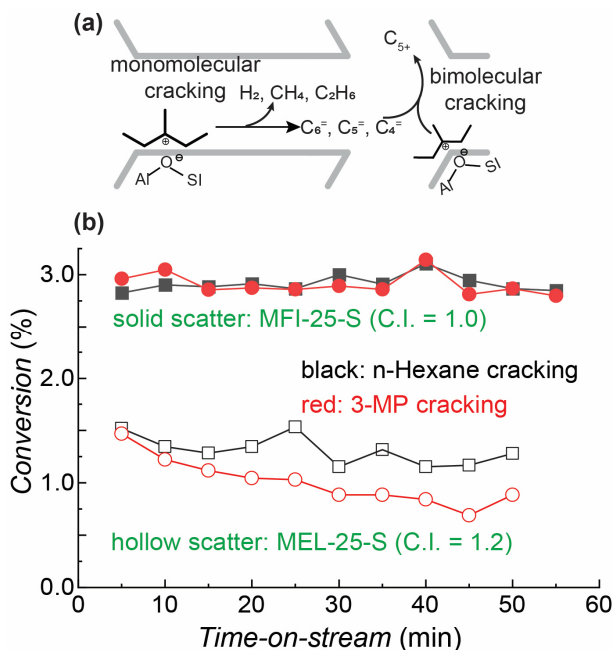


Figure 2.10. Reaction mechanism of monomolecular cracking and bimolecular cracking of 3-MP carbenium ions on BAS at channels and intersections, respectively^[41, 53] (a); *n*-hexane and 3-MP cracking over MFI-25-S (solid scatter, top) and MEL-25-S (hollow scatter, bottom) with function of TOS (b). CI was estimated by the ratio of unreacted *n*-hexane and 3-MP. Cracking conditions: $T = 400\text{ }^\circ\text{C}$, $m_{\text{cat}} = 20\text{ mg}$ (150–212 μm), 1 bar, carrier gas He = 40 mL/min, C6 paraffin partial pressure = 2.3 kPa in the presence of 2,4-DMQ (<0.1 kPa).

higher Al fraction (Si/Al = 25) in the intersections. The exceptional case is MFI-50-S. It exhibits the second highest 3-MP conversion of 3.3% among all studied materials, which might indicate the extraordinarily high proportion of Al located at the intersection and the lower selectivity to propylene than MFI/MEL-50-L.

2.4 Discussion

The objective of this study was to reveal key performance parameters of three 10-MR zeolite catalysts, *viz.* MFI, MEL, and a mixed MFI/MEL structure, in the MTO reaction, with the focus on MTO activity, product selectivity (propylene) and stability for two Si/Al ratios. MEL has a similar channel/intersection system as MFI with similar (slightly larger) nano-scale dimensions, but with only straight channels, while MFI/MEL samples contain an MFI and MEL intergrowth structure, which is more than simply a physical mixture.

MTO tests and *operando* UV–vis spectroscopy measurements reveal completely different product distributions and MTO lifetimes coupled with the different features of retained hydrocarbons in all three zeolite structures. With the same Al content (origin of the BAS) and BAS strength, the MEL-type zeolite is shown as the most propylene-selective catalyst in the MTO test, which is in line with reported observations.^[32, 91] Unlike the shorter MTO lifetime of MEL-type zeolites than of MFI-type zeolites in^[32], in our study MEL-25-S exhibits the highest MeOH conversion capacity, more than 50% higher than MFI-25-S and MFI/MEL-25-S. On the other hand, MFI/MEL-50-L shows the higher selectivity to propylene than MFI-50-S. Even two MFI-type samples with Si/Al of 25 exhibit different MTO performance regarding conversion capacity and product selectivity. All these observations indicate that besides the zeolite topology and Al content (BAS density) other parameters are involved in controlling their catalytic performance.

Of the various techniques applied only the 3-MP cracking, and the ²⁷Al MAS NMR spectra analysis revealed a clear correlation between the propylene selectivity in MTO with the Al located in the channels of the zeolites, regardless of zeolite framework and crystal size (**Figure 2.9**): the more Al located in the channels, the higher the selectivity to propylene and butylenes is observed. This seems the primary key performance parameter in this reaction. This suggests that 1D 10-MR zeolites, containing only channels would be the preferred catalysts, completely suppressing the aromatics-based cycle. Indeed, no aromatic products were observed for ZSM-22 and ZSM-23 catalysts, although ZSM-48 with slightly wider channels did.^[72, 92] Aromatics were formed in all catalysts, but were trapped in the former systems and only could diffuse out of the latter, similarly as for 1D 12-MR ZSM-12^[93]. Comparing ZSM-22 with ZSM-5 and ZSM-11 revealed, however, a lower propylene selectivity, ~38% versus ~50%, and a much shorter lifetime.^[30] Introduction of mesoporosity by desilication and acid treatment doubled the ZSM-22 lifetime with retained shape selectivity^[32], suggesting an easier escape of coke precursors like in the case of ZSM-48^[72]. So, the high propylene and butylene selectivity of the 10-MR MEL-25-S is attributed to its high fraction of Al located in the channels, similar as for the mixed phase MFI/MEL-50-L. The latter has the highest light olefin selectivity, indicating that an optimal BAS concentration exists for an optimal performance^[30]. Our results confirm the results of Wang *et al.*^[32] observing Al enrichment in the intersections of ZSM-5 and in the channels of ZSM-11. We further extend this rule to the intergrowth MFI/MEL samples. These findings provide a rational basis

for the targeted synthesis of 3D 10-MR zeolites with only Al located in the channels for improved olefin production. An enrichment of Al in the channels was indeed obtained by Li *et al.*^[81] by preparation of B-Al-ZSM-5 and removal of B that preferentially resided in the intersections. This indeed improved the propylene and butylene selectivity in MTO. These post-synthesis approaches confirm the attempts to concentrate Al in the channels of ZSM-5 (or remove it from the intersections) to improve the MeOH selectivity towards the lower olefins, in agreement with the results for theta-1 (TON-type, 1D zeolite)^[33, 94].

The correlation between Al located in the channels and MeOH selectivity towards propylene (or light olefins) holds for all three zeolite structures, which further suggests the Al location is a more significant factor than zeolite structure, at least among MFI, MEL, and MFI/MEL in MTO, while other properties (crystal size, Al-content and external BAS) are of secondary influence (less pronounced), affecting selectivity, coke deposition, and time-on-stream MTO activity.

It is rather difficult to determine a single key parameter controlling the MTO deactivation in this study. Smaller crystals provide shorter diffusion distances for (poly)aromatics to escape and a larger external area (capacity) for coke deposition. In larger crystals, the lower coke deposition in the outer crystal regions can limit accessibility to the BAS resulting in a faster deactivation and less coke. This might also explain the fast deactivation for MFI-25-M in comparison with other catalysts with the smaller crystal size.

Co(II) ion-exchange coupled with *ex-situ* UV-vis analysis reveals that a large fraction of Al_{pair} is located in the intersection regardless of Si/Al and zeolite structure. But there is no clear correlation between Al_{pair} information (fraction or location) with the MTO deactivation. Both MEL and MFI/MEL catalysts with the same Al content contain ca. 46% Al_{pair} with more than 70% of them in the intersection, but the MEL-type zeolite is shown as the most stable, while MFI/MEL-25-S the least stable catalyst in the MTO test. Another notorious example is MFI/MEL-50-L, which contains the smallest fraction of Al_{pair} but deactivates quickly in MTO. By applying 1,3,5-TIPB cracking, probing the acidity on the external surface of the samples, combined with XPS analysis, a heterogeneous distribution of Al within the zeolite particle is observed. As the uncontrolled alkylation of hydrocarbons leading to coke deposition on the external BAS in MTO could block the pores for further access to the internal active sites^[80], a less acidic outer surface expectedly correlates with the longer MTO lifetime and vice-versa. It explains the exceptionally high level of external BAS coupled with the low MeOH conversion capacity on MFI-25-M. The

intergrowth sample with Si/Al of 25 shows the highest level of external BAS, corresponding with the lowest MeOH conversion capacity in comparison with the MFI-type and MEL-type samples with the same Al content and crystal size. However, MEL-25-S exceptionally contains a higher fraction of external BAS but shows a higher MeOH conversion capacity than MFI-25-S, while MFI/MEL-50-L shows negligible external BAS coupled with a much lower MeOH conversion capacity than MFI-50-S. Clearly, the impact of Al distribution in the framework cannot be ignored. The MTO deactivation is closely related to the activity of the aromatic-based cycle, as polyaromatics are commonly described as the coke species. The higher level of Al located in the channels not only directs the MeOH selectivity towards light olefins, but also reduces the contribution of the competing aromatic-based cycle eventually leading to polyaromatics deposition. This might explain the high production of light olefins coupled with the largest MeOH conversion capacity for the MEL-type catalyst.

2.5 Conclusions

The property-performance relationship in the MTO process for three zeolite structures of MFI, MEL, and intergrowth MFI/MEL were evaluated via a series of characterization techniques and probe reactions. The MTO test combined with *operando* UV–vis spectroscopy shows that product selectivity, MeOH conversion capacity, and retained hydrocarbons before deactivation are significantly different for the studied zeolites. Besides the morphology and Al content, more intrinsic aspects concerning Al distribution were revealed and their correlations with the catalytic performance were discussed. Through ^{27}Al MAS NMR analysis and 3-MP cracking, an excellent correlation between Al location and MeOH selectivity towards propylene and butylenes is observed regardless of the different zeolite frameworks. The higher level of Al located in the channels (straight or sinusoidal) suppresses the propagation of the aromatic cycle, which requires spacious space like intersections, and favours the olefinic cycle. Therefore, the MeOH selectivity towards $\text{C}_3\text{-C}_4$ light olefins is considerably improved for MEL-type and one MFI/MEL intergrowth zeolite containing the highest fraction of Al in the channels. The intergrowth of MFI and MEL phases accelerates the catalyst deactivation rate evidenced by the lowest MeOH conversion capacities in the MTO process.

Other zeolite parameters as Al_{pair} and external BAS concentration, evaluated via Co ion-exchange technique and 1,3,5-TIPB cracking, showed lack of a clear correlation with MeOH selectivity and suggests these parameters are of less

pronounced influence on product distribution, specifically the production of propylene. No correlation between these parameters and MeOH conversion capacity was obtained, revealing MTO deactivation is a rather complex process, which cannot be captured by a single parameter. Crystal size, Al-content, external BAS and Al-distribution in the framework all affect the deactivation. All these characterizations and probe reactions still comprise part of catalyst properties that potentially affect the catalytic performance. More key parameters, such as diffusivity within the zeolite micropore^[95] are not analysed quantitatively in this study, but their impact on the MTO mechanism especially for the intergrowth MFI/MEL samples cannot be ignored.

This work not only provides the direct relationship between zeolite acidic properties and their catalytic influence in the MTO process benefiting the rational catalyst design for the MTO process but also reveals that MeOH transformation in the zeolite is an extremely complex process, which is affected by multiple parameters to a different level. Our study also highlights the importance of an integrated approach to characterizing and analysing all intrinsic properties of zeolite catalysts in the MTO process.

References

- (1) Olah, G. A. *Angewandte Chemie International Edition* **2005**, *44* (18), 2636-2639.
- (2) Olah, G. A.; Goepfert, A.; Prakash, G. S. *The Journal of Organic Chemistry* **2008**, *74* (2), 487-498.
- (3) Mota, F. M.; Kim, D. H. *Chemical Society Reviews* **2019**, *48* (1), 205-259.
- (4) Keil, F. J. *Microporous and Mesoporous Materials* **1999**, *29* (1), 49-66.
- (5) Tian, P.; Wei, Y.; Ye, M.; Liu, Z. *ACS Catalysis* **2015**, *5* (3), 1922-1938.
- (6) Wei, X. US 201013505908 A, **2012**.
- (7) Svelle, S.; Joensen, F.; Nerlov, J.; Olsbye, U.; Lillerud, K.-P.; Kolboe, S.; Bjørgen, M. *Journal of the American Chemical Society* **2006**, *128* (46), 14770-14771.
- (8) Xu, S.; Zheng, A.; Wei, Y.; Chen, J.; Li, J.; Chu, Y.; Zhang, M.; Wang, Q.; Zhou, Y.; Wang, J.; Deng, F.; Liu, Z. *Angewandte Chemie International Edition* **2013**, *52* (44), 11564-11568.
- (9) Olsbye, U.; Svelle, S.; Lillerud, K.; Wei, Z.; Chen, Y.; Li, J.; Wang, J.; Fan, W. *Chemical Society Reviews* **2015**, *44* (20), 7155-7176.
- (10) Wu, X.; Xu, S.; Zhang, W.; Huang, J.; Li, J.; Yu, B.; Wei, Y.; Liu, Z. *Angewandte Chemie International Edition* **2017**, *56* (31), 9039-9043.
- (11) Li, C.; Paris, C.; Martínez-Triguero, J.; Boronat, M.; Moliner, M.; Corma, A. *Nature Catalysis* **2018**, *1* (7), 547-554.
- (12) Yarulina, I.; De Wispelaere, K.; Bailleul, S.; Goetze, J.; Radersma, M.; Abou-Hamad, E.; Vollmer, I.; Goesten, M.; Mezari, B.; Hensen, E. J. M.; Martínez-Espin, J. S.; Morten, M.; Mitchell, S.; Perez-Ramirez, J.; Olsbye, U.; Weckhuysen, B. M.; Van Speybroeck, V.; Kapteijn, F.; Gascon, J. *Nature Chemistry* **2018**, *10* (8), 804-812.
- (13) McCann, D. M.; Lesthaeghe, D.; Kletnieks, P. W.; Guenther, D. R.; Hayman, M. J.; Van Speybroeck, V.; Waroquier, M.; Haw, J. F. *Angewandte Chemie International Edition* **2008**, *47* (28), 5179-5182.
- (14) Ilias, S.; Bhan, A. *Journal of Catalysis* **2012**, *290*, 186-192.
- (15) Hwang, A.; Bhan, A. *Accounts of Chemical Research* **2019**, *52* (9), 2647-2656.
- (16) Yarulina, I.; Chowdhury, A. D.; Meirer, F.; Weckhuysen, B. M.; Gascon, J. *Nature Catalysis* **2018**, *1* (6), 398-411.
- (17) Stöcker, M. *Microporous and Mesoporous Materials* **1999**, *29* (1), 3-48.
- (18) Olsbye, U.; Svelle, S.; Bjørgen, M.; Beato, P.; Janssens, T. V. W.; Joensen, F.; Bordiga, S.; Lillerud, K. P. *Angewandte Chemie International Edition* **2012**, *51* (24), 5810-5831.
- (19) Ilias, S.; Bhan, A. *ACS Catalysis* **2013**, *3* (1), 18-31.
- (20) Bjørgen, M.; Olsbye, U.; Petersen, D.; Kolboe, S. *Journal of Catalysis* **2004**, *221* (1), 1-10.
- (21) Song, W.; Fu, H.; Haw, J. F. *Journal of the American Chemical Society* **2001**, *123* (20), 4749-4754.
- (22) Olsbye, U.; Svelle, S.; Bjørgen, M.; Beato, P.; Janssens, T. V.; Joensen, F.; Bordiga, S.; Lillerud, K. P. *Angewandte Chemie International Edition* **2012**, *51* (24), 5810-5831.
- (23) Ilias, S.; Khare, R.; Malek, A.; Bhan, A. *Journal of Catalysis* **2013**, *303*, 135-140.
- (24) Khare, R.; Liu, Z.; Han, Y.; Bhan, A. *Journal of Catalysis* **2017**, *348*, 300-305.
- (25) Wei, R.; Li, C.; Yang, C.; Shan, H. *Journal of Natural Gas Chemistry* **2011**, *20* (3), 261-265.

- (26) Danilina, N.; Krumeich, F.; Castelanelli, S. A.; van Bokhoven, J. A. *The Journal of Physical Chemistry C* **2010**, *114* (14), 6640-6645.
- (27) Pashkova, V.; Sklenak, S.; Klein, P.; Urbanova, M.; Dědeček, J. *Chemistry – A European Journal* **2016**, *22* (12), 3937-3941.
- (28) Smit, B.; Maesen, T. L. *Nature* **2008**, *451* (7179), 671-678.
- (29) Hereijgers, B. P.; Bleken, F.; Nilsen, M. H.; Svelle, S.; Lillerud, K.-P.; Bjørgen, M.; Weckhuysen, B. M.; Olsbye, U. *Journal of Catalysis* **2009**, *264* (1), 77-87.
- (30) Dyballa, M.; Becker, P.; Trefz, D.; Klemm, E.; Fischer, A.; Jakob, H.; Hunger, M. *Applied Catalysis A: General* **2016**, *510*, 233-243.
- (31) Yu, Q.; Cui, C.; Zhang, Q.; Chen, J.; Li, Y.; Sun, J.; Li, C.; Cui, Q.; Yang, C.; Shan, H. *Journal of Energy Chemistry* **2013**, *22* (5), 761-768.
- (32) Wang, S.; Wang, P.; Qin, Z.; Chen, Y.; Dong, M.; Li, J.; Zhang, K.; Liu, P.; Wang, J.; Fan, W. *ACS Catalysis* **2018**, *8* (6), 5485-5505.
- (33) Dyballa, M.; Obenaus, U.; Rosenberger, M.; Fischer, A.; Jakob, H.; Klemm, E.; Hunger, M. *Microporous and Mesoporous Materials* **2016**, *233*, 26-30.
- (34) Teketel, S.; Olsbye, U.; Lillerud, K. P.; Beato, P.; Svelle, S. *Applied Catalysis A: General* **2015**, *494*, 68-76.
- (35) Wang, J.; Wei, Y.; Li, J.; Xu, S.; Zhang, W.; He, Y.; Chen, J.; Zhang, M.; Zheng, A.; Deng, F. *Catalysis Science & Technology* **2016**, *6* (1), 89-97.
- (36) Baerlocher, C.; McCusker, L. B. *Database of Zeolite Structures*, <http://www.iza-structure.org/databases>.
- (37) Millward, G. R.; Ramdas, S.; Thomas, J. M.; Barlow, M. T. *Journal of the Chemical Society, Faraday Transactions 2: Molecular and Chemical Physics* **1983**, *79* (7), 1075-1082.
- (38) Conte, M.; Xu, B.; Davies, T. E.; Bartley, J. K.; Carley, A. F.; Taylor, S. H.; Khalid, K.; Hutchings, G. J. *Microporous and Mesoporous Materials* **2012**, *164*, 207-213.
- (39) Zhong, J.; Han, J.; Wei, Y.; Liu, Z. *Journal of Catalysis* **2021**, *396*, 23-31.
- (40) Emeis, C. *Journal of Catalysis* **1993**, *141* (2), 347-354.
- (41) Yokoi, T.; Mochizuki, H.; Namba, S.; Kondo, J. N.; Tatsumi, T. *The Journal of Physical Chemistry C* **2015**, *119* (27), 15303-15315.
- (42) Petrakis, L. *Journal of Chemical Education* **1967**, *44* (8), 432.
- (43) Chen, K. *International Journal of Molecular Sciences* **2020**, *21* (16), 5666.
- (44) Holzinger, J.; Beato, P.; Lundegaard, L. F.; Skibsted, J. *The Journal of Physical Chemistry C* **2018**, *122* (27), 15595-15613.
- (45) Liang, T.; Chen, J.; Qin, Z.; Li, J.; Wang, P.; Wang, S.; Wang, G.; Dong, M.; Fan, W.; Wang, J. *ACS Catalysis* **2016**, *6* (11), 7311-7325.
- (46) Dědeček, J.; Tabor, E.; Sklenak, S. *ChemSusChem* **2019**, *12* (3), 556-576.
- (47) Dědeček, J.; Kaucký, D.; Wichterlová, B. *Microporous and Mesoporous Materials* **2000**, *35-36*, 483-494.
- (48) Dědeček, J.; Kaucký, D.; Wichterlová, B.; Gonsiorová, O. *Physical Chemistry Chemical Physics* **2002**, *4* (21), 5406-5413.
- (49) Verberckmoes, A. A.; Weckhuysen, B. M.; Schoonheydt, R. A. *Microporous and Mesoporous Materials* **1998**, *22* (1-3), 165-178.
- (50) Tabor, E.; Bernauer, M.; Wichterlová, B.; Dědeček, J. *Catalysis Science & Technology* **2019**, *9* (16), 4262-4275.
- (51) Namba, S.; Nakanishi, S.; Yashima, T. *Journal of Catalysis* **1984**, *88* (2), 505-508.
- (52) Namba, S.; Inaka, A.; Yashima, T. *Zeolites* **1986**, *6* (2), 107-110.
- (53) Krannila, H.; Haag, W. O.; Gates, B. C. *Journal of Catalysis* **1992**, *135* (1), 115-124.

- (54) Haag, W. O.; Lago, R. M.; Weisz, P. B. *Faraday Discussions of the Chemical Society* **1981**, *72*, 317-330.
- (55) Frillette, V. J.; Haag, W. O.; Lago, R. M. *Journal of Catalysis* **1981**, *67* (1), 218-222.
- (56) Janssens, T. V. W. *Journal of Catalysis* **2009**, *264* (2), 130-137.
- (57) Goetze, J.; Meirer, F.; Yarulina, I.; Gascon, J.; Kapteijn, F.; Ruiz-Martinez, J.; Weckhuysen, B. M. *ACS Catalysis* **2017**, *7* (6), 4033-4046.
- (58) Borodina, E.; Sharbini Harun Kamaluddin, H.; Meirer, F.; Mokhtar, M.; Asiri, A. M.; Al-Thabaiti, S.; Basahel, S. N.; Ruiz-Martinez, J.; Weckhuysen, B. *ACS Catalysis* **2017**, *7* (8), 5268-5281.
- (59) Nijhuis, T. X.; Tinnemans, S. J.; Visser, T.; Weckhuysen, B. M. *Physical Chemistry Chemical Physics* **2003**, *5* (20), 4361-4365.
- (60) Bordiga, S.; Lamberti, C.; Bonino, F.; Travert, A.; Thibault-Starzyk, F. *Chemical Society Reviews* **2015**, *44* (20), 7262-7341.
- (61) Nachtigall, P.; Delgado, M. R.; Nachtigallova, D.; Areán, C. O. *Physical Chemistry Chemical Physics* **2012**, *14* (5), 1552-1569.
- (62) Almutairi, S. M. T.; Mezari, B.; Pidko, E. A.; Magusin, P. C. M. M.; Hensen, E. J. M. *Journal of Catalysis* **2013**, *307*, 194-203.
- (63) Gabrienko, A. A.; Danilova, I. G.; Arzumanov, S. S.; Pirutko, L. V.; Freude, D.; Stepanov, A. G. *The Journal of Physical Chemistry C* **2018**, *122* (44), 25386-25395.
- (64) Dwyer, J.; Fitch, F.; Nkang, E. *The Journal of Physical Chemistry* **1983**, *87* (26), 5402-5404.
- (65) Liu, C.; Li, G.; Hensen, E. J.; Pidko, E. A. *Journal of Catalysis* **2016**, *344*, 570-577.
- (66) Wang, N.; Zhi, Y.; Wei, Y.; Zhang, W.; Liu, Z.; Huang, J.; Sun, T.; Xu, S.; Lin, S.; He, Y. *Nature Communications* **2020**, *11* (1), 1-12.
- (67) Hu, S.; Shan, J.; Zhang, Q.; Wang, Y.; Liu, Y.; Gong, Y.; Wu, Z.; Dou, T. *Applied Catalysis A: General* **2012**, *445-446*, 215-220.
- (68) Jeon, M. Y.; Kim, D.; Kumar, P.; Lee, P. S.; Rangnekar, N.; Bai, P.; Shete, M.; Elyassi, B.; Lee, H. S.; Narasimharao, K. *Nature* **2017**, *543* (7647), 690.
- (69) Mei, C.; Wen, P.; Liu, Z.; Liu, H.; Wang, Y.; Yang, W.; Xie, Z.; Hua, W.; Gao, Z. *Journal of Catalysis* **2008**, *258* (1), 243-249.
- (70) Wu, L.; Degirmenci, V.; Magusin, P. C. M. M.; Lousberg, N. J. H. G. M.; Hensen, E. J. M. *Journal of Catalysis* **2013**, *298*, 27-40.
- (71) Bleken, F. L.; Chavan, S.; Olsbye, U.; Boltz, M.; Ocampo, F.; Louis, B. *Applied Catalysis A: General* **2012**, *447-448*, 178-185.
- (72) Teketel, S.; Skistad, W.; Benard, S.; Olsbye, U.; Lillerud, K. P.; Beato, P.; Svelle, S. *ACS Catalysis* **2012**, *2* (1), 26-37.
- (73) Khare, R.; Millar, D.; Bhan, A. *Journal of Catalysis* **2015**, *321*, 23-31.
- (74) Arstad, B.; Kolboe, S. *Journal of the American Chemical Society* **2001**, *123* (33), 8137-8138.
- (75) Bjørgen, M.; Bonino, F.; Arstad, B.; Kolboe, S.; Lillerud, K. P.; Zecchina, A.; Bordiga, S. *ChemPhysChem* **2005**, *6* (2), 232-235.
- (76) Goetze, J.; Weckhuysen, B. M. *Catalysis Science & Technology* **2018**, *8* (6), 1632-1644.
- (77) Wang, C.; Xu, J.; Qi, G.; Gong, Y.; Wang, W.; Gao, P.; Wang, Q.; Feng, N.; Liu, X.; Deng, F. *Journal of Catalysis* **2015**, *332*, 127-137.
- (78) Palumbo, L.; Bonino, F.; Beato, P.; Bjørgen, M.; Zecchina, A.; Bordiga, S. *The Journal of Physical Chemistry C* **2008**, *112* (26), 9710-9716.

- (79) Bjørgen, M.; Svelle, S.; Joensen, F.; Nerlov, J.; Kolboe, S.; Bonino, F.; Palumbo, L.; Bordiga, S.; Olsbye, U. *Journal of Catalysis* **2007**, *249* (2), 195-207.
- (80) Mores, D.; Stavitski, E.; Kox, M. H. F.; Kornatowski, J.; Olsbye, U.; Weckhuysen, B. M. *Chemistry – A European Journal* **2008**, *14* (36), 11320-11327.
- (81) Li, C.; Vidal-Moya, A.; Miguel, P. J.; Dedecek, J.; Boronat, M.; Corma, A. *ACS Catalysis* **2018**, *8* (8), 7688-7697.
- (82) Han, O. H.; Kim, C.-S.; Hong, S. B. *Angewandte Chemie International Edition* **2002**, *41* (3), 469-472.
- (83) Dědeček, J.; Sobalík, Z.; Wichterlová, B. *Catalysis Reviews* **2012**, *54* (2), 135-223.
- (84) Wang, S.; Chen, Y.; Wei, Z.; Qin, Z.; Ma, H.; Dong, M.; Li, J.; Fan, W.; Wang, J. *The Journal of Physical Chemistry C* **2015**, *119* (51), 28482-28498.
- (85) Sarv, P.; Fernandez, C.; Amoureux, J.-P.; Keskinen, K. *The Journal of Physical Chemistry* **1996**, *100* (50), 19223-19226.
- (86) Dědeček, J.; Lucero, M. J.; Li, C.; Gao, F.; Klein, P.; Urbanova, M.; Tvaruzkova, Z.; Sazama, P.; Sklenak, S. *The Journal of Physical Chemistry C* **2011**, *115* (22), 11056-11064.
- (87) Zhang, M.; Wang, M.; Xu, B.; Ma, D. *Joule* **2019**, *3* (12), 2876-2883.
- (88) Kubo, K.; Iida, H.; Namba, S.; Igarashi, A. *Journal of the Japan Petroleum Institute* **2018**, *61* (1), 10-19.
- (89) Imyen, T.; Wannapakdee, W.; Limtrakul, J.; Wattanakit, C. *Fuel* **2019**, *254*, 115593.
- (90) Voogd, P.; Van Bekkum, H. *Applied Catalysis* **1990**, *59* (1), 311-331.
- (91) Bleken, F.; Skistad, W.; Barbera, K.; Kustova, M.; Bordiga, S.; Beato, P.; Lillerud, K. P.; Svelle, S.; Olsbye, U. *Physical Chemistry Chemical Physics* **2011**, *13* (7), 2539-2549.
- (92) Teketel, S.; Olsbye, U.; Lillerud, K.-P.; Beato, P.; Svelle, S. *Microporous and Mesoporous Materials* **2010**, *136* (1-3), 33-41.
- (93) Liu, Z.; Chu, Y.; Tang, X.; Huang, L.; Li, G.; Yi, X.; Zheng, A. *The Journal of Physical Chemistry C* **2017**, *121* (41), 22872-22882.
- (94) Jamil, A. K.; Muraza, O.; Yoshioka, M.; Al-Amer, A. M.; Yamani, Z. H.; Yokoi, T. *Industrial & Engineering Chemistry Research* **2014**, *53* (50), 19498-19505.
- (95) Cnudde, P.; Demuynck, R.; Vandenbrande, S.; Waroquier, M.; Sastre, G.; Speybroeck, V. V. *Journal of the American Chemical Society* **2020**, *142* (13), 6007-6017.

APPENDIX A - An integrated approach to the
key parameters in MTO reaction catalyzed by
MFI/MEL zeolite materials

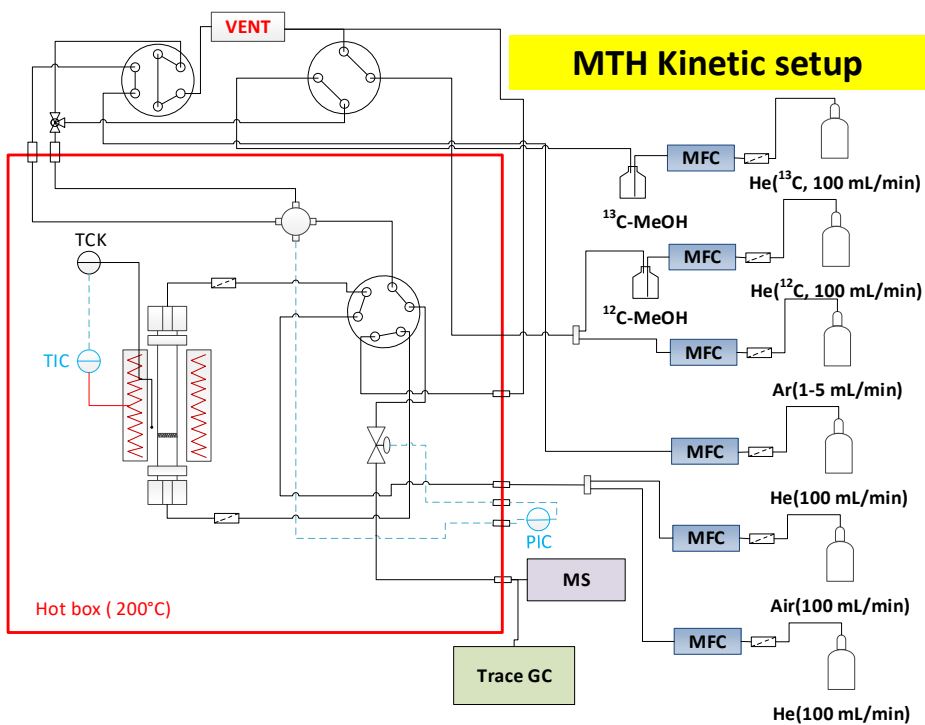


Figure A1. Scheme of MTH kinetic setup used in this thesis.

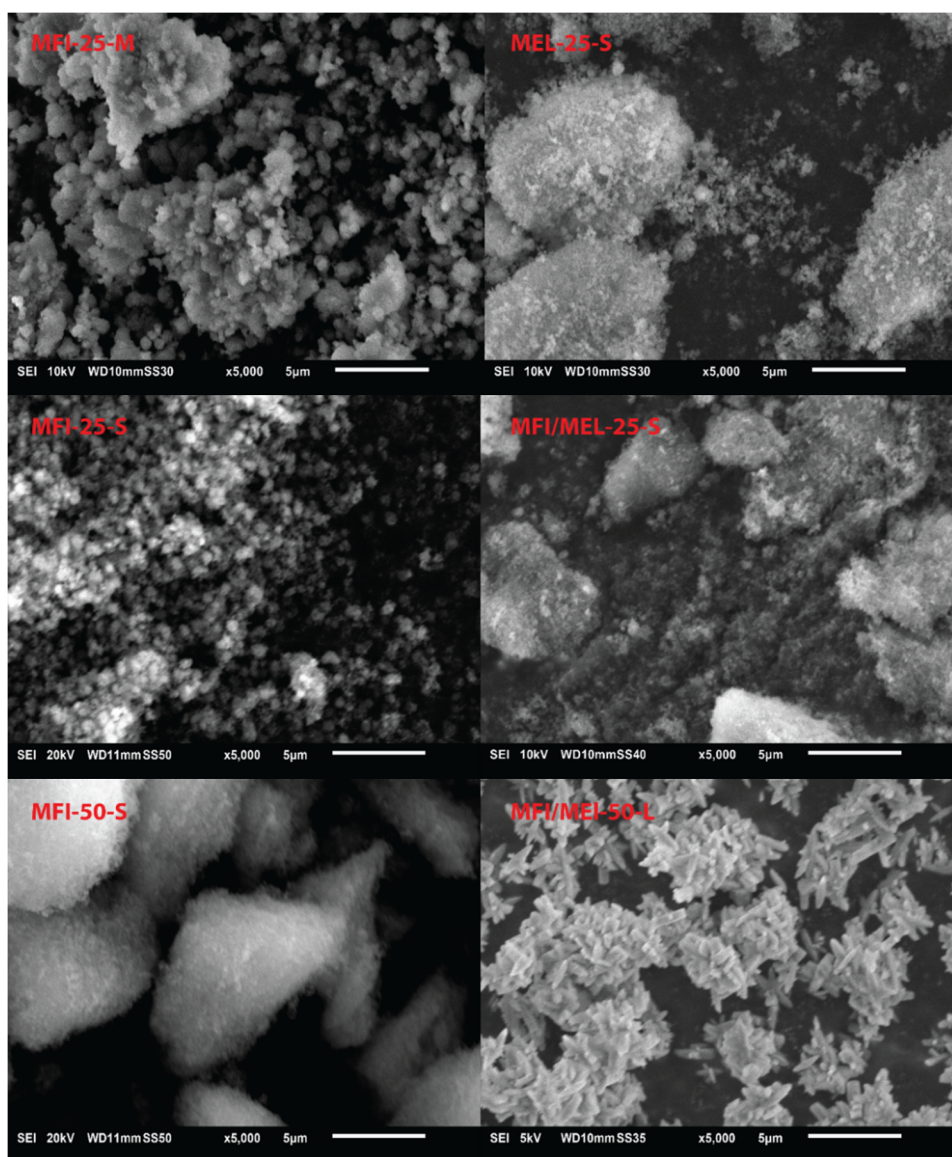


Figure A2. Scanning electron microscopy (SEM) images of all samples under study. Scale bar 5 μm.

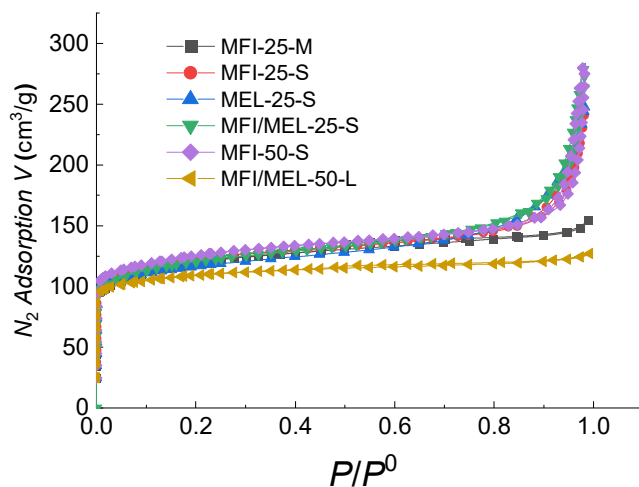


Figure A3. N₂ physisorption isotherms of selected zeolites under study.

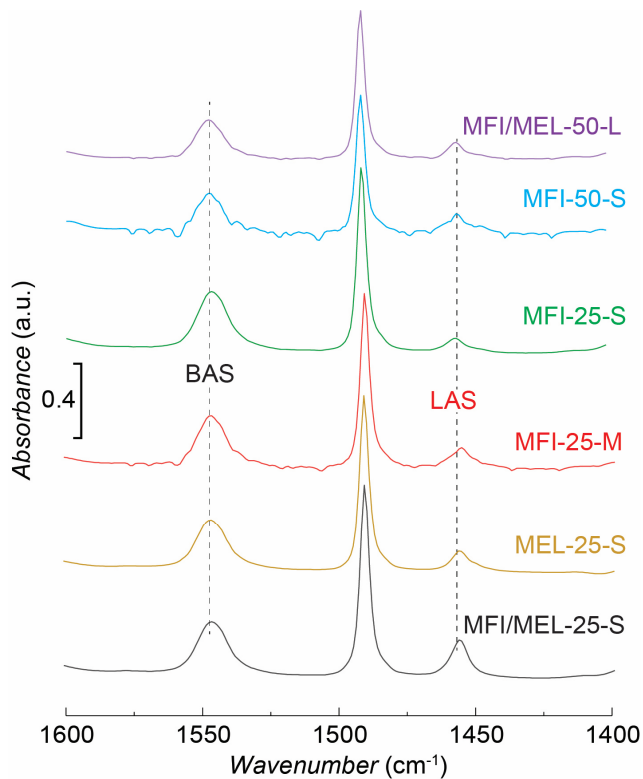


Figure A4. FT-IR spectrum in 1600–1400 cm⁻¹ range of pyridine adsorption on all studied materials.

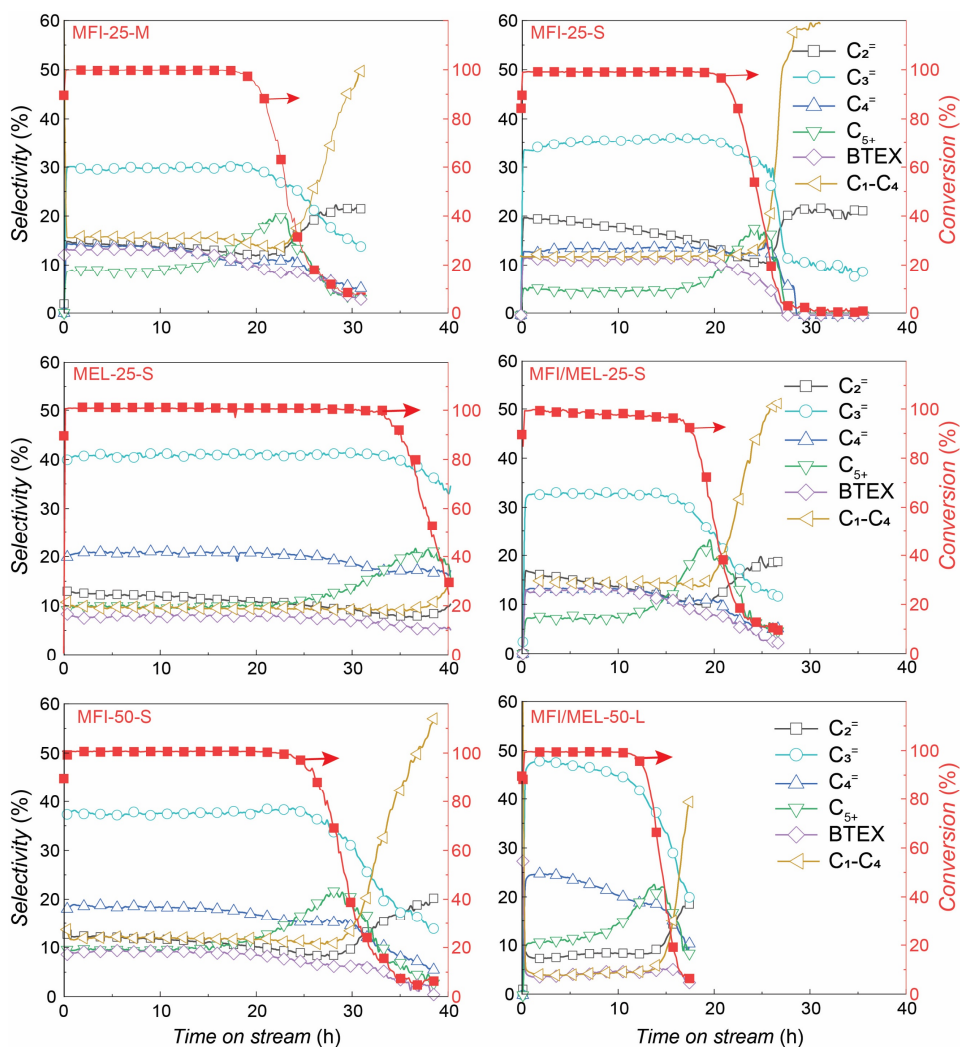


Figure A5. Time-on-stream MTO conversion and selectivity profiles for all catalysts investigated. “ $C_2=$ ”, “ $C_3=$ ” and “ $C_4=$ ” represent ethylene, propylene, and butenes, respectively. “BTEX” represents the aromatic group of benzene, toluene, ethylbenzene and xylenes (*m*-, *p*- and *o*-). “ C_1-C_4 ” represents the C_1-C_4 alkanes. “ C_{5+} ” represents heavier hydrocarbons with carbon number higher than 4. Reaction conditions: $T = 450\text{ }^\circ\text{C}$, $P_{\text{tot}} = 1\text{ bar}$, $m_{\text{cat}} = 40\text{ mg}$ (150–212 μm), $WHSV = 5.2\text{ g}_{\text{MeOH}}\text{g}_{\text{cat}}^{-1}\text{h}^{-1}$, carrier gas $\text{N}_2 = 50\text{ mL/min}$.

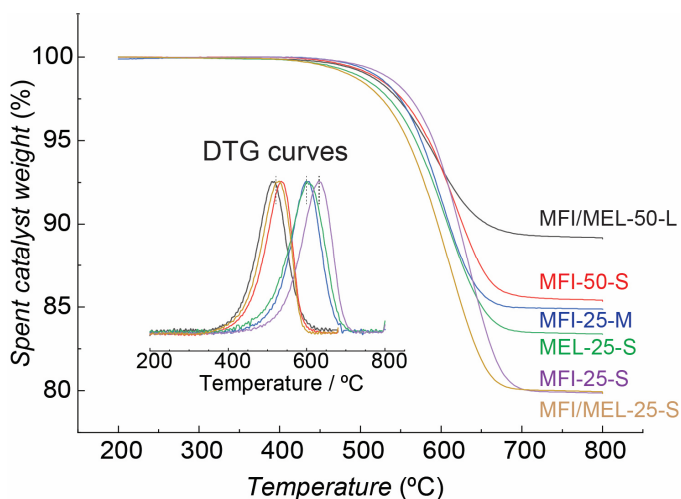


Figure A6. Spent catalyst weight loss profiles as a function of temperature. TGA conditions: 200–800 °C with 5 °C/min in 20 mL/min air. The coke content increases from 10 wt.% on MFI/MEL-50-L to ca. 20 wt.% on MFI/MEL-25-S and MFI-25-S. Although MFI/MEL-25-S and MFI-25-S contain a similar coke content, the nature of the coke is quite different. The peak temperature (inflection point) of DTG curves are at 525 °C and 625 °C for MFI/MEL-25-S and MFI-25-S, respectively, indicating the presence of “harder” coke components on MFI-25-S than on MFI/MEL-25-S.

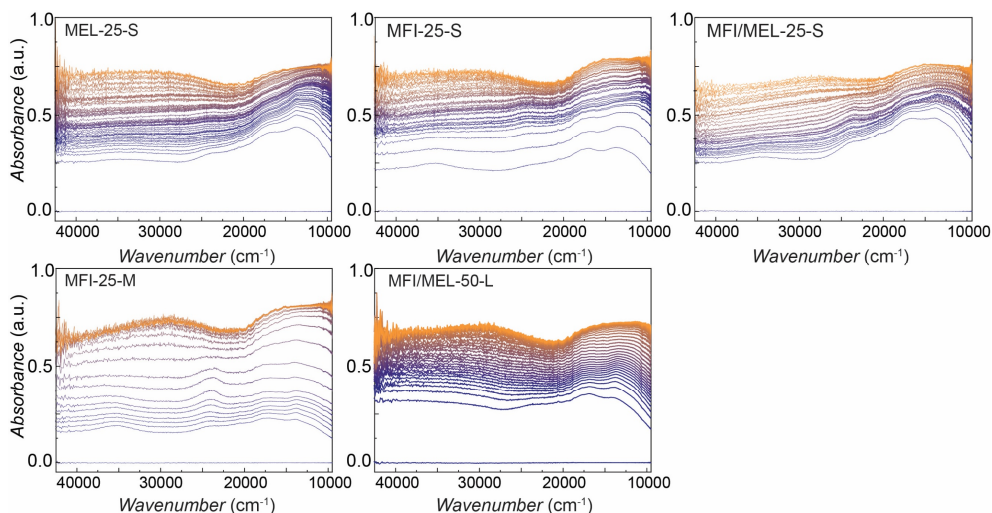


Figure A7. Time-resolved *operando* UV-vis spectra during MeOH conversion at 450 °C over of all catalysts under study. Spectra interval is 1 min.

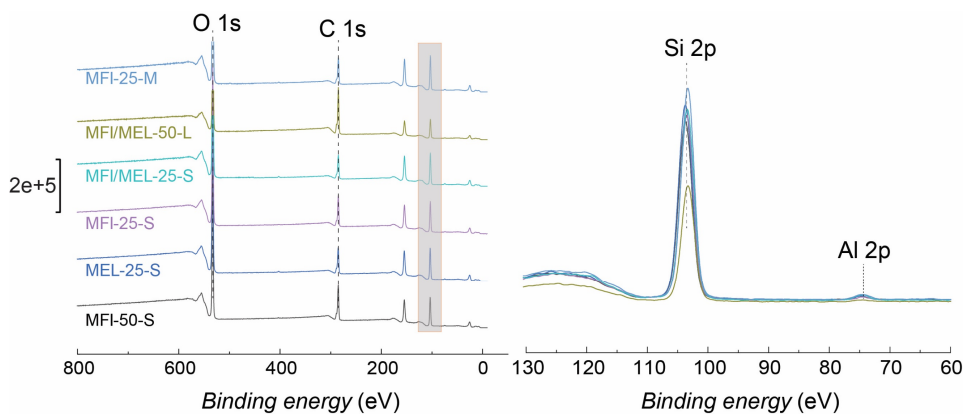


Figure A8. Survey scans (a) and Si2P and Al2P region (b) of XPS spectra for catalysts.

Table A1. Calculated % Al proportion of Al_{pair} and Al_{single} through ICP-AES analysis of Co-ion exchange samples.

	Al _{single} / %	Al _{pair} / %	Al _{pair} distribution / %		
			α	β	γ
MEL-25-S	53	47	10	77	13
MFI/MEL-25-S	54	46	10	77	13
MFI-25-M	70	30	13	71	16
MFI-25-S	71	29	14	72	14
MFI-50-S	58	42	17	73	10
MFI/MEL-50-L	87	13	14	68	18

Appendix A

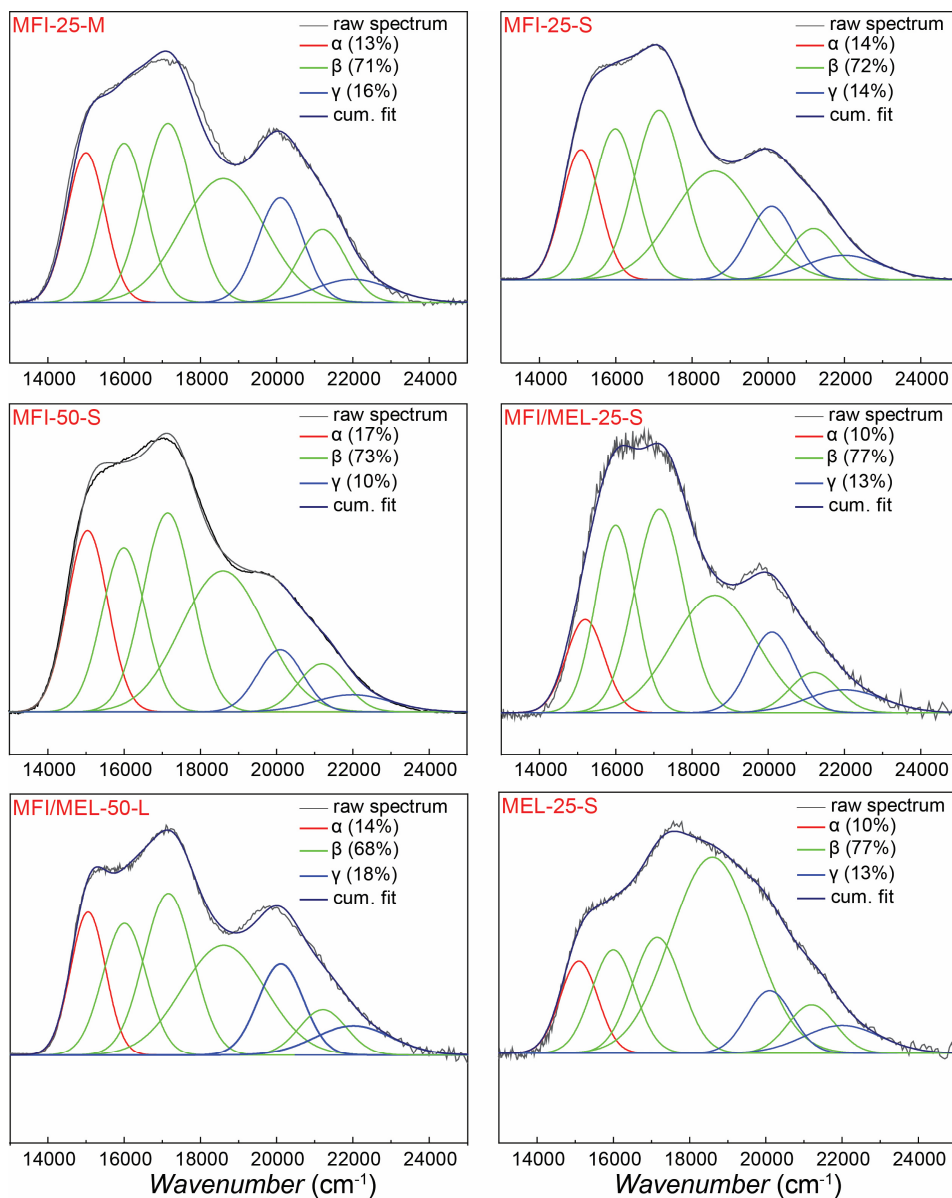


Figure A9. UV-vis spectra of Co fully exchanged samples. The fraction of Co(II) at different positions (straight channel α , intersection β and sinusoidal channel γ) were measured by deconvolution of UV-vis spectra of dehydrated samples^[1, 2]. Note that both α and γ represents straight channels in MEL-1 sample.

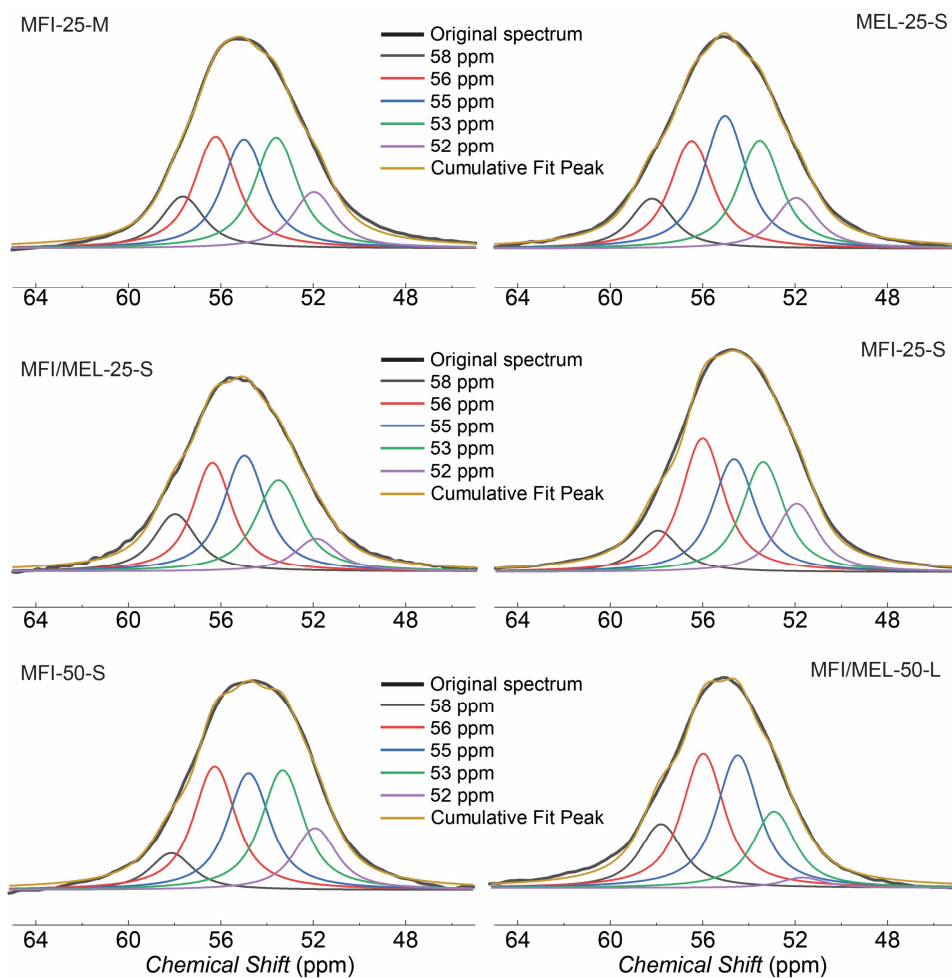


Figure A10. Deconvolution of ^{27}Al MAS NMR spectrum at 65–45 ppm of all samples under study. Voigt function ($G/L = 0.5$) was applied for the deconvolution process.

References

- (1) Dědeček, J.; Kaucký, D.; Wichterlová, B.; Gonsiorová, O. *Physical Chemistry Chemical Physics* **2002**, 4 (21), 5406-5413.
- (2) Dědeček, J.; Kaucký, D.; Wichterlová, B. *Microporous and Mesoporous Materials* **2000**, 35-36, 483-494.

Chapter 3. Direct discerning reaction pathways in MTH reactions by transient operation - FASPA

A new direct technique called ‘fast scanning-pulse analysis’ (FASPA) by gas chromatography analysis was reported allowing the direct characterization and detailed kinetic analysis of intimately interweaved catalytic paths occurring within the catalyst bed. The power and potential of the FASPA approach are demonstrated with methanol-to-hydrocarbons (MTH) process over H-ZSM-5 zeolite. Over a fresh catalyst, the hydrocarbon pool (HCP) is built-up upon exposure to methanol (MeOH) during the induction period, followed by a transition regime to a *quasi*-steady state MTH operation. This FASPA technique allows sub-second resolution of the full temporal products spectrum response upon a MeOH pulse providing direct and quantitative insight into the MTH reactions in these initial periods. Globally two consecutive pathways can be discerned: a very fast primary product formation in the presence of MeOH in a narrow active MTH reaction zone, followed by a slower formation of light aromatics, which is closely related to the decomposition and release of HCP species and secondary reactions in absence of MeOH in the downstream part of the catalyst bed. The time delay between the appearance of the inert tracer and primary products represents the time needed to build-up the HCP in the induction period, where methane is the first observed product. The primary products (alkanes, olefins, and light aromatics) are nearly instantaneously formed from the pulsed MeOH. These results demonstrate the highly dynamic character of the HCP in the MTH process over H-ZSM-5.

This Chapter has been submitted for publication as:

Liu, C., Uslamin, E.A., Pidko, E.A. and Kapteijn, F., Direct discerning reaction pathways in methanol-to-hydrocarbons by transient operation – FASPA.

3.1 Introduction

Elucidating the reaction mechanism and kinetics analysis is essential for rational catalyst design and process optimization. However, the direct characterization of multistep reaction networks under operating conditions remains challenging because of the strong interplay between the substrates involved in different elementary steps. Moreover, limiting tools to determine the product distribution in a transient study of a complex reaction network hinders the direct monitoring of the reaction mechanism and the quantitative analysis to harvest the full kinetic information. The hydrocarbon conversion such as methanol-to-hydrocarbons (MTH) in the zeolite-type catalysts represents a prominent case of a catalytic process facing these complexities. The synthesis of hydrocarbons from the MTH process presents an alternative way to reduce fossil fuel reliance, while methanol (MeOH) can be generated from various substrates such as CO₂, natural gas, and biomass.^[1-5]

Even though the MTH reaction mechanism has been studied extensively for more than 40 years, there are still ongoing debates over two key aspects: 1) the initial direct C–C bond formation and 2) the reaction pathways for the formation of various hydrocarbons and their connection to intra-zeolite ‘hydrocarbon pool’ (HCP) species. The lack of versatile experimental research methods, which must be space- and time-resolved and applicable under actual reactive conditions, adds to the challenge of investigating such a complex system. Although the recent advent of sophisticated characterization technologies such as *in situ* solid-state NMR provided more solid experimental evidence and further insights explaining the initial direct C–C bond formation,^[6-9] solid experimental evidence obtained under real experimental MTH conditions (e.g., > 400 °C) is still very limited. Note that olefins and other products are generated almost immediately after a relatively short induction period after the initial C–C formation, especially at industrial temperature levels, resulting in the so-called *quasi* steady-state operation.^[10] An HCP mechanism was proposed especially in CHA-type zeolites (such as H-SAPO-34 and H-SSZ-13) with a cage-window structure (in contrast with the channel-intersection structure of MFI-type H-ZSM-5) to explain the final hydrocarbon formation.^[11] Based on this concept, formed HCP intermediates (preferably described as cyclic or aromatic compounds) are trapped in the cage. The final products such as light olefins are split-off products from these active pool species. Studying these reaction routes of MTH and the accompanying kinetic research under industrially-relevant conditions are challenging due to the

extremely fast MeOH conversion rate (autocatalytic process), where many closely related elementary steps occur nearly instantaneously.^[12] In fixed bed operation generally full MeOH conversion is obtained, implying a small reaction zone that gradually moves through the catalyst bed during the slow catalyst deactivation.^[13, 14]

So far, several transient kinetic techniques such as the temporal analysis of products (TAP) and $^{12}\text{C}/^{13}\text{C}$ isotope labeling have been utilized to obtain highly specific mechanistic and kinetic information, especially on the MTH mechanism.^[15, 16] However, the challenging transient data analysis heavily relying on mass spectrometry in the TAP setup^[17] limits the discrimination of specific individual reaction steps such as olefin methylation or cracking in the MTH^[16, 18], since they can affect each other in such a complex reaction network. Detailed mechanistic and kinetic information can be extracted from $^{12}\text{C}/^{13}\text{C}$ labeling experiments, but the off-line GC-MS analysis implies that a continuous and instant temporal product distribution is not accessible. Pulse-quench methods combined with spectroscopic measurements are also used to investigate the transition from the induction period to the steady-state formation of hydrocarbons on a running zeolite catalyst.^[19, 20] *Ex-situ* ^{13}C CP/MAS NMR spectroscopy measurements on the quenched zeolite catalysts after the ethylene pulse revealed that 1,3-dimethylcyclopentenyl carbenium ions were produced almost instantaneously above 350 °C. At elevated temperatures, the presence of such species on a working zeolite catalyst greatly decreases the induction duration and speeds up the methylation rate in the ethylene-to-toluene process, suggesting active participation of these species in the MTH process.^[19, 20] More intriguingly, if the time interval between ethylene pulses is long, the kinetic induction phase is resumed, indicating the reactive and dynamic nature of these HCP species. However, owing to the rapid generation and degradation (in seconds) of these entrapped species, including methylcyclopentadienes and methylbenzenes via, respectively, deprotonation and ring expansion of 1,3-dimethylcyclopentenyl ions^[20], online measurement of gaseous hydrocarbon products is difficult, especially on the working catalyst.

In this work, a newly developed transient kinetics technique is introduced, based on a combination of stimulus-response operation with fast scanning-pulse analysis by GC, coined FASPA, and *in situ* DRIFT spectroscopy measurement. The combination of repetitive MeOH pulse injection and fine control of the online GC sampling delay allows a quantitative mapping of the fast temporal evolution

of the products responses upon a MeOH pulse, even when the GC analysis is far slower. After a careful validation of this new approach, the dynamic features of the MTH process over H-ZSM-5, including direct MeOH transformation, secondary reactions after MeOH depletion, and decomposition/desorption processes, are decoupled and analyzed quantitatively. Combining pulse and *in situ* DRIFT experiments, the fast instantaneous formation of aliphatic species and aromatics is attributed to the induction-transition period for HCP build-up, whereas a following second aromatics formation is a result of desorption/decomposition of HCP species and secondary reactions in the downstream region of the bed.

3.2 Experimental methods

3.2.1 Zeolite samples and chemicals

ZSM-5 (NH₄-ZSM-5, Si/Al 25) and silicalite-1 were received from BASF. After calcination in air at 550 °C (2 °C/min) for 6 h, the obtained zeolites are further denoted as H-ZSM-5 (protonic form) and Sil-1, respectively. The calcined zeolite powder was compressed, crushed, and sieved to a particle size fraction of 150–212 μm before loading into the reactor.

All reagents in the catalytic tests were of reagent grade and used without further purifications: MeOH (Sigma-Aldrich, for HPLC, ≥99.9%), dimethyl ether (DME, 25 vol% in Ar), propylene (8 vol% in He), and deionized water.

3.2.2 Catalyst characterizations

Zeolite morphology was determined by carrying out scanning electron microscopy (SEM) imaging using a JEOL JSM-6010LA with a standard beam potential of 10 kV and an Everhart-Thornley detector.

X-ray powder diffraction (XRD) was performed in Bragg-Brentano geometry with a Bruker D8 Advance X-ray diffractometer using monochromatic Co K α ($\lambda = 1.788970 \text{ \AA}$) radiation between $2\theta = 5^\circ$ and 55° . Microporous properties of H-ZSM-5 sample were assessed from N₂ physisorption isotherms at -196 °C using Tristar II 3020. Prior to the measurements, the sample was dried and degassed at 350 °C for 6 h under constant N₂ flow.

Transmission FT-IR spectroscopy of adsorbed pyridine as a probe molecule was used to quantify the acid site density. H-ZSM-5 sample (~25 mg) was pressed in a self-supported wafer with a diameter of 1.6 cm and then placed in an

IR quartz cell. The spectra were collected at 2 cm^{-1} resolution using a Nicolet Nexus spectrometer equipped with an extended KBr beam splitting and an MCT detector. The concentration of Brønsted acid sites (BAS) and Lewis acid sites (LAS) was derived from the absorbance at 1545 and 1456 cm^{-1} using the integrated molar extinction coefficients of 0.73 and 1.11 , respectively.^[21] Assuming that one pyridine molecule is only adsorbed on one BAS/LAS, the following equations were used to estimate C_{BAS} and C_{LAS} :

$$C_{\text{BAS}} = 4.30 \times IA(\text{BAS})R^2 / W \quad (3.1)$$

$$C_{\text{LAS}} = 2.83 \times IA(\text{LAS})R^2 / W \quad (3.2)$$

where IA (BAS , LAS) represents the integrated absorbance of the band at 1545 and 1456 cm^{-1} , respectively, R is the radius of a sample wafer (cm), and W is the weight of a sample wafer (g).

SEM images, N_2 physisorption isotherms with BET analysis, XRD patterns, and acid site concentrations of the used zeolite materials can be found in **Figure B1**, Appendix B.

3.3 Catalytic testing

Three types of experiments were all carried out with freshly activated catalyst samples:

- FASPA experiments with MeOH over different catalyst loadings, reacting temperatures, MeOH injected amounts and MS analysis
- FASPA experiments with propylene
- Pulse series experiments with *in situ* DRIFT measurements using DME

Pulse tests and MTH continuous performance tests were carried out at 300 – $420\text{ }^\circ\text{C}$ using a fixed-bed reactor setup. A 4 mm (ID) quartz tube reactor was filled with catalyst amounts of 4.5 , 50 , 100 or 200 mg sieved zeolite fraction (particle size 150 – $212\text{ }\mu\text{m}$). Samples below 100 mg were diluted with SiC to a bed volume equivalent to 100 mg catalyst. The catalyst was activated at $550\text{ }^\circ\text{C}$ with 10 mL/min air for 1 h before cooling down to the reaction temperature. After passing through the thermostatic saturator with liquid MeOH, a mixture of

Table 3.1. Quantitative experimental data of stimulus-response experiments.

Sample mass (mg)	200	100		50	4.5	
#BAS sites (μmol)*	104	52		26	2.3	
Pulse size (mL)	0.25	0.25	2.0	0.25	0.25	2.0
(μmol)**	1.21	1.21	7.60	1.21	1.21	7.60
MeOH/BAS (mol/mol)	0.012	0.023	0.146	0.047	0.526	3.304
# pulses used***	165	134	140	152	65	143

*: BAS concentration was measured by FT-IR spectroscopy using pyridine as probe at 160 °C.

** : The MeOH concentration in all pulses was 12 and 9 vol% in helium in 0.25-mL and 2.0-mL sample loop, respectively.

***: Total # pulses used for reconstruction of a MeOH pulse response composition by FASPA.

MeOH/Ar/He (Ar used as internal standard) was fed into the sample loop of the six-port valve equipped with a universal actuator (VICI VALCO, USA). The reactant mixture was pulsed to the reactor using 20 mL_{NTP}/min He as a carrier gas. The products were analyzed by an online MS (Pfeiffer, Thermostar GSD320-QMG220) and a Thermo Trace GC. The reaction products ranging from methane to trimethylbenzene (TriMB) with only traces of tetramethylbenzene (TetraMB) were observed.

3.3.1 FASPA test protocol

The conventional GC analysis of the MTH product mixture takes too long to obtain a real-time quantitative mapping of the temporal product spectrum upon a MeOH pulse injection. An option is to sample the product response to a MeOH pulse over the MTH catalyst by a multiposition sampling valve and analysis offline^[19, 20], which obviously yields a lower density of data points during the transient operation. In our study we have chosen a fast scanning-pulse GC analysis, FASPA, a technique analogous to the step-scan technique in IR spectroscopy^[22]. To achieve the fine synchronization between MeOH pulse injection and GC sampling, a program was designed in the Labview platform, which allows to control following parameters during the experiment: first the switching of a six-way valve is controlled to achieve the repetitive MeOH pulses into the reactor with a pre-set pulse interval; Upon MeOH pulsing, a delayed GC sampling was initiated at the same time. More importantly, the time delay of each GC sampling stepwisely increases from zero to 3.75 min in order to record the product information along time upon the MeOH pulse, while the time step is adjustable during the operation to modify the time resolution of product responses in some specified periods.

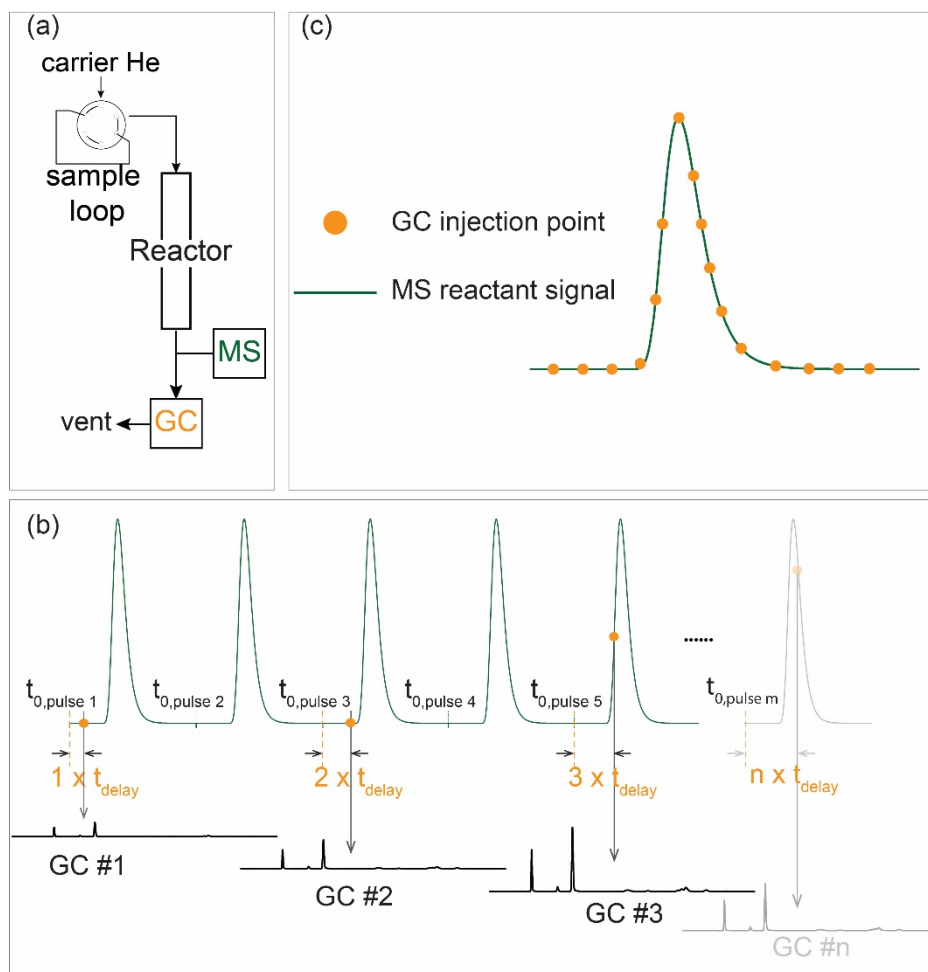


Figure 3.1. Overview of the FASPA approach. (a) A flow scheme of FASPA setup; (b) Normalized MS reactant signal and GC injections in a typical FASPA experiment. The MeOH pulse interval and time delay of GC sampling are initially set in the control program; (c) Normalized mapping of a typical FASPA experiment after collection of all GC points.

After the completion of the test, all GC points will be collected to build up the full map of quantitative product responses after a MeOH pulse. The FASPA test protocol is illustrated in **Figure 3.1**.

In a typical FASPA experiment in this study, an initial time delay of 1 s was chosen for GC sampling when the MeOH pulse interval is 3.75 min. In a later stage, the time step is increased to 4 s when changes in product concentrations are lower. In total, a sequence of ~ 75 GC sample injections (corresponding to

~150 pulses of MeOH) were collected to reconstruct the whole temporal product profiles of a MeOH pulse.

3.3.2 Product analysis-Gas chromatography

A Thermo Trace GC with two individual channels was connected downstream of MS. One channel is equipped with an RTX-1 column (2 m, 0.32 mm, 5.00 μm) and $\text{Al}_2\text{O}_3/\text{KCl}$ column (15 m, 0.32 mm, 10 μm) connected to a flame ionization detector (FID) for the analysis of C_1 to C_4 hydrocarbons. The other is equipped with an RTX-VMS column (30 m, 0.33 mm, 3.00 μm) also connected to an FID for C_{5+} hydrocarbons analysis. Examples of GC chromatograms collected from the two separate channels are shown in **Figure 3.2**. Since the GC is located downstream of the MS a synchronization delay of 2–4 s is observed for GC analysis. Therefore, MS signals were adjusted to the GC-pulse analysis timing by adding a time difference based on the breakthrough time difference between $m/z = 41$ and 40 in MS.

The MeOH+DME conversion, selectivity and yield were then calculated on a carbon molar basis as follows:

$$X = \frac{(\phi_{C,MeOH_{in}} - \phi_{C,MeOH_{out}} - 2\phi_{C,DME_{out}})}{\phi_{C,MeOH_{in}}} \times 100\% \quad (3.3)$$

$$S_{C_n} = \frac{n \cdot \phi_{C_n}}{(\phi_{C,MeOH_{in}} - \phi_{C,MeOH_{out}} - 2\phi_{C,DME_{out}})} \times 100\% \quad (3.4)$$

$$Y_{C_n} = \frac{X \times S_{C_n}}{100} \% \quad (3.5)$$

where X , ϕ_{C_n} , S_{C_n} and Y_{C_n} represent the carbon-based conversion of MeOH plus DME, molar flow rate and carbon selectivity to a certain hydrocarbon product with carbon number equal to n and the corresponding carbon yield, respectively.

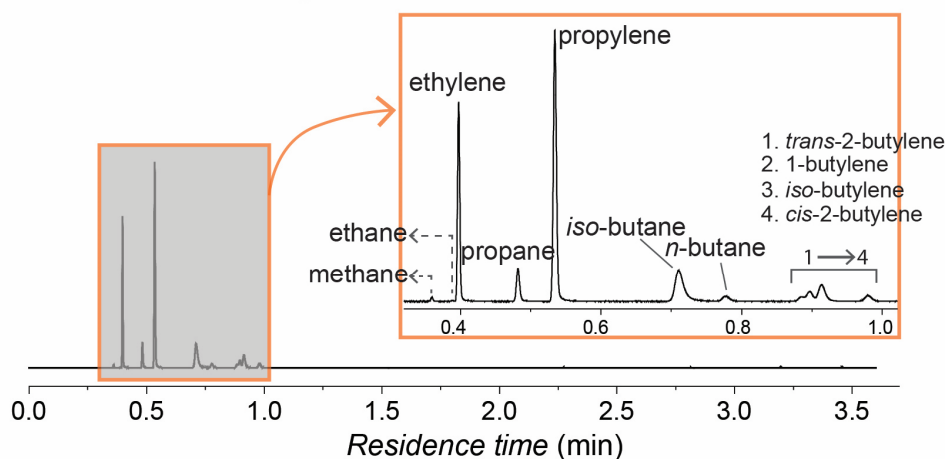
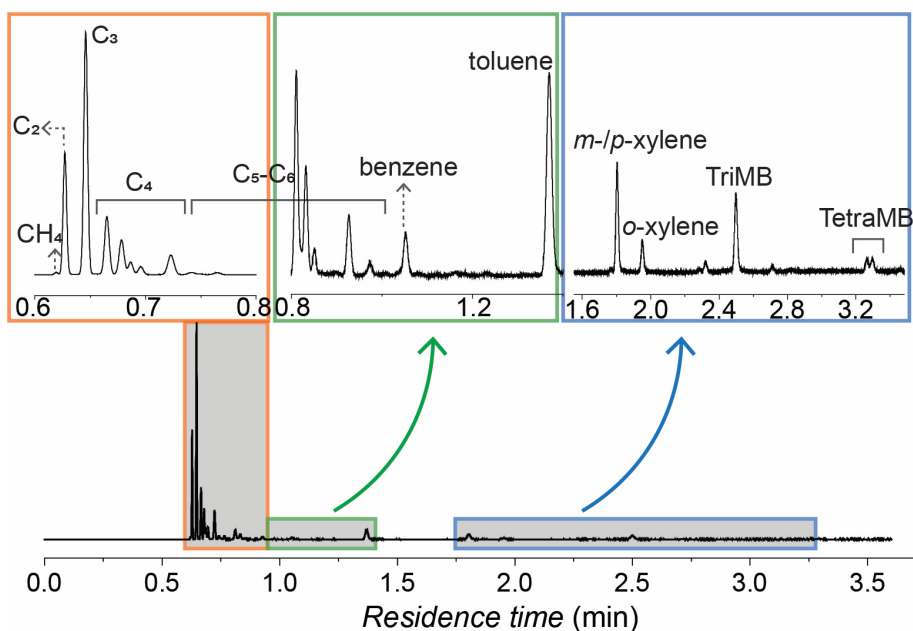
(a) FID chromatograph @38 seconds for C₁-C₄ aliphatics(b) FID chromatograph @38 seconds for C₅₊

Figure 3.2. Two examples of FID chromatograms with peak assignments for C₁-C₄ aliphatics (a), aromatics and heavier hydrocarbons (b). Conditions: $m_{\text{cat}} = 100$ mg (H-ZSM-5, Si/Al 25, 150–212 μm), $P_{\text{reactor}} = 1$ bar, pulse quantity = 1.2 μmol_C per pulse, carrier gas He = 20 mL_{NTP}/min, pulse interval = 3.75 min.

3.3.3 Statistical moments analysis of pulse data – Turn-over frequency

The interpretation and data analysis of the temporal pulse responses are based on the statistical moment analysis of the response curve from FASPA experiments upon injection of a tracer pulse^[23, 24].

The normalized n^{th} *absolute* moment on the origin of a response is defined as

$$\mu_n = \frac{\int_0^{\infty} t^n c(t) dt}{\int_0^{\infty} c(t) dt} \quad (3.6)$$

here $c(t)$ is the concentration of tracer at the outlet as a function of time-on-stream upon a pulse.

And the normalized n^{th} *central* moment on the mean as

$$\mu_n' = \frac{\int_0^{\infty} (t - \mu_1)^n c(t) dt}{\int_0^{\infty} c(t) dt} \quad (3.7)$$

Both are normalized by the amount of tracer injected N_{inj} (mol), the 0th moment, and have the dimension of time.

$$\mu_0 = \int_0^{\infty} c(t) dt = N_{inj} \quad (3.8)$$

The normalized first moment represents the average residence time τ in the system

$$\mu_1 = \frac{\int_0^{\infty} t \cdot c(t) dt}{\int_0^{\infty} c(t) dt} = \tau \quad (3.9)$$

The normalized second central moment represents the variance σ^2 of the response curve

$$\mu_2' = \frac{\int_0^{\infty} (t-\tau)^2 c(t) dt}{\int_0^{\infty} c(t) dt} = \sigma^2 \quad (3.10)$$

The third moment is a measure of the asymmetry or skewness of the response curve, but in most studies, only the 1st and 2nd moments are analyzed since the weight of the tail of a response signal increases with t^n , whereas the accuracy of that tail signal usually diminishes.

For Gas-Solid Chromatography analysis Kubín and Kučera derived expressions for the moments of the response curve of a tracer pulse injection to a 1-dimensional packed bed of porous particles, taking into account the axial dispersion in the packed bed, mass transfer to and diffusion into the porous particles, and linear adsorption-desorption at the particles' surface^[25-31]. For small injection amounts the Henry regime applies for adsorption. This is the basis for our analysis of the pulse responses.

The normalized first moment consists of contributions from the residence time spent in the gas phase of the system under consideration (tubings, represented by τ_{set-up}), in the packed bed (interparticle and intraparticle space, represented by $\tau_{interparticle}$ and $\tau_{intraparticle}$, respectively), and the residence time spent in the adsorbed state (τ_{ads}):

$$\mu_1 = \tau_{set-up} + \tau_{interparticle} + \tau_{intraparticle} + \tau_{ads} \quad (3.11)$$

$$\mu_1 = \tau_{set-up} + \frac{L_b}{u} \left[\varepsilon_b + (1 - \varepsilon_b) \varepsilon_p + (1 - \varepsilon_b) \rho_p K_A \right] \quad (3.12)$$

where L_b is the length of the catalyst bed, u is the superficial velocity of carrier flow in the reactor, ε_b and ε_p represent the external porosity and internal porosity, respectively in the catalyst bed with packed zeolite pellets, and ρ_p is the particle density.

It is noted that only the adsorption term appears in the expression for the first moment of a nonreactive system. In this work, only the zeroth and first moments are used. This expression can further be simplified for cases with specific assumptions (*e.g.* non-porous particles, or no adsorption, etc.).

In case a non-ideal Dirac tracer pulse is used (*e.g.* a Gaussian or a block pulse^[32]) the first moment satisfies the relation (eq. 3.13), so the ‘true’ moment of the system can be obtained by taking a proper (*e.g.* non-adsorbing) tracer response as input reference, in our case from the argon injected together with the species under investigation (*vide infra*). This corrects for the non-ideal pulse shape and at the same time eliminates the residence time in the system and the bed and particle porosities.^[25]

$$\mu_1 = \mu_{1,response} - \mu_{1,input} \quad (3.13)$$

For a nonreactive adsorbing component holds then:

$$\tau_{ads,HC} = \mu_{1,HC} - \mu_{1,Ar} \quad (3.13a)$$

$$\tau_{ads,HC} = \frac{L_b}{u} \left[(1 - \varepsilon_b) \rho_p K_A \right] \quad (3.13b)$$

These first moments are used to estimate the minimum turn-over frequencies for the products’ formation, TOF_{prod} . For this purpose, the maximum number of active sites involved, N_{act} , is equated to the number of MeOH molecules pulsed (see **Table 3.1**). This implies that only a small zone of the catalyst sample is involved in this conversion, although this will still be an overestimation.

The characteristic hydrocarbon product formation time $\tau_{prod,HC}$ is the first moment of the specific product minus that of argon for the hydrocarbons to account for the system delay over H-ZSM-5, and comprises the characteristic times of adsorption and of the formation process(es) of the component under consideration.

$$\tau_{prod,HC} = \mu_{1,HC} - \mu_{1,Ar} = \tau_{adsorption} + \tau_{formation} \quad (3.14)$$

$$TOF_{prod} \geq \frac{N_{prod}}{\tau_{prod} N_{act}} \quad (3.15)$$

For first-order reaction systems, Chan *et al.* showed that the statistical method of moments can be applied to determine the rate constants of individual reactions from the transient batch reactor operation, being the reciprocal of the $\tau_{formation}$.^[33] Since the $\tau_{adsorption}$ in (eq. 3.14) is not known, the estimated *TOFs* by (eq. 3.15) are lower limit estimates. Also for the pulse-response analysis in the TAP reactor system^[34], based on diffusive transport, moments-based relations have been derived to extract kinetic information.^[35, 36] The derivation of the kinetic relations follows a slightly different approach, but the first moment relation for a non-reactive system is identical to that for the adsorption-desorption process in packed beds presented above. The TAP system has recently been used for the analysis of light alkene reactions over H-ZSM-22.^[16] In the figures the time-corrected MS response of the argon tracer, injected together with the MeOH, has been included.

The two-peak response of the light aromatics (benzene, toluene and xylene) were deconvoluted by fitting the exponentially modified Gaussian (EMG) peak function GaussMod, used in chromatography:

$$f(x) = y_0 + \frac{A}{t_0} e^{\frac{1}{2}(\frac{w}{t_0})^2 - \frac{x-x_c}{t_0}} \int_{-\infty}^z \frac{1}{\sqrt{2\pi}} e^{-\frac{y^2}{2}} dy \quad (3.16)$$

with

$$z = \frac{x-x_c}{w} - \frac{w}{t_0} \quad (3.17)$$

here y_0 , A , w , x_c represent offset, area, full width at half maximum and center of the response. t_0 is used to estimate the first moment of the response, $\mu_1 = x_c + t_0$.

3.3.4 *In situ* DRIFT spectroscopy measurement

In situ DRIFT (Diffuse Reflectance Infrared Fourier Transformed) spectra were recorded using a Nicolet Magna 550 spectrometer, equipped with a liquid-nitrogen-cooled MCT detector and a Praying Mantis diffuse reflection accessory (Harrick Scientific) with a high-temperature reaction chamber. The temperature is controlled via the thermocouple under the sample. To mitigate the impact of water on spectra measurement, MeOH is replaced by DME (25 vol% in N₂) as a reactant. Previous study revealed that DME-to-hydrocarbons similarly undergoes the initial C–C bond formation, followed by an autocatalytic process (HCP mechanism), despite the inclusion of distinct kinetic factors.^[37] The flow of gases was controlled by mass flow controllers (Bronkhorst). ~10 mg H-ZSM-5 in powder form was loaded in the reaction cell equipped with CaF₂ windows. Prior to the measurements, sample powders were exposed to an air flow (10 mL_{NTP}/min) at 400 °C for 1 h. Subsequently, the system was cooled to 300 °C for reaction. DME was dosed via the six-way valve with a sample loop (~10 mL). The corresponding pulse quantity is 0.2 mmol_C per pulse. 20 mL_{NTP}/min He was used as the carrier gas. The pulse interval is 2.5 min. The spectra were acquired every 4 seconds to follow the pretreatment, reaction, and evolution of surface species within 4000–1400 cm⁻¹ with a resolution of 4 cm⁻¹. In particular, characteristic IR bands within 1700–1400 cm⁻¹ assigned to various aromatic surface species are summarized in **Table 3.2**.

Table 3.2. Assignments of characteristic IR bands in 1700–1400 cm⁻¹ region from various literature sources.

Wavenumber (cm ⁻¹)	Assignments	Sources
1456 and 1570	alkylbenzenes	[38]
1465	CH ₃ or CH ₂ deformation of butylene or (<i>mono-/di-/tri-</i>)enyl carbenium ions	[39-41]
1480	C–H stretching in polycyclic aromatics	[38, 42]
1493	cyclopentenyl ions with methyl-substituted at C-2	[40]
1495	tetramethyl(<i>n</i> -propyl)cyclopentenyl	[40]
1505–1500	allylic stretch of trienyl cations	[43, 44]
1510–1480 and 3125	alkyl-substituted cyclopentenyl cations	[40]
1510	1,2,3-trimethylcyclopentenyl cation	[45]
1510	allylic stretch of polyalkyl-substituted cyclopentenyl cations with a proton in the C-2 position	[40]
1525	allylic stretch of 1,3-dimethylcyclopentenyl cation	[46]
1554	2,4-dimethylpentenyl	[40, 47]
1543, 1567	<i>mono-/di-</i> enyl cations	[40, 47]
1588	C=C of conjugated triene	[39-41, 47-49]
1591, 1616	C=C or C–H of alkylbenzenes	[38]
1619	tetramethylbenzenium ion	[40]
broad band between 1619 and 1610	polymethylbenzenium ion or C=C of olefins interacting with BAS	[39, 40, 43, 47, 50]

3.4 Results

3.4.1 Fast Scanning-Pulse Analysis (FASPA) validation

The basic condition for the applicability of FASPA is that during this sampling process the catalyst changes (*i.e.*, deactivation, HCP build-up) do not affect the temporal product responses. First, to verify the catalyst performance is not modified during the entire pulse sequence, a continuous MTH operation test was carried out before and after the entire pulse sequence. The obtained steady-state product distributions from GC before and after the pulse sequence are then compared in **Figure 3.3(a)**.

More than 540 pulses were injected during the entire test, which in total equals to 1.3 mol MeOH per mol of Brønsted acid sites (BAS). MTH data in a continuous MTH test reveal that this H-ZSM-5 catalyst can convert more than 11000 mol MeOH per BAS before MeOH conversion drops below 100% at 400 °C. The catalytic results (**Figure 3.3(a)**) show that the product selectivity is not changed after the FASPA test. A dark grey zone indicating coke deposition

mainly at the top of the catalyst bed can be observed (**Figure 3.3(b)**) after the entire experiment.^[13] Moreover, as shown in **Figure 3.3(c)**, the MS signal of $m/z = 41$, qualitatively representing light hydrocarbon (e.g., propylene, butylenes, butanes) production in the FASPA test, reaches a constant *quasi* steady-state profile within ~ 10 MeOH pulses until the end of the test.

A second proof justifying the FASPA application condition follows from the preservation of the temporal product responses (ethylene, propylene, butanes, and xylenes) of two consecutive FASPA sequences (**Figure 3.3(d)**). The systematic sampling order could possibly have introduced a systematic error in the response profiles. However, the asynchronous MeOH pulsing and GC sampling in the recent paper of Kosinov *et al.*^[51], implying a random collection of data points, yielded similar product response profiles, e.g. the two production profiles of the aromatic species shown in section 3.4.2.

Therefore, we conclude that during the FASPA test the catalyst bed is at *quasi* steady-state conditions providing a constant product distribution in the exit flow. Under the studied conditions (~ 100 MeOH pulses, 100 mg catalyst. $1.2 \mu\text{mol}_c$ per pulse at 400°C), the temporal product responses are not substantially affected by any preliminary coke deposition or HCP build-up. So, the FASPA technique can be safely applied as a characterization method without disturbing a consecutive continuous steady-state MTH operation. Furthermore, in comparison with the TAP reactor, the FASPA approach is relatively cheap and allows investigation of the catalyst bed performance at typical operating temperatures (e.g., $>400^\circ\text{C}$) in standard catalyst testing equipment.

It is worth noting that based on the same concept of (un)synchronizing GC sampling and reactant pulsing, Kosinov *et al.* very recently reported a so-called scanning pulse reaction technique for transient kinetic analysis.^[51] In their approach, GC acquisition and reactant pulsing were collected both in a repeating manner without the fine time-delay control program as used in the FASPA technique.

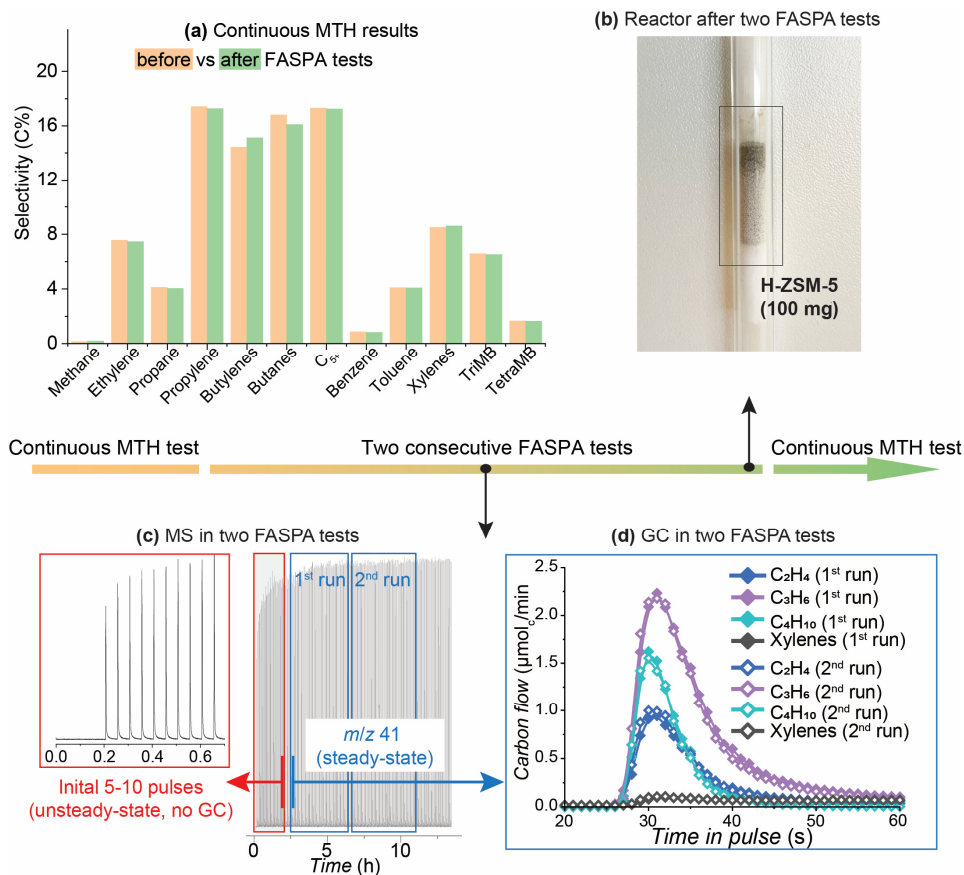


Figure 3.3. (a) Carbon selectivity in continuous MTH operation before and after the pulse test; (b) instant view of the reactor after ~ 540 MeOH pulses; (c) MS signal of $m/z = 41$ representing light hydrocarbons along time during the FASPA test; (d) GC temporal responses of selected hydrocarbons in two consecutive FASPA tests. Reaction conditions: $T = 400$ °C, $m_{\text{cat}} = 50$ mg (150–212 μm), $P_{\text{reactor}} = 1$ bar, $WHSV = 226$ mol_C mol_{BAS}⁻¹h⁻¹ in continuous MTH test, MeOH pulse quantity = 1.2 μmol_C per pulse, carrier gas He = 20 mL_{NTP}/min, pulse interval = 3 min, $t_{\text{delay}} = 1$ s.

3.4.2 Dynamic formation of hydrocarbons in the pulse experiments

The typical temporal evolution of the MTH product distribution at the reactor outlet and the retained species in H-ZSM-5 upon MeOH pulses are presented in **Figure 3.4**, as resulting from the respective FASPA test and *in-situ* DRIFT spectroscopy.

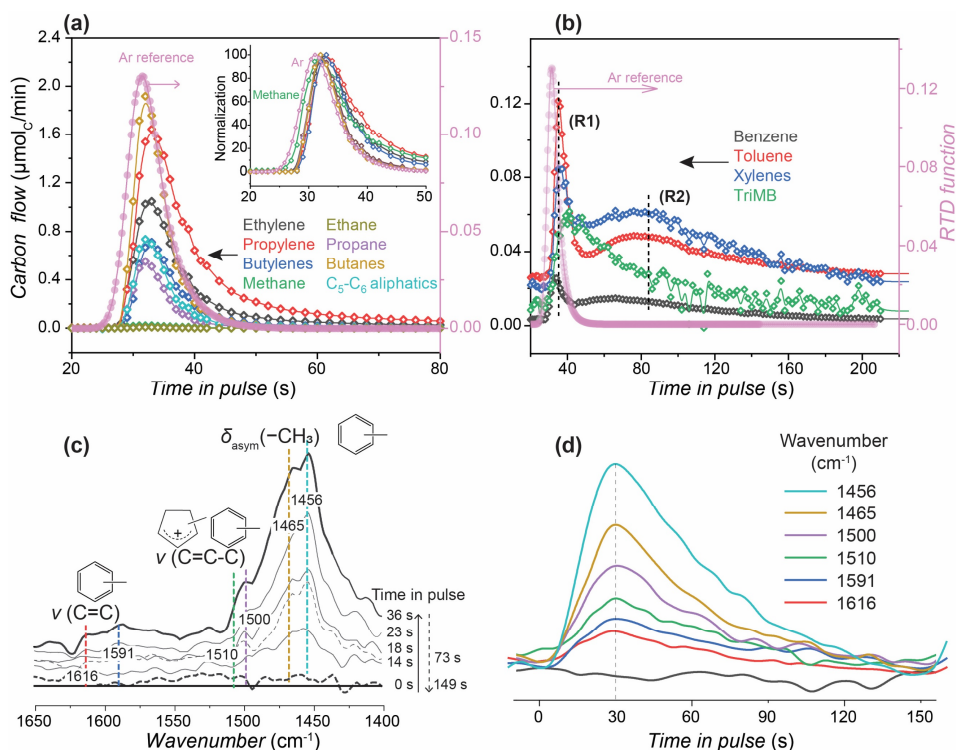


Figure 3.4. The FASPA temporal responses of aliphatic (a) and aromatic products (b); Temporal evolution of DRIFT spectra in the $1650-1400\text{ cm}^{-1}$ region (c) and the changes of characteristic IR bands along time (d). Normalized responses of selected aliphatic products were added in (a). FASPA experimental conditions: $T = 400^\circ\text{C}$, $m_{\text{cat}} = 100\text{ mg}$ (H-ZSM-5, Si/Al 25, $150-212\ \mu\text{m}$), $P_{\text{reactor}} = 1\text{ bar}$, MeOH pulse quantity $1.2\ \mu\text{mol}_C$ per pulse, carrier gas He = $20\text{ mL}_{\text{NTP}}/\text{min}$, pulse interval = 3.75 min; *In-situ* DRIFT experimental conditions: $T = 300^\circ\text{C}$, $m_{\text{cat}} = \sim 10\text{ mg}$ (H-ZSM-5, Si/Al 25, powder form), $P_{\text{reactor}} = 1\text{ bar}$, pulse quantity 0.2 mmol_C per pulse, carrier gas He = $20\text{ mL}_{\text{NTP}}/\text{min}$, pulse interval 2.5 min. To mitigate the impact of water on the IR signal, DME (23 vol% in N_2) was pulsed instead of MeOH. More quantitative conditions can be found in **Table 3.3**.

Table 3.3. The product selectivity and statistical moment analysis for MeOH pulse responses over H-ZSM-5 with different loadings

	$\mu_0, \mu\text{molc}$								
weight mg	Ethylene	Propylene	Butylenes	Methane	Ethane	Propane	Butanes	C5-C6	TriMB
200	0.185	0.259	0.082	0.004	0.002	0.089	0.216	0.069	0.058
100	0.172	0.301	0.101	0.004	0.001	0.063	0.211	0.094	0.076
50	0.145	0.372	0.134	0.005	0.001	0.042	0.171	0.095	0.064
4.5	0.059	0.448	0.209	0.004	-	0.011	0.084	0.216	0.023
weight mg	Benzene R1	Toluene R1	Xylenes R1	Benzene R2	Toluene R2	Xylenes R2	C balance Cout/Cin		
200	0.0033	0.0288	0.0105	0.0183	0.0335	0.0331	0.912		
100	0.0031	0.0126	0.0121	0.0150	0.0326	0.0688	0.972		
50	0.0035	0.0085	0.0181	0.0103	0.0315	0.0546	0.962		
4.5	0.0053	0.0066	0.0187	0.0041	0.0137	0.0323	0.944		
	μ_1, s								
weight mg	Ethylene	Propylene	Butylenes	Methane	Ethane	Propane	Butanes	C5-C6	TriMB
200	36.3	39.4	36.5	36.9	33.4	33.2	33.3	34.5	108
100	36.2	38.3	35.9	36.5	34	33.8	33.8	34.3	72.5
50	36.1	37.2	35.4	40.6	34	34	33.9	34.1	66.7
4.5	35.3	34.3	33.7	39.4	-	33.2	32.7	33.4	63.6
weight mg	Benzene R1	Toluene R1	Xylenes R1	Benzene R2	Toluene R2	Xylenes R2	Ar Reference		
200	41.2	39.5	52.6	105.5	142.3	160	32.6		
100	36.8	37.9	42.2	95.9	112.7	115.8	33.1		
50	35.7	35.6	41.7	87.7	95.7	99.3	33.1		
4.5	35.8	36.9	49.7	108.9	122.1	131.1	32.2		

At the studied conditions, the amount of MeOH (or DME in the DRIFT measurements) in the pulse is far less than the BAS concentration in the catalyst bed (~2% of BAS for 100 mg H-ZSM-5, see **Table 3.1**), resulting in the complete conversion of MeOH. A nearly instantaneous formation of hydrocarbons (alkanes, alkenes, and light aromatics) is observed after ~2 s delay after the argon response. The latter represents all non-adsorption and non-reaction phenomena in the setup. The major alkane and alkene responses are the butanes (predominantly isobutane) and propylene, followed by ethylene and butylenes (**Figure 3.4(a)**). Especially the alkenes show more tailing than the argon response, further evidenced by the higher first moments of alkenes than of alkanes seen in **Table 3.3**. This indicates a longer formation duration of alkenes in the sample.

Interestingly, the order of magnitude lower production of light aromatics (benzene, toluene, xylenes (BTX) in **Figure 3.4(b)**) is a convolution of a fast formation on the time scale of the aliphatics formation (R1) and a slower second formation over a longer period (R2). The similar peak locations of R1 at 35–40 s as the BTX pulse responses for adsorption presented in **Figure B2** also suggest the almost instantaneous formation of aromatics. Unlike BTX responses, TriMB does not exhibit the two-peak profile implying no slower formation of TriMB in the later stage (>60 s) of the pulse response. Furthermore, characteristic IR bands, assigned to different cyclic surface species (detailed assignments can be found in **Table 3.2**), also reach their maximum at ~30 s (**Figure 3.4(c-d)**). After that, their intensities slowly return to zero. No net increase in IR signal intensity level after a complete pulse (**Figure 3.4(d)**) indicates that a *quasi* steady-state MTH pulse activity is attained. The close correlation between IR bands and product responses suggests a dynamic rather than a static hydrocarbon pool as a reservoir of active species where MeOH is converted into hydrocarbons.^[11, 52] The involved surface species are highly reactive and unstable. They are rapidly formed but also subsequently completely decomposed, as indicated by IR bands during the pulse, releasing final products. Compared to the formation, the decomposition of hydrocarbon pool species is relatively slow. Based on the IR assignments from literature^[38-47, 50] (see **Table 3.2**), we speculate these surface species are mainly alkylated mono-/di-/trienyl carbenium ions (1465, 1480–1510 cm^{-1}) such as cyclopentenyl carbenium ions and alkylbenzenes (1456, 1591, 1616 cm^{-1}), with the latter being the result of deprotonation and cycle expansion processes of the former.^[53] Their rapid formation and slow decomposition are well in line with reported ^{13}C CP-MAS NMR results that 1,3-dimethylcyclopentenyl carbenium ions were detected in less than 1 s after pulsing ethylene, while their transformation into methylbenzenes (predominantly pentamethylbenzenes^[54]) took seconds at 350°C.^[19, 20]

Additional mechanistic information lies in the methane response, which helps to link the possible first C–C formation mechanism and the subsequent steady-state formation of hydrocarbons. Methane is readily formed ~2 s earlier than other aliphatics, although in much smaller quantities (**Figure 3.5**). Recently proposed first C–C bond formation mechanisms such as the CO^[55-57]-/formaldehyde^[58]-mediated or extraframework alumina-assisted^[59] routes involve the formation of methane as a side product in the MeOH decomposition or disproportionation reactions^[8].

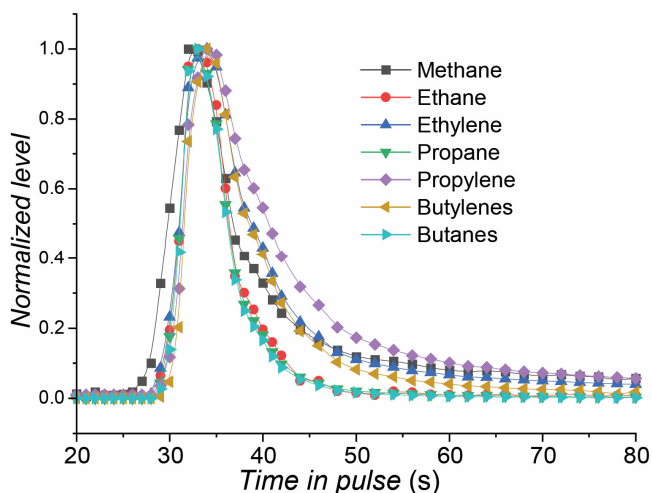


Figure 3.5. Normalized formation responses of light aliphatics upon pulsing MeOH over H-ZSM-5 at 400 °C. Other FASPA conditions are as in **Figure 3.4**.

After the rapid formation of hydrocarbons giving the response over 20–40 s, methane exhibits a longer tailing than other alkanes (**Figure 3.4(a)**), while the latter species are believed to be the side products of bimolecular cracking reactions^[60] eventually leading to aromatics formation with alkylated cyclopentenyl ions as intermediates (see **Figure 3.4(c-d)**).^[19, 40, 54, 61] Beyond 60 s response time, the further (secondary) reactions such as (monomolecular) cracking^[62] of those highly alkylated cyclic or methylated aromatic species give the second broad peak of light aromatics and the long tail of methane.

So, in brief, upon a MeOH pulse aliphatics and aromatics are nearly instantaneously formed, escape from the catalyst bed and are detected shortly after the non-adsorbing Ar tracer (**Figure 3.4(a)**). At later response times, tailing alkene responses and a second appearance of BTX are observed spread over a broad time range, and tentatively attributed to the slow decomposition of retained surface species.

At these reaction conditions, the MeOH pulse only probes ~2% of the BAS, so a very thin reaction zone is active in the catalyst bed, responsible for the fast primary product formation (**Figure 3.4(a-b)**).

3.4.3 Impact of secondary reactions

To probe the impact of secondary reactions on the product distribution and product responses, FASPA experimental results over H-ZSM-5 catalysts samples

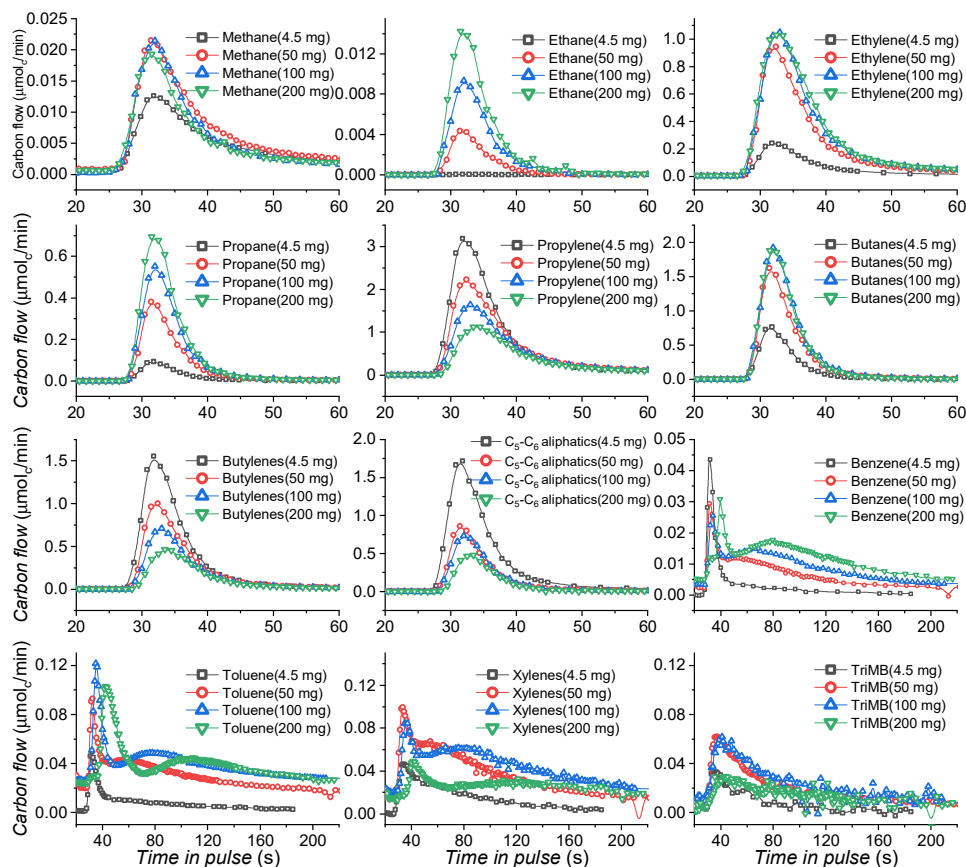


Figure 3.6. Comparison of hydrocarbons responses upon pulsing MeOH over 4.5–200 mg H-ZSM-5 at 400 °C. Conditions: H-ZSM-5 (Si/Al 25, 150–212 μm), $P_{\text{reactor}} = 1$ bar, MeOH pulse quantity = 1.2 μmol_C per pulse, carrier gas He = 20 mL_{NTP}/min, pulse interval = 3.75 min. More quantitative experimental data can be found in **Table 3.3**. Response profiles were time-shifted based on the Ar responses using 100-mg H-ZSM-5 sample as reference.

of 4.5–200 mg were compared. The output of a smaller sample can be considered as input for the downstream region of a larger sample. Accordingly, the additional changes in responses for larger catalyst samples must be due to secondary reactions in that downstream region of the bed. Results are presented in **Figure 3.6** and the quantities of individual components in **Table 3.3**.

With increasing catalyst sample from 4.5 to 200 mg (**Figure 3.7**), C_5 – C_6 aliphatics gradually decrease, while aromatics and C_1 – C_4 alkanes simultaneously increase, indicating the H-transfer and aromatization from heavier aliphatics to aromatics continue in the downstream region of the catalyst bed in absence of

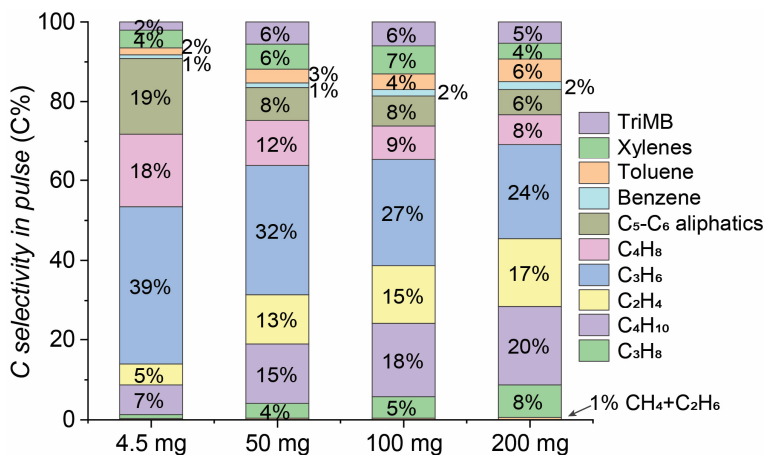


Figure 3.7. Total carbon selectivity of hydrocarbons over H-ZSM-5 with varied loadings in the FASPA experiments. Other FASPA conditions are as in **Figure 3.6**.

MeOH, eventually increasing the selectivity to aromatics. Similarly, olefins also decrease in the catalyst with longer beds, indicating olefins are further converted in these regions. The selectivity to propylene and butylenes decreases, while that to ethylene increases with sample amount. The increasing alkanes production is mainly due to the butanes.

The lower selectivity to aromatics for the 200 mg sample is attributed to residual aromatics still adsorbed in this sample at the end of the pulse. The MeOH pulse injection time interval is slightly too short for full desorption from this sample. The lower carbon balance of ~ 0.9 for this 200 mg catalyst also suggests ~ 0.1 μmol carbon (probably in form of aromatics) remained still on the surface when a next pulse injection was given.

With decreasing catalyst amount, both R1 and R2 components (representing the fast and slow BTX formation, as denoted in **Figure 3.6** appear at shorter residence time. For 4.5 mg catalyst, R2 of BTX almost disappears suggesting the slow formation of BTX is profoundly suppressed with the shortest catalyst bed.

For the 4.5 to 200 mg catalyst samples, the only difference is the downstream catalyst region since MeOH is rapidly consumed forming the identical surface species (hydrocarbon pool species) at the entrance region of the catalyst bed in the pulse experiments. In Section 3.2, we concluded that R2 stems from the slow desorption/decomposition of strongly adsorbed surface species, evidenced by the slow decreasing intensity of characteristic IR bands. However, the R2 response over 4.5 mg H-ZSM-5 is almost completely absent at full MeOH conversion.

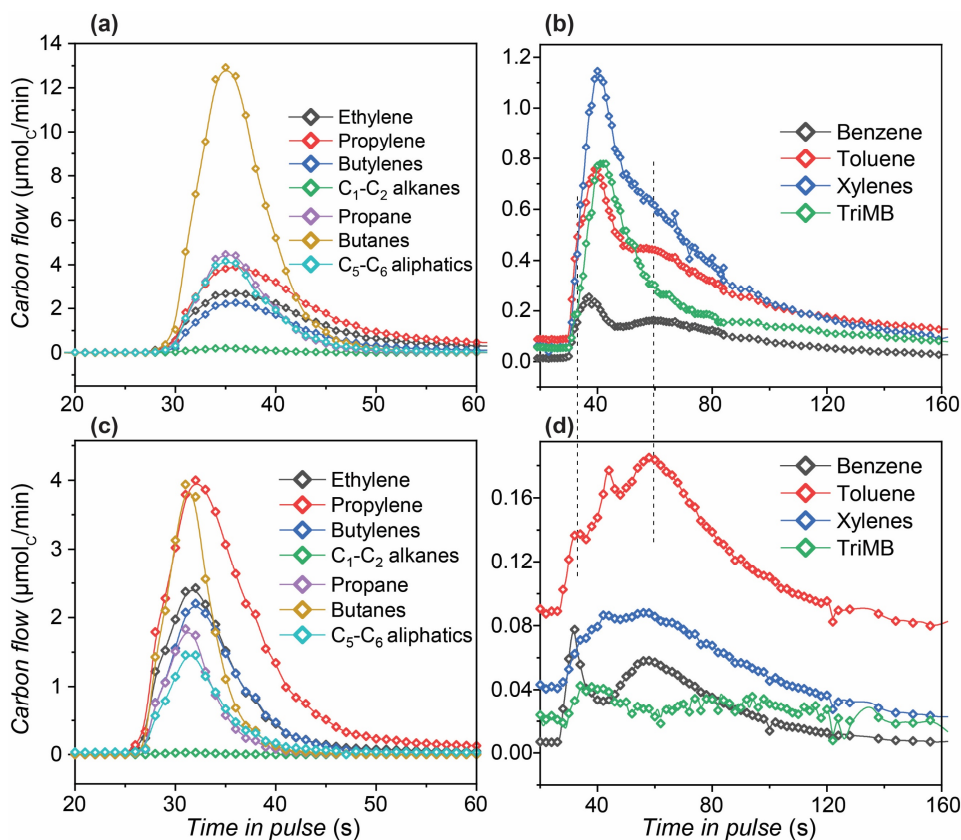


Figure 3.8. Temporal responses of hydrocarbons upon pulsing MeOH (a-b) and propylene (c-d) to activated H-ZSM-5 at 400 °C. Conditions: $m_{\text{cat}} = 100$ mg (H-ZSM-5, Si/Al 25, 150–212 μm), $P_{\text{reactor}} = 1$ bar, MeOH pulse quantity = 7.6 μmol_C per pulse, propylene pulse quantity = 1.9 μmol_C per pulse (sample loop 0.25 mL, 8 vol% propylene in He), carrier gas He = 20 mL_{NTP}/min, pulse interval = 3.75 min.

Furthermore, the component distribution of all responses (zero moments, see **Table 3.3**) varies with catalyst mass. All these observations cannot be solely explained by the slow desorption/decomposition of surface species. It must suggest that besides the desorption/decomposition of surface species, secondary reactions like H-transfer and aromatization reaction also contribute to the second formation of aromatics. Especially the long tailing of propylene for all catalysts and the much higher formations of propylene and C₅-C₆ aliphatics over the shortest 4.5 mg bed than over larger samples are strong indicators. Accordingly, two distinct aromatization pathways are discerned in the FASPA experiments. The MeOH-mediated aromatization proceeds quickly giving component R1. After that, secondary reactions including slow decomposition of surface species

and H-transfer reactions (probably from propylene/butylenes and also C₅-C₆ aliphatics) result in a broad BTX formation referred to as R2 at later stages.

This is further evidenced when propylene is pulsed over 100 mg H-ZSM-5 at 400°C, giving similar BTX responses as the 2nd BTX maxima observed in the MeOH pulse test (**Figure 3.8**). Clearly, pulsing propylene only also results in MTH reactions, contributing to aromatization products and the appearance of the retarded 2nd BTX response maxima via an HCP-like mechanism.

3.4.4 Impact of temperature

The impact of temperature on the product responses is investigated by conducting the FASPA experiments at 390–420 °C. The full temporal responses and corresponding moment analysis values are present in **Figure 3.9-10** and **Table 3.4**.

The time difference between Ar and hydrocarbon breakthrough ascribed to the induction period prior to the first hydrocarbon formation significantly drops from >4 s at 390 °C to ~2.5 s at 420 °C (**Figure 3.9**). However, the impact on the selectivity (**Table 3.4**) of aliphatics is less pronounced than that on light aromatics in this narrow temperature range. With increasing temperature, the selectivity to light alkanes including methane, ethane and propane is monotonically increased, as a result of the promoted monomolecular cracking of heavier hydrocarbons. The small rise of ethylene and propylene with temperature at the expense of butylenes and C₅₊ aliphatics might indicate that increased temperature promotes the cracking of heavier hydrocarbons into shorter olefins, *i.e.*, ethylene and propylene.

For BTX responses, the location of the R1 component of all aromatic species is consistently located near 40 s, a few seconds later than the Ar reference response, whereas its amount decreases with increasing temperature. Moreover, the R2 component increases and gradually shifts towards earlier response times at the higher temperature, ascribed to a faster (activated) decomposition/and release of surface species in the later stage of the response. So, at the higher temperature, the next MeOH pulse arrives at a cleaner zeolite surface, resulting in less BTX displacement and lowering the R1 component.

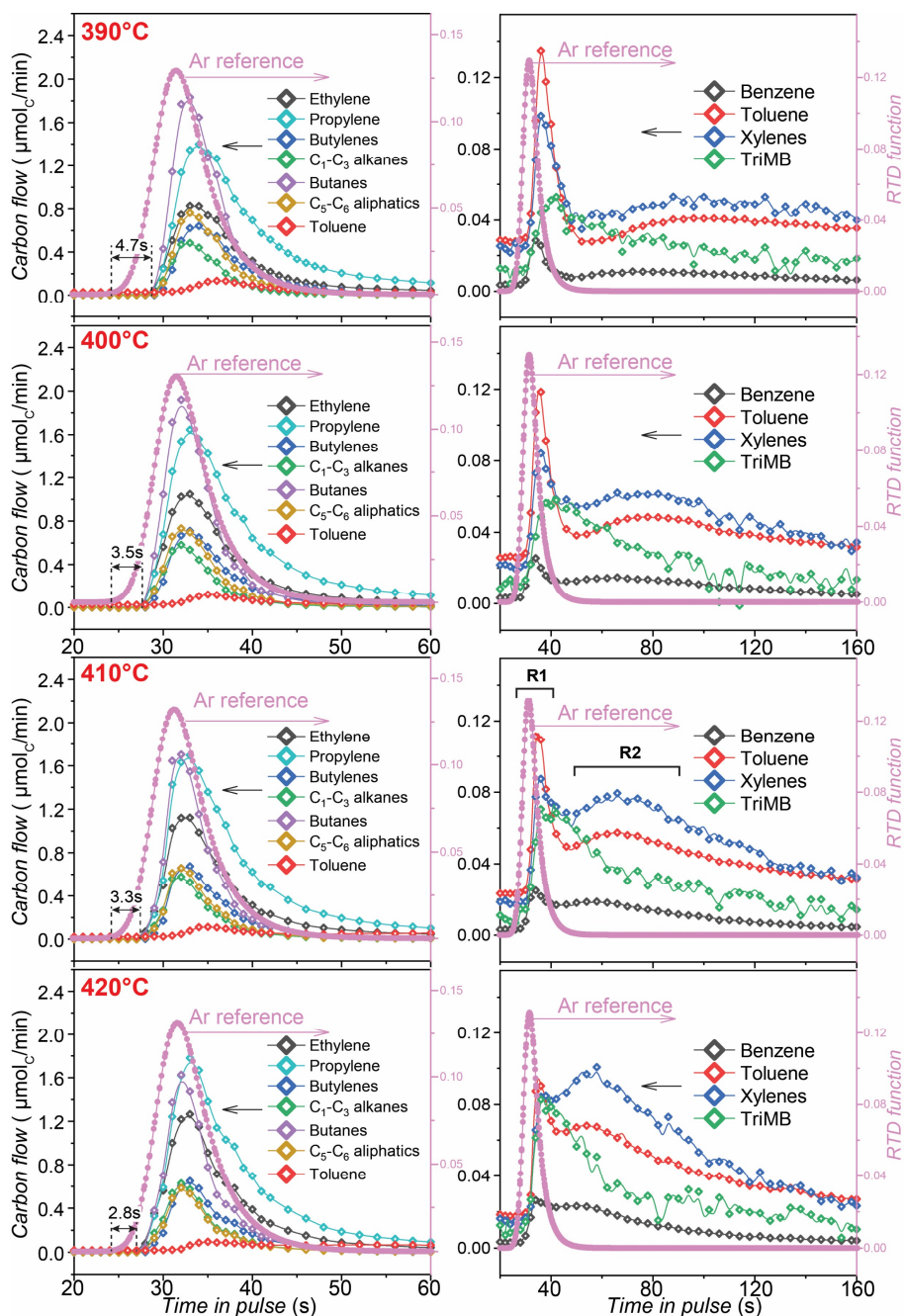


Figure 3.9. Hydrocarbons responses upon pulsing MeOH over H-ZSM-5 at 390–420 °C. Conditions: $m_{\text{cat}} = 100$ mg (H-ZSM-5, Si/Al 25, 150–212 μm), $P_{\text{reactor}} = 1$ bar, MeOH pulse quantity = 1.2 μmol_C per pulse, carrier gas He = 20 $\text{mL}_{\text{NTP}}/\text{min}$, pulse interval = 3.75 min.

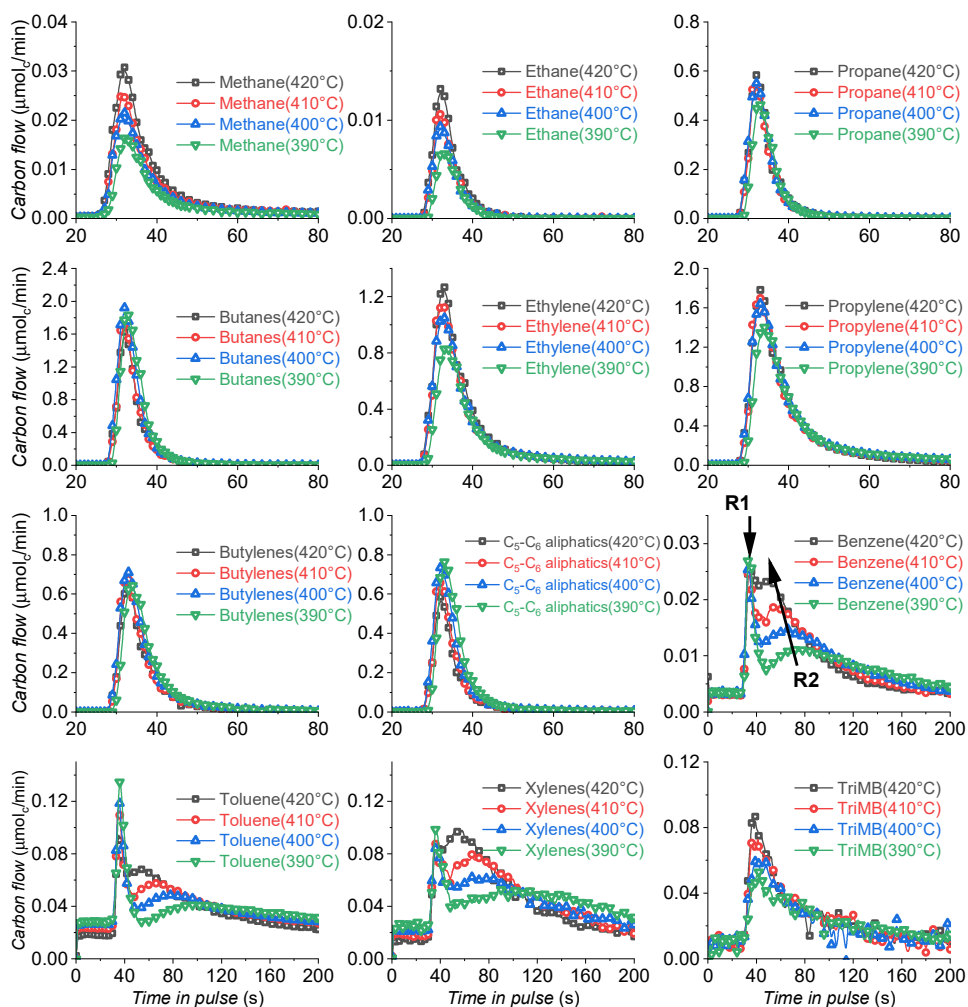


Figure 3.10. Hydrocarbons responses upon pulsing MeOH over H-ZSM-5 at 390–420 °C. Conditions: $m_{\text{cat}} = 100$ mg (H-ZSM-5, Si/Al 25, 150–212 μm), $P_{\text{reactor}} = 1$ bar, MeOH pulse quantity = 1.2 μmol_C per pulse, carrier gas He = 20 mL_{NTP}/min, pulse interval = 3.75 min.

Table 3.4. The product selectivity and statistical moment analysis (zeroth moment μ_0 and first moment μ_1) for MeOH pulse responses of **Figure 3.9** after BTX deconvolution of **Figure B4** in Appendix B.

		Carbon selectivity in pulse, C%									
T °C	Ethylene	Propylene	Butylenes	Methane	Ethane	Propane	Butanes	C5-C6	TriMB		
420	17.6%	27.7%	7.7%	0.5%	0.1%	5.8%	15.5%	5.8%	3.8%		
410	16.0%	27.5%	8.5%	0.4%	0.1%	5.5%	16.7%	6.8%	4.6%		
400	15.2%	27.2%	9.2%	0.3%	0.1%	5.8%	19.5%	8.0%	3.6%		
390	13.2%	25.5%	11.0%	0.3%	0.1%	5.3%	20.3%	8.9%	3.9%		
		Benzene Toluene Xylenes									
T °C	R1	R1	R1	R2	R2	R2					
420	0.4%	1.2%	1.1%	1.2%	4.5%	7.1%					
410	0.3%	0.9%	1.2%	1.2%	3.8%	6.5%					
400	0.2%	1.0%	0.9%	1.2%	2.5%	5.3%					
390	0.2%	1.3%	1.1%	1.1%	2.1%	5.7%					
		$\mu_0, \mu\text{molc}$									
T °C	Ethylene	Propylene	Butylenes	Methane	Ethane	Propane	Butanes	C5-C6	TriMB		
420	0.223	0.352	0.098	0.006	0.002	0.074	0.197	0.073	0.049		
410	0.199	0.342	0.106	0.005	0.001	0.068	0.208	0.084	0.057		
400	0.197	0.352	0.118	0.004	0.001	0.074	0.251	0.103	0.046		
390	0.159	0.307	0.132	0.003	0.001	0.064	0.244	0.107	0.047		
		Benzene Toluene Xylenes						C balance sumC			
T °C	R1	R1	R1	R2	R2	R2	Cout/Cin (μmol)				
420	0.005	0.015	0.014	0.015	0.057	0.090	1.059		1.270		
410	0.004	0.011	0.014	0.015	0.048	0.081	1.036		1.243		
400	0.003	0.013	0.012	0.015	0.033	0.069	1.076		1.291		
390	0.003	0.015	0.013	0.013	0.025	0.068	1.002		1.202		
		μ_1, s									
T °C	Ethylene	Propylene	Butylenes	Methane	Ethane	Propane	Butanes	C5-C6	TriMB		
420	35.7	37.7	35.7	35.7	34.0	33.8	33.8	34.0	62.5		
410	35.8	37.7	35.8	35.8	34.1	33.9	33.9	34.3	74.1		
400	35.9	38.0	35.9	35.9	34.0	33.8	33.8	34.3	72.5		
390	36.7	39.1	37.1	36.7	34.9	34.8	34.8	35.4	90.4		
		Benzene Toluene Xylenes									
T °C	R1	R1	R1	R2	R2	R2					
420	42.7	42.4	44.6	80.6	109.7	96.4					
410	39.8	37.6	44.3	85.9	107	105.3					
400	36.8	37.9	42.2	95.9	112.7	115.8					
390	36.4	38.6	41.2	119.7	148.8	148.6					

3.4.5 Impact of MeOH injection amount

To evaluate the impact of MeOH on the product temporal responses, in particular when the MeOH conversion is below 100%, the FASPA experiments were compared for two pulse sizes (1.2 and 7.6 $\mu\text{mol}_c/\text{pulse}$) over 4.5 mg H-ZSM-5 at 400 °C and results were shown in **Figure 3.11**. The full map of product responses and quantitative moment estimates can be found in **Figure B5** and **Table B3**.

With the larger pulse size of 7.6 μmol_c , the MeOH conversion is ~95%. In that case, The response time delay between argon and the products has almost completely disappeared, evidenced by the narrower time span between MS signals m/z 40 and 41 in FASPA tests in **Figure 3.11(a)**. Accordingly, MeOH is available across the entire catalyst bed with the larger pulse size in the FASPA test, MTH reactions proceed towards bulkier hydrocarbons resulting in the higher selectivity to C_{5+} aliphatics and aromatics (BTX and TriMB) mainly at the expense of propylene (**Figure 3.11(b-c)**). For the BTX response in **Figure 3.11(d)**, ascribed to the suppressed secondary reactions (such as hydrogen transfer reactions) at the presence of MeOH two BTX formations peaks were completely convolved into one broad peak sitting at ~35 s, just after the aliphatic responses (**Figure B5**).

At the incomplete MeOH conversion level, the estimated zeroth and first statistical moments for 4.5 mg H-ZSM-5 with 7.6 μmol_c per pulse help to calculate the minimum turn-over frequencies (eq. 3.15) assuming BAS as the active site in the induction period and the autocatalysis process once fully developed. The real product formation rates must be higher than the reported values in **Table B3**, since the adsorption/desorption increases the residence time (first moment, μ_1) of hydrocarbons. The estimated minimum turn-over frequency of propylene is 0.44 $\text{mol}_c/\text{mol}_{\text{BAS}}/\text{s}$, in good agreement with the reported range of 0.24–1.8 $\text{mol}_c/\text{mol}_{\text{BAS}}/\text{s}$ at 400 °C^[63, 64] confirming the feasibility of conducting a kinetic investigation of MTH reactions through the FASPA experiment.

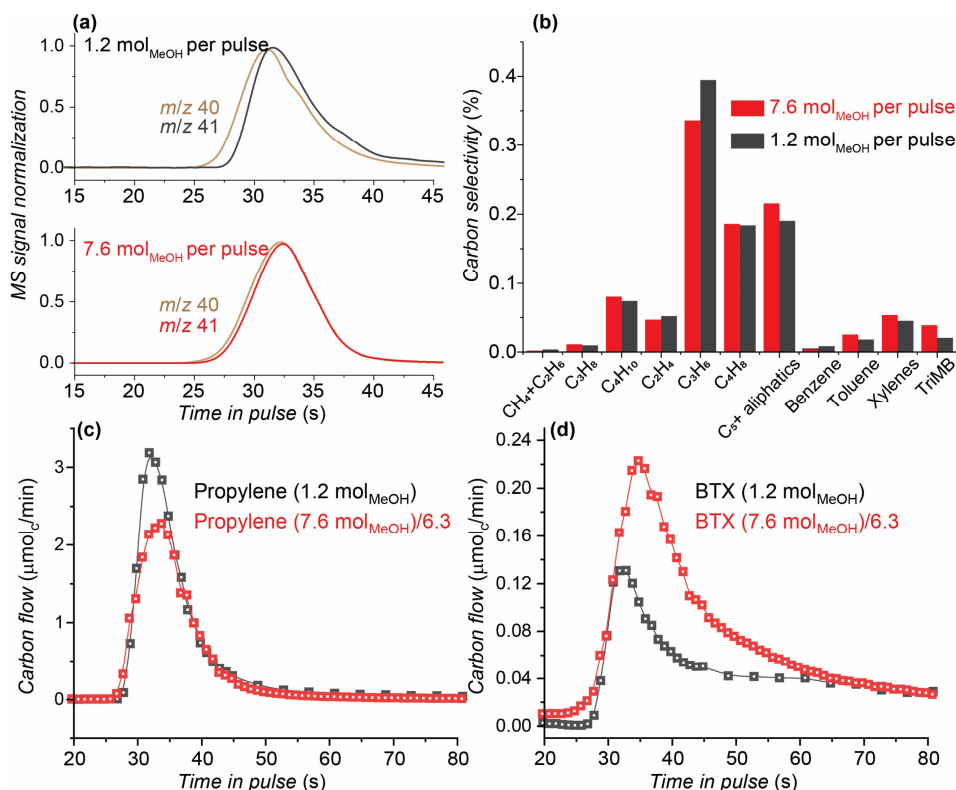


Figure 3.11. (a) Normalized MS-pulse responses of m/z 40 and 41 referring to Ar and aliphatic products; (b) total carbon selectivity of hydrocarbons; (c) propylene and (d) BTX temporal responses over H-ZSM-5 with different MeOH injection quantities in FASPA tests. Conditions: $T = 400$ °C, $m_{\text{cat}} = 4.5$ mg (H-ZSM-5, Si/Al 25, 150–212 μm), $P_{\text{reactor}} = 1$ bar, MeOH pulse quantity 1.2 and 7.6 μmol_{C} per pulse, carrier gas He = 20 $\text{mL}_{\text{NTP}}/\text{min}$, pulse interval = 3.75 min. Note: carbon flows of propylene and BTX responses with 7.6 μmol_{C} per pulse were divided by 6.3 for the direct comparison with those with 1.2 μmol_{C} per pulse in the FASPA tests. More quantitative results and full scale of FASPA responses can be found in **Table B3** and **Figure B5**.

3.5 Discussion

The objective of this study is to introduce and validate a newly developed fast scanning-pulse analysis (FASPA) technique with GC quantification, combined with *in situ* DRIFT spectroscopy, and demonstrate its applicability to shed light on reaction pathways in the complex network of the MTH process on a working H-ZSM-5 catalyst under industrially-relevant conditions.

The experimentally validated FASPA approach (**Figure 3.2**) allows the quantitative mapping of the product spectrum response upon a small reactant pulse with a high time resolution, even when the GC analysis time is much larger than the pulse response. In the presented quantitative results, the second resolution is easily achieved for the full spectrum of gaseous products in the MTH over H-ZSM-5, achieved with relatively cheap instrumentation, something that is even beyond reach with advanced instrumentation like the TAP system, TOF-MS analysis or Spaci-MS operation due to the reliance on MS analysis.^[16, 55, 65, 66]

The quantitative data interpretation is based on the statistical moment analysis^[23, 24], that has been applied extensively for transient non-reactive gas-solid chromatography established by Kubín and Kučera^[25-31, 67] and greatly used since the 1970s. Later this has been extended to reactive transient data of batch and pulse reactors.^[33, 35, 36] The pulse-response technique combined with moments analysis for the investigation of hydrocarbons adsorption on zeolitic materials demonstrates the applicability of this approach to a packed bed reactor system in this study, and provides the basis of the current study of the MTH process over H-ZSM-5 catalyst under reaction conditions. In this study only the zeroth and first moments are used. The use of an inert tracer (argon) is essential to account for set-up contributions.^[68, 69] The moment analysis then provides information about the adsorption-desorption behavior and rate parameters (turn-over frequencies, *TOFs*) of MTH species. This approach could provide kinetic information on the formation of individual products to bring us closer to a more quantitative understanding of this complex process.^[12] The apparent adsorption enthalpies of BTX estimated using a Van 't Hoff relation (**Table B1-2**) are well in line with the wide range of values reported in literature^[70-77]. The evident temperature influence on BTX adsorption on H-ZSM-5 implies that the quick MeOH conversion and hydrocarbon formation rates are tightly associated with thermodynamics of sluggish BTX adsorption-desorption processes, particularly at temperatures below 400 °C. Packed bed reactors therefore behave spatially as chromatographic reactors, making the kinetic examination of the MTH process in the zeolite catalyst at lower temperatures challenging.^[13, 78]

This study represents a showcase of the FASPA approach applied to study the MTH process by conducting experiments on different amounts of a model H-ZSM-5 catalyst, covering both temporal and spatial compositions. The analysis of the product response of MeOH pulses to an active H-ZSM-5 catalyst the genesis of hydrocarbon pool species in the induction period, their dynamics

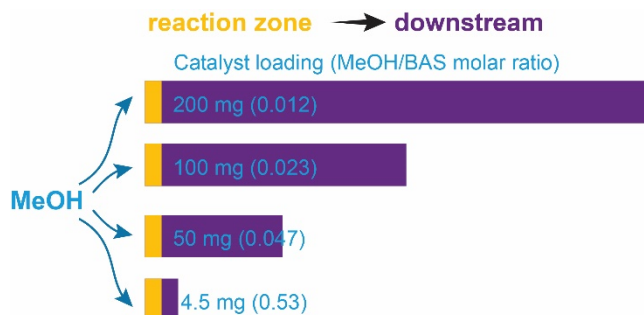


Figure 3.12. Varying catalyst loadings (4.5–200 mg) affect the length of the downstream region, in which the secondary reactions occur after MTH reactions in the reaction zone.

during the autocatalytic formation of reaction products in the transition period, and their final decomposition could be followed. Specifically, two different aromatization routes at operating conditions were observed.

In the MeOH pulse experiment over 4.5 mg catalyst, its product response composition is input to the rest of the catalyst bed for the larger sample (**Figure 3.12**), resulting in the composition development in **Figure 3.6-7**. Since the injected amount of MeOH ($1.2 \mu\text{mol}_C$ per pulse) is only a fraction of the total number of Brønsted acid sites (**Table 3.1**), the catalyst bed downstream of the active MTH zone, corresponding with an increasing amount of H-ZSM-5 (from 4.5 to 200 mg), can only affect processes like adsorption/desorption and secondary reactions in absence of MeOH. In particular, propylene and butylenes decrease while ethylene, butanes, propane, benzene, and toluene increase with increasing bed length, implying the simultaneous occurrence of (de-)alkylation, aromatization, and hydrogen transfer reactions specifically in the downstream zone of the bed. Ilias and Bhan proposed the ratio of ethylene to isobutane (mol C basis) as a qualitative descriptor to assess the relative contribution of the aromatic and olefinic cycle.^[12] For the pulse experiments with $1.2 \mu\text{mol}$ MeOH (**Table 3.3**) these ratios amount to 0.76 and 0.93 for the 4.5 and 100 mg samples, respectively, indicating that care must be taken with applying this descriptor in full MeOH conversion cases. The increasing ratio here does, however, point to further reactions downstream of the active reaction zone in the longer catalyst bed.

Unlike aliphatics, BTX exhibits a two-peak response to the MeOH pulse over H-ZSM-5. The first response ‘R1’ appears nearly simultaneously with the aliphatics and the quick build-up of cyclic surface species (**Figure 3.4**), implying that those aromatics are formed instantly from MeOH. With increasing catalyst

amount this R1 response shows a chromatographic adsorption-desorption delay of BTX (*cf.* **Figure B2**). The observed broad second BTX response ‘R2’ also shows a delay, but much longer, and therefore cannot solely be an adsorption-desorption phenomenon of BTX species. Since in this response time frame no MeOH is present any more, they must originate from another source. In absence of MeOH the HCP will no longer be maintained, resulting in the breakdown of HCP species, comprising polyolefinic, substituted cyclopentenyl, and aromatic species^[53, 79], in line with reported spectroscopic observations.^[19, 20] Schulz attributed the activity loss in H-ZSM-5 at low temperatures (<300 °C) to the formation of polyalkylated benzene species that cannot leave the MFI framework.^[13] The reduced formation of propylene and butylenes with increasing catalyst amount indicates such alkylation by olefins. These blocking species may further undergo dealkylation (coined ‘reanimation’ by Schulz), releasing retarded BTX, which can undergo similar alkylation/de-alkylation processes further down the bed. The prolonged residence time in the bed allows the increasing formation of ethylene from substituted dimethyl benzenes (**Figure 3.6**) as in the aromatic cycle.^[15, 80] This continuous olefin alkylation/de-alkylation of substituted benzenes can explain the broad retarded second maximum in the BTX appearance, showing the dynamics of this process with the appearance of a chromatographic reactor.^[81]

Temperature has an evident effect on the time delay between Ar and hydrocarbons demonstrating the induction period for the HCP build-up/restoration can be greatly shortened when the temperature is just increased by 30 °C from 390 to 420 °C. Besides, methane is observed about 1 s prior to other hydrocarbons, which may be associated to the first C–C bond formation by CO^[55-57]-/formaldehyde^[58]-mediated or extraframework alumina-assisted^[59] pathways with methane formation as a byproduct in the induction phase. Temperature also affects the first and second aromatic responses, yet the overall selectivity to aromatics increases slightly as the temperature rises from 390 to 420 °C (**Table 3.4**). First, higher temperatures accelerate the desorption of aromatics, resulting in a cleaner zeolite surface prior to the next MeOH pulse, as seen by the lower BTX baselines in **Figure 3.10**. Secondary processes, such as hydrogen transfer, cyclization, aromatization and desorption, are preferred at higher temperatures once MeOH is depleted, resulting in the 2nd BTX response moving to a shorter response time and increasing intensity leading to the increasing selectivity to the secondary formation of BTX (R2) after pulse time of 60 s, which specifically occurs in the downstream region of the catalyst bed.^[82]

With a larger pulse size of $7.6 \mu\text{mol}_c$ over the 4.5 mg H-ZSM-5, MeOH conversion is $\sim 95\%$ indicating the availability of MeOH across the catalyst bed. Accordingly, the convolved BTX responses (R1 and R2) can be explained by the suppressed secondary processes (hydrogen transfer and olefin alkylation/dealkylation) in the presence of MeOH. Moreover, the time delay in this case is much shorter than that obtained with a smaller pulse size of $1.2 \mu\text{mol}_c$. Müller *et al.* have identified two separated hydrogen transfer pathways, with one of them involving the participation of MeOH finally leading to a faster aromatic formation rate than the conventional olefin-mediated hydrogen transfer route.^[83] As explicated, MeOH decomposition and disproportionation occur possibly over Lewis acid sites (*e.g.*, extraframework Al) forming formaldehyde and methane. Accordingly, the olefins react with formaldehyde demonstrating a faster reaction pathway to aromatics. In our FASPA results, the shortened time delay between Ar and hydrocarbons with a larger pulse size also indicates that the induction process for the HCP build-up or restoration is promoted by MeOH (with methane as a byproduct in this process), further leading to the higher selectivity to C_{5+} aliphatics and aromatics once the HCP is built up (**Figure 3.11**).

The introduced FASPA technique is illustrated here for MTH over H-ZSM-5, but other conditions, catalysts and reactions can be analyzed by this method using quite standard research equipment. In principle, next to pulse-response also step-response experiments are amenable, yielding quantitative temporal composition information during the transient, relevant for mechanistic insight and design of multifunctional and non-steady state operated reactors.^[84-86]

3.6 Conclusions

The newly developed fast scanning-pulse analysis (FASPA) technique shows the potential to extract highly dynamic information and enables to distinguish highly coupled processes in the complex reaction network, for example, the MTH process. The zeolite catalysed MTH fixed-bed process often proceeds with the full conversion of the MeOH fed, producing a mixture of alkanes, olefins, and aromatics next to water over a gradually deactivating catalyst. Within this complex reaction network, many reactions including MeOH-mediated reactions and secondary reactions occur simultaneously, and vary both in the temporal and spatial dimensions. This indicates a highly dynamic feature of the MTH process from the start-up induction period to the following steady-state process in the whole catalyst bed. Compared to the conventional steady-state operation for

reaction mechanism studies, transient operations using the robust FASPA approach discloses rich insights in the highly dynamic MTH process at realistic reaction conditions over freshly activated H-ZSM-5 catalyst. In particular:

The second resolution of gas phase product responses upon the MeOH pulse reveals the fast consecutive reactions occurring in a narrow active MTH zone. All products appear nearly simultaneously after a short delay (a few seconds) upon MeOH injection, attributed to the HCP build-up induction period. This induction period can be sufficiently reduced by slightly elevating the reacting temperature by 30 °C or by increasing the MeOH quantity in each pulse. Methane is observed prior to other hydrocarbons, possibly related to the primary MeOH decomposition and disproportionation and the first C–C bond formation.

Depending on the presence of MeOH or not, two consecutive pathways for aromatics formation were directly discerned and kinetically decoupled: a very fast primary product formation in the presence of MeOH, followed by a slower second formation of aromatics when MeOH is depleted. By combining *in situ* DRIFTS and FASPA experiments, the fast formation of BTX and aliphatics is primarily related to the build-up of hydrocarbon pool species including cyclopentenyl species and methylated benzenes. The secondary formation of BTX is then related to the rather slow decomposition/desorption of HCP species.

Downstream of the active MTH zone where MeOH is fully converted, secondary reactions occur with increasing catalyst amount. Decomposed HCP species and olefins undergo aromatization and alkylation-dealkylation reactions, retarding the appearance of BTX and resulting in their broad secondary formation. The associated hydrogen transfer reactions result in an increased alkane formation, with (iso)butanes as the major component.

The core of the FASPA technique lies in the (un)synchronizing program that allows the fine control of online GC (or other instruments in other cases) sampling in transient operations. As long as the prerequisites for *quasi* steady-state operating conditions are met, this (un)synchronization mechanism combining the pulse technique and online quantification tools can be easily extended to other reaction systems extracting transient kinetic information, which is of vital value for understanding the complex reaction mechanism and related catalyst design and improvement.

References

- (1) Sheldon, R. A. *Green Chemistry* **2014**, *16* (3), 950-963.
- (2) Sun, Z.; Bottari, G.; Afanassenko, A.; Stuart, M. C.; Deuss, P. J.; Fridrich, B.; Barta, K. *Nature Catalysis* **2018**, *1* (1), 82-92.
- (3) Wei, J.; Ge, Q.; Yao, R.; Wen, Z.; Fang, C.; Guo, L.; Xu, H.; Sun, J. *Nature Communications* **2017**, *8* (1), 1-9.
- (4) Bruijninx, P. C.; Weckhuysen, B. M. *Angewandte Chemie International Edition* **2013**, *52* (46), 11980-11987.
- (5) Tian, P.; Wei, Y.; Ye, M.; Liu, Z. *ACS Catalysis* **2015**, *5* (3), 1922-1938.
- (6) Wang, W.; Buchholz, A.; Seiler, M.; Hunger, M. *Journal of the American Chemical Society* **2003**, *125* (49), 15260-15267.
- (7) Liu, Y.; Müller, S.; Berger, D.; Jelic, J.; Reuter, K.; Tonigold, M.; Sanchez-Sanchez, M.; Lercher, J. A. *Angewandte Chemie International Edition* **2016**, *55* (19), 5723-5726.
- (8) Chowdhury, A. D.; Houben, K.; Whiting, G. T.; Mokhtar, M.; Asiri, A. M.; Al-Thabaiti, S. A.; Basahel, S. N.; Baldus, M.; Weckhuysen, B. M. *Angewandte Chemie International Edition* **2016**, *55* (51), 15840-15845.
- (9) Sun, T.; Chen, W.; Xu, S.; Zheng, A.; Wu, X.; Zeng, S.; Wang, N.; Meng, X.; Wei, Y.; Liu, Z. *Chem* **2021**, *7* (9), 2415-2428.
- (10) Yarulina, I.; Chowdhury, A. D.; Meirer, F.; Weckhuysen, B. M.; Gascon, J. *Nature Catalysis* **2018**, *1* (6), 398-411.
- (11) Dahl, I. M.; Kolboe, S. *Catalysis Letters* **1993**, *20* (3), 329-336.
- (12) Ilias, S.; Bhan, A. *ACS Catalysis* **2013**, *3* (1), 18-31.
- (13) Schulz, H. *Catalysis Letters* **2018**, *148* (5), 1263-1280.
- (14) Yarulina, I.; Kapteijn, F.; Gascon, J. *Catalysis Science & Technology* **2016**, *6* (14), 5320-5325.
- (15) Svelle, S.; Joensen, F.; Nerlov, J.; Olsbye, U.; Lillerud, K.-P.; Kolboe, S.; Bjørgen, M. *Journal of the American Chemical Society* **2006**, *128* (46), 14770-14771.
- (16) Redekop, E. A.; Lazzarini, A.; Bordiga, S.; Olsbye, U. *Journal of Catalysis* **2020**, *385*, 300-312.
- (17) Dewaele, O.; Geers, V. L.; Froment, G. F.; Marin, G. B. *Chemical Engineering Science* **1999**, *54* (20), 4385-4395.
- (18) Brogaard, R. Y.; Henry, R.; Schuurman, Y.; Medford, A. J.; Moses, P. G.; Beato, P.; Svelle, S.; Nørskov, J. K.; Olsbye, U. *Journal of Catalysis* **2014**, *314*, 159-169.
- (19) Haw, J. F.; Nicholas, J. B.; Song, W.; Deng, F.; Wang, Z.; Xu, T.; Heneghan, C. S. *Journal of the American Chemical Society* **2000**, *122* (19), 4763-4775.
- (20) Zhang, L.; Wang, S.; Qin, Z.; Wang, P.; Wang, G.; Dong, M.; Fan, W.; Wang, J. *Molecular Catalysis* **2021**, *516*, 111968.
- (21) Emeis, C. *Journal of Catalysis* **1993**, *141* (2), 347-354.
- (22) Manning, C. J.; Palmer, R. A.; Chao, J. L. *Review of Scientific Instruments* **1991**, *62* (5), 1219-1229.
- (23) Do, D. D., in *Adsorption analysis: Equilibria and kinetics*, Imperial College Press, London, **1998**, pp. 775-795.
- (24) Ruthven, D. M., in *Principles of Adsorption and Adsorption Processes*, John Wiley, New York, **1984**, pp. 220-273.
- (25) Moulijn, J. A. *Stimulus/response experimenten in gepakte bedden*, University of Amsterdam, Amsterdam, **1974**, PhD Thesis (in Dutch).

- (26) Kubin, E. *Collect. Czech. Chem. Commun.* **1965**, *30*, 2900-2907.
- (27) Kubin, E. *Collect. Czech. Chem. Commun.* **1965**, *30* (4), 1104-1118.
- (28) Kučera, E. *Journal of Chromatography A* **1965**, *19*, 237-248.
- (29) Grubner, O.; Ralek, M.; Zikánová, A. *Collect. Czech. Chem. Commun.* **1966**, *31*, 852-862.
- (30) Grubner, O.; Zikánová, A.; Rálek, M. *Journal of Chromatography A* **1967**, *28*, 209-218.
- (31) Schneider, P.; Smith, J. M. *AIChE Journal* **1968**, *14* (5), 762-771.
- (32) Qamar, S.; Abbasi, J. N.; Javeed, S.; Shah, M.; Khan, F. U.; Seidel-Morgenstern, A. *Journal of Chromatography A* **2013**, *1315*, 92-106.
- (33) Chan, K. K.; Bolger, M. B.; Pang, K. S. *Analytical Chemistry* **1985**, *57* (11), 2145-2151.
- (34) Gleaves, J. T.; Ebner, J. R.; Kuechler, T. C. *Catalysis Reviews* **1988**, *30* (1), 49-116.
- (35) Yablonskii, G. S.; Shekhtman, S. O.; Chen, S.; Gleaves, J. T. *Industrial & Engineering Chemistry Research* **1998**, *37* (6), 2193-2202.
- (36) Shekhtman, S. O.; Yablonsky, G. S.; Gleaves, J. T.; Fushimi, R. *Chemical Engineering Science* **2003**, *58* (21), 4843-4859.
- (37) Kirchberger, F. M.; Liu, Y.; Plessow, P. N.; Tonigold, M.; Studt, F.; Sanchez-Sanchez, M.; Lercher, J. A. *Proceedings of the National Academy of Sciences* **2022**, *119* (4), e2103840119.
- (38) Valecillos, J.; Epelde, E.; Albo, J.; Aguayo, A. T.; Bilbao, J.; Castaño, P. *Catalysis Today* **2020**, *348*, 243-256.
- (39) Pazè, C.; Sazak, B.; Zecchina, A.; Dwyer, J. *The Journal of Physical Chemistry B* **1999**, *103* (45), 9978-9986.
- (40) Hernandez, E. D.; Jentoft, F. C. *ACS Catalysis* **2020**, *10* (10), 5764-5782.
- (41) Meunier, F. C.; Domokos, L.; Seshan, K.; Lercher, J. A. *Journal of Catalysis* **2002**, *211* (2), 366-378.
- (42) Bauschlicher, C. W.; Peeters, E.; Allamandola, L. J. *The Astrophysical Journal* **2009**, *697* (1), 311-327.
- (43) Kiricsi, I.; Förster, H. *Journal of the Chemical Society, Faraday Transactions 1: Physical Chemistry in Condensed Phases* **1988**, *84* (2), 491-499.
- (44) Förster, H.; Kiricsi, I.; Seebode, J., in *Studies in Surface Science and Catalysis, Vol. 37*, Elsevier, **1988**, pp. 435-442.
- (45) Stepanov, A. G.; Sidelnikov, V. N.; Zamaraev, K. I. *Chemistry – A European Journal* **1996**, *2* (2), 157-167.
- (46) Mosley, J. D.; Young, J. W.; Agarwal, J.; Schaefer III, H. F.; Schleyer, P. v. R.; Duncan, M. A. *Angewandte Chemie International Edition* **2014**, *53* (23), 5888-5891.
- (47) Kiricsi, I.; Förster, H.; Tasi, G.; Nagy, J. B. *Chemical Reviews* **1999**, *99* (8), 2085-2114.
- (48) Trombetta, M.; Busca, G.; Rossini, S. A.; Piccoli, V.; Cornaro, U. *Journal of Catalysis* **1997**, *168* (2), 334-348.
- (49) Jang, H.-G.; Min, H.-K.; Hong, S. B.; Seo, G. *Journal of Catalysis* **2013**, *299*, 240-248.
- (50) Demidov, A. V.; Davydov, A. A. *Materials Chemistry and Physics* **1994**, *39* (1), 13-20.
- (51) Liutkova, A.; Us lamin, E.; Parastayev, A.; Bolshakov, A.; Mezari, B.; Hensen, E. J. M.; Kosinov, N. *Catalysis Today* **2022**, *in press*.

- (52) Haag, W. O.; Lago, R. M.; Rodewald, P. G. *Journal of Molecular Catalysis* **1982**, *17* (2-3), 161-169.
- (53) Zhang, W.; Zhang, M.; Xu, S.; Gao, S.; Wei, Y.; Liu, Z. *ACS Catalysis* **2020**, *10* (8), 4510-4516.
- (54) Wang, C.; Sun, X.; Xu, J.; Qi, G.; Wang, W.; Zhao, X.; Li, W.; Wang, Q.; Deng, F. *Journal of Catalysis* **2017**, *354*, 138-151.
- (55) Wu, X.; Xu, S.; Zhang, W.; Huang, J.; Li, J.; Yu, B.; Wei, Y.; Liu, Z. *Angewandte Chemie International Edition* **2017**, *56* (31), 9039-9043.
- (56) Yang, L.; Yan, T.; Wang, C.; Dai, W.; Wu, G.; Hunger, M.; Fan, W.; Xie, Z.; Guan, N.; Li, L. *ACS Catalysis* **2019**, *9* (7), 6491-6501.
- (57) Yang, L.; Wang, C.; Dai, W.; Wu, G.; Guan, N.; Li, L. *Fundamental Research* **2022**, *2* (2), 184-192.
- (58) Liu, Y.; Kirchberger, F. M.; Müller, S.; Eder, M.; Tonigold, M.; Sanchez-Sanchez, M.; Lercher, J. A. *Nature Communications* **2019**, *10* (1), 1462.
- (59) Comas-Vives, A.; Valla, M.; Copéret, C.; Sautet, P. *ACS Central Science* **2015**, *1* (6), 313-319.
- (60) Yokoi, T.; Mochizuki, H.; Namba, S.; Kondo, J. N.; Tatsumi, T. *The Journal of Physical Chemistry C* **2015**, *119* (27), 15303-15315.
- (61) Forester, T. R.; Howe, R. F. *Journal of the American Chemical Society* **1987**, *109* (17), 5076-5082.
- (62) Kubo, K.; Iida, H.; Namba, S.; Igarashi, A. *Journal of the Japan Petroleum Institute* **2018**, *61* (1), 10-19.
- (63) Khare, R.; Arora, S. S.; Bhan, A. *ACS Catalysis* **2016**, *6* (4), 2314-2331.
- (64) Khare, R.; Millar, D.; Bhan, A. *Journal of Catalysis* **2015**, *321*, 23-31.
- (65) Morgan, K.; Touitou, J.; Choi, J.-S.; Coney, C.; Hardacre, C.; Pihl, J. A.; Stere, C. E.; Kim, M.-Y.; Stewart, C.; Goguet, A.; Partridge, W. P. *ACS Catalysis* **2016**, *6* (2), 1356-1381.
- (66) Morgan, K.; Maguire, N.; Fushimi, R.; Gleaves, J. T.; Goguet, A.; Harold, M. P.; Kondratenko, E. V.; Menon, U.; Schuurman, Y.; Yablonsky, G. S. *Catalysis Science & Technology* **2017**, *7* (12), 2416-2439.
- (67) Gangwal, S. K.; Hudgins, R. R.; Silveston, P. L. *The Canadian Journal of Chemical Engineering* **1979**, *57* (5), 609-620.
- (68) Fierro, V.; Schuurman, Y., in *Studies in Surface Science and Catalysis, Vol. 160*, Elsevier, Amsterdam, **2007**, pp. 241-247.
- (69) Boz, E. B.; Taşdemir, A.; Biçer, E.; Yürüm, A.; Alkan Gürsel, S. *International Journal of Hydrogen Energy* **2021**, *46* (65), 32858-32870.
- (70) Stach, H.; Lohse, U.; Thamm, H.; Schirmer, W. *Zeolites* **1986**, *6* (2), 74-90.
- (71) Pope, C. G. *The Journal of Physical Chemistry* **1984**, *88* (25), 6312-6313.
- (72) Pope, C. G. *The Journal of Physical Chemistry* **1986**, *90* (5), 835-837.
- (73) Pope, C. G. *Journal of the Chemical Society, Faraday Transactions* **1993**, *89* (7), 1139-1141.
- (74) Lee, C. K.; Chiang, A. S. T. *Journal of the Chemical Society, Faraday Transactions* **1996**, *92* (18), 3445-3451.
- (75) Mukti, R. R.; Jentys, A.; Lercher, J. A. *The Journal of Physical Chemistry C* **2007**, *111* (10), 3973-3980.
- (76) Jentys, A.; Mukti, R. R.; Tanaka, H.; Lercher, J. A. *Microporous and Mesoporous Materials* **2006**, *90* (1-3), 284-292.
- (77) Kanervo, J. M.; Kouva, S.; Kanervo, K. J.; Kolvenbach, R.; Jentys, A.; Lercher, J. A. *Chemical Engineering Science* **2015**, *137*, 807-815.

- (78) Omojola, T. *Chemical Engineering Science* **2022**, *251*, 117424.
- (79) Lin, S.; Zhi, Y.; Chen, W.; Li, H.; Zhang, W.; Lou, C.; Wu, X.; Zeng, S.; Xu, S.; Xiao, J.; Zheng, A.; Wei, Y.; Liu, Z. *Journal of the American Chemical Society* **2021**, *143* (31), 12038-12052.
- (80) Wang, C.; Yi, X.; Xu, J.; Qi, G.; Gao, P.; Wang, W.; Chu, Y.; Wang, Q.; Feng, N.; Liu, X.; Zheng, A.; Deng, F. *Chemistry – A European Journal* **2015**, *21* (34), 12061-12068.
- (81) Russo, V.; Tesser, R.; Rossano, C.; Vitiello, R.; Turco, R.; Salmi, T.; Di Serio, M. *Chemical Engineering Journal* **2019**, *377*, 119692.
- (82) Khare, R.; Bhan, A. *Journal of Catalysis* **2015**, *329*, 218-228.
- (83) Müller, S.; Liu, Y.; Kirchberger, F. M.; Tonigold, M.; Sanchez-Sanchez, M.; Lercher, J. A. *Journal of the American Chemical Society* **2016**, *138* (49), 15994-16003.
- (84) Krishna, R. *Chemical Engineering Science* **2002**, *57* (9), 1491-1504.
- (85) Renken, A. *Chemie Ingenieur Technik* **1990**, *62* (9), 724-733.
- (86) Kalz, K. F.; Kraehnert, R.; Dvoyashkin, M.; Dittmeyer, R.; Gläser, R.; Krewer, U.; Reuter, K.; Grunwaldt, J.-D. *ChemCatChem* **2017**, *9* (1), 17-29.

APPENDIX B - Direct discerning reaction pathways in methanol-to-hydrocarbons by transient operation - FASPA

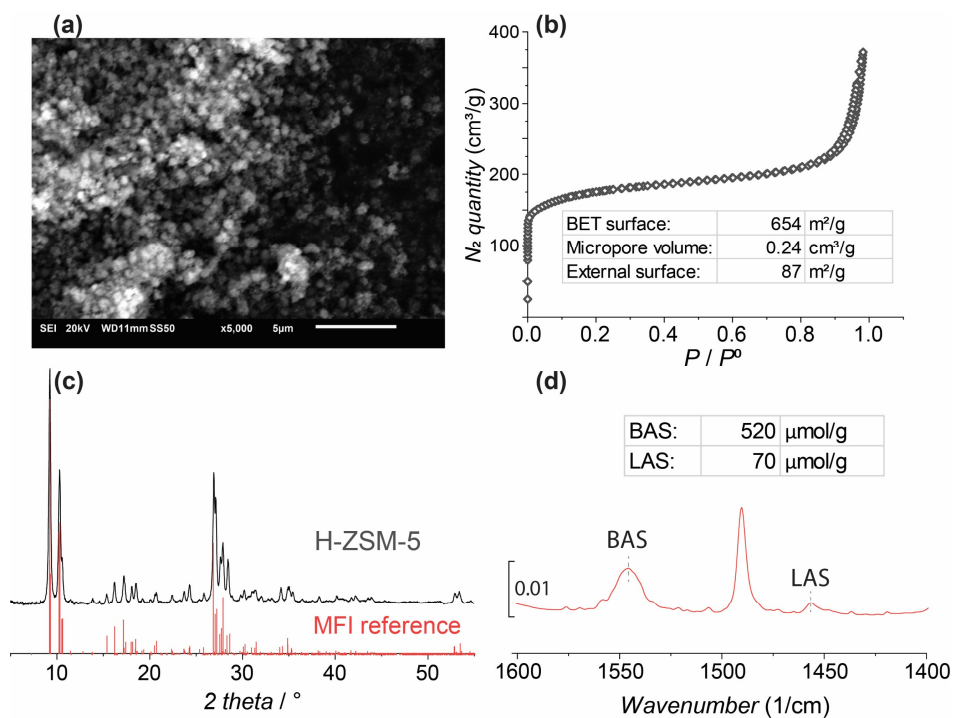


Figure B1. Characterization results of H-ZSM-5: SEM image with the scale bar of 5 μm (a); N_2 physisorption isotherm with estimated BET surface area, micropore volume and external surface area from t-plot analysis (b); XRD pattern in 5–55 $^\circ$ with theoretical MFI phase diffractions (c); FT-IR spectrum in 1600–1400 cm^{-1} range of pyridine adsorption (d).

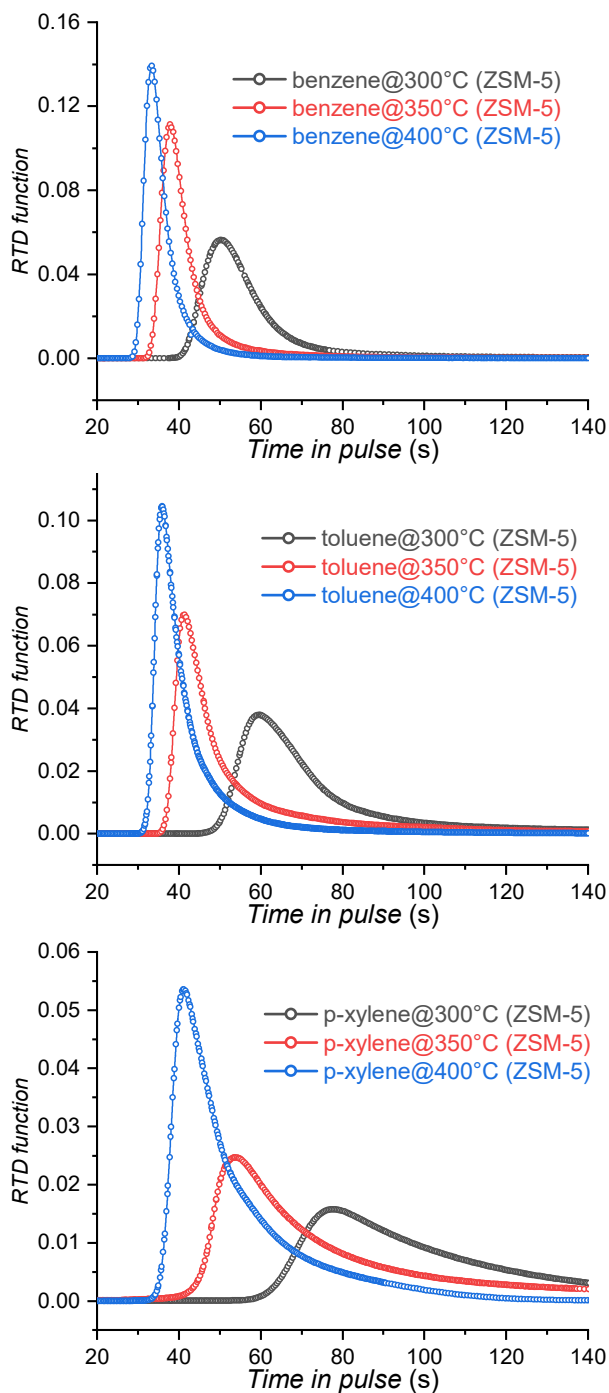


Figure B2. MS response curves of different BTX tracers over 100 mg H-ZSM-5 in the range 300–400 °C.

Appendix B

Table B1. Normalized 1st moment values for different tracers over empty reactor tube, or reactor tubes packed with 100 mg Sil-1 or H-ZSM-5 in the range 270–400 °C.

T °C	Ar	Ar	<i>p</i> -xylene	<i>p</i> -xylene	<i>p</i> -xylene	toluene	toluene	benzene	benzene
	Sil-1	ZSM-5#	empty reactor	Sil-1	ZSM-5	Sil-1	ZSM-5	Sil-1	ZSM-5
	s	s	s	s	s	s	s	s	s
400	31.2	31.6	32.7		53.3	33.1	43.8		37.6
350	31.5	32.5	33.0	38.8	91.0	35.0	60.0	34.0	43.7
320	31.9	32.9		42.4		38.0	79.8		51.9
310	32.1	32.9	33.1	46.5		39.6	107.8	37.2	56.5
300	32.2	32.9	33.3	50.2	249.0	41.8	121.1		62.1
280	32.5							41.8	
270	32.7							43.9	

#: reactor inner diameter was ~0.1 mm larger than others (4.0 mm)

Table B2. Apparent adsorption enthalpies of BTX in Sil-1 and H-ZSM-5.

ΔH_{ads} (kJ/mol)	ZSM-5			Sil-1		
	<i>p</i> -xylene	toluene	benzene	<i>p</i> -xylene	toluene	benzene
	-70.9	-72.2	-66.9	-52.8	-51.2	-52.1

These apparent values are in line with the wide range of values reported for these aromatics in literature^[1-8], and will contain contributions from stronger adsorption at the SiOHAl groups and weaker adsorption at SiOH groups (*e.g.* 54 and 24 kJ/mol, respectively, for benzene in ref^[7]). It is noted that the toluene and *p*-xylene pulse data are accompanied by some 5% conversion at the highest temperature due to (de)methylation.

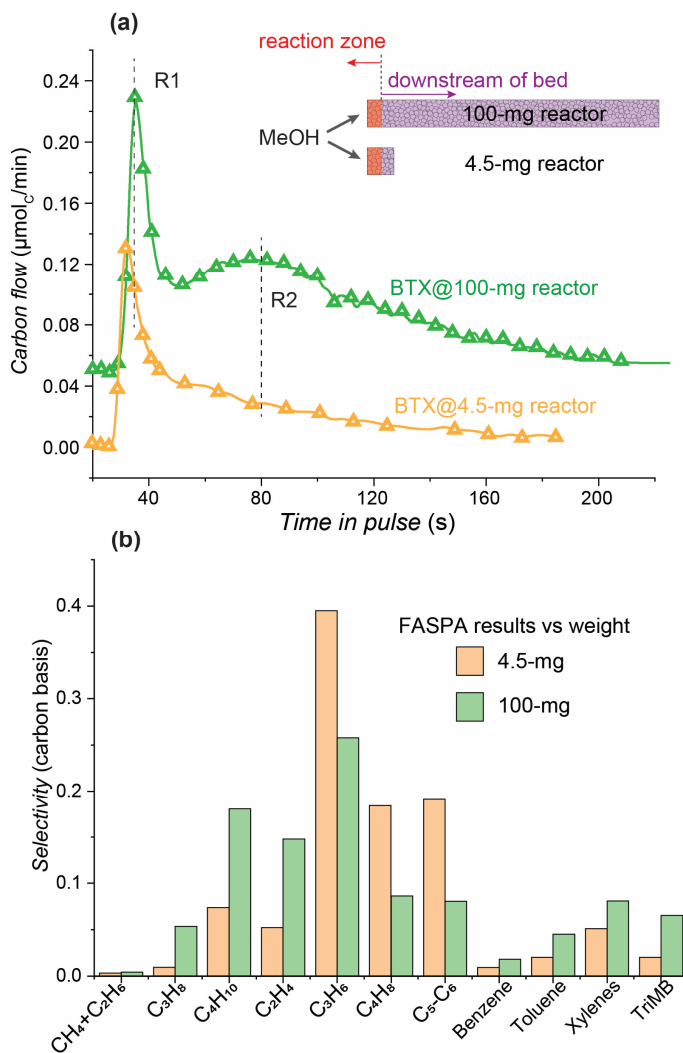


Figure B3. BTX temporal responses (a) and total carbon selectivity of hydrocarbons (b) over 4.5 and 100 mg H-ZSM-5 in the FASPA experiments. Conditions: $T = 400\text{ }^\circ\text{C}$, $m_{\text{cat}} = 4.5$ or 100 mg (H-ZSM-5, Si/Al 25, 150–212 μm), $P_{\text{reactor}} = 1$ bar, MeOH pulse quantity 1.2 μmol_C per pulse, carrier gas He = 20 $\text{mL}_{\text{NTP}}/\text{min}$, pulse interval = 3.75 min.

Appendix B

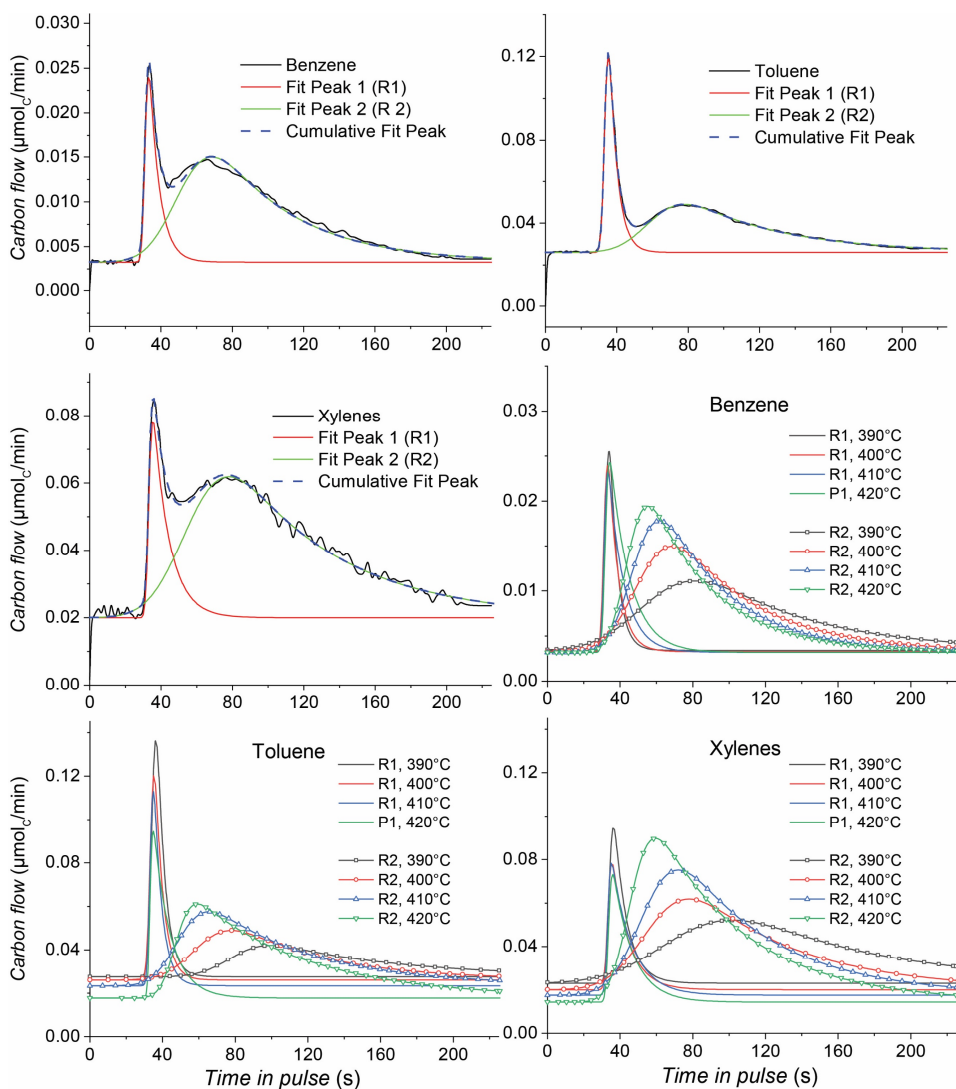


Figure B4. Example of aromatics response deconvolution by two-peak fitting using GaussMod function (eq. 3.16-17) over 100-mg H-ZSM-5 at 400 °C, and summarized deconvolution results of BTX responses at 390–420 °C.

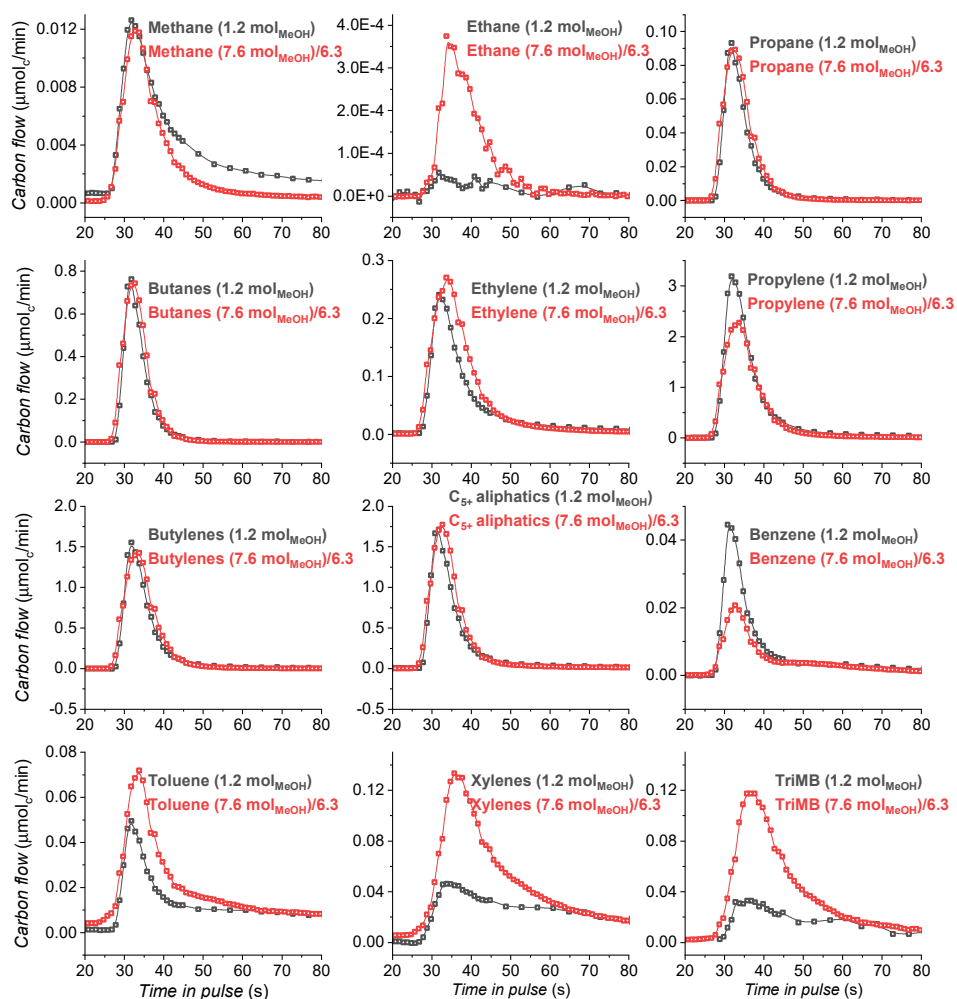


Figure B5. Comparison of hydrocarbon responses over 4.5 mg H-ZSM-5 with different MeOH quantities per pulse at 400 °C. Conditions: H-ZSM-5 (Si/Al 25, 150–212 μm), $P_{\text{reactor}} = 1$ bar, MeOH pulse quantity = 1.2 and 7.6 μmol_c per pulse, carrier gas He = 20 $\text{mL}_{\text{NTP}}/\text{min}$, pulse interval = 3.75 min. More quantitative experimental data can be found in **Table B3**.

Appendix B

Table B3. Statistical moment analysis for MeOH pulse responses over H-ZSM-5 with different injection amounts.

$\mu_0, \mu\text{molc}$									
Inject amount $\mu\text{molMeOH}$	Ethylene	Propylene	Butylenes	Methane	Ethane	Propane	Butanes	C ₅ -C ₆	TriMB
7.60	0.344	2.488	1.377	0.016	0.000	0.082	0.594	1.594	0.286
1.21	0.059	0.448	0.209	0.004	-	0.011	0.084	0.216	0.023
Inject amount $\mu\text{molMeOH}$	Benzene	Toluene	Xylenes	C balance $C_{\text{out}}/C_{\text{in}}$					
7.60	0.033	0.188	0.394	0.973					
1.21	0.009	0.020	0.051	0.938					
μ_1, s									
Inject amount $\mu\text{molMeOH}$	Ethylene	Propylene	Butylenes	Methane	Ethane	Propane	Butanes	C ₅ -C ₆	TriMB
7.60	36.6	35.3	34.5	36.8	39.4	34.0	33.3	34.0	46.0
1.21	35.3	34.3	33.7	39.4	-	33.2	32.7	33.4	63.6
Inject amount $\mu\text{molMeOH}$	Benzene	Toluene	Xylenes	Ar Reference					
7.60	47.4	48.8	51.8	32.8					
1.21	64.3	90.8	98.0	32.2					
$TOF, \text{molc/molBAS/s}$									
Inject amount $\mu\text{molMeOH}$	Ethylene	Propylene	Butylenes	Methane	Ethane	Propane	Butanes	C ₅ -C ₆	TriMB
7.60	0.039	0.440	0.340	0.002	0.000	0.030	0.560	0.570	0.010
1.21	0.016	0.180	0.120	0.000	-	0.009	0.150	0.150	0.001
Inject amount $\mu\text{molMeOH}$	Benzene	Toluene	Xylenes						
7.60	0.001	0.005	0.009						
1.21	0.000	0.000	0.001						

In order to verify if internal diffusion transport may affect the MeOH conversion rate the so-called Weisz-Prater or Wheeler-Weisz^[9] criterion can be used. This ‘observable’ Φ is based on the observed volumetric rate of an irreversible reaction, characteristic particle diffusion dimension, effective diffusivity and concentration, and reads for spherical particles

$$\Phi = \frac{r_v^{obs} \cdot L^2}{D_{eff} \cdot c_s} < 0.08 \quad (\text{B3.1})$$

In the current case the observed rate is estimated from the MeOH consumption in a pulse experiment at 400 °C. A pulse of MeOH in He contains 1.2 μmol MeOH, and it is assumed that this amount is fully converted over the same number of 1.2 μmol active Al sites, corresponding to a fraction of 0.0234 BAS in 100 mg H-ZSM-5 catalyst (Si/Al=25). So, in the further calculation it is assumed that only less than an initial 2.34% of the catalyst bed (2.34 mg) contributes. This would represent an upper limit since all products contain more than one carbon species formed from more MeOH molecules over less sites (autocatalysis process).

With an MFI density $r = 1.766 \text{ g/mL}$, and particle porosity $\varepsilon_p = 0.35$ this corresponds with a catalyst particle volume of 2.03 nL in the active zone of the bed.

As characteristic reaction time, the first moment of the C₂-C₄ alkanes production is taken (33.8–34.0 s, **Table 3.3**) minus the first moment of argon (33.1 s) in that experiment. These species will show the least adsorption delay downstream in the rest of the catalyst bed. So, the alkanes are produced almost instantaneously, and a reaction time of 0.7 s yields for the minimum volumetric MeOH conversion rate:

$$r_{v,obs} = 860 \text{ mol}_{MeOH} s^{-1} m^{-3} \quad (\text{B3.2})$$

Table B4. Operating conditions and texture data of the particulate catalyst used for Wheeler-Weisz criterion calculation

$T = 673 \text{ K}$	$\tau_p = 2.5$ (assumed)	$V_{\text{meso}} = 0.12 \text{ cm}^3 \text{ g}^{-1}$
$p_{\text{tot}} = 1 \text{ atm}$	$\text{Si/Al} = 25 \text{ mol mol}^{-1}$	$S_{\text{ext}} = 87 \text{ m}^2 \text{ g}^{-1}$
$y_{\text{MeOH}} = 0.12$	Crystal size = 428 Å	$S_{\text{BET}} = 654 \text{ m}^2 \text{ g}^{-1}$
$d_p = 150\text{-}212 \text{ }\mu\text{m}$	$V_{\text{total}} = 0.36 \text{ cm}^3 \text{ g}^{-1}$	$\text{BAS} = 530 \text{ }\mu\text{mol g}^{-1}$
$\varepsilon_p = 0.35$	$V_{\text{micro}} = 0.24 \text{ cm}^3 \text{ g}^{-1}$	$\text{LAS} = 74 \text{ }\mu\text{mol g}^{-1}$
MFI density = 1.766 g cm ⁻³	topological density = 960	$V_{\text{unit cell}}^* = 5211.3 \text{ \AA}^3$
$\varepsilon_{\text{zeo}}^{**} = 0.0981$	pure $V_{\text{zeo}}^{***} = 0.056 \text{ cm}^3 \text{ g}^{-1}$	$V_{\text{part}}^{****} = 0.30 \text{ cm}^3 \text{ g}^{-1}$

*: calculated based on MFI model, Si₉₆O₁₉₂; **: pure zeolite porosity; ***: calculated based on the accessible MFI pore volume 511 Å³ (9.81%); ****: particle volume, which is total pore volume (V_{total}) excluding pure zeolite pores (pure V_{zeo}). This is the volume used for the diffusional transport to the zeolite crystals to calculate the average transport pore size r_{pore} .

Relations:

$$L = \frac{V_p}{S_p} = \frac{d_p}{6} = (2.5 - 3.53) \cdot 10^{-5} \text{ m} \quad (\text{B3.3})$$

$$c_s \approx c_b = \frac{y_{\text{MeOH}} P_{\text{tot}}}{R \cdot T} = 2.166 \text{ mol/m}^3 \quad (\text{B3.4})$$

$$D_{\text{eff}} = \frac{\varepsilon_p}{\tau_p} D = 0.14D \quad (\text{B3.5})$$

$$\frac{1}{D} = \frac{1}{D_{\text{Kn}}} + \frac{1}{D_{\text{MeOH} \rightarrow \text{He}}} \quad (\text{B3.6})$$

For the Knudsen diffusivity the average pore size of the catalyst particle is used, which is based on the pore space for transport V_{pore} and the specific external surface area S_{ext} from the t -plot analysis (see texture data in **Table B1**):

$$r_{pore} = \frac{2V_{pore}}{S_{ext}} = 6.99 \cdot 10^{-9} \text{ m} \quad (\text{B3.7})$$

$$D_{Kn} = \frac{2r_{pore}}{3} \sqrt{\frac{8RT}{\pi M_{MeOH}}} = 3.110 \cdot 10^{-6} \text{ m}^2 \text{ s}^{-1}$$

For the molecular diffusivity of MeOH in helium the relation of Fuller, Schettler and Giddings yields:

$$D_{MeOH \rightarrow He} = \frac{10^{-7} T^{1.75} \left(\frac{1}{M_{MeOH}} + \frac{1}{M_{He}} \right)^{\frac{1}{2}}}{P_{tot} \left[\sqrt[3]{v_{MeOH}} + \sqrt[3]{v_{He}} \right]^2} = 1.623 \cdot 10^{-4} \text{ m}^2 \text{ s}^{-1} \quad (\text{B3.8})$$

with

$$v_{He} = 2.67$$

$$v_{MeOH} = v_c + v_O + 4v_H = 15.9 + 6.11 + 4 \cdot 2.31 = 31.35$$

$$D = \frac{1}{\frac{1}{D_{Kn}} + \frac{1}{D_{MeOH \rightarrow He}}} = 3.051 \cdot 10^{-6} \text{ m}^2 \text{ s}^{-1}$$

$$D_{eff} = 4.27 \cdot 10^{-7} \text{ m}^2 \text{ s}^{-1}$$

Finally, the resulting value of the Wheeler-Weisz parameter for the lower and upper particle sizes becomes:

$$\Phi = ? .58 - 1.16? > 0.08 \quad (\text{B3.9})$$

This parameter could be further larger than the criterion suggests for the absence of pore diffusion limitations when using a reaction time of alkanes less than 0.7 s if correcting for some adsorption delay.

This result strongly indicates that the conversion of MeOH in the pulse is severely intraparticle diffusion controlled, the more bearing in mind the high (upper) number of assumed active sites involved.

References

- (1) Kanervo, J. M.; Kouva, S.; Kanervo, K. J.; Kolvenbach, R.; Jentys, A.; Lercher, J. A. *Chemical Engineering Science* **2015**, *137*, 807-815.
- (2) Lee, C. K.; Chiang, A. S. T. *Journal of the Chemical Society, Faraday Transactions* **1996**, *92* (18), 3445-3451.
- (3) Mukti, R. R.; Jentys, A.; Lercher, J. A. *The Journal of Physical Chemistry C* **2007**, *111* (10), 3973-3980.
- (4) Pope, C. G. *The Journal of Physical Chemistry* **1984**, *88* (25), 6312-6313.
- (5) Pope, C. G. *The Journal of Physical Chemistry* **1986**, *90* (5), 835-837.
- (6) Pope, C. G. *Journal of the Chemical Society, Faraday Transactions* **1993**, *89* (7), 1139-1141.
- (7) Jentys, A.; Mukti, R. R.; Tanaka, H.; Lercher, J. A. *Microporous and Mesoporous Materials* **2006**, *90* (1-3), 284-292.
- (8) Stach, H.; Lohse, U.; Thamm, H.; Schirmer, W. *Zeolites* **1986**, *6* (2), 74-90.
- (9) Weisz, P. B.; Prater, C. D., in *Advances in Catalysis, Vol. 6*, Academic Press, **1954**, pp. 143-196.

Chapter 4. Revealing main reaction paths to olefins and aromatics in the MTH process over H-ZSM-5

The identification of nature of hydrocarbon pool (HCP) intermediates in the methanol-to-hydrocarbons (MTH) process has been fairly well developed, especially for the BEA- and CHA-type zeolite catalysts like H-beta and H-SAPO-34, respectively. Results in this chapter demonstrate that the HCP species in the medium-pore H-ZSM-5 zeolite catalyst exhibits rather dynamic features. In particular, the production of aromatics upon pulsing methanol (MeOH) is directly discerned involving the displacement, HCP reactions and secondary formations. The role of water in the MTH process is emphasized to compete with primarily formed aromatics accelerating the desorption of aromatics from the bed, accordingly suppressing the aromatic cycle reactions and possible polyaromatization reactions leading to the catalyst deactivation. The MTH products from ^{13}C -/ ^{12}C -MeOH/water switch experiments were then analyzed by online mass spectrometer and the newly developed FASPA (Fast Scanning Pulse Analysis) approach, allowing a (semi-)quantitative determination of isotope compositions in aromatics and main aliphatic products. The faster isotope scrambling process in olefin products than that in aromatics, provides direct experimental evidence confirming the olefin-based HCP via the methylation/cracking reactions is kinetically preferred rather than the aromatic-based one. After that, the paring instead of the side-chain mechanism explains the isotope incorporation process within aromatics suggesting it to be the dominant mechanism after the olefin-based cycle within H-ZSM-5.

4.1 Introduction

The methanol (MeOH) conversion by zeolite catalysts proceeds via a complex network of transformations. This involves cooperation between zeolite Brønsted acid sites and the confined hydrocarbon intermediates, commonly referred to as the hydrocarbon pool (HCP) mechanism.^[1] Instead of direct conversion, MeOH is first transformed into long linear or cyclic hydrocarbons, which are trapped in the zeolite pores. These bulky intermediates split off light olefins and aromatics like propylene and toluene, and may subsequently undergo methylation with MeOH.

Owing to the shape-selectivity feature, distinct HCP species may be generated depending on the zeolite pore size and acid strength, resulting in an entirely different product distribution throughout the MeOH transformation process. Assisted by the fast development of advanced spectroscopy techniques, especially *in situ/operando* NMR spectroscopy, the identification of these HCP species progresses enormously. For instance, heptamethyl-benzenium ions are readily formed in H-Beta, whereas the MeOH conversion mainly proceeds via penta- and hexamethyl-benzenes in H-SAPO-34 zeolite catalysts. Within H-ZSM-5 zeolite having a larger channel diameter and possessing channel intersections instead of cavities than H-SAPO-34 higher methylbenzenes like penta- and hexamethylbenzenes are virtually unreactive.^[1d] Instead, methylated cyclopentenyl ions, tri- and tetramethyl benzenes are proven to be the HCP intermediates.^[2] Meanwhile, the large pore opening (0.5–0.6 nm) of H-ZSM-5 ensures the diffusing out of BTX (benzene, toluene, and xylenes) and trimethylbenzenes (TriMB).

Next to the HCP identity, the kinetic study of MeOH interacting with HCP species leading to the final products is rather difficult from a purely experimental point of view due to the complex reaction network and limited spatial-/temporal analysis tools to study the ongoing activities within zeolite micropore under operational conditions. So far, transient kinetic techniques such as the temporal analysis of products (TAP) and ¹²C/¹³C isotope labeling have been utilized to obtain highly specific mechanistic and kinetic information about the MTH mechanism.^[3] However, the challenging transient data analysis relying on mass spectrometry in the TAP setup limits the discrimination of specific individual reaction steps like olefin methylation or cracking in the MTH^[3b, 4] since they can affect each other in such a complex reaction network. Enormous mechanistic and

kinetic information can be extracted from $^{12}\text{C}/^{13}\text{C}$ labeling experiments. As early as 1982, Dessau and coworkers used ^{13}C -MeOH co-feeding ^{12}C -olefins/aromatics reactions to study the MTH mechanism. That study reveals that olefins are produced via continuous methylation/cracking, an indirect route.^[5] In a later study, Dahl and Kolboe used the isotope labeling technique, further developing this indirect route and proposing the HCP mechanism.^[1] Furthermore, based on the time evolution of the ^{13}C composition in light olefins and aromatic effluent products after switching from ^{12}C -MeOH feeding to ^{13}C -MeOH feeding in H-ZSM-5, Olsbye and co-workers proposed the dual-cycle mechanism within H-ZSM-5, suggesting that C_{3+} olefins are formed from the methylation and cracking of the longer olefinic intermediates in the so-called olefin cycle, while ethylene and aromatics are formed by methylation and dealkylation of methyl benzenes in the aromatic cycle.^[6] Therefore, the isotope labeling technique plays a substantial role in the study into the MTH mechanism. However, due to a limited time resolution, the commonly applied off-line GC-MS analysis of effluent products and trapped species in the zeolite might miss key information during the fast transient after switching. Moreover, the co-feeding of ^{13}C -olefin or aromatics in excess over their real formation levels in the MTH process might saturate the zeolite catalyst, leading to a misunderstanding of the role of these species in the HCP mechanism. Recently, Pérez-Ramírez *et al.* have employed photoion photoelectron coincidence (PEPICO) spectroscopy as a potent analytical tool that provides extensive information on the gas phase reaction intermediates in the MTH process.^[7] Due to the highly interweaved reactions almost simultaneously occurring, PEPICO spectroscopy operating under steady-state circumstances is rather difficult to offer direct experimental evidence for an intrinsic kinetic study.

In this chapter, a quantitative analysis of HCP species in H-ZSM-5 zeolite catalysts and their reactivity with MeOH in the MTH process relying on the isotope labeling technique and the fast scanning-pulse analysis (FASPA) is given. This recently developed FASPA technique allows the quantitative GC mapping of the fast temporal evolution of the product responses upon a MeOH pulse over the catalyst. The online MS analysis of different effluent products in the ^{13}C -MeOH/ ^{12}C -MeOH/water switch pulse experiments directly reveals the highly dynamic character of the HCP in H-ZSM-5 in its contribution to the production of aromatics and light olefins. Four consecutive pathways from MeOH to aromatics are directly and quantitatively discerned under the MeOH-pulsing conditions. The ^{13}C - ^{12}C distribution within various products is assessed semi-quantitatively, showing that light olefins are predominantly produced via the

olefin cycle while light aromatics (and light olefins) are produced via the paring mechanism rather than the side-chain mechanism in the aromatic cycle.

4.2 Experimental methods

4.2.1 Catalyst characterizations

The same H-ZSM-5 zeolite catalyst is used as in **Chapter 3**. Therefore, the physicochemical properties of zeolite materials can be found in **Figure B1**, Appendix B.

4.2.2 Catalytic testing

The FASPA tests were carried out at 400°C using a fixed-bed reactor loaded with 100 or 4.5 mg H-ZSM-5 zeolite catalyst (150–212 μm size). The details of the FASPA experimental protocol can be found and the gas chromatographic analysis of FASPA responses is the same as in **Chapter 3**.

For the $^{13}\text{C-MeOH} \Leftrightarrow ^{12}\text{C-MeOH}$ switch experiments, a 2-mL sample loop was used filled with ~9 vol% MeOH (either $^{12}\text{C-MeOH}$ or $^{13}\text{C-MeOH}$, 99 mol%, Aldrich Sigma) yielding a 7.6 μmol_C pulse (quantified by GC analysis) in helium from two saturators kept at ~14 °C containing $^{12}\text{C-MeOH}$ and $^{13}\text{C-MeOH}$, respectively, each connected to a helium flow line (20 mL_{NTP}/min, conditions referred to as NTP, normal temperature and pressure at $T = 23$ °C, $P = 1$ atm). The desired He flow line was selected by a four-way valve upstream of the sample loop. For the $^{12}\text{C-MeOH} \Rightarrow \text{water}$ switch experiment, a third helium flow saturator with water at room temperature was used, corresponding to an injection of ~2.4 μmol_{water}/pulse.

Before switching, five pulses of $^{13}\text{C-MeOH}$ (or $^{12}\text{C-MeOH}$ in $^{12}\text{C-MeOH} \Rightarrow \text{water}$ switch test) were fed for reaching *quasi* steady-state conditions on the catalyst surface, as apparent from the corresponding MS responses (**Figure 4.1**).

The product mixture was continuously analysed by online MS (Pfeiffer, Thermostar GSD320-QMG220) with a continuous capillary leak inlet. Mass signals at relevant selected (m/z) units were measured with 50 ms time intervals. In the $^{13}\text{C}/^{12}\text{C-MeOH}/\text{water}$ experiments, m/z signals of 40, 39–47, and 91–98 were selected to record the changes of Ar, light aliphatics (C_{3+}), light aromatics fragments (toluene, xylenes and trimethylbenzenes), respectively in the switch.

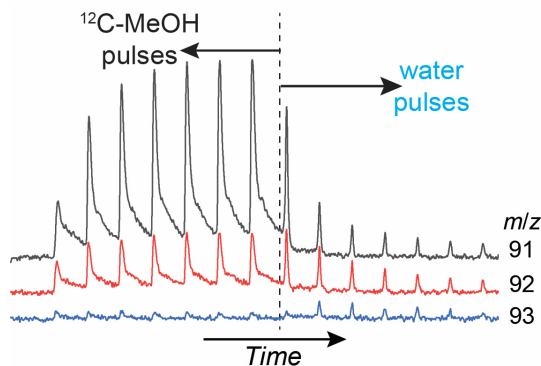


Figure 4.1. MS responses of $m/z = 91$ and 92 (mainly attributed to toluene, xylenes, and trimethylbenzenes) upon $^{12}\text{C-MeOH} \Rightarrow \text{water}$ pulses over 100 mg H-ZSM-5 @ 400 °C indicating *quasi* steady state conditions approach.

MS signals of $m/z = 91\text{--}97$ in the last $^{13}\text{C-MeOH}$ pulse (or $92\text{--}98$ in the last $^{12}\text{C-MeOH}$ pulse) still exhibit residual intensities, which are attributed to non-isotopic effects, such as impurities in the $^{12}\text{C-}/^{13}\text{C-MeOH}$ liquid or MS fragments from the same molecule. Therefore, for MS signals of $m/z = 91\text{--}98$ a correction was performed before the fragmentation composition calculation. This correction is based on the fragmentation contribution relative to $m/z = 98$ and $m/z = 91$ in the last $^{13}\text{C-MeOH}$ and $^{12}\text{C-MeOH}$ pulse, respectively.

4.3 Results

Upon a MeOH pulse ($7.6 \mu\text{mol}_\text{c}$) to a 100 mg H-ZSM-5 catalyst bed, a clear time delay of ~ 1.5 s was observed between the appearance of the co-injected tracer Ar and all formed hydrocarbons, which is attributed to the induction period required to build up or restore the HCP from MeOH until the first hydrocarbon product in the effluent leaving the catalytic bed. From ~ 28 s, all aliphatic species (**Figure 4.2(a)**) are observed and rapidly reach their max around ~ 36 s. After that, these responses slowly decrease to zero in terms of concentration in the exit flow until the end (before the next MeOH pulse). Combined with *in situ* DRIFT spectroscopy, the previous study in **Chapter 3** revealed that the hydrocarbon productions are closely associated with the HCP build-up within the zeolite upon the MeOH pulse. Once the injected MeOH is rapidly depleted, the decomposition and desorption of the formed HCP species, which are mainly methylated cyclopentenyl and (poly-)methylated benzenes, within the zeolite micropores explain the long tailing of the observed responses as shown in **Figure 4.2(b)**,

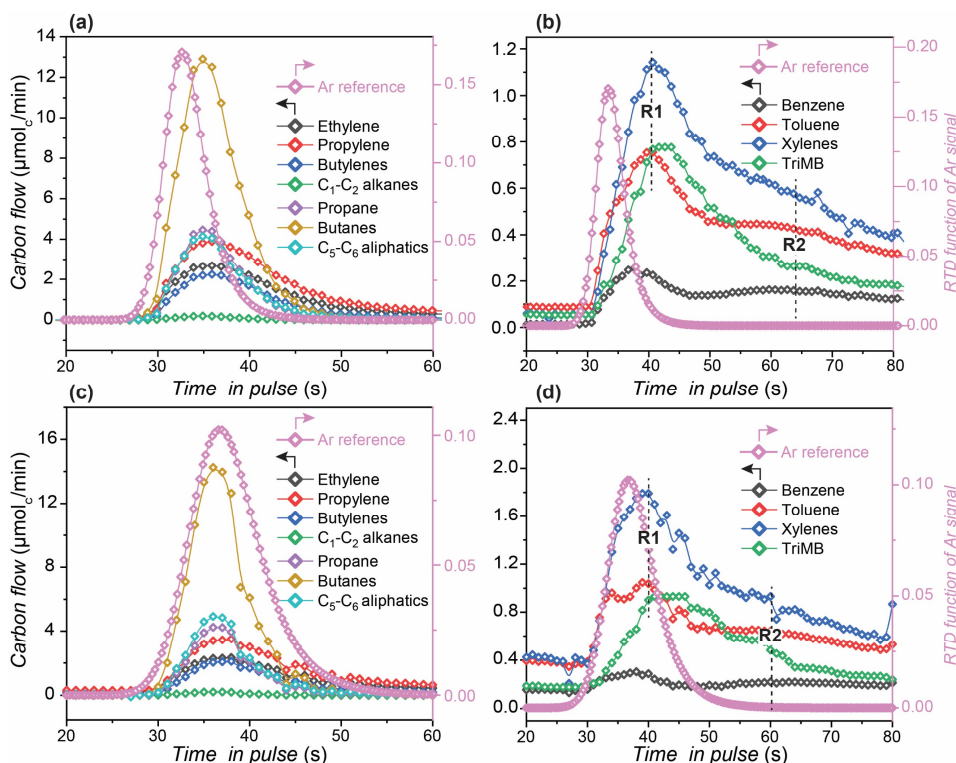


Figure 4.2. The FASPA temporal responses of aliphatic (**a**, **c**) and aromatic products (**b**, **d**) upon MeOH pulse into H-ZSM-5 zeolite catalyst with 3.75 (*top*) and 1.25 (*bottom*) min interval. FASPA experimental conditions: $T = 400^{\circ}\text{C}$, $m_{\text{cat}} = 100$ mg (H-ZSM-5, Si/Al 25, 150–212 μm), $P_{\text{reactor}} = 1$ bar, MeOH pulse quantity 7.6 μmol_{C} per pulse, carrier gas He = 20 mL_{NTP}/min, time delay = 1 s. Xylenes refer to sum of *o*-, *m*-, and *p*-xylene. TriMB is the abbreviation of trimethylbenzenes. Ar (MS signal $m/z=40$) was used as inert tracer to account for the set-up response.

demonstrating the dynamic character of the HCP in the medium-pore H-ZSM-5 zeolite catalyst. In particular, a sharp first response (R1) is observed for benzene, toluene, xylenes and TriMB (trimethylbenzenes) at a response time of ~ 40 s (**Figure 4.2(b)**), appearing ~ 4 s later than the aliphatic peaks (**Figure 4.2(a)**) ascribed to the stronger adsorption of the former species in the zeolite catalyst. After 40 s, a second broad low-concentration response R2 of benzene (also of toluene and xylenes) is observed around ~ 60 s, which indicates a secondary formation of aromatics within the H-ZSM-5 catalyst. A detailed discussion on the origin of the second peak of benzene, toluene and xylenes can be found in **Chapter 3**. It is worth noting that olefins (ethylene, propylene and butylenes) decay relatively slower than alkanes (methane, ethane, propane and butanes). The

Table 4.1. Carbon selectivity and statistical moment analysis of results of FASPA tests over 100 and 4.5 mg H-ZSM-5 catalysts for pulses of 7.6 μmol MeOH at 400 °C.

Carbon selectivity in pulse, C%										
Weight mg	interval min	Ethylene	Propylene	Butylenes	Methane	Ethane	Propane	Butanes	C5-C6	TriMB
100	3.75	10.1%	15.8%	7.2%	0.3%	0.2%	8.6%	23.5%	9.5%	7.6%
100	1.25	10.7%	15.4%	7.2%	0.3%	0.2%	8.7%	27.1%	10.3%	4.9%
4.5	3.75	4.8%	34.8%	19.3%	0.2%	-	1.1%	8.3%	22.3%	4.1%
Weight mg	interval min	Benzene R1	Toluene R1	Xylenes R1	Benzene R2	Toluene R2	Xylenes R2			
100	3.75	0.7%	3.2%	4.3%	1.9%	3.7%	5.4%			
100	1.25	0.4%	2.3%	5.5%	0.4%	2.2%	4.1%			
4.5	3.75	0.4%	1.5%	4.0%	-	-	-			
$\mu_0, \mu\text{molC}$										
Weight mg	interval min	Ethylene	Propylene	Butylenes	Methane	Ethane	Propane	Butanes	C5-C6	TriMB
100	3.75	0.743	1.166	0.529	0.019	0.013	0.630	1.733	0.699	0.561
100	1.25	0.715	1.027	0.479	0.022	0.013	0.582	1.805	0.688	0.328
4.5	3.75	0.344	2.488	1.377	0.016	0.000	0.082	0.594	1.594	0.291
Weight mg	interval min	Benzene R1	Toluene R1	Xylenes R1	Benzene R2	Toluene R2	Xylenes R2	C balance Cout/Cin	sumC (μmol)	
100	3.75	0.050	0.239	0.321	0.139	0.271	0.397	0.990	7.410	
100	1.25	0.025	0.155	0.368	0.029	0.143	0.274	0.875	6.653	
4.5	3.75	0.031	0.110	0.285	-	-	-	0.940	7.150	

butanes (mainly *i*-C₄ and some *n*-C₄) show the highest response demonstrating their highest product selectivity (**Table 4.1**).

With the pulse interval reduced to 1.25 min, aromatics are not fully desorbed from the catalyst bed resulting in a higher baseline level of toluene and xylenes than for a 3.75-min interval (**Figure 4.2(b)** versus **(d)**). Furthermore, the responses of benzene and xylenes in **Figure 4.2(b)** and **(d)** still show a clear dual-peak profile and toluene even a convolution of three contributions, suggesting multiple reactions sequentially contribute to the formation of aromatics.

To probe the reactivity of HCP species and the proceeding reactions with MeOH, isotopic labeling was used. The experiment was conducted in such way that a series of repetitive ¹³C-MeOH pulses were sent over a freshly activated H-ZSM-5 catalyst until reaching a *quasi* steady state. Then a switch was made to ¹²C-MeOH pulses. An online mass spectrometer monitored the transient evolution of the isotopes in the entire experiment. The results are presented in **Figure 4.3**.

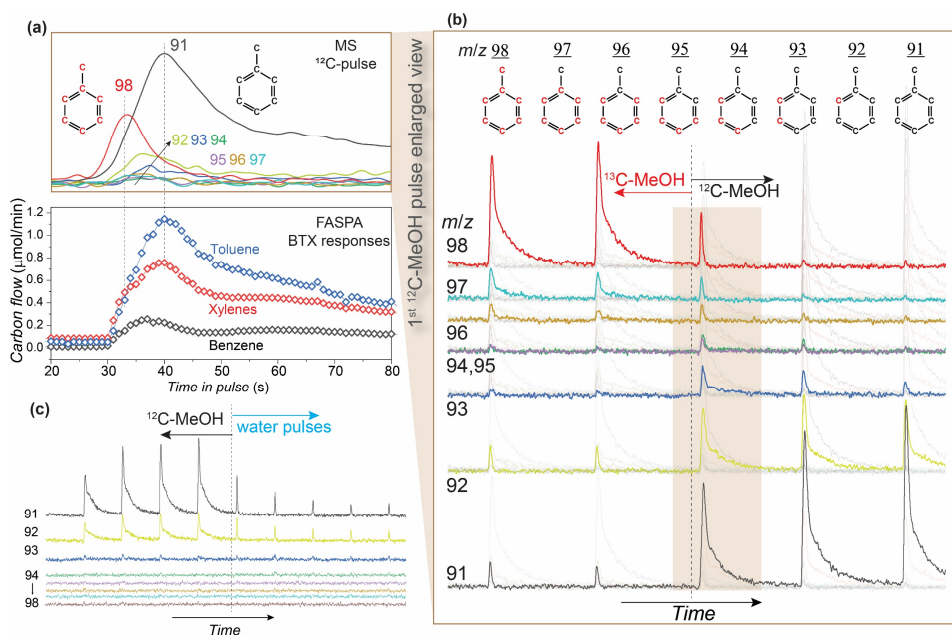


Figure 4.3. Temporal responses of $^{13}\text{C}/^{12}\text{C}$ -MeOH/ H_2O pulse switch experiments: comparison of BTX (benzene, toluene, and xylenes) responses in the FASPA test and MS fragmentation ($m/z = 91-98$) responses in the first ^{12}C -MeOH pulse after switching from ^{13}C -MeOH (a); enlarged view of MS fragmentation ($m/z = 91-98$) responses in ^{13}C -MeOH \Rightarrow ^{12}C -MeOH switch test (b); MS fragmentation ($m/z = 91-98$) analysis of ^{12}C -MeOH \Rightarrow H_2O switch test (c). Key: Injection of either ^{12}C - or ^{13}C -MeOH in He, $7.6 \mu\text{mol}/\text{pulse}$ or with H_2O saturated He ($\sim 2.4 \mu\text{mol}_{\text{water}}/\text{pulse}$). $T = 400 \text{ }^\circ\text{C}$, $m_{\text{cat}} = 100 \text{ mg}$ (H-ZSM-5, Si/Al = 25, $150-212 \mu\text{m}$), $P_{\text{reactor}} = 1 \text{ bar}$, carrier gas He = $20 \text{ mL}_{\text{NTP}}/\text{min}$, pulse interval = 3.75 min. In the toluene structures presented in (b) to represent the different m/z values the ^{13}C position is only schematically indicated, which can be randomly distributed. The MS intensities in (a) have been corrected for the fragmentation contributions relative to $m/z = 91$ and 98 .

The $m/z = 91-98$ intensities were selected to represent the isotopically labeled and unlabeled toluene, xylenes and TriMB (all having their most abundant unlabeled fragment at $m/z = 91$ ^[8]) responses in the MTH experiments. During the last ^{13}C -MeOH pulse the most abundant MS fragment, $m/z = 98$, mainly referring to aromatic $^{13}\text{C}_7\text{H}_7$, rapidly reaches a maximum and then slowly decays to zero (**Figure 4.3(b)**). MS fragments like $m/z = 92$ and 91 , ascribed to the impurity in ^{13}C -labeling, display a similar trend but of much lower intensity, which confirms the full labeling of toluene, xylenes and TriMB before switching to ^{12}C -MeOH.

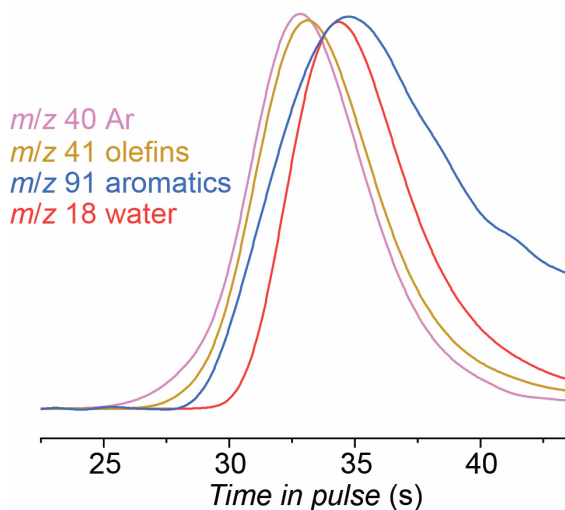


Figure 4.4. Normalized MS signals upon MeOH pulse over into 100 mg H-ZSM-5 zeolite catalyst. Other reaction conditions are as in **Figure 4.2**. Pulse interval is 3.75 min.

After switching to ^{12}C -MeOH, in the first pulse response, the fully unlabeled aromatic $^{12}\text{C}_7\text{H}_7$ fragment $m/z = 91$, immediately grows and reaches its maximum with a more than 5-fold higher intensity than those of the isotopic ^{13}C -containing intermediates ($m/z = 92\text{--}97$, **Figure 4.3(a-b)**). Clearly, the fast formation of aromatics stems mainly from the direct transformation of the newly injected ^{12}C -MeOH. The second most abundant response is a sharp peak at $m/z = 98$ representing fully labeled species directly released upon the first ^{12}C -MeOH pulse even before the appearance of the $m/z = 91$ peak after switching. This response is attributed to organic species present in the zeolite catalyst sample at the end of the ^{13}C -MeOH pulse series.

Comparing the BTX (benzene, toluene, and xylenes) responses from the FASPA experiment (**Figure 4.3(a)**), with the MS responses of $m/z = 98$ and 91, the latter are perfectly in line with the shoulder and the maximum of the temporal BTX responses in the FASPA analysis. This further indicates that the fast appearance of BTX at 35-40 s initially comes from the displacement of retarded species from the previous pulse. A displacement effect by water in the pulse response of toluene/xylene fragments is confirmed by the ^{12}C -MeOH \Rightarrow H $_2$ O switch experiment presented in **Figure 4.3(c)**, although this is not observed for benzene fragments probably due to the lower quantity of less retarded benzene (**Figure C1**). Also, the last product that appeared in the exit flow upon a MeOH pulse is water ($m/z = 18$, **Figure 4.4**) confirming the adsorption of water in the

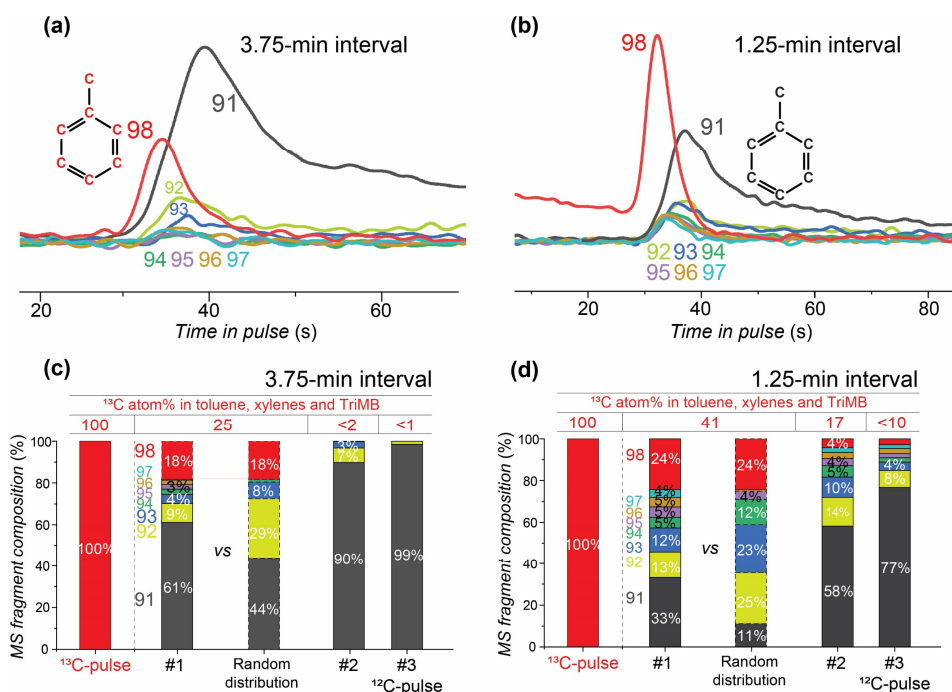


Figure 4.5. Fragmentation corrected intensities of $m/z = 91-98$ signals in the first ^{12}C -MeOH pulse response after pulsing ^{13}C -MeOH (*top*, 3.75-min interval) and integral C_7 fragments composition (*bottom*, 1.25-min interval) with ^{13}C content (at%) in the last ^{13}C -MeOH pulse and the following three ^{12}C -MeOH pulses. The same $^{12}\text{C}/^{13}\text{C}$ atomic ratios (91% and 9% excluding the displacement peak, $m/z = 98$) in the first ^{12}C -MeOH pulse was used to estimate the random distribution of $m/z = 91-97$ fragments. Conditions further as in **Figure 4.3**.

catalyst bed is the strongest under operating conditions.^[9] After the displacement process, the MS peak of $m/z = 91$ has a much higher intensity than those of $m/z = 92-97$ suggesting that newly formed aromatics predominantly stem from the injected ^{12}C -MeOH.

Similar results were obtained when the pulse interval was reduced from 3.75 to 1.25 min, resulting in an even larger displacement response at $m/z = 98$ upon the first ^{12}C -MeOH pulse (**Figure 4.5(b)**). Its decaying baseline before the switching supports the interpretation of an unfinished wash out of this species from the catalyst bed.

The displacement of aromatics in the catalyst bed was further addressed by reducing the catalyst weight from 100 to 4.5 mg. Owing to the 20-time lower concentration of Brønsted acid sites in this bed, the total conversion of MeOH is

with ~95% nearly complete, and the primary response products will directly leave the bed. In case of a 100 mg catalyst bed these response products move through and interact with the rest of the catalyst bed and their wash out takes longer. Therefore, the displacement feature is almost negligible in the first ^{12}C -MeOH pulse response after switching for the 4.5 mg catalyst bed and 3.75 min pulse interval (**Figure C5(b)**). In the case of faster pulsing (1.25 min interval, 4.5 mg H-ZSM-5, **Figure C5(b)**), a displacement peak of fully labeled C_7 fragment ($m/z = 98$) was also detected like in case of the 100 mg catalyst sample. Notably, two sharp MS signals with $m/z = 95-96$ were observed upon the switch for the 4.5 mg catalyst bed. These MS fragments probably originate from dimethylated cyclohexenes^[8]. In the 100 mg case, these contributions are absent suggesting these aliphatics are extremely reactive and short-lived before being converted into aromatics after the MeOH depletion in a longer catalyst bed.

The isotopic ^{13}C - ^{12}C distribution in selected products during the switch was followed by monitoring the MS fragments in the range of $m/z = 91-98$, representative for TriMB/toluene/xylenes, and in the range $m/z = 39-47$ representative for C_{3+} aliphatics. The distribution of the integrated $m/z = 91-98$ responses after correction for fragmentation to the first ^{12}C -MeOH pulse and the overall ^{13}C - ^{12}C atomic content in each pulse are presented in **Figure 4.5(c-d)**, including the case for a random isotope distribution in MS fragment C_7H_7 .^[1a] The full random distribution pattern as function of ^{13}C - ^{12}C content is given by **Figure C4**. There is no difference in reactivity of these different isotopic fragments in the MTH reactions.^[1a]

The estimated ^{13}C - ^{12}C distribution in **Figure 4.5(c)** suggests that 18 at% of the total C first leaves the catalyst bed in the form of the fully labeled $^{13}\text{C}_7\text{H}_7$ (originating from toluene, xylenes or TriMB) during the abovementioned displacement process. On the other hand, 61 at% C-content was observed in the form of fully unlabeled $^{12}\text{C}_7\text{H}_7$ ($m/z = 91$), directly after the displacement process, which completely stems from the newly injected ^{12}C -MeOH via aromatization. The isotopic mixed products are represented by the fragment intermediates from $m/z = 92$ to 97. In total 25 at% ^{13}C was collected during the first ^{12}C -MeOH pulse response arising from the displacement (18 at%) and the following mixed isotope products (7 at%). In the second and third ^{12}C -MeOH pulse responses the ^{13}C content quickly dropped, indicating that the ^{13}C -HCP is nearly fully replaced by a few repeated ^{12}C -MeOH pulses.

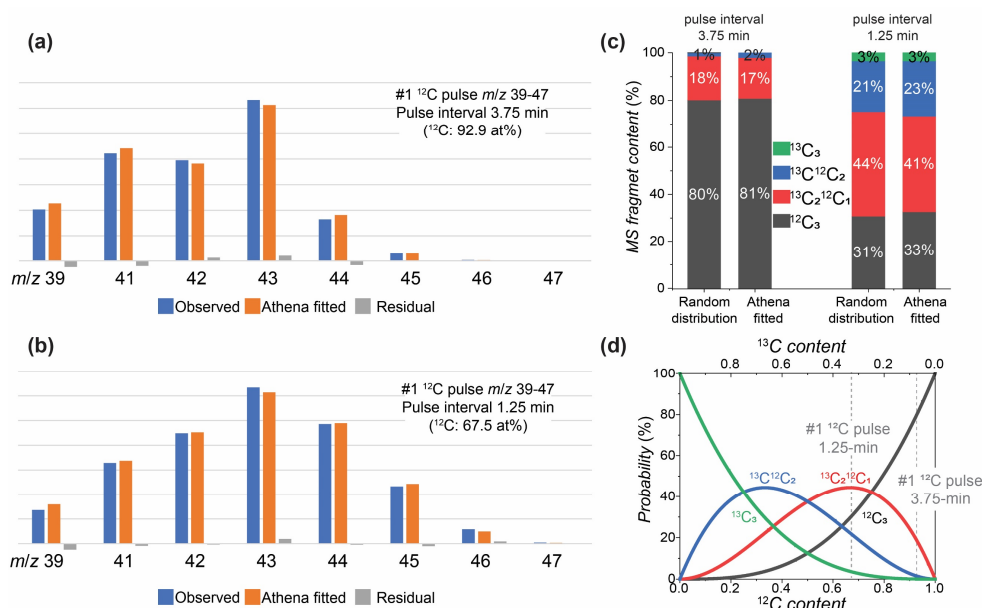


Figure 4.6. MS analysis of $m/z = 39–47$ for C_3+ components produced upon the first ^{12}C -MeOH after switching. The fitted MS fragment pattern with 3.75-min (a) and 1.25-min (b) pulse interval; The comparison of fitted MS fragments with random distribution assuming the same $^{13}\text{C}/^{12}\text{C}$ content shown in a and b (c); The random distribution composition for $m/z = 39–47$ as function of $^{13}\text{C}/^{12}\text{C}$ content (d). Note: m/z 41 refers to $^{12}\text{C}_3\text{H}_5^+$, m/z 42 refers to $^{12}\text{C}_2^{13}\text{C}_1\text{H}_5^+$, m/z 43 refers to $^{12}\text{C}_1^{13}\text{C}_2\text{H}_5^+$, and m/z 44 refers to $^{13}\text{C}_3\text{H}_5^+$ as shown in (d).

In a random distribution model with the same $^{13}\text{C}/^{12}\text{C}$ atomic ratio (7/75 at% ignoring the displacement process), the most abundant isotopic aromatic fragment would be $m/z = 92$, followed by 93, 94, and 91 referring to $^{13}\text{C}_1^{12}\text{C}_6\text{H}_7$, $^{13}\text{C}_2^{12}\text{C}_5\text{H}_7$, $^{13}\text{C}_3^{12}\text{C}_4\text{H}_7$, and $^{12}\text{C}_7\text{H}_7$, respectively. This differs completely from the observed ^{13}C - ^{12}C distribution, in which $m/z = 91$ shows a higher contribution in the first ^{12}C -MeOH pulse response. Note that 18 at% ^{13}C in the form of $^{13}\text{C}_7\text{H}_7$ directly leaves the bed without participating in the consecutive reactions and is accordingly not taken into account in this model. When shortening the pulse interval to 1.25 min (faster MeOH pulsing), the total ^{13}C content in aromatic C_7 fragments in the first ^{12}C -MeOH pulse response after switching is 41 at% (**Figure 4.5(d)**), higher than the 25 at% for 3.75-min pulse interval, indicating more retarded organic species are present in the catalyst. Still, in comparison with a random distribution, a much higher contribution of $m/z = 91$ (fully unlabeled toluene, xylenes or TriMB) is observed in the first ^{12}C -MeOH pulse response.

Table 4.2. Observed MS intensity of $m/z = 37\text{--}47$ in the last ^{12}C -MeOH pulse, the last ^{13}C -MeOH pulse, and the first ^{12}C -MeOH pulse after switching for 1.25 min and 3.75 min pulse intervals. The MS responses can be found in **Figure C2-3**. MS intensity was normalized to the MS signals in bold for comparison.

^{12}C -MeOH pulse			^{13}C -MeOH pulse			1 st ^{12}C -pulse after switch		
m/z	1.25 min	3.75 min	m/z	1.25 min	3.75 min	m/z	1.25 min	3.75 min
37	6	6	39	1	1	39	21	32
38	13	12	40	7	7	41	52	67
39	52	51	41	13	12	42	71	62
41	100	100	42	51	49	43	100	100
42	67	68	43	13	13	44	77	26
43	122	127	44	100	100	45	37	5
44	13	14	45	69	69	46	9	1
			46	119	122	47	1	0
			47	7	8			

The incorporation of the carbon isotope in the light aliphatic products was analysed from the C_3 MS response signals at $m/z = 39\text{--}47$, comprising mainly contributions from the major products propylene, *iso*- and *n*-butane, propane. Due to the argon tracer co-injection $m/z = 40$ was not used. The fragmentation patterns of the *quasi* steady state responses of ^{13}C -MeOH pulses and ^{12}C -MeOH pulses served as references (**Table 4.2**). It is assumed that upon the $^{13}\text{C}/^{12}\text{C}$ -MeOH switch the component (molar) response composition does not change, but only the isotopic composition, and that these components behave similarly with regards to fragmentation in the mass spectrometer. Then the pure component fragmentation patterns for each species are not needed for the isotopic mixture analysis, only the data of the pure ^{12}C or ^{13}C product pulses after shifting 1, 2, or 3 m/z units for the different C_3 fragments ($^{12}\text{C}_3$, $^{12}\text{C}_2\text{-}^{13}\text{C}$, $^{12}\text{C}\text{-}^{13}\text{C}_2$, $^{13}\text{C}_3$). The isotopic composition analysis of the first ^{12}C -MeOH pulse after switching from ^{13}C -MeOH was performed by the constrained parameter estimation of the linear algebra relations in Athena Visual Studio^[10] with zero values as the lower limit.

As presented in **Figure C2-3**, olefins do not exhibit the displacement response observed for aromatics. In addition, no indication for fully labeled $^{13}\text{C}_3$ species was obtained for the fragmentation patterns in the 3.75-min case, and only a tiny percentage (3 %) for the 1.25-min case. The total ^{13}C contents in C_3 MS fragments are approximately 8 at% and 33 at% for the 3.75-min and 1.25-min pulse intervals, respectively, indicating much less ^{13}C -HCP species with

increasing pulse interval. The random distribution model in both cases (3.75-min and 1.25-min pulse intervals) predicts a similar fragmentation composition as the observed (or Athena fit, **Figure 4.6**), suggesting a fast isotope scrambling process in the investigated C_{3+} species.

4.4 Discussion

Combining the product responses from the FASPA tests and the online MS analysis yields unprecedented gas phase product information for unraveling consecutive reaction steps such as aromatic displacement, HCP reactions and secondary reactions following a MeOH pulse. The subsequent statistical analysis of characteristic MS fragmentation in the $^{13}C/^{12}C$ switch experiments reveals a faster isotope scrambling process in olefin products than that in aromatics, providing direct experimental confirmation of the kinetically preferred olefin-based rather than the aromatic-based reaction mechanism, the latter via the paring route in the MTH process.

For the displacement peak of light aromatics upon the first ^{12}C -MeOH/water pulse (**Figure 4.3**), we speculate that these retarded organic species are displaced mainly by water, stemming from the fast dehydration of MeOH. The DFT-calculated adsorption energy of MeOH, water and related hydrocarbons decreases in the order MeOH ($-105 \text{ kJ/mol}^{[11]}$) > water ($-83 \text{ kJ/mol}^{[11]}$) > toluene/*p*-xylenes ($-62/-71 \text{ kJ/mol}^{[12]}$) > ethylene/propylene ($-37/-53 \text{ kJ/mol}^{[13]}$). Further evidence arises from the delayed appearance of water in the exit flow after olefins and aromatics upon a MeOH pulse (**Figure 4.4**). Clearly, water competes with olefins and aromatics occupying part of Brønsted acid sites, which makes them only accessible for MeOH and pushes out primarily formed aromatics.^[14] This also explains that co-feeding water in the MTH process allows for increasing the selectivity to olefins and prolonging the catalyst lifetime.^[14d, 15] In the case of a 100 mg catalyst bed these response products move through and interact with the rest of the catalyst bed and their wash out takes longer. Therefore, the displacement feature is almost negligible in the first ^{12}C -MeOH pulse response after switching for the 4.5 mg catalyst bed and 3.75 min pulse interval (**Figure C5(b)**). In the case of faster pulsing (1.25 min interval, 4.5 mg H-ZSM-5, **Figure C5(a)**), a displacement peak of fully labeled C_7 fragment was still detected like in the case of the 100 mg catalyst sample. Additional evidence follows from pulsing small quantities of only toluene or xylenes over a 100-mg H-ZSM-5 catalyst bed at 400 °C. The obtained residence time distribution profiles presented

in **Chapter 3** show that toluene and xylenes are still slowly desorbing from the bed after around 80 s.

Within the medium pore size H-ZSM-5 zeolite catalyst, a dual-cycle (olefin and aromatic cycle) mechanism involving the consecutive methylation/cracking of olefins and alkylation/split-off of aromatics, respectively, has been accepted to account for the production of olefins and light aromatics.^[3a] The aromatic cycle is further categorized into paring and side-chain mechanistic routes initially for a CHA-type zeolite catalyst like H-SAPO-34. In the paring mechanism^[16], the contraction of an aromatic ring generates methylated cyclopentenyl species, which then undergo cracking reactions to split off light olefins. The final step is the methylation of cyclopentenyl species followed by ring expansion (isomerization), eventually closing the cycle. In the side-chain mechanism^[17], the deprotonation of heptamethyl-benzenium ions generates a C=C double bond in the alkyl side groups on the benzene ring. The further methylation followed by the dealkylation of the alkyl side group produces ethylene, whereas a multi-methylation/dealkylation produces longer olefins. An important distinction between these two mechanisms is that in the paring route, carbon atoms from the benzene ring end up in products and not in the side-chain route.

Leaving the displacement phenomenon of aromatics out of consideration, a random distribution of ^{13}C in MS fragments of C_7 species, which relies on the assumption of the equal reactivity of ^{13}C atoms in the ^{13}C -containing HCP species (still present after the last ^{13}C -MeOH pulse) towards the newly fed ^{12}C reactant, is not observed (**Figure 4.5**). Instead, the observed C_7 MS fragment responses suggest a finite incorporation rate of ^{12}C into ^{13}C -containing aromatics next to a rapid build-up of new aromatics. This latter production of aromatics mainly stems from the direct aromatization of newly injected ^{12}C -MeOH leading to the dominant contribution of $m/z = 91$ in the first ^{12}C -MeOH pulse response, much higher than a random distribution predicts (**Figure 4.5**). A sequential temporal appearance of $m/z = 97$ to 92 (**Figure 4.5**), and $m/z = 84$ to 78 (**Figure C3**), referring to the fully labeled to fully unlabeled C_7 and C_6 fragments, respectively, indeed shows successive incorporation of ^{12}C into the present ^{13}C aromatics, ultimately replacing all ^{13}C atoms. This finding strongly suggests an operational role of the paring route in the aromatic cycle. To compare, the analysis of the ^{12}C - ^{13}C composition for C_{3+} aliphatics gave a pattern highly similar to that predicted by the random distribution model (**Figure 4.6(c)**), indicating a fast incorporation

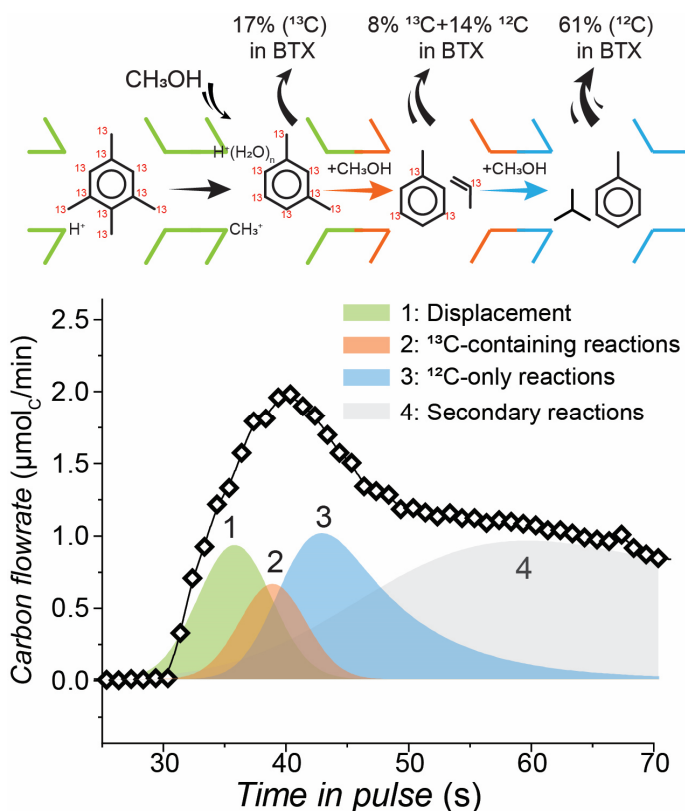


Figure 4.7. Schematic illustration of aromatic products formation processes in MTH upon ^{12}C -MeOH pulse into H-ZSM-5 with pre-built ^{13}C -HCP.

of ^{12}C into ^{13}C -containing aliphatics, which is consistent with the higher activity of the olefin cycle than the aromatic cycle.^[18]

Finally, the reactions leading to aromatic products upon MeOH pulsing to a working H-ZSM-5 zeolite catalyst in the MTH process are schematically summarized in **Figure 4.7** based on the FASPA analysis and $^{13}\text{C}/^{12}\text{C}$ switch experiments. Upon MeOH arriving at the active zone of the catalyst bed, all products are immediately formed after a rather short induction period. Water first displaces retarded aromatic HCP species still retained in the catalyst bed from the previous MeOH pulse, resulting in the first fast appearance of aromatics in the exit flow (contribution #1). In the presence of MeOH, the remaining HCP species further react with MeOH, predominantly forming aliphatics via the cracking reactions and aromatics via the paring route (contribution #2). Meanwhile, the olefinic cycle and direct aromatization of MeOH are also operative, giving the major production of new unlabeled aromatics represented by contribution #3. In

the end, the broad aromatics contribution #4 in **Figure 4.7** comprises the secondary formation of aromatics from decomposition/desorption of primary formed HCP species and retarded olefins in absence of MeOH, which has been discussed in **Chapter 3**. This fourth contribution is only observed for catalyst beds after full MeOH conversion. The relative contributions of these four processes depend on the pulse size and injection frequency relative to the catalyst amount.

4.5 Conclusions

The MTH process over zeolites offers a sustainable route for the production of important commodities such as light olefins and aromatics. Depending on the pore structure of utilized zeolites, the dominant MTH reaction path in the HCP mechanism varies and exhibits different properties. In the medium-pore H-ZSM-5 zeolite catalyst, the highly dynamic HCP species are rapidly formed and lead to the nearly instantaneous production of light olefins and aromatics upon pulsing MeOH. The unprecedented gas phase product information from the FASPA temporal product responses and online MS analysis unravels consecutive reaction steps including aromatic displacement, HCP reactions and secondary reactions following a MeOH pulse.

The retained HCP species, probably methylated benzenes, are potentially displaced by locally formed water over the hydrated Brønsted acid sites giving the fast formation of toluene, benzene and xylenes in the next MeOH pulse. After that, the faster isotope scrambling process in olefin products than that in aromatics, providing direct experimental evidence confirming the olefin-based cycle via the methylation/cracking reactions is kinetically preferred rather than aromatics-based cycle in the dual-cycle mechanism. Meanwhile, the paring instead of the side-chain mechanism explains the isotope incorporation process within aromatics suggesting it to be the dominant mechanism after the olefin-based cycle within H-ZSM-5.

References

- (1) Dahl, I. M.; Kolboe, S. *Catalysis Letters* **1993**, *20* (3), 329-336.
- (2) Olsbye, U.; Svelle, S.; Bjørgen, M.; Beato, P.; Janssens, T. V. W.; Joensen, F.; Bordiga, S.; Lillerud, K. P. *Angewandte Chemie International Edition* **2012**, *51* (24), 5810-5831.
- (3) Ilias, S.; Bhan, A. *ACS Catalysis* **2013**, *3* (1), 18-31.
- (4) Bjørgen, M.; Svelle, S.; Joensen, F.; Nerlov, J.; Kolboe, S.; Bonino, F.; Palumbo, L.; Bordiga, S.; Olsbye, U. *Journal of Catalysis* **2007**, *249* (2), 195-207.
- (5) Yarulina, I.; Chowdhury, A. D.; Meirer, F.; Weckhuysen, B. M.; Gascon, J. *Nature Catalysis* **2018**, *1* (6), 398-411.
- (6) Wang, C.; Chu, Y.; Zheng, A.; Xu, J.; Wang, Q.; Gao, P.; Qi, G.; Gong, Y.; Deng, F. *Chemistry – A European Journal* **2014**, *20* (39).
- (7) Svelle, S.; Joensen, F.; Nerlov, J.; Olsbye, U.; Lillerud, K.-P.; Kolboe, S.; Bjørgen, M. *Journal of the American Chemical Society* **2006**, *128* (46), 14770-14771.
- (8) Redekop, E. A.; Lazzarini, A.; Bordiga, S.; Olsbye, U. *Journal of Catalysis* **2020**, *385*, 300-312.
- (9) Brogaard, R. Y.; Henry, R.; Schuurman, Y.; Medford, A. J.; Moses, P. G.; Beato, P.; Svelle, S.; Nørskov, J. K.; Olsbye, U. *Journal of Catalysis* **2014**, *314*, 159-169.
- (10) Dessau, R. M.; LaPierre, R. B. *Journal of Catalysis* **1982**, *78* (1), 136-141.
- (11) Cesarini, A.; Mitchell, S.; Zichittella, G.; Agrachev, M.; Schmid, S. P.; Jeschke, G.; Pan, Z.; Bodi, A.; Hemberger, P.; Pérez-Ramírez, J. *Nature Catalysis* **2022**, *5* (7), 605-614.
- (12) Stein, S. E., *NIST/EPA/NIH Mass Spectral Library (EI)*, NIST Standard Reference Database 1A (National Institute of Standards and Technology, United States), <https://www.nist.gov/srd/nist-standard-referencedatabase-1a> (September, 2022).
- (13) Ison, A.; Gorte, R. J. *Journal of Catalysis* **1984**, *89* (1), 150-158.
- (14) Wang, S.; Chen, Y.; Wei, Z.; Qin, Z.; Ma, H.; Dong, M.; Li, J.; Fan, W.; Wang, J. *The Journal of Physical Chemistry C* **2015**, *119* (51), 28482-28498.
- (15) Fečík, M.; Plessow, P. N.; Studt, F. *ACS Catalysis* **2020**, *10* (15), 8916-8925.
- (16) *Athena Visual Studio*, Athenavisual, inc., **2022**, <https://athenavisual.com/>.
- (17) Van der Mynsbrugge, J.; Moors, S. L. C.; De Wispelaere, K.; Van Speybroeck, V. *ChemCatChem* **2014**, *6* (7), 1906-1918.
- (18) Jentys, A.; Mukti, R. R.; Tanaka, H.; Lercher, J. A. *Microporous and Mesoporous Materials* **2006**, *90* (1-3), 284-292.
- (19) Svelle, S.; Tuma, C.; Rozanska, X.; Kerber, T.; Sauer, J. *Journal of the American Chemical Society* **2009**, *131* (2), 816-825.
- (20) Marchi, A. J.; Froment, G. F. *Applied Catalysis* **1991**, *71* (1), 139-152.
- (21) Wu, X.; Anthony, R. G. *Applied Catalysis A: General* **2001**, *218* (1), 241-250.
- (22) Park, Y. K.; Baek, S. W.; Ihm, S. K. *Journal of Industrial and Engineering Chemistry* **2001**, *7* (3), 167-172.
- (23) De Wispelaere, K.; Wondergem, C. S.; Ensing, B.; Hemelsoet, K.; Meijer, E. J.; Weckhuysen, B. M.; Van Speybroeck, V.; Ruiz-Martínez, J. *ACS Catalysis* **2016**, *6* (3), 1991-2002.
- (24) Wang, H.; Hou, Y.; Sun, W.; Hu, Q.; Xiong, H.; Wang, T.; Yan, B.; Qian, W. *ACS Catalysis* **2020**, *10* (9), 5288-5298.
- (25) Sullivan, R. F.; Egan, C. J.; Langlois, G. E.; Sieg, R. P. *Journal of the American Chemical Society* **1961**, *83* (5), 1156-1160.

- (26) Mole, T.; Bett, G.; Seddon, D. *Journal of Catalysis* **1983**, *84* (2), 435-445.
- (27) Kumar, P.; Thybaut, J. W.; Svelle, S.; Olsbye, U.; Marin, G. B. *Industrial & Engineering Chemistry Research* **2013**, *52* (4), 1491-1507.
- (28) Standl, S.; Hinrichsen, O. *Catalysts* **2018**, *8* (12), 626.

APPENDIX C - Revealing main reaction paths
to olefins and aromatics in the MTH process
over H-ZSM-5

Appendix C

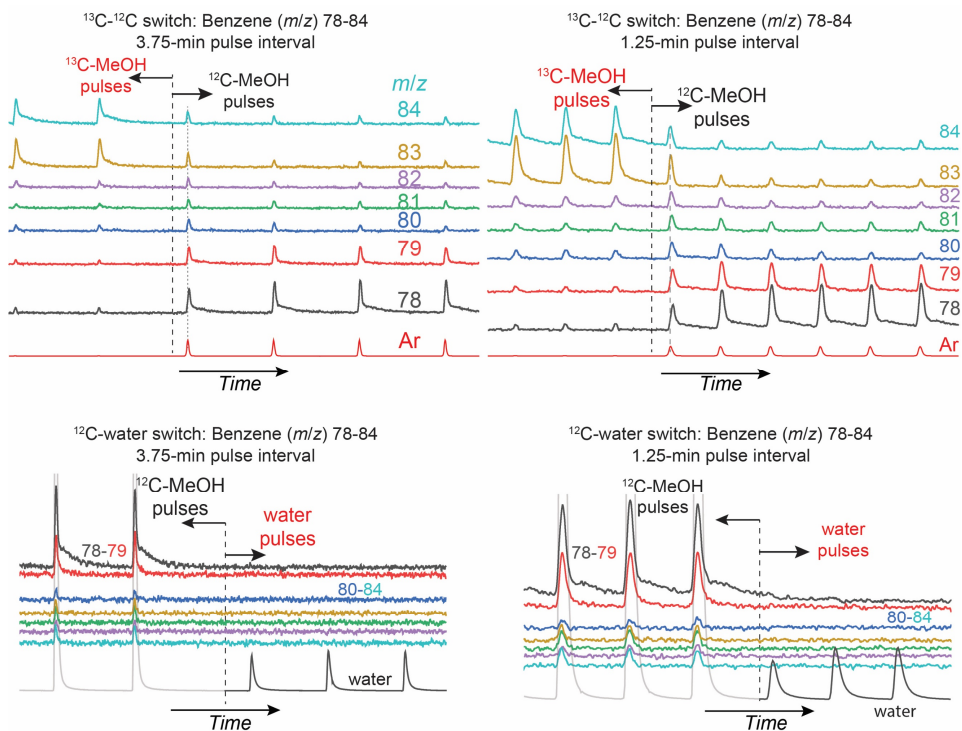


Figure C1. Comparison of raw MS responses of benzene fragments (*m/z* = 78–84) for two different MeOH pulse intervals in MeOH switch experiments at 400 °C. Pulse size used 7.6 $\mu\text{mol}/\text{pulse}$.

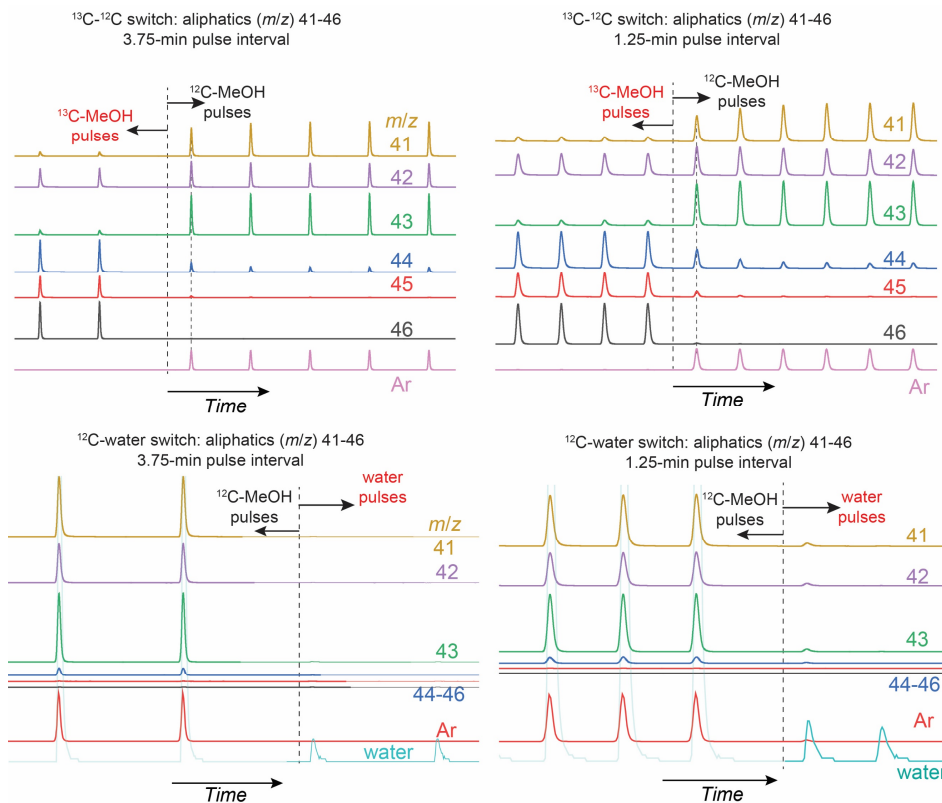


Figure C2. Comparison of raw MS responses of aliphatic fragments ($m/z = 41-46$) for two different MeOH pulse intervals in MeOH switch experiments 400 °C. Pulse size used 7.6 $\mu\text{mol}_C/\text{pulse}$.

Appendix C

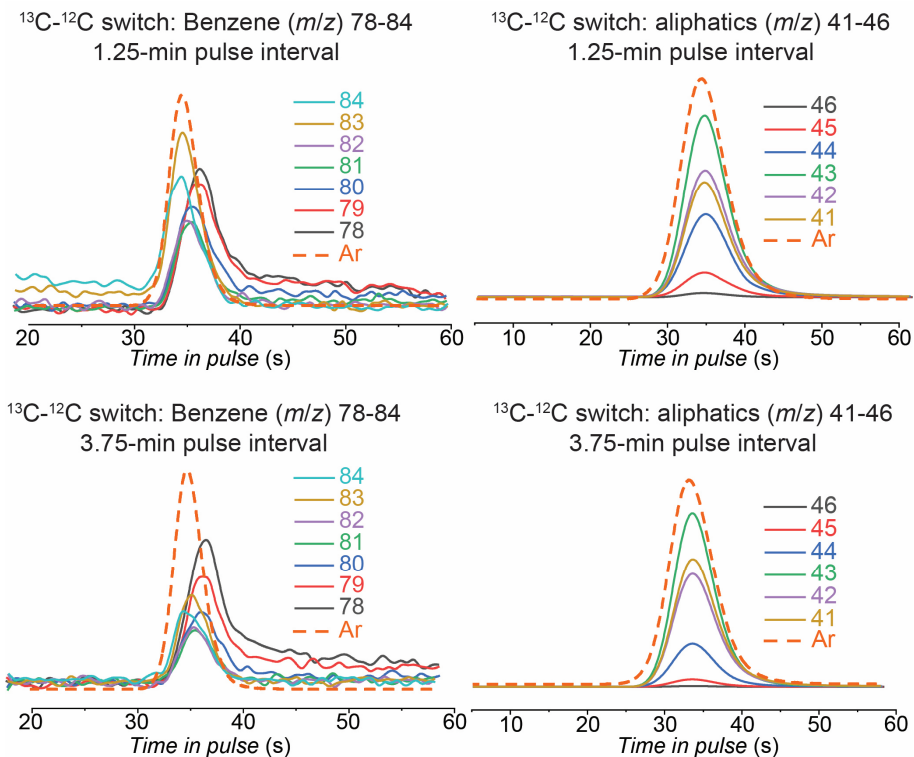


Figure C3. Raw MS responses of benzene fragments ($m/z = 78-84$) and aliphatic fragments ($m/z = 41-46$) in the first ^{12}C -MeOH pulse in MeOH switch experiments $400\text{ }^\circ\text{C}$. Pulse size used $7.6\text{ }\mu\text{mol}_\text{C}$ /pulse.

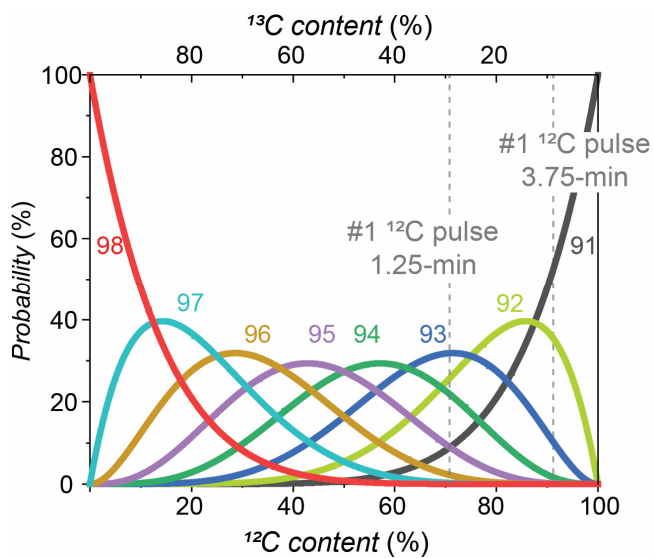
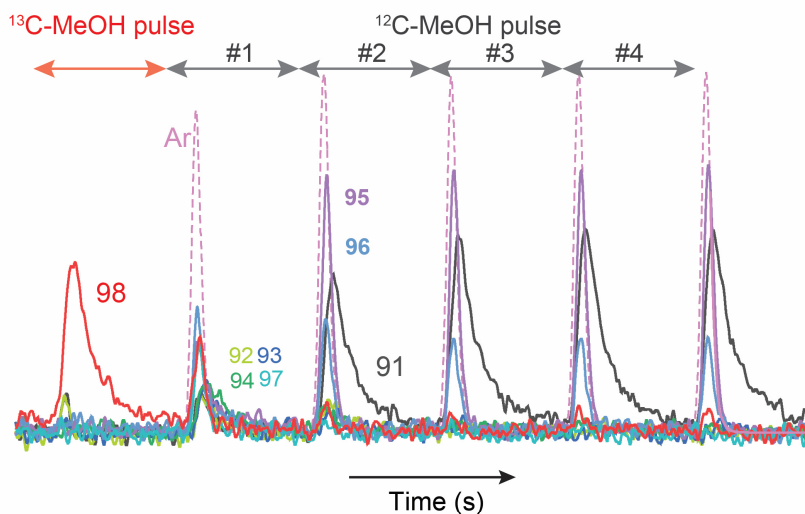


Figure C4. The random carbon distribution composition (referring to MS intensity) for $m/z = 91-98$ as function of $^{12}\text{C}/^{13}\text{C}$ content (atom%). Dashed lines refer to the estimated $^{13}\text{C}/^{12}\text{C}$ contents in the first ^{12}C -MeOH pulse with 1.25-min and 3.75-min pulse interval, respectively.

(a) 1.25-min pulse interval



(b) 3.75-min pulse interval

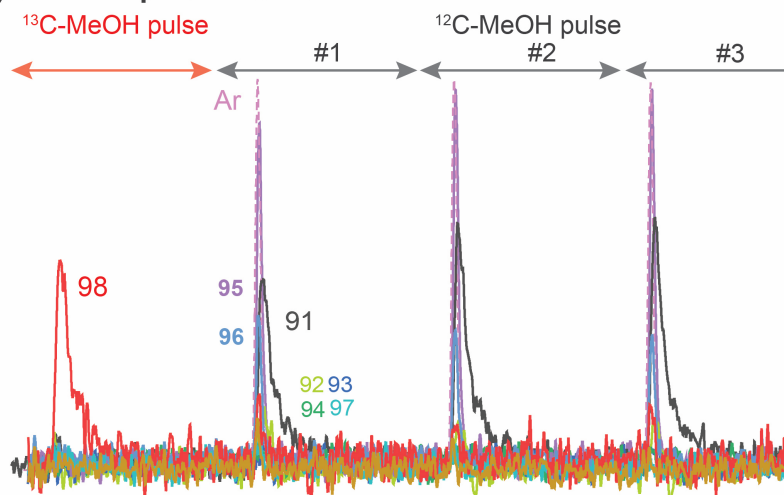


Figure C5. MS responses of $m/z = 91\text{--}98$ and 40 (Ar) in the $^{13}\text{C-MeOH} \Rightarrow ^{12}\text{C-MeOH}$ pulse switch experiment with pulse interval of 1.25 (a) and 3.75 (b) min. Conditions: Injection of either $^{12}\text{C-}$ or $^{13}\text{C-MeOH}$ in He, $7.6 \mu\text{mol}_\text{C}/\text{pulse}$, $T = 400 \text{ }^\circ\text{C}$, $m_{\text{cat}} = 4.5 \text{ mg}$ (H-ZSM-5, Si/Al = 25, $150\text{--}212 \mu\text{m}$), $P_{\text{reactor}} = 1 \text{ bar}$, carrier gas He = $20 \text{ mL}_{\text{NTP}}/\text{min}$. Note: the sharp $m/z = 95\text{--}96$ contributions are from C_{7-10} aliphatic fragments. In the 100 mg case, these contributions are absent suggesting these aliphatics are further converted specifically in the downstream region of the 100-mg catalyst bed.

Chapter 5. High stability of MTA process over bimetallic Ca,Ga-modified ZSM-5

The production of valuable aromatics and the rapid catalyst deactivation due to coking are intimately related in the zeolite-catalysed aromatization reactions. In this chapter, we demonstrate that these two processes can be decoupled by promoting Ga/H-ZSM-5 aromatization catalyst with Ca. The resulting bimetallic catalysts combine high selectivity to light aromatics with an extended catalyst lifetime in the methanol-to-aromatics process. Evaluation of catalytic performance combined with detailed catalyst characterization suggests that added Ca interacts with the Ga-LAS (Lewis acid sites), with a strong effect on the aromatization processes. A genetic algorithm approach complemented by *ab initio* thermodynamic analysis is used to elucidate possible structures of bimetallic extraframework species formed under reaction conditions. The promotion effect of minute amounts of Ca is attributed to the stabilization of the intra-zeolite extraframework gallium oxide clusters with moderated dehydrogenation activity.

Part of this chapter has been published as:

Liu, C., Uslamin, E.A., Khramenkova, E., Sireci, E., Ouwehand, L.T., Ganapathy, S., Kapteijn, F. and Pidko, E.A., *ACS catalysis*, **2022**, 12(5), pp.3189-3200.

Elena Khramenkova is acknowledged for her contribution of computational modelling in this work

5.1 Introduction

Aromatic compounds, namely benzene, toluene, ethylbenzene, *o*-/*m*-/*p*-xylenes (BTEX) are the basic platform chemicals for the production of polymers, coatings, solvents, and other functional materials.^[1-3] Currently the production of aromatics solely relies on fossil feedstocks such as the naphtha steam cracking. The methanol-to-aromatics (MTA) process is a promising route to meet an ever-increasing demand in sustainable BTEX. Methanol (MeOH) is readily available from various sources including shale gas, biomass, and CO₂.^[4-8]

MeOH conversion by zeolite catalysts proceeds via a complex network of transformations, involving the cooperation between zeolite Brønsted acid sites (BAS) and confined hydrocarbon intermediates, commonly referred to as the hydrocarbon pool.^[9-13] A dual-cycle mechanism has been proposed to describe the conversion of MeOH over H-ZSM-5 where light olefins are formed from the methylation/cracking of the longer olefins, while BTEX and ethylene originate from the alkylation/dealkylation process of methylated aromatic species.^[14]

A typical strategy to increase the selectivity to aromatics in MeOH conversion involves zeolite modification by Zn^[15-22], Ga^[23-30], Ag^[31, 32]. The aromatization process is then a result of the direct dehydrogenation reactions catalyzed by the formed Lewis acid sites (LAS). However, the increase in selectivity to aromatic intermediates accelerates the formation of the polycyclic aromatics causing catalyst deactivation.^[26, 29, 33-38] To improve catalyst stability, several approaches have been proposed. For instance, hierarchical mesoporous materials^[39] and nano-sized zeolites^[40] can be used to tune the diffusion of the reaction products from zeolite micropores. Post-synthetic modifications such as mild steaming^[41] are employed to adjust the acidic properties of the zeolite. Modifications of the entire process such as H₂ co-feeding could suppress the transformation of the active intra-zeolite species to polycyclic aromatics coke precursors.^[42] Recent studies reveal that the catalyst deactivation can be moderated by presence of Ca-LAS in the methanol-to-olefins process.^[43] However, most of the methods targeting the extended process lifetime result in a significant decrease in aromatics selectivity.

Herein we present the investigation of the catalytic properties of bimetallic [Ca,Ga]/H-ZSM-5 with improved stability and high yield of BTEX in the MTA process. The structural and acidic properties of Ca-doped Ga/H-ZSM-5 were evaluated by X-ray diffraction, N₂ physisorption, and FT-IR spectroscopic

analysis of pyridine adsorption. To figure out the mechanistic basis for the catalytic effect of Ca addition, the computational modelling was employed. A genetic algorithm approach was used to determine the structures of intra-zeolite metal clusters, followed by the *ab initio* thermodynamics analysis to assess their stability under catalytically relevant conditions. The reactivity of the most stable configurations was probed using ethane dehydrogenation as a model reaction. Transient kinetic insights in the MTA process were disclosed by employing the newly developed FASPA approach introduced in **Chapter 3-4** over the studied bimetallic [Ca,Ga]/H-ZSM-5.

5.2 Experimental Methods

5.2.1 Catalyst preparation

Protonic H-ZSM-5 (CBV5020E) with Si/Al ratio of 25 was purchased from Zeolyst Int. and denoted as H-ZSM-5. More physicochemical information can be found in **Chapter 2**. Ga-modified ZSM-5 sample was prepared *via* incipient wetness impregnation with an aqueous solution of $\text{Ga}(\text{NO}_3)_3 \cdot x\text{H}_2\text{O}$ (gallium(III) nitrate hydrate, $x = 10.6$, Sigma Aldrich, 99.9% trace metals basis). After the impregnation, the sample was first dried at 80 °C overnight and then calcined at 550 °C (ramp rate 2 °C/min) in static air for 6 h. To increase the dispersion of Ga species in the zeolite micropores, the calcined Ga/H-ZSM-5 sample was further reduced at 500 °C (2 °C/min) in a 30 vol% H_2 in Ar flow for 7 h. After that, the sample was cooled to 150 °C and re-oxidized in a flow of air for 1 h.^[37] Samples containing 1, 2 and 3 wt% Ga were prepared, denoted as Ga(x) ($x = 1, 2, \text{ or } 3$) where the value between brackets represents the weight loading of the metal. Ca(0.02) and Ca(1) samples, containing 0.02 wt% and 1 wt% Ca, respectively, were prepared *via* the same incipient wetness impregnation procedure with calcium nitrate tetrahydrate solutions, followed by calcination at 550 °C (ramp rate 2 °C/min) under static air for 6 h without the final reduction-oxidation step.

A second incipient wetness impregnation was carried out with the prepared Ga(2) to obtain the bimetallic catalyst. Aqueous solutions with different concentrations of $\text{Ca}(\text{NO}_3)_2 \cdot 4\text{H}_2\text{O}$ (calcium nitrate tetrahydrate, Sigma Aldrich, ACS reagent, 99%) were used. After impregnation, the as-prepared sample went through drying and calcination steps under the same conditions as described above. The notation is Ca(x)Ga(2) where x represents the wt% loading of Ca. To check the relevance of the addition order, one sample was prepared according to

the above procedures in which the Ca was added first and then Ga. This sample is denoted as Ga(2)Ca(0.02).

5.2.2 Catalytic tests

MTA catalytic runs were performed at 450 °C using a fixed-bed reactor setup. In a typical experiment, a 4 mm (ID) quartz reactor tube was filled with 40 mg sieved zeolite fraction (particle size 150–212 μm). MeOH was fed into the reactor through a thermostatted saturator with liquid MeOH (Sigma Aldrich, for HPLC, ≥99.9%) using N₂ as a carrier gas. The reaction products were analyzed with an online Thermo Trace GC (Trace 1300 Ultra, ThermoFisher) equipped with a thermal conductivity detector (TCD) coupled with a Poraplot Q pre-column (2 m; i.d. 0.32 mm; film thickness 20 μm) and Molsieve 5Å column (10 m; i.d. 0.32 mm) for the analysis of permanent gases, a flame ionization detector (FID) equipped with RTX-1 column (2 m; i.d. 0.32 mm; film thickness 5 μm) and Al₂O₃/KCl column (15 m; i.d. 0.32 mm; film thickness 10 μm) for the analysis of C₁ to C₄ hydrocarbons and another FID equipped with RTX-VMS column (30 m; i.d. 0.33 mm; film thickness 3 μm) for C₅₊ hydrocarbons. See **Chapter 2**.

Prior to reaction, the catalyst was activated in 50 mL/min air up to 550 °C (5 °C/min) for 1 h and then cooled down to the reaction temperature of 450 °C. The initial partial pressure of MeOH in the feed flow was set at 5.2 kPa. The corresponding *WHSV* amounted 5.3 g_{MeOH}g_{cat}⁻¹h⁻¹. The MeOH conversion (excluding DME), reaction selectivity, and yield were calculated on a carbon molar basis as follows:

$$X = \frac{(\phi_{C,MeOH_{in}} - \phi_{C,MeOH_{out}} - 2\phi_{C,DME_{out}})}{\phi_{C,MeOH_{in}}} \times 100\% \quad (5.1)$$

$$S_{Cn} = \frac{n \cdot \phi_{Cn}}{(\phi_{C,MeOH_{in}} - \phi_{C,MeOH_{out}} - 2\phi_{C,DME_{out}})} \times 100\% \quad (5.2)$$

$$Y_{Cn} = \frac{X \times S_{Cn}}{100} \% \quad (5.3)$$

where X , S_{Cn} , and Y_{Cn} represent the conversion of MeOH and dimethyl ether (DME), carbon selectivity of certain hydrocarbon products and the corresponding carbon yield in the product mixture with carbon number equal to n , respectively.

After catalytic tests, thermogravimetric analysis of the spent catalyst samples was performed on a Mettler Toledo TGA/SDTA 851e TGA analyser. 20 mg Spent catalyst was first treated at 200 °C with 20 mL/min air for 1 h to remove water and other volatile species, and then heated in the same air flow up to 800 °C at 5 °C/min while recording the sample mass.

5.2.3 Catalyst characterization

The elemental composition of each sample was assessed with inductively coupled plasma atomic emission spectrometry (ICP-AES) using a Perkin Elmer Optima 5300DV instrument (torch: Si+saffire injector). Before measurement, ca. 50 mg sample was digested in an aqueous solution of 4.5 mL 30% HCl + 1.5 mL 65% HNO₃ + 0.2 mL 40% HF using a microwave heater operating at maximal power for ca. 60 min. The resulting solutions were then diluted to 50 mL with deionized water.

The X-ray powder diffraction (XRD) patterns were obtained in Bragg-Brentano geometry with a Bruker D8 Advance X-ray diffractometer using monochromatic *Co K α* ($\lambda = 1.788970 \text{ \AA}$) radiation between $2\theta = 5^\circ$ and 55° . X-ray diffraction was measured for all catalysts after the final calcination. The patterns were analyzed by parametric Rietveld refinement^[44] using TOPAS (Topas Academic V6, Bruker AXS GmbH) to extract the unit cell parameters (orthorhombic cell; *Pnma* space group) in the MFI framework. The crystal size analysis was carried out by applying the Scherrer method:

$$D = \frac{K \times \lambda}{B \times \cos \theta} \quad (5.4)$$

where D represents the diameter of a spherical nanocrystal with $K = 0.89$, λ is the wavelength of X-ray, θ is the diffraction angle of the band at 9.1° ($hkl = 101$), and B is the corrected half width of the observed half width considering the instrumental impact.

N₂ physisorption analysis was performed to evaluate the microporous properties of each sample using Tristar II 3020 at -196 °C. Prior to measurements, samples were dried and degassed at 350 °C for 6 h under constant N₂ flow.

HAADF-STEM (high angle annular dark field-scanning transmission electron microscopy) images were acquired using a double Cs-corrected microscope (FEI cubed Titan), operated at 80–300 kV with a HAADF detector.

EDX (energy dispersive X-ray analysis) maps were obtained using the 4 detector ChemiSTEM of Thermo Fisher.

Transmission FT-IR spectroscopy of adsorbed pyridine (anhydrous, Sigma Aldrich, 99.8%) as a probe molecule was used to accomplish the acidity characterization. Sample (20 mg) was pressed into a self-supporting wafer with a diameter of 1.6 cm and then placed in an IR quartz cell. Before pyridine adsorption, the specimen was activated at 400 °C (1 °C/min) for 7 h under vacuum and then cooled down to room temperature. Pyridine vapor was dosed in the IR cell *via* a separate chamber containing pyridine with known volume and pressure. The specimen was then heated at 160 °C to allow the sufficient diffusion of the probe molecule for 1 h and then cooled down to room temperature for spectra collection. The spectra were collected using a Nicolet 6700 FT-IR (Thermo Scientific) at 2 cm⁻¹ resolution equipped with an extended KBr beam splitting and an MCT detector. The amount of BAS and LAS (Lewis acid sites) was derived from the absorbance at 1545 and 1458–1446 cm⁻¹ using the integrated molar extinction coefficients of 0.73 and 1.11, respectively.^[45] Assuming that one pyridine molecule is only adsorbed on one BAS/LAS, the following equations were used to estimate C_{BAS} and C_{LAS} :

$$C_{BAS} = 4.30 \times IA(BAS)R^2 / W \quad (5.5)$$

$$C_{LAS} = 2.83 \times IA(LAS)R^2 / W \quad (5.6)$$

where IA (BAS , LAS) represents the integrated absorbance of the band at 1545 and 1458–1446 cm⁻¹, R is the radius (cm) and W is the weight of the self-supporting sample wafer (g).

For FT-IR spectroscopy with adsorbed acetonitrile-d₃ (CD₃CN, Sigma Aldrich, ≥99.8 atom% D), the same wafer was prepared and then pretreated under the same conditions as described above. CD₃CN vapor was dosed in the IR cell. IR spectra were collected continuously at RT until saturation (CD₃CN ~2 mbar).

Solid state magic angle spinning (MAS) NMR measurements of samples were performed on a Bruker Ascend 500 magnet (11.7 T) equipped with a NEO console operating at a ¹H resonance frequency of 500 MHz, using a Bruker 3.2 mm two-channel MAS probe head. Prior to measurement, the sample was dehydrated at 400 °C (2 °C/min) in the air for 7 h and transferred to the sealed

rotor in the glovebox for spectra collection. The MAS rate was set to 8 kHz for all measurements. Single pulse one-dimensional (1D) measurements were recorded with a pulse length of 1 μ s, a recycle delay of 120 s, and 192 scans each.

For 3-methylpentane (3-MP) cracking tests, 20 mg catalyst (150–212 μ m) was pretreated at 550 °C in 50 mL/min air prior to reaction at 400 °C. 2,4-Dimethyl quinoline base was added in flow to deactivate surface acid sites.^[46] The partial pressure of 3-MP in 50 mL/min N₂ was adjusted to control the total conversion of 3-MP below 10%. Besides the formed H₂ as a side product of direct dehydrogenation over Ga-LAS, hydrogen, methane and ethane are also selectively formed through the monomolecular cracking of the pentacoordinated carbonium ion formed by the protonation of the 3-MP molecule on the BAS. Moreover, the energetically favorable bimolecular cracking (H-transfer reaction)^[47] via primary carbenium ions forms mainly only hydrocarbons beyond C₃. See also **Chapter 2.2**.

5.2.4 Computational Modeling

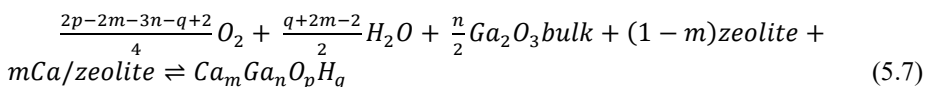
The stability and reactivity of extraframework cations in cation-modified ZSM-5 zeolites were computationally studied using the cluster modeling approach. 22T cluster models representing the different environments of the alpha-, beta-, gamma sites of ZSM-5 were constructed to accommodate the cationic ensembles. For each ZSM-5 cluster model, two Si⁴⁺ atoms were substituted with two Al³⁺ generating a negative charge in the system, which was compensated by extraframework oxygenated Ga or Ca-Ga cationic clusters. Ga/Al ratio of 1 was assumed for all models. The -OH dangling bonds were used to terminate the cluster models. Various chemical compositions of the cluster models were considered and the preferred structures were determined by using a fully automated genetic algorithm optimization strategy. The relative stabilities of the extraframework species with different stoichiometries under the catalytically relevant conditions were evaluated using the *ab initio* thermodynamic analysis.

Generic algorithm (GA) applies the principles from evolutionary biology by learning the structural features of a “good” solution throughout the operations of fitness assignment, crossover, mutation, and selection.^[48, 49] In this study, the GA was executed and controlled using the Atomic Simulation Environment (ASE) employing a semi-empirical tight-binding calculator GFN1-xTB.^[50-54] A GA developed by Vilhelmsen and Hammer was utilized.^[54] The whole zeolitic framework was kept fixed during the GA runs. The workflow of GA starts by

initializing a population consisting of 20 structures in random arrangements. The operation of selection uses an energy-based fitness function to rank the candidates and the crossover operator picks the candidates as parents for new structures generation. The mutation probability was set to a 30% rate with equal probabilities for mirror and rattle mutations. The candidates were found to be converged as the maximum energy difference, the maximum interatomic distances and the maximum difference in interatomic difference reached 0.02 eV, 0.015 Å and 0.7 Å, respectively. In each run, the maximum number of cycles given to the algorithm to converge was 120. The calculation was considered to have converged if no significant change was recorded in the last 5 generations. The structures generated within the GA runs are provided in the ESI.

The global minima obtained from the GA runs were further optimized using the PBE-D3(BJ)^[55-59] (level of theory implementing a modified version of the mixed Gaussian and plane-wave code CP2K/Quickstep^[60-64]). Using this method, the electronic charge density is calculated using plane waves, while the Kohn-Sham orbitals get extended in contracted Gaussians. A Gaussian basis set DZVP-MOLOPT-GTH basis was used^[65], and the density cutoff of 280 Ry was employed. The Goedecker-Teter-Hutter pseudopotentials^[66] with a combination of a non-periodic wavelet-based Poisson solver^[67] were employed to calculate the electron repulsion integrals. During the DFT-level optimization, only the positions of the dangling H atoms of the cluster models were kept fixed to their original positions, while the atoms of the zeolite framework and extraframework ensemble were fully relaxed.

The energies of the lowest-lying structures after the optimization at the DFT level of theory were further employed for *ab initio* thermodynamics analysis. *Ab initio* thermodynamics analysis was conducted to account for the temperature and pressure effects in the presence of water on the stability of the extraframework species. The relative energies were computed with reference to water, pure Ca-ZSM-5, H-ZSM-5 and bulk β -Ga₂O₃ structures, which are provided in the ESI. The equilibria between species were established to have the following general form for the formation of the Ca-Ga and Ga-only structures:



where the $Ca_mGa_nO_pH_q$ is the total electronic energy of one of the global minima, $(1 - m)zeolite$ is the energy of the H-form of ZSM-5 structure with two framework Al atoms, $Ca/zeolite$ is the total energy of ZSM-5 structure with two framework Al atoms compensated by an exchangeable Ca^{2+} cation. The O_2 , H_2O , Ga_2O_3bulk are the total energies of gaseous O_2 , H_2O and bulk Ga_2O_3 , respectively. The vibrational and pressure-volume contributions of solids were neglected and their Gibbs free energies are approximated as their respective electronic energies. The chemical potentials of gaseous water and oxygen species were calculated with respect to the reference state at 0K 1bar using tabulated thermodynamic tables.^[68]

The reaction Gibbs free energy $\Delta G(T, p)$ equals to:

$$\Delta G(T, p) = \Delta E - \frac{2p-2m-3n-q+2}{4}\Delta\mu_o - \frac{q+2m-2}{2}\Delta\mu_{H_2O} \quad (5.8)$$

where the reaction energy ΔE and the chemical potential of water $\mu_{H_2O}(T, p)$ at arbitrary temperature T and pressure p are defined as follows:

$$\Delta E = Ca_mGa_nO_pH_q - \frac{2p-2m-3n-q+2}{4}O_2 - \frac{q+2m-2}{2}H_2O - \frac{n}{2}Ga_2O_3bulk - (1 - m)zeolite - mCa/zeolite \quad (5.9)$$

$$\mu_{H_2O}(T, p) = E_{H_2O} + \Delta\mu_{H_2O}(T, p) \quad (5.10)$$

The expression for the chemical potential change includes the temperature- and pressure-dependent free energy contributions as follows

$$\Delta\mu_{H_2O}(T, p) = \Delta\mu_{H_2O}(T, p^0) + RT\ln\left(\frac{p_{H_2O}}{p_{H_2O}^0}\right) = H(T, p^0, H_2O) - H(0 K, p^0, H_2O) - T(S(T, p^0, H_2O) - S(0 K, p^0, H_2O)) + RT\ln\left(\frac{p_{H_2O}}{p_{H_2O}^0}\right) \quad (5.11)$$

Ethane dehydrogenation was chosen as the representative model reaction to computationally assess the dehydrogenation reactivity of the extraframework LAS. The Lewis acidic cationic clusters were stabilized within the periodic ZSM-5 model with the optimized unit cell lattice parameters of $a = 20.2 \text{ \AA}$, $b = 20.0 \text{ \AA}$, $c = 13.4 \text{ \AA}$, $\alpha = \beta = \gamma = 90^\circ$, which were kept fixed throughout the calculations. Periodic density functional theory (DFT) calculations were carried out at the PBE-D3(BJ) level of theory^[69, 70] using the Vienna Ab Initio Simulation Package

(VASP 5.3.5)^[71, 72]. The plane wave basis set with an energy cut-off of 450 eV and the projector augmented wave (PAW)^[73] method were used. Brillouin zone sampling was restricted to the Γ point. The convergence was considered to be reached when the forces acting on each atom were below 0.05 eV \AA^{-1} . The minimum reaction energy path and the transition states search were performed by employing the nudged-elastic band (CI-NEB) method.^[74] The geometry corresponding to the maximum energy structure along the reaction path was further optimized via a quasi-Newton algorithm, where only the relevant atoms of the extraframework species were relaxed. The finite difference method was used to calculate the vibrational frequencies (0.02 \AA atomic displacements). The energy barrier for the β -H elimination was disregarded on the grounds of earlier reports that indicate that this elementary step depends only slightly on the coordination environment of the Ga atom^[75] and therefore cannot give rise to the diverging dehydrogenation activity.

5.3 Results and discussion

5.3.1 Catalyst characterization

The results present in **Table 5.1** show that the elemental composition of each sample is well in line with calculations. The obtained XRD patterns shown in **Figure 5.1(a)** and unit cell parameters of bimetallic samples in **Table 5.2** confirm that main diffractions corresponding to MFI-type zeolite framework were preserved, while the crystallinity is slightly decreased for Ca,Ga-modified catalysts except for Ca(0.05)Ga(2) after metal addition and following thermal treatments (reduction, oxidation and calcination). The pore structure of each sample is assessed by N_2 physisorption tests. The results given in **Figure 5.1(b)** show that the micropore volume was slightly reduced from 0.15 to 0.14 cm^3/g , while the BET surface area decreased from ~ 420 to 379 m^2/g for H-ZSM-5 and Ga(2), respectively. Due to the small loading of Ca (0.02–0.5 wt%) on Ga(2), the changes of pore volumes and BET surface area related to Ca addition are negligible as shown in **Figure 5.1(b)**.

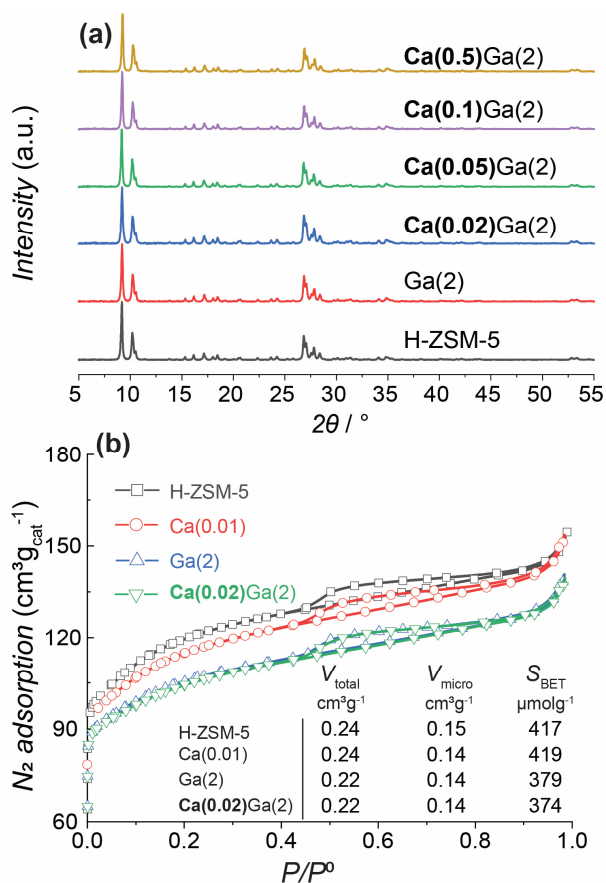


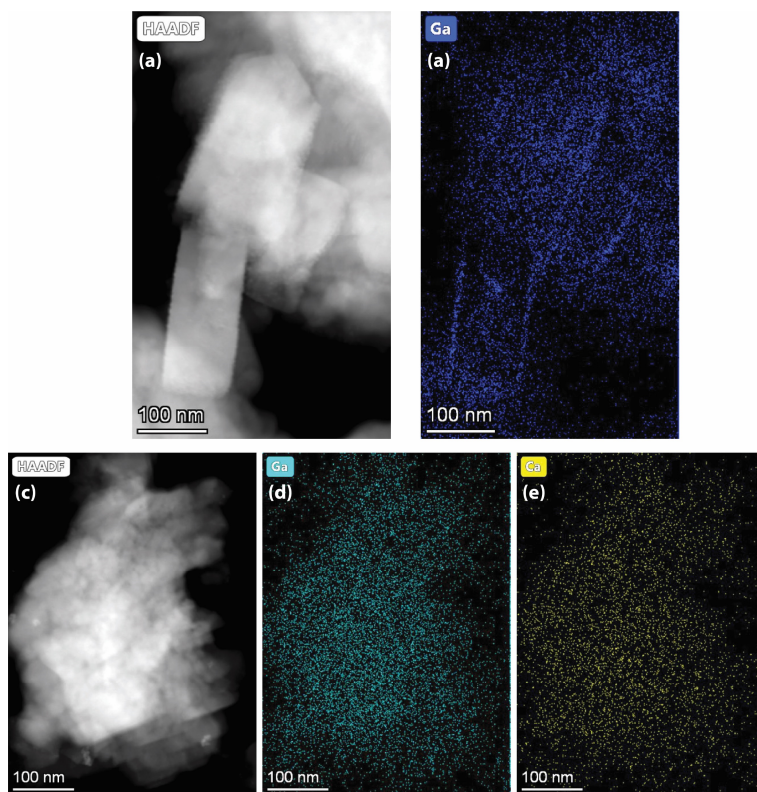
Figure 5.1. X-ray diffraction data comparing patterns for the investigated samples (a), and N_2 adsorption-desorption isotherms (b).

Table 5.1. Prepared samples with metal contents determined by ICP analysis.

	Si/Al molar ratio	Ca(wt%)	Ga(wt%)	Al(wt%)	Ca/Al molar ratio	Ga/Al molar ratio
H-ZSM-5	25	-	-	1.60	-	-
Ga(2)	25	-	2.15	1.57	-	0.530
Ca(1)	25	0.90	-	1.60	0.380	-
Ca(0.02)Ga(2)	25	0.03	2.18	1.57	0.009	0.538
Ca(0.05)Ga(2)	25	0.04	2.05	1.58	0.017	0.502
Ca(0.1)Ga(2)	25	0.07	2.22	1.60	0.030	0.537
Ca(0.5)Ga(2)	25	0.62	2.15	1.62	0.258	0.514
Ga(2)Ca(0.02)	25	0.02	2.07	1.61	0.008	0.496

Table 5.2. Unit-cell lattice parameters and crystallinity results of all catalysts under study.

	Crystallinity (%)	a (Å)	b (Å)	c (Å)	Crystal size (Å)
H-ZSM-5	97.0	20.090	19.882	13.391	644
Ga(2)	96.5	20.108	19.908	13.391	606
Ca(0.02)Ga(2)	93.2	20.094	19.905	13.393	601
Ca(0.05)Ga(2)	97.3	20.084	19.901	13.390	611
Ca(0.1)Ga(2)	92.1	20.094	19.893	13.386	638
Ca(0.5)Ga(2)	93.7	20.164	19.902	13.369	588

**Figure 5.2.** HAADF-STEM images and EDX mappings of Ga and Ca of selected samples: Ga(2) (*top*, a and b) and Ca(0.02)Ga(2) (*bottom*, c, d, and e). Scale bar: 100 nm.

Morphology and Ca,Ga maps of bimetallic catalysts are presented in **Figure 5.2**. The EDX mapping (**Figure 5.2(a, d, and e)**) indicates that both metals are quite homogeneously distributed in the as-prepared bimetallic zeolite catalysts.

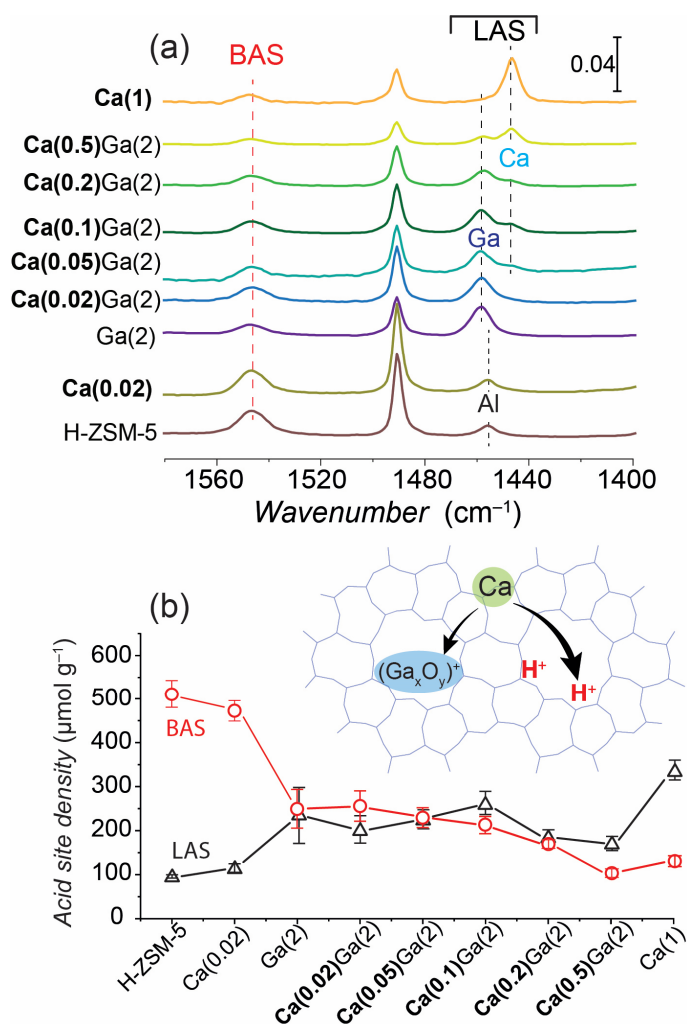


Figure 5.3. Acidity characterization of mono- and bimetallic [Ca,Ga]/H-ZSM-5 catalysts by FT-IR measurements using pyridine as probe. (a) FT-IR spectra with pyridine adsorption on zeolites with different metal loadings and (b) acid site density of BAS and LAS determined by integrating bands at 1550 cm⁻¹ and 1460–1440 cm⁻¹. The spectra with pyridine adsorption were obtained at 160 °C. Schematic illustration of Ca doping on Ga oxide species and BAS in H-ZSM-5 zeolite framework was shown in (b). Error bars represent the standard deviations of the quantitative analysis results from at least two measurements for each sample.

Figure 5.3 shows the characterization of acid sites of bimetallic catalysts obtained from FT-IR spectroscopy measurements with pyridine as probe molecule. The IR spectra feature the characteristic bands of pyridine adsorbed on BAS and LAS (**Figure 5.3(b)**). A band at 1547 cm⁻¹ observed for all catalysts

corresponds to pyridine interacting with the BAS.^[45] Pyridine interaction with LAS gives rise to bands in 1458–1446 cm^{-1} range.^[27, 76-78] The band at 1455 cm^{-1} observed for H-ZSM-5 and Ca(0.02) is assigned to the extraframework Al species.^[78, 79] At Ca loading >0.1 wt% a band at 1446 cm^{-1} appears which can be attributed to the formation of Ca-LAS at the ion-exchange sites (BAS). Ga-promoted catalysts feature a characteristic band at 1458 cm^{-1} due to the formation of Ga-LAS.^[80] Previous research reveals that these observed IR band shifts in 1458–1446 cm^{-1} range can be attributed to the formation of LAS with different strengths and therefore different adsorption energies.^[78] Therefore, the Ga-LAS featuring the FT-IR band at 1458 cm^{-1} possess the strongest acidity in comparison with extraframework Al (1455 cm^{-1}) and Ca-LAS (1446 cm^{-1}).

The quantitative analysis (**Figure 5.3(b)**) of these bands shows that the addition of 2 wt% Ga introduces ca. 150 $\mu\text{mol g}^{-1}$ of Ga-LAS at the expense of 230 $\mu\text{mol g}^{-1}$ BAS. 0.02 wt% Ca addition to the parent H-ZSM-5 shows a substantial decrease (~ 20 $\mu\text{mol g}^{-1}$) in BAS concentration. This increase in BAS concentration was confirmed via the ^1H MAS NMR (**Figure D1**). 1 wt% Ca addition significantly reduces the BAS concentration from 512 to 130 $\mu\text{mol g}^{-1}$ for H-ZSM-5 and Ca(1), respectively. This is ascribed to the high affinity of Ca to accommodate at the ion-exchange sites (BAS, **Figure 5.3(b)**), resulting in a BAS IR band of lower intensity and Ca-LAS band of higher intensity (compare Ca(1) with H-ZSM-5 in **Figure 5.3(a)**). For the same reason, the addition of larger amounts of Ca (>0.05 wt%) on Ga(2) reduces the BAS concentration while the concentration of newly formed Ca-LAS increases. Up to 0.05 wt% Ca addition no visible changes in BAS concentration for Ga(2) can be noted. However, the concentration of Ga-LAS decreases with a simultaneous Ca-LAS increase upon Ca addition (**Figure 5.3(a)**). This is interpreted as that at these conditions Ca interacts with Ga extraframework species rather than exchanges with protons of BAS (**Figure 5.3(b)**).

The additional evidence for the change of the acidity after Ca addition comes from the results of FT-IR spectroscopy measurements using CD_3CN as a probe. As shown in **Figure 5.4**, the spectrum of the parent H-ZSM-5 features the prominent band at 2300 cm^{-1} with two weak bands at 2285 cm^{-1} and 2265 cm^{-1} due to CD_3CN adsorbed on BAS, silanol (SiOH) groups, and physisorbed CD_3CN , respectively.^[81, 82] The band at 2320 cm^{-1} is attributed to Lewis acidic EFAl sites. For Ga(2), the intensity of the BAS band at 2300 cm^{-1} decreases, while two new bands at 2316 and 2326 cm^{-1} appear in the spectrum due to the formation of new

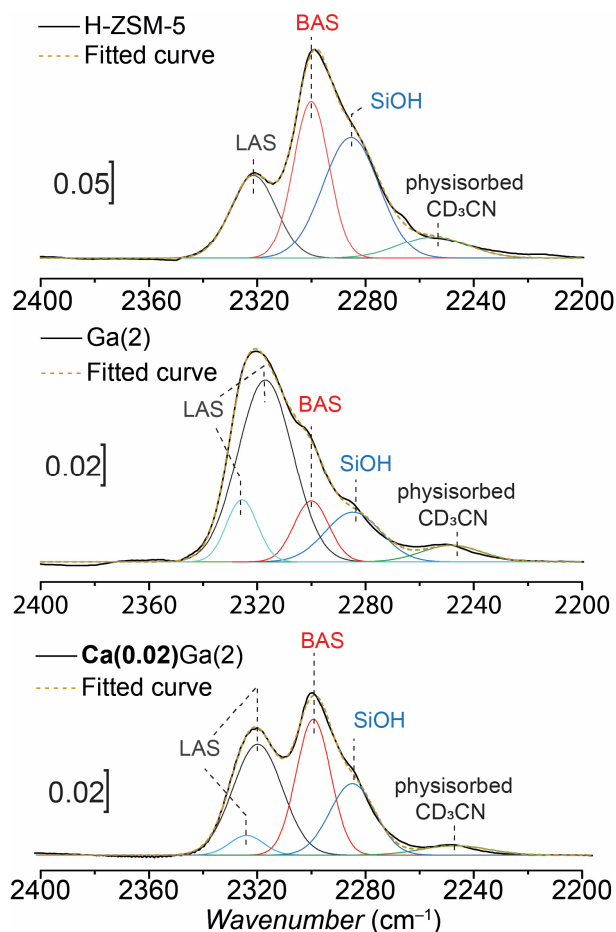


Figure 5.4. FT-IR spectra of acetonitrile- d_3 (CD_3CN) adsorbed on H-ZSM-5, Ga(2), and Ca(0.02)(Ga2). Spectra were collected at room temperature by periodically dosing a little amount of CD_3CN vapour till saturation (~ 2 mbar). The curve fitting was performed using Gaussian function.^[83]

Ga LAS sites with different strengths formed upon the exchange of the parent BAS in the zeolite. The addition of 0.02 wt% Ca gives rise to further substantial changes of the IR spectrum of adsorbed CD_3CN . The maximum of the band due to Ga-LAS shifts from 2326 to 2323 cm^{-1} and decreases in intensity (relative to BAS) suggesting the weaker Lewis acidity of the respective sites formed after the introduction of Ca.

5.3.2 MTA activity tests

Ga-modified zeolites are well-known to catalyze the dehydrogenation of various substrates such as alkanes into olefins and aromatics.^[26, 27, 37, 84, 85] Accordingly, in the MTA process MeOH is first converted to the primary hydrocarbons^[86, 87], after which the aromatization proceeds via the dehydrogenation reaction path over Ga-LAS^[27, 37, 38] with the danger of further condensation to polyaromatics, deactivating the catalyst. To test the stability of the as-prepared catalysts under industrially steady-state conditions, the MTA was carried out under the same WHSV ($5.3 \text{ g}_{\text{MeOH}}/\text{g}_{\text{cat}}\text{-h}^{-1}$) when MeOH is fully converted into primary hydrocarbons (MeOH conversion is 100%). Along with MTA reactions proceeding, MeOH conversion drops quickly after different times on stream and finally stabilizes at ca. 10 % (**Figure 5.5**). Accordingly, the cumulative product yield was calculated by integrating the carbon yield during the entire lifetime (MeOH conversion from 100% to 20%). The main results of the MTA conversion over monometallic Ga-, Ca- as well as bimetallic Ca,Ga-modified H-ZSM-5 zeolite catalysts are presented in **Figure 5.5-6**.

Catalytic tests for Ga-modified H-ZSM-5 catalysts with varying Ga loadings (**Figure 5.5**) show that the carbon yield of BTEX increased from 13% (at cumulative MeOH throughput of $5 \text{ g}_{\text{carbon}}/\text{g}_{\text{cat}}$) for parent H-ZSM-5 to 18% and then to 24% for Ga(1) and Ga(2) samples. A further increase in Ga content, however, had a rather negative effect on BTEX selectivity. This can be attributed to a previously reported agglomeration of Ga species and a decreased Ga dispersion at high Ga loadings.^[37] Therefore, Ga(2) catalyst ensured the highest BTEX selectivity and was chosen as the starting material for Ca doping.

Figure 5.6-7 summarizes the MTA results obtained for bimetallic Ca,Ga-modified H-ZSM-5 samples with 2 wt% Ga and Ca loading ranging from 0.02 to 0.5 wt%. The results indicate that upon addition of only 0.02 wt% Ca to Ga(2), the total MeOH throughput increases from 16 to $23 \text{ g}_{\text{carbon}}/\text{g}_{\text{cat}}$ for Ga(2) and Ca(0.02)Ga(2), respectively. Accordingly, the integral yield of BTEX increases from 3 to $4 \text{ g}_{\text{carbon}}/\text{g}_{\text{cat}}$ and that of light olefins increased from 8 to $12 \text{ g}_{\text{carbon}}/\text{g}_{\text{cat}}$ for Ga(2) and Ca(0.02)Ga(2) demonstrating a strong effect of low Ca loadings on the catalytic performance of Ga-modified zeolites. The lifetime extension impact gradually diminishes with a further increase in Ca loading to 0.05 and 0.1 wt%. Upon 0.5 wt% addition to Ga(2) the MeOH conversion rapidly drops, resulting in a total MeOH throughput and integral BTEX yield of only 12 and $2 \text{ g}_{\text{carbon}}/\text{g}_{\text{cat}}$, respectively. Unlike Ca,Ga-modified catalysts, Ca(1) exhibits the incomplete

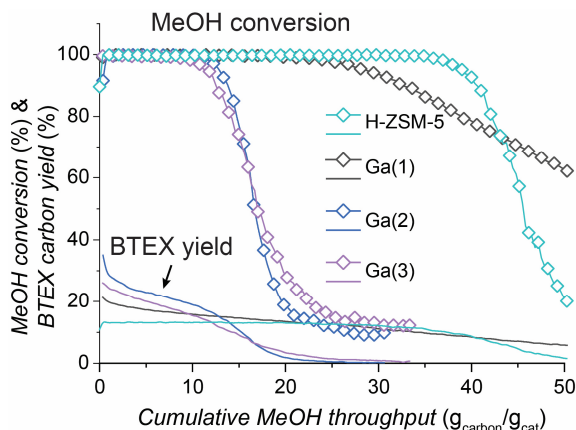


Figure 5.5. MeOH conversion and carbon yields of BTEX as a function of cumulative MeOH throughput over parent H-ZSM-5 and Ga-modified ZSM-5 catalysts. Reaction conditions: $T = 450\text{ }^{\circ}\text{C}$, $m_{\text{cat}} = 40\text{ mg}$ (150–212 μm), $P_{\text{reactor}} = 1\text{ bar}$, $WHSV = 5.3\text{ g}_{\text{MeOH}}/\text{g}_{\text{cat}}\text{-h}^{-1}$, carrier gas $\text{N}_2 = 50\text{ mL min}^{-1}$.

MeOH conversion immediately followed by a slow deactivation. As a result, the total MeOH throughput is 23 $\text{g}_{\text{carbon}}/\text{g}_{\text{cat}}$, in which more than 18 $\text{g}_{\text{carbon}}/\text{g}_{\text{cat}}$ is converted into bulky C_{5+} aliphatics. This can be attributed to the limited cracking activity of Ca(1) at a relatively low temperature of 450 $^{\circ}\text{C}$ used in this study giving rise to the accumulation of the oligomeric species in the zeolite pores and, consequently, catalyst deactivation (**Figure 5.6(b)**).^[43, 88] TGA analysis of spent catalysis after the MTA test shown in **Figure 5.8** indicates that Ga(2) demonstrates the highest coke accumulation, whereas the deactivation process is suppressed, corresponding less deposition on Ca(0.02)Ga(2).

The increased dehydrogenation over Ga-modified and bimetallic samples was further confirmed after assessing temporal product responses in FASPA tests. **Figure 5.9** demonstrates that the responses of light olefins (ethylene, propylene and butylenes) and C_{5+} aliphatics over Ga(2) and Ca(0.02-0.05)Ga(2) catalysts clearly shift towards a longer response time, while their amounts are noticeably lower than those of parent H-ZSM-5. This longer response time indicates a longer characteristic reaction time (**Chapter 3**, Appendix B). As a result, the selectivity to aromatics (BTX and TriMB) increases from 22 to 77 C% for H-ZSM-5 and Ga-modified catalysts (**Table 5.3**), showing an even more significant impact of the Ga modification than from the steady-state tests (**Figure 5.5**).

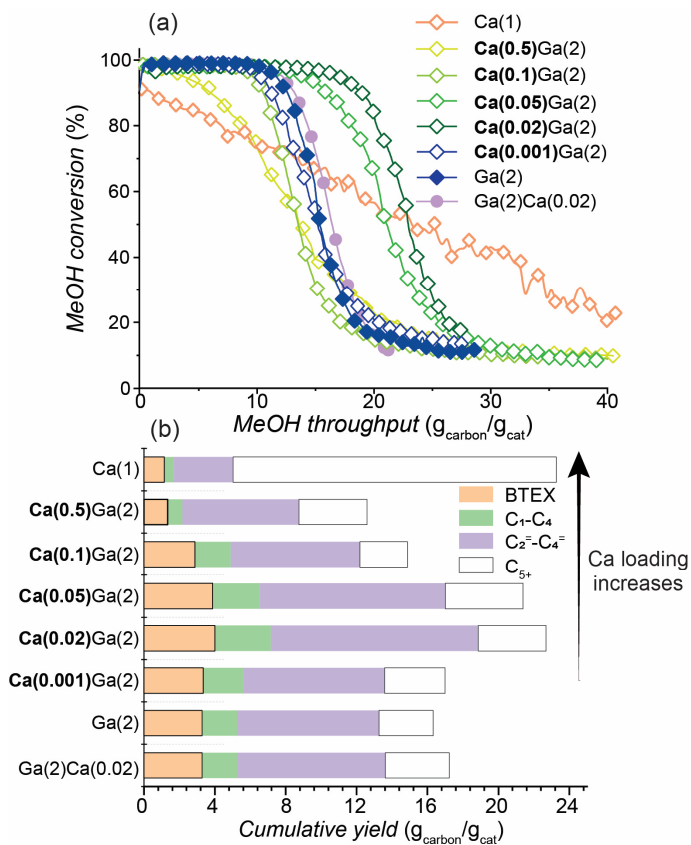


Figure 5.6. Summary of the catalytic results of MTA over Ca,Ga-modified catalysts: (a) MeOH conversion as a function of MeOH conversion per gram of catalyst; (b) Integral yields of the main groups of MTA products before MeOH conversion drops below 20%. MTA reaction conditions: $T = 450\text{ }^{\circ}\text{C}$, $m_{\text{cat}} = 40\text{ mg}$ (150–212 μm), $P_{\text{reactor}} = 1\text{ bar}$, $WHSV = 5.3\text{ g}_{\text{MeOH}}\text{g}_{\text{cat}}^{-1}\text{h}^{-1}$, carrier gas $\text{N}_2 = 50\text{ mL min}^{-1}$. C₅⁺: aliphatics with the carbon number higher than 4; C₁-C₄: C₁ to C₄ alkanes; C₂⁼-C₄⁼: C₂ to C₄ olefins.

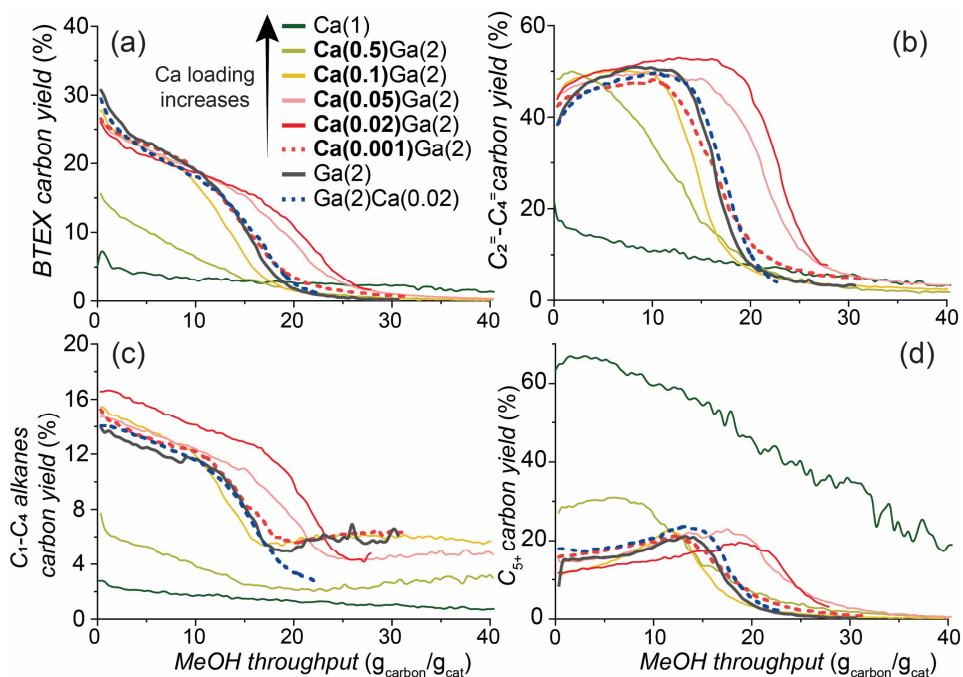


Figure 5.7. Carbon yields of MTA products (BTEX, C_1 - C_4 , C_2^- - C_4^- and others) as a function of cumulative MeOH throughput over Ga,Ca-modified ZSM-5 catalysts. Reaction conditions: $T = 450\text{ }^\circ\text{C}$, $m_{\text{cat}} = 40\text{ mg}$ (150–212 μm), $P_{\text{reactor}} = 1\text{ bar}$, $WHSV = 5.3\text{ g}_{\text{MeOH}}/\text{g}_{\text{cat}}\text{-h}^{-1}$, carrier gas $\text{N}_2 = 50\text{ mL min}^{-1}$.

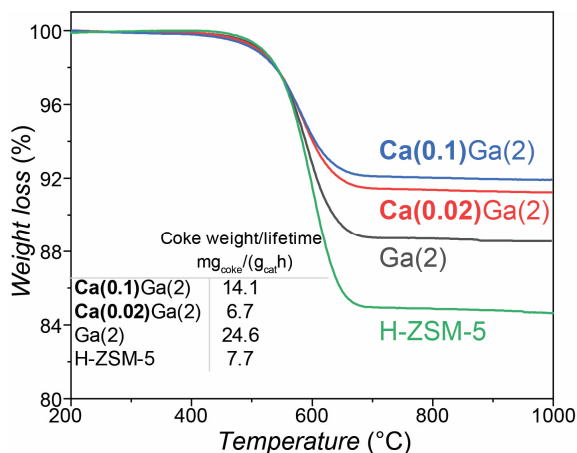


Figure 5.8. TGA analysis in air of spent catalysts obtained after MTA tests. The total coke weight divided by lifetime (defined by TOS until MeOH conversion below 95%).

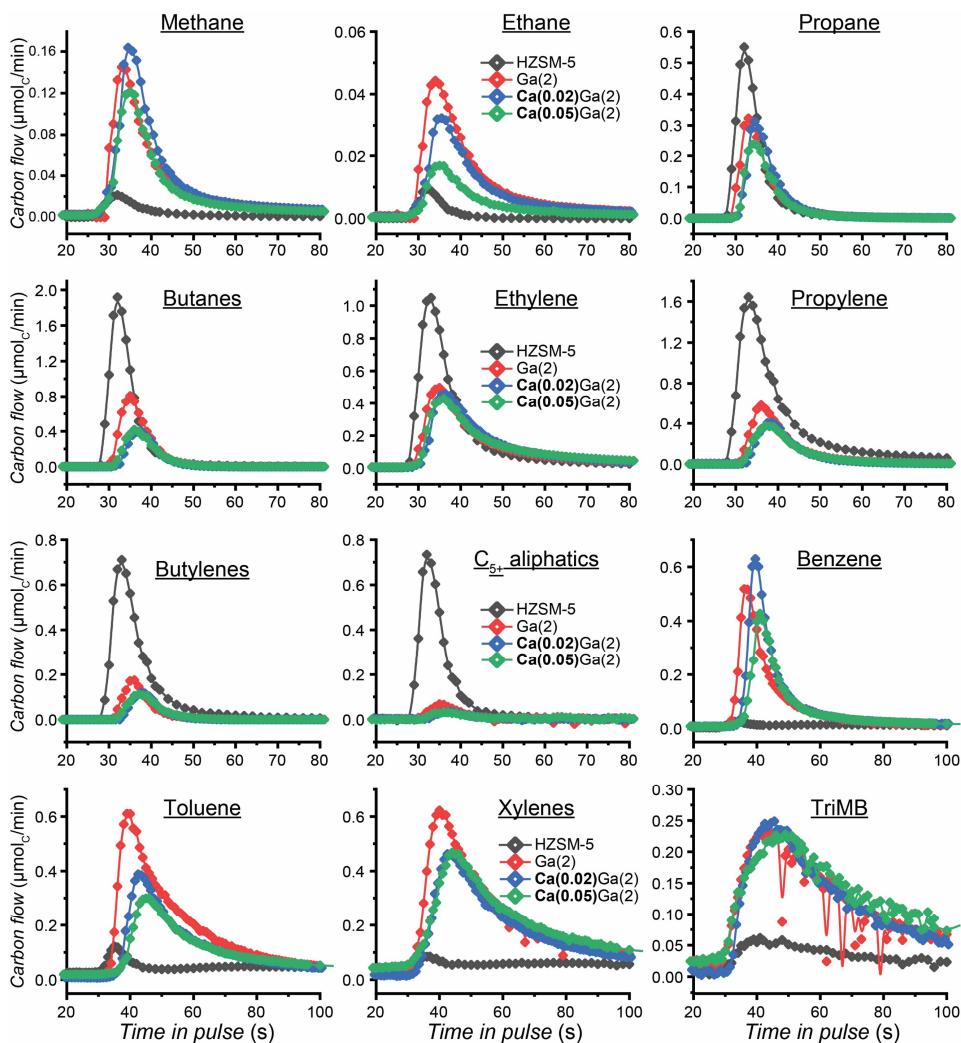


Figure 5.9. Comparison of hydrocarbons responses upon pulsing MeOH over parent H-ZSM-5, Ga(2), Ca(0.02)Ga(2), and Ca(0.05)Ga(2) at 400 °C. Conditions: catalyst pellet size = 150–212 μm , catalyst loading = 100 mg, $P_{\text{reactor}} = 1$ bar, MeOH pulse quantity = 1.2 μmol_C per pulse, carrier gas He = 20 mL_{NTP}/min, pulse interval = 3.75 min. Response profiles were time-shifted based on the Ar responses using 100-mg H-ZSM-5 sample as reference.

Table 5.3. The product selectivity and statistical moment analysis for MeOH pulse responses over parent H-ZSM-5, Ga(2), Ca(0.02)Ga(2), and Ca(0.05)Ga(2) at 400 °C.

Carbon selectivity in pulse, C%									
Catalyst	Ethylene	Propylene	Butylenes	Methane	Ethane	Propane	Butanes	C5-C6	TriMB
H-ZSM-5*	17.80%	31.20%	10.50%	0.40%	0.10%	6.50%	21.90%	9.70%	7.90%
Ga(2)	12.60%	10.80%	2.30%	2.70%	1.00%	4.70%	11.50%	1.00%	14.70%
Ca(0.02)Ga(2)	14.70%	9.30%	2.00%	3.40%	0.80%	5.10%	7.00%	0.70%	21.70%
Ca(0.05)Ga(2)	14.80%	10.20%	2.30%	2.70%	0.50%	4.40%	8.20%	0.70%	24.30%
Carbon selectivity in pulse, C%									
Catalyst	Benzene R1	Toluene R1	Xylenes R1	Benzene R2	Toluene R2	Xylenes R2			
H-ZSM-5	0.30%	1.30%	1.30%	1.60%	3.40%	7.10%			
Ga(2)	9.60%	22.70%	27.30%	-	-	-			
Ca(0.02)Ga(2)	11.30%	17.00%	27.90%	-	-	-			
Ca(0.05)Ga(2)	9.00%	14.80%	29.20%	-	-	-			
μ_0 , μmolc									
Catalyst	Ethylene	Propylene	Butylenes	Methane	Ethane	Propane	Butanes	C5+	TriMB
H-ZSM-5	0.172	0.301	0.101	0.004	0.001	0.063	0.211	0.094	0.076
Ga(2)	0.114	0.098	0.021	0.025	0.009	0.043	0.104	0.009	0.134
Ca(0.02)Ga(2)	0.115	0.073	0.016	0.026	0.007	0.04	0.055	0.005	0.169
Ca(0.05)Ga(2)	0.109	0.076	0.017	0.02	0.003	0.033	0.061	0.005	0.18
C balance									
Catalyst	Benzene R1	Toluene R1	Xylenes R1	Benzene R2	Toluene R2	Xylenes R2	Cout/Cin		
H-ZSM-5	0.003	0.013	0.012	0.015	0.033	0.069	0.965		
Ga(2)	0.087	0.207	0.249	-	-	-	0.91		
Ca(0.02)Ga(2)	0.089	0.133	0.218	-	-	-	0.781**		
Ca(0.05)Ga(2)	0.067	0.11	0.217	-	-	-	0.741**		
μ_1 , s									
Catalyst	Ethylene	Propylene	Butylenes	Methane	Ethane	Propane	Butanes	C5-C6	TriMB
H-ZSM-5	36.2	38.3	35.9	36.5	34	33.8	33.8	34.3	72.5
Ga(2)	42.3	40.2	37.4	38.3	40.2	36	37	37	65
Ca(0.02)Ga(2)	44.9	41.6	39.3	38.8	41.6	37.5	38.7	39.6	69.6
Ca(0.05)Ga(2)	45.1	41.7	39.2	38.5	41.1	37.2	38.5	39.9	77.7
Ar Reference									
Catalyst	Benzene R1	Toluene R1	Xylenes R1	Benzene R2	Toluene R2	Xylenes R2			
H-ZSM-5	36.8	37.9	42.2				33.1		
Ga(2)	41.9	54.3	56.9	-	-	-	33.1		
Ca(0.02)Ga(2)	43.1	57.3	62.7	-	-	-	33.1		
Ca(0.05)Ga(2)	45.1	59.8	63.2	-	-	-	33.1		

*: H-ZSM-5 sample used in the FASPA test is received from BASF, which contains similar physicochemical properties as the one used for metal modifications and MTA tests as shown in other results in this chapter. Detailed characterization results of these two H-ZSM-5 materials can be found in **Chapter 2**.

***: For unknown reasons, the carbon balance for bimetallic samples in the FASPA tests is incomplete.

The R2 component, referring to the second retarded BTX peak as present over H-ZSM-5 in **Figure 5.5**, is almost disappeared or convoluted with R1 near 40 s for Ga(2) and Ca(0.02–0.05)Ga(2). According to the extensive FASPA analysis in **Chapter 3**, the second formation peak (R2) of BTX is ascribed to secondary processes, namely olefin aromatization and aromatics alkylation/dealkylation occurring after MeOH depletion in the downstream region of the H-ZSM-5 bed. Accordingly, the changes in olefin and aromatic responses upon Ga and bimetallic Ca,Ga modification on H-ZSM-5 are attributed to the enhanced secondary reactions over Ga-LAS, ultimately leading to a shorter residence time of BTX (compared to the first moment of R2 of BTX over H-ZSM-5 in **Table 5.3**) in the bed and therefore a greater aromatization rate. Due to the incomplete carbon balance in the FASPA results over Ca(0.02–0.05)Ga(2), the impact of Ca on the product responses in the FASPA tests is not quantified.

To ensure that the observed changes in MTA performance are not related to the preparation procedure of bimetallic samples, a Ga(2) catalyst containing trace amounts of Ca (~0.001%) was prepared, following the same procedure. For this sample, no changes in performance as compared to pure Ga(2) catalyst were observed (**Figure 5.6**). Moreover, the same reaction performance was also observed for Ga(2)Ca(0.02), the sample prepared following a similar protocol but with metals addition in reversed order.

To further elucidate the catalytic impact of 0.02 wt% of Ca on Ga(2) in the MeOH aromatization process, hydrogen formation is used as a descriptor of dehydrogenation reaction (**Figure 5.10(a)**).^[27] As shown in **Figure 5.10(b)**, during MTA tests a negligible amount of hydrogen is formed over the parent H-ZSM-5. In turn, the lower hydrogen formation is observed for Ca(0.02)Ga(2) compared to Ga(2) suggesting the direct dehydrogenation is suppressed in the presence of Ca. Combining all these results we propose that the increased MeOH throughput and BTEX production over Ca(0.02)Ga(2) are related to the small amount of Ca affecting the intra-zeolite Ga species and their (Lewis) acidic properties, moderating the dehydrogenation activity.

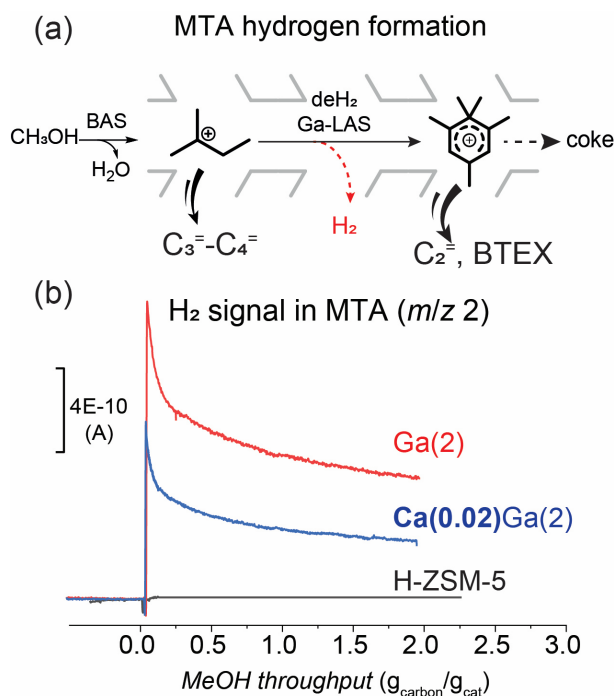


Figure 5.10. Schematic illustration of MeOH aromatization with hydrogen formation over Ga-LAS (a) and hydrogen formation along MeOH throughput at the initial stage of MTA tests over parent H-ZSM-5 and Ca,Ga-modified catalysts (b).

We have carried out the additional characterization of selected catalysts using the 3-MP cracking as the probe (**Figure 5.11**). Compared to H-ZSM-5, 3-MP cracking conversion and H₂ formation simultaneously increase over Ga modified catalysts evidencing the promoted dehydrogenation over Ga-LAS (top route in **Figure 5.11(a)**). Upon 0.02-0.5 wt% Ca addition to Ga(2), the selectivity to methane and ethane significantly decreases indicating the suppression of the monomolecular cracking (mid route in **Figure 5.11(b)**). Simultaneously, the H₂ formation also decreases slightly in line with the proposed moderated dehydrogenation activity of Ca(0.02)Ga(2). The higher 3-MP conversion over Ca(0.02)Ga(2) than over Ga(2) is therefore attributed to the increased rate of the bimolecular cracking, via H-transfer reactions (bottom route in **Figure 5.11(a)**). At 0.5 wt% of Ca loading, the formation of methane, ethane and H₂ is suppressed suggesting the prevalence of the bimolecular cracking path. These results point to the higher rate of the H-transfer reactions over Ca(0.02)Ga(2) due to the moderated dehydrogenation activity. Increased Ca loading, however, reduces the

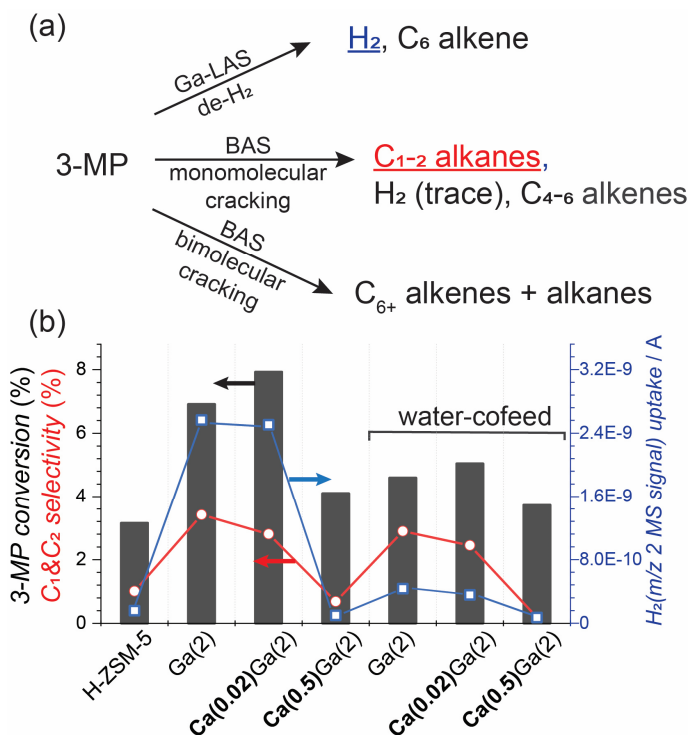


Figure 5.11. Reaction mechanisms of 3-methylpentane (3-MP) cracking over Ga modified catalysts (a); 3-MP cracking conversion and light cracking products over parent H-ZSM-5 and Ca,Ga-modified catalysts (b). 3-MP cracking conditions: $T = 400$ °C, $m_{\text{cat}} = 20$ mg (150–212 μm), 1 bar, carrier gas $\text{N}_2 = 50$ mL/min, 3-MP partial pressure = 3.8 kPa in the presence of 2,4-dimethylquinoline (<0.1 kPa) to prevent the cracking over BAS at the external catalyst surface^[89], $P_{\text{H}_2\text{O}} = 0.6$ kPa. The conversion and product selectivity are averaged values within $\text{TOS} = 0.1\text{--}0.4$ h.

rates of cracking and dehydrogenation caused by BAS exchanged by Ca. In the presence of water, both 3-MP conversion and H_2 formation decrease over selected catalysts implying the decreasing dehydrogenation activity with the degree of hydration of the Ca,Ga clusters.

Overall, the bimetallic Ca(0.02)Ga(2) catalyst demonstrates improved stability and increased yield of BTEX in MTA in comparison with Ga(2). On the contrary, the catalysts in which Ca loadings are higher than 0.05 wt% show decreased stability because Ca exchanges with protons of BAS forming Ca-LAS.^[43] For Ca(1), the incomplete MeOH conversion followed by a slow deactivation is observed. Following the previous investigations in the group, the presence of Ca-LAS next to BAS decreases the stability and growth rate of

aromatic hydrocarbon pool intermediates^[43, 90], which also explains the highest yield of C₅₊ over Ca(1) (**Figure 5.6(b)**). At 450 °C which is below the reported >500 °C for Ca modified ZSM-5 in MTO in refs^[43, 90], the cracking of these C₅₊ aliphatics is also limited over the remaining BAS in Ca(1) eventually causing the gradual deactivation.

On the basis of these data at small loadings (Ca <0.05 wt%), we propose that Ca first interacts with extraframework Ga species and the synergy of Ca and Ga moderates the dehydrogenation rate. This leads to the lower hydrogen formation and eventually reduces the deactivation rate in MTA. At higher Ca loadings (>0.05 wt%) on Ga(2), the dehydrogenation-aromatization rate is further suppressed. However, more Ca inevitably interact with BAS forming Ca-LAS (**Figure 5.3(b-c)**). Newly formed Ca-LAS force the MeOH transformations into C₅₊ aliphatics rather than olefins (cracking) or BTEX (dehydrogenation) causing the fast deactivation of Ca(1) or Ca(0.5)Ga(2) as presented in **Figure 5.6** and **Figure 5.7**. Note that the catalyst preparation approach employed in this study cannot decouple the formation of CaGa binuclear species and Ca exchanging with protons of BAS. Our data suggest that when targeting higher Ca loadings, the latter process becomes dominant resulting in the replacement of BAS with exchangeable Ca²⁺ ions and, accordingly, the overall deterioration of the catalyst performance.

5.3.3 Computational results

In an attempt to provide a molecular proposal for the observed reactivity changes upon Ca modification of Ga/H-ZSM-5, model DFT calculations were carried out. Following the hypothesis on Ca-mediated reactivity changes in extraframework Ga sites, a fully automated analysis of the interaction modes^[51] between Ca²⁺ and representative binuclear Ga₂O_xH_y moiety was carried out. The calculations were expanded into the *operando* regime through the *ab initio* thermodynamics (aiTD) analysis to find out the extraframework complexes potentially formed under the MTA conditions.^[91]

Following on earlier works on Ga-modified H-ZSM-5 materials, we have considered the model of the active site consisting of a binuclear Ga cluster stabilized by two negatively charged aluminum, incorporated in the MFI framework with a different environment such as alpha-, beta-, gamma sites.^[92-94] The alpha- and beta- sites are the 6-membered rings along the straight channel, whereas the gamma site is the 8-membered ring on the wall of the sinusoidal

channel.^[95] The effect of Ca addition was studied by introducing one Ca^{2+} cation. The overall charge neutrality of the pure Ga or CaGa bimetallic species was achieved by introducing the O^{2-} and OH^- ligands, whose quantity varied to represent different water content. This resulted in the structures containing a water content of 0–5 H_2O molecules, giving 6 stoichiometries for pure Ga and 6 for CaGa structures.

To find the global minima structures corresponding to these stoichiometries, a genetic algorithm optimization process was carried out, with the electronic structure evaluation calculated by an accelerated xTB semi-empirical method.^[50, 54] As the exhaustive computational search of the 96 T periodic atom-system is currently prohibitively demanding, the cluster models representing the Ga pure and CaGa bimetallic active sites confined in the sites of the ZSM-5 was utilized.^[51] The outcome of each genetic algorithm procedure was 20 lowest-lying configurations of the corresponding stoichiometry, with indicated structural diversity, whose geometries were further refined at PBE-D3(BJ) level of theory with Gaussian DZVP-MOLOPT-GTH basis set as implemented in CP2K 6.1.^[55, 56, 58, 60-66] The stability of the lowest high-level refined structures of each stoichiometry was further assessed at experimentally relevant conditions employing aiTD (eq. 5.7-5.11).^[96] The cluster models of the global minima for all stoichiometries are shown in **Figure D2-5**.

The optimized geometries of the most stable pure Ga and bimetallic CaGa configurations within each stoichiometry and their relative stabilities as a function of reaction conditions expressed water chemical potential $\mu(\text{H}_2\text{O})$, are shown in **Figure 5.12**. The comparison of the optimized geometries reveals that at all hydration levels Ga ions in both Ga pure and Ga,Ca extraframework clusters tend to adapt a distorted tetrahedral coordination environment. The only observed exception is the trigonal bipyramide coordination formed around one of the gallium centers in the $\text{Ga}_2\text{O}_2(\text{H}_2\text{O})_4^{2+}$ model (**Figure D3**). The coordination of the Ca ions in the bimetallic clusters depends more strongly on the water content. In the presence of 1 or 2 water molecules (**Figure D4**), the coordination of the Ca^{2+} center in the Ga,Ca clusters is best described as the square pyramidal, whereas at a higher solvation level (with 3, 4 or 5 added H_2O molecules), distorted pentagonal bipyramidal or octahedral coordinations of the Ca centres are realized in the extraframework clusters (**Figure D4(d)**, **Figure D5(a, d)**).

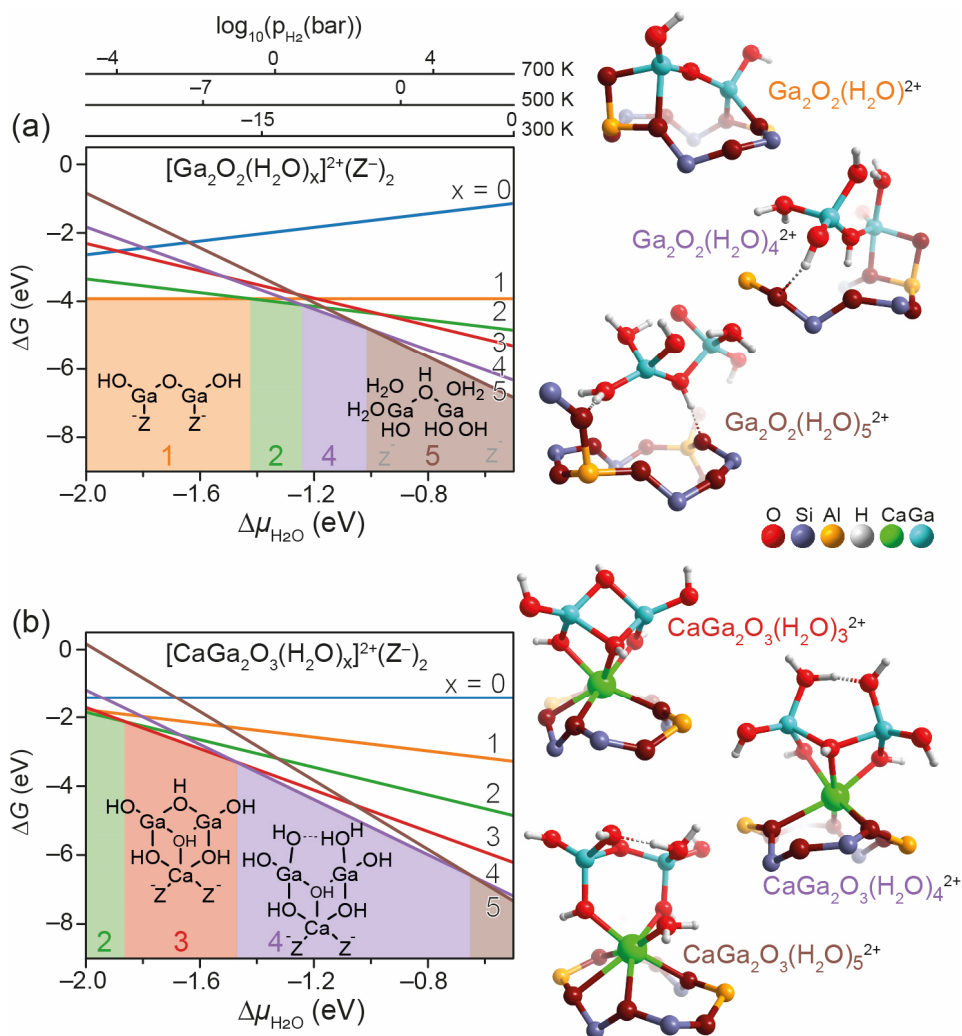


Figure 5.12. Stability and geometries of cationic extraframework species in ZSM-5 zeolite with different water contents (up to five water molecules). **(a)** The aiTD analysis on the pure Ga complexes. The geometries of the most stable configurations amongst the following stoichiometries: $\text{Ga}_2\text{O}_2(\text{H}_2\text{O})_2^{2+}$, $\text{Ga}_2\text{O}_2(\text{H}_2\text{O})_4^{2+}$, $\text{Ga}_2\text{O}_2(\text{H}_2\text{O})_5^{2+}$ are displayed. The geometry of the $\text{Ga}_2\text{O}_2(\text{H}_2\text{O})_5^{2+}$ illustrates the detaching from the framework. **(b)** The aiTD analysis on the bimetallic CaGa complexes. The geometries of the most stable configurations amongst the following stoichiometries: $\text{CaGa}_2\text{O}_3(\text{H}_2\text{O})_3^{2+}$, $\text{CaGa}_2\text{O}_3(\text{H}_2\text{O})_4^{2+}$, $\text{CaGa}_2\text{O}_3(\text{H}_2\text{O})_5^{2+}$ are displayed.

Accordingly, at the low values of the water chemical potential ($-2.0 \text{ eV} < \Delta\mu < -1.2 \text{ eV}$), pure Ga-oxo species tend to coordinate one or two water molecules, whereas bimetallic CaGa species favor the hydration with up to 4

water molecules. At intermediate and high values of $\Delta\mu$ (> -1.2 eV), pure Ga species can coexist with configurations having the various degrees of hydration ($\Delta\mu \sim -1$ eV) and eventually get hydrolysed ($\Delta\mu > -1$ eV). At high water chemical potential, the coordination of 5 water molecules to the pure Ga species leads to the hydrolysis of Si-O-Ga bonds resulting in the detachment of the species from the framework, as in structure $\text{Ga}_2\text{O}_2(\text{H}_2\text{O})_5^{2+}$ in **Figure 5.12(a)**. However, the bimetallic cations remain effectively attached to the cation site at all $\Delta\mu$ through coordinating Ca to the framework Al sites. This effect is illustrated with the most stable bimetallic $\text{CaGa}_2\text{O}_3(\text{H}_2\text{O})_4^{2+}$ and $\text{CaGa}_2\text{O}_3(\text{H}_2\text{O})_5^{2+}$ configurations (**Figure 5.12(b)**) suggesting that Ca acts as an anchor, preventing the highly hydrated extraframework species from washing away from the cation site and agglomerate. The aiTD diagrams indicate that Ca addition stabilizes the bimetallic species with a higher degree of hydration (containing more water molecules) rather than pure Ga configurations at the same conditions.

Furthermore, the dehydrogenation activity of the pure Ga and CaGa complexes, stabilized at intermediate water chemical potentials (mimicking the MTA conditions), was assessed by using ethane dehydrogenation as a model test reaction.^[75, 93, 97-99] Specifically, the reactivity of $\text{Ga}_2\text{O}_2(\text{H}_2\text{O})^{2+}$, $\text{Ga}_2\text{O}_2(\text{H}_2\text{O})_2^{2+}$ and their Ca-containing counterparts $\text{CaGa}_2\text{O}_3(\text{H}_2\text{O})_2^{2+}$, $\text{CaGa}_2\text{O}_3(\text{H}_2\text{O})_4^{2+}$ were computationally assessed. Ethane dehydrogenation proceeds via the following elementary steps, namely, the heterolytic C-H-bond cleavage, β -elimination, and H_2 recombination (**Figure 5.13-14**). The reaction energies and activation barriers of the respective steps are summarized in **Table 5.4**.

DFT calculations indicate that the Lewis acidity and the dehydrogenation activity of the intrazeolite clusters decrease with the increasing hydration levels, which are more favored for the bimetallic Ca,Ga clusters (**Figure 5.13-14**). Under the conditions relevant for the MTA reaction ($\Delta\mu_{\text{H}_2\text{O}} > -1.2$ eV), the dominant bimetallic $\text{CaGa}_2\text{O}_3(\text{H}_2\text{O})_4^{2+}$ cluster exhibits computed barriers for the C-H activation and H_2 recombination that are 32 and 10 kJ/mol, respectively, higher compared to its Ga-only counterpart $\text{Ga}_2\text{O}_2(\text{H}_2\text{O})_2^{2+}$. The current reactivity assessment specifically focused on the impact of the change of the properties of the Lewis acidic Ga center on the dehydrogenation activity. We anticipate that similar to other intrazeolite active complexes, the reactivity of the Ga-containing multinuclear clusters depends on a wide variety of secondary effects such as the presence of multiple reaction channels^[100], active site dynamics^[101] and the variation of the local zeolite environment^[102]. The detailed investigation of these

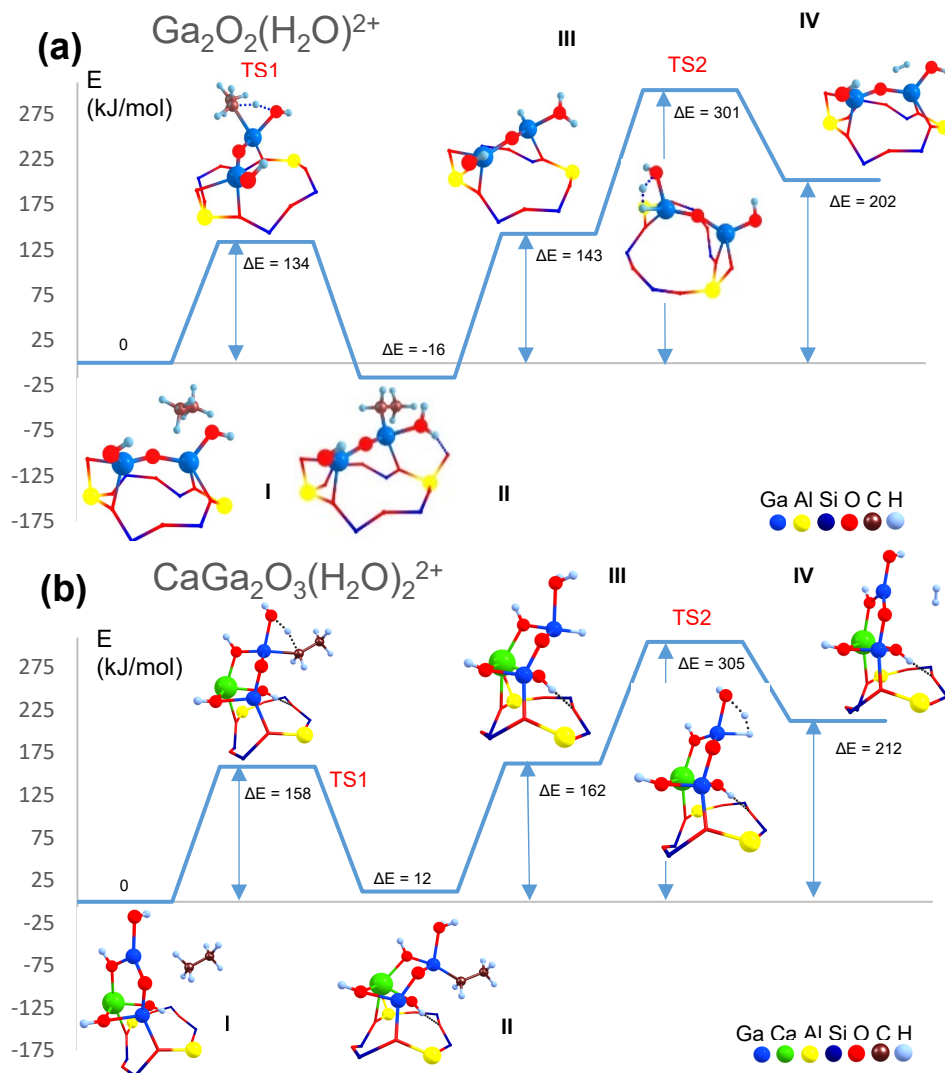


Figure 5.13. DFT-computed reaction energy diagrams and local optimized structures of the key intermediates and transition states for ethane dehydrogenation over (a) $\text{Ga}_2\text{O}_2(\text{H}_2\text{O})_2^{2+}$ (b) and $\text{CaGa}_2\text{O}_3(\text{H}_2\text{O})_2^{2+}$ clusters in ZSM-5 zeolite thermodynamically favored at low H_2O partial pressures ($-2.0 \text{ eV} < \Delta\mu_{\text{H}_2\text{O}} < -1.2 \text{ eV}$).

factors is beyond the scope of the present study and is a focus of the ongoing computational efforts in our group.

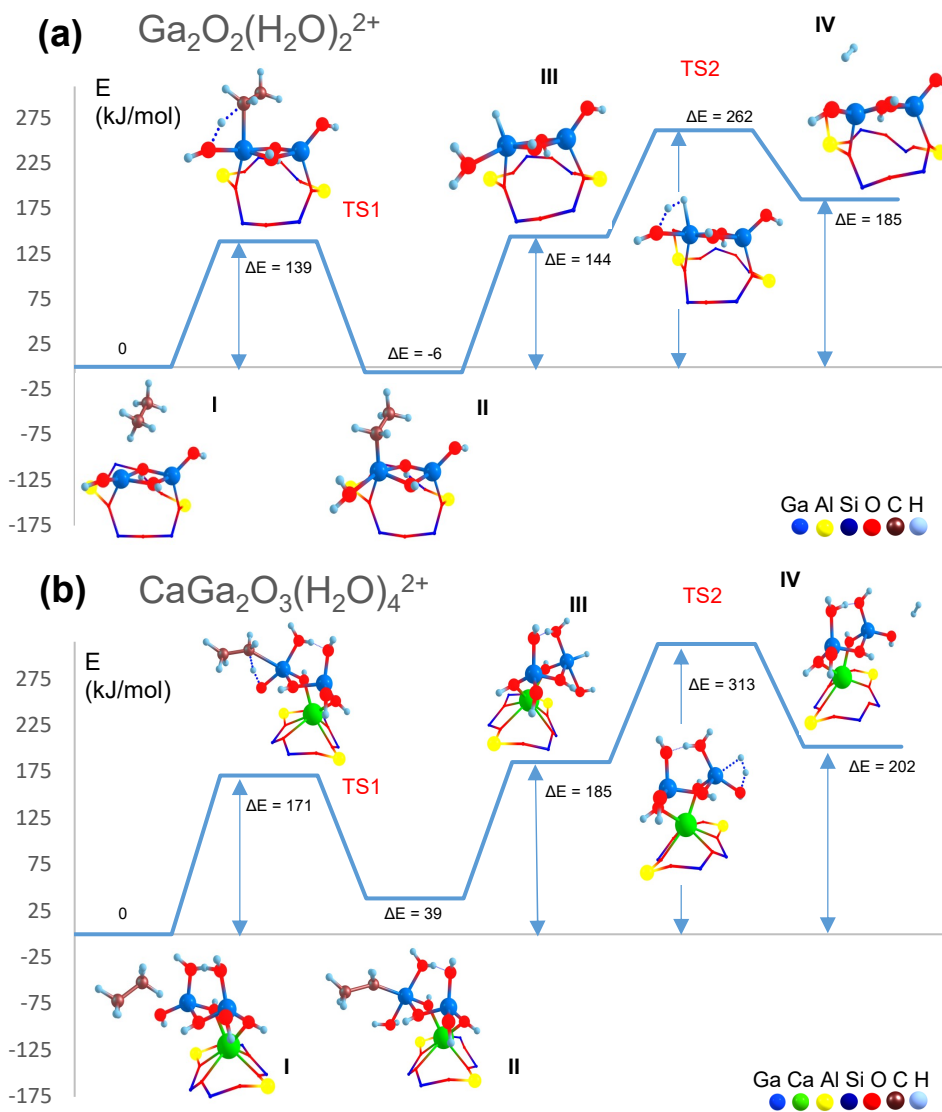


Figure 5.14. DFT-computed reaction energy diagrams and local optimized structures of the key intermediates and transition states for ethane dehydrogenation over (a) $\text{Ga}_2\text{O}_2(\text{H}_2\text{O})_2^{2+}$ and (b) $\text{CaGa}_2\text{O}_3(\text{H}_2\text{O})_4^{2+}$ clusters in ZSM-5 zeolite thermodynamically favored at H_2O partial pressures relevant to the MTA process ($\Delta\mu_{\text{H}_2\text{O}} > -1.2$ eV).

Table 5.4. The reaction energies (ΔE) and the activation barriers (E_{act}) of the C-H-bond activation, β -elimination and H_2 recombination steps of ethane dehydrogenation.

Reaction step	C-H-bond activation		β -elimination		H_2 recombination	
	ΔE	E_{act}	ΔE	E_{act}	ΔE	E_{act}
Structures						
$\text{Ga}_2\text{O}_2(\text{H}_2\text{O})^{2+}$	-16	134	159	/	59	158
$\text{Ga}_2\text{O}_2(\text{H}_2\text{O})_2^{2+}$	-6	139	150	/	41	118
$\text{CaGa}_2\text{O}_3(\text{H}_2\text{O})_2^{2+}$	12	158	150	/	50	143
$\text{CaGa}_2\text{O}_3(\text{H}_2\text{O})_4^{2+}$	39	171	147	/	16	128

Therefore, we propose that the addition of Ca allows to sustain the catalytic CaGa complexes in a more hydrated state during the MTA reaction. The higher degree of hydration for the CaGa system results in a higher barrier for the C-H bond cleavage, moderating thus effectively the rate of the dehydrogenation paths of the MTA reaction.

5.4 Conclusions

MTA over Ga-modified zeolites offers a sustainable route for the production of important commodities such as benzene, ethylbenzene, toluene and xylenes. The increase in the selectivity towards the aromatics is accompanied by issues of enhanced coke deposition and subsequent early deactivation of the catalyst. The addition of minute amounts of Ca (0.02 wt%) prolongs the lifetime of the catalyst while maintaining a high selectivity towards aromatics. The Ca(0.02)Ga(2) converted 43% more MeOH and gave 33 % higher yield of BTEX than Ga/H-ZSM-5 before the catalyst was fully deactivated. Higher Ca loadings (>0.05 wt%) not only gives rise to Ca-LAS formation but also diminishes the impact of lifetime extension in MTA.

The mechanistic basis of the catalytic impact of Ca in the MTA process depending on Ca loading is still unclear. Based on the MTA performance and IR spectroscopy analysis, we propose that the minute addition of Ca to Ga-modified zeolites ensures the formation of CaGa extraframework clusters, reducing the Ga-LAS, before Ca starts exchanging with protons of BAS. The interaction of Ca and Ga results in a moderated dehydrogenation rate evidenced by the lower hydrogen formation over Ca(0.02)Ga(2) than Ga(2) in the MeOH aromatization process. The computational modeling suggests that the Ca^{2+} cation added to the Ga extraframework structure allows accommodating more water molecules exhibiting a lower Lewis acidity and a higher stability under water-containing conditions. Accordingly, the higher C-H bond activation energy barrier over

Chapter 5

CaGa clusters leads to reduced dehydrogenation activity and a slower deactivation process.

The targeted modification of Ga extraframework species with small quantities of Ca is demonstrated as a promising approach for the further optimization and practical implementation of the MTA process.

References

- (1) Wittcoff, H. A.; Reuben, B. G.; Plotkin, J. S., in *Industrial Organic Chemicals*, John Wiley & Sons, **2012**, pp. 323-373.
- (2) Wittcoff, H. A.; Reuben, B. G.; Plotkin, J. S., in *Industrial Organic Chemicals*, John Wiley & Sons, **2012**, pp. 375-382.
- (3) Harold A. Wittcoff, B. G. R., Jeffery S. Plotkin, in *Industrial Organic Chemicals*, John Wiley & Sons, **2012**, pp. 383-405.
- (4) Sheldon, R. A. *Green Chemistry* **2014**, *16* (3), 950-963.
- (5) Sun, Z.; Bottari, G.; Afanasenko, A.; Stuart, M. C.; Deuss, P. J.; Fridrich, B.; Barta, K. *Nature Catalysis* **2018**, *1* (1), 82-92.
- (6) Wei, J.; Ge, Q.; Yao, R.; Wen, Z.; Fang, C.; Guo, L.; Xu, H.; Sun, J. *Nature Communications* **2017**, *8* (1), 1-9.
- (7) Bruijninx, P. C.; Weckhuysen, B. M. *Angewandte Chemie International Edition* **2013**, *52* (46), 11980-11987.
- (8) Tian, P.; Wei, Y.; Ye, M.; Liu, Z. *ACS Catalysis* **2015**, *5* (3), 1922-1938.
- (9) Dahl, I. M.; Kolboe, S. *Catalysis Letters* **1993**, *20* (3), 329-336.
- (10) Olsbye, U.; Svelle, S.; Bjørgen, M.; Beato, P.; Janssens, T. V. W.; Joensen, F.; Bordiga, S.; Lillerud, K. P. *Angewandte Chemie International Edition* **2012**, *51* (24), 5810-5831.
- (11) Ilias, S.; Bhan, A. *ACS Catalysis* **2013**, *3* (1), 18-31.
- (12) Bjørgen, M.; Svelle, S.; Joensen, F.; Nerlov, J.; Kolboe, S.; Bonino, F.; Palumbo, L.; Bordiga, S.; Olsbye, U. *Journal of Catalysis* **2007**, *249* (2), 195-207.
- (13) Yarulina, I.; Chowdhury, A. D.; Meirer, F.; Weckhuysen, B. M.; Gascon, J. *Nature Catalysis* **2018**, *1* (6), 398-411.
- (14) Svelle, S.; Joensen, F.; Nerlov, J.; Olsbye, U.; Lillerud, K.-P.; Kolboe, S.; Bjørgen, M. *Journal of the American Chemical Society* **2006**, *128* (46), 14770-14771.
- (15) Almutairi, S. M. T.; Mezari, B.; Magusin, P. C. M. M.; Pidko, E. A.; Hensen, E. J. M. *ACS Catalysis* **2012**, *2* (1), 71-83.
- (16) Miyake, K.; Hirota, Y.; Ono, K.; Uchida, Y.; Tanaka, S.; Nishiyama, N. *Journal of Catalysis* **2016**, *342*, 63-66.
- (17) Niu, X.; Gao, J.; Miao, Q.; Dong, M.; Wang, G.; Fan, W.; Qin, Z.; Wang, J. *Microporous and Mesoporous Materials* **2014**, *197*, 252-261.
- (18) Pinilla-Herrero, I.; Borfecchia, E.; Holzinger, J.; Mentzel, U. V.; Joensen, F.; Lomachenko, K. A.; Bordiga, S.; Lamberti, C.; Berlier, G.; Olsbye, U. *Journal of Catalysis* **2018**, *362*, 146-163.
- (19) Shen, X.; Kang, J.; Niu, W.; Wang, M.; Zhang, Q.; Wang, Y. *Catalysis Science & Technology* **2017**, *7* (16), 3598-3612.
- (20) Wang, K.; Dong, M.; Niu, X.; Li, J.; Qin, Z.; Fan, W.; Wang, J. *Catalysis Science & Technology* **2018**, *8* (21), 5646-5656.
- (21) Xin, Y.; Qi, P.; Duan, X.; Lin, H.; Yuan, Y. *Catalysis Letters* **2013**, *143* (8), 798-806.
- (22) Zhang, G. Q.; Bai, T.; Chen, T. F.; Fan, W. T.; Zhang, X. *Industrial & Engineering Chemistry Research* **2014**, *53* (39), 14932-14940.
- (23) Choudhary, V. R.; Mondal, K. C.; Mulla, S. A. R. *Angewandte Chemie International Edition* **2005**, *44* (28), 4381-4385.
- (24) Dai, W.; Yang, L.; Wang, C.; Wang, X.; Wu, G.; Guan, N.; Obenaus, U.; Hunger, M.; Li, L. *ACS Catalysis* **2018**, *8* (2), 1352-1362.

- (25) Dooley, K. M.; Chang, C.; Price, G. L. *Applied Catalysis A: General* **1992**, *84* (1), 17-30.
- (26) Freeman, D.; Wells, R. P. K.; Hutchings, G. J. *Journal of Catalysis* **2002**, *205* (2), 358-365.
- (27) Gao, P.; Xu, J.; Qi, G.; Wang, C.; Wang, Q.; Zhao, Y.; Zhang, Y.; Feng, N.; Zhao, X.; Li, J.; Deng, F. *ACS Catalysis* **2018**, *8* (10), 9809-9820.
- (28) Hsieh, C. Y.; Chen, Y. Y.; Lin, Y. C. *Industrial & Engineering Chemistry Research* **2018**, *57* (23), 7742-7751.
- (29) Lopez-Sanchez, J. A.; Conte, M.; Landon, P.; Zhou, W.; Bartley, J. K.; Taylor, S. H.; Carley, A. F.; Kiely, C. J.; Khalid, K.; Hutchings, G. J. *Catalysis Letters* **2012**, *142* (9), 1049-1056.
- (30) Mentzel, U. V.; Højholt, K. T.; Holm, M. S.; Fehrmann, R.; Beato, P. *Applied Catalysis A: General* **2012**, *417-418*, 290-297.
- (31) Inoue, Y.; Nakashiro, K.; Ono, Y. *Microporous Materials* **1995**, *4* (5), 379-383.
- (32) Zeng, D.; Yang, J.; Wang, J.; Xu, J.; Yang, Y.; Ye, C.; Deng, F. *Microporous and Mesoporous Materials* **2007**, *98* (1-3), 214-219.
- (33) Arstad, B.; Kolboe, S. *Catalysis Letters* **2001**, *71* (3), 209-212.
- (34) Song, W.; Fu, H.; Haw, J. F. *The Journal of Physical Chemistry B* **2001**, *105* (51), 12839-12843.
- (35) Fu, H.; Song, W.; Haw, J. F. *Catalysis Letters* **2001**, *76* (1), 89-94.
- (36) Hereijgers, B. P.; Bleken, F.; Nilsen, M. H.; Svelle, S.; Lillerud, K.-P.; Bjørgen, M.; Weckhuysen, B. M.; Olsbye, U. *Journal of Catalysis* **2009**, *264* (1), 77-87.
- (37) Uslamin, E. A.; Luna-Murillo, B.; Kosinov, N.; Bruijninx, P. C. A.; Pidko, E. A.; Weckhuysen, B. M.; Hensen, E. J. M. *Chemical Engineering Science* **2018**, *198*, 305-316.
- (38) Uslamin, E. A.; Saito, H.; Kosinov, N.; Pidko, E.; Sekine, Y.; Hensen, E. J. *Catalysis Science & Technology* **2020**, *10* (9), 2774-2785.
- (39) Meng, L.; Zhu, X.; Wannapakdee, W.; Pestman, R.; Goesten, M. G.; Gao, L.; van Hoof, A. J. F.; Hensen, E. J. M. *Journal of Catalysis* **2018**, *361*, 135-142.
- (40) Youming, N.; Sun, A.; Wu, X.; Hai, G.; Hu, J.; Li, T.; Li, G. *Microporous and Mesoporous Materials* **2011**, *143*, 435-442.
- (41) Wei, Z.; Chen, L.; Qingsheng, C.; Wen, Z.; Zhuo, Z.; Xu, Y.; Zhu, X. *Fuel Processing Technology* **2017**, *162*, 66-77.
- (42) Arora, S. S.; Nieskens, D. L. S.; Malek, A.; Bhan, A. *Nature Catalysis* **2018**, *1* (9), 666-672.
- (43) Yarulina, I.; De Wispelaere, K.; Bailleul, S.; Goetze, J.; Radersma, M.; Abou-Hamad, E.; Vollmer, I.; Goesten, M.; Mezari, B.; Hensen, E. J. M.; Martínez-Espín, J. S.; Morten, M.; Mitchell, S.; Perez-Ramirez, J.; Olsbye, U.; Weckhuysen, B. M.; Van Speybroeck, V.; Kapteijn, F.; Gascon, J. *Nature Chemistry* **2018**, *10* (8), 804-812.
- (44) Stinton, G. W.; Evans, J. S. *Journal of Applied Crystallography* **2007**, *40* (1), 87-95.
- (45) Emeis, C. A. *Journal of Catalysis* **1993**, *141* (2), 347-354.
- (46) Namba, S.; Nakanishi, S.; Yashima, T. *Journal of Catalysis* **1984**, *88* (2), 505-508.
- (47) Haag, W. O.; Lago, R. M.; Weisz, P. B. *Faraday Discussions of the Chemical Society* **1981**, *72*, 317-330.
- (48) Hussein, H. A.; Johnston, R. L., in *Frontiers of Nanoscience, Vol. 12*, Elsevier, **2018**, pp. 145-169.

- (49) Jennings, P. C.; Lysgaard, S.; Hummelshøj, J. S.; Vegge, T.; Bligaard, T. *npj Computational Materials* **2019**, *5* (1), 46.
- (50) Bannwarth, C.; Caldeweyher, E.; Ehlert, S.; Hansen, A.; Pracht, P.; Seibert, J.; Spicher, S.; Grimme, S. *WIREs Computational Molecular Science* **2021**, *11* (2), e1493.
- (51) Grimme, S.; Bannwarth, C.; Shushkov, P. *Journal of Chemical Theory and Computation* **2017**, *13* (5), 1989-2009.
- (52) Bannwarth, C.; Ehlert, S.; Grimme, S.; Tight-Binding, B. P. S.-C. *J. Chem. Theory Comput* **2019**, *15*, 1652-1671.
- (53) Pracht, P.; Caldeweyher, E.; Ehlert, S.; Grimme, S. *A robust non-self-consistent tight-binding quantum chemistry method for large molecules*, *ChemRxiv* **2019**, preprint.
- (54) Vilhelmsen, L. B.; Hammer, B. *The Journal of Chemical Physics* **2014**, *141* (4), 044711.
- (55) Schütt, O.; Messmer, P.; Hutter, J.; VandeVondele, J. *Electronic Structure Calculations on Graphics Processing Units* **2016**, 173-190.
- (56) Borštnik, U.; VandeVondele, J.; Weber, V.; Hutter, J. *Parallel Computing* **2014**, *40* (5), 47-58.
- (57) Maintz, S.; Deringer, V. L.; Tchougréeff, A. L.; Dronskowski, R. *Journal of Computational Chemistry* **2016**, *37* (11), 1030-1035.
- (58) Ehrlich, S.; Moellmann, J.; Reckien, W.; Bredow, T.; Grimme, S. *ChemPhysChem* **2011**, *12* (17), 3414-3420.
- (59) Perdew, J. P. *Rev. Lett.* **1996**, *77*, 3865.
- (60) Frisch, M.; Trucks, G.; Schlegel, H.; Scuseria, G.; Robb, M.; Cheeseman, J.; Scalmani, G.; Barone, V.; Mennucci, B.; Petersson, G. Gaussian 09, Revision C.01 Gaussian Inc., Wallingford CT, **2010**.
- (61) Frigo, M.; Johnson, S. G. *Proceedings of the IEEE* **2005**, *93* (2), 216-231.
- (62) Kolafa, J. *Journal of Computational Chemistry* **2004**, *25* (3), 335-342.
- (63) VandeVondele, J.; Hutter, J. *The Journal of Chemical Physics* **2003**, *118* (10), 4365-4369.
- (64) Lippert, B. G.; Parrinello, J. H.; Michele. *Molecular Physics* **1997**, *92* (3), 477-488.
- (65) VandeVondele, J.; Hutter, J. *The Journal of Chemical Physics* **2007**, *127* (11), 114105.
- (66) Goedecker, S.; Teter, M.; Hutter, J. *Physical Review B* **1996**, *54* (3), 1703-1710.
- (67) Genovese, L.; Deutsch, T.; Goedecker, S. *The Journal of Chemical Physics* **2007**, *127* (5), 054704.
- (68) Stull, D. R. *JANAF Thermochemical Tables*; U.S. Dept. of Commerce, National Bureau of Standards, **1971**.
- (69) Perdew, J. P.; Burke, K.; Ernzerhof, M. *Physical Review Letters* **1996**, *77* (18), 3865-3868.
- (70) Grimme, S.; Ehrlich, S.; Goerigk, L. *J Comput Chem* **2011**, *32* (7), 1456-1465.
- (71) Kresse, G.; Furthmüller, J. *Physical Review B* **1996**, *54* (16), 11169-11186.
- (72) Kresse, G.; Joubert, D. *Physical Review B* **1999**, *59* (3), 1758-1775.
- (73) Blöchl, P. E. *Physical Review B* **1994**, *50* (24), 17953-17979.
- (74) Henkelman, G.; Uberuaga, B. P.; Jónsson, H. *The Journal of Chemical Physics* **2000**, *113* (22), 9901-9904.
- (75) Pidko, E. A.; Hensen, E. J. M.; van Santen, R. A. *The Journal of Physical Chemistry C* **2007**, *111* (35), 13068-13075.

- (76) Corma, A.; Martínez, C.; Doskocil, E. *Journal of Catalysis* **2013**, *300*, 183-196.
- (77) Lercher, J. A.; Grundling, C.; Eder-Mirth, G. *Catalysis Today* **1996**, *27* (3), 353-376.
- (78) Bailleul, S.; Yarulina, I.; Hoffman, A. E. J.; Dokania, A.; Abou-Hamad, E.; Chowdhury, A. D.; Pieters, G.; Hajek, J.; De Wispelaere, K.; Waroquier, M.; Gascon, J.; Van Speybroeck, V. *Journal of the American Chemical Society* **2019**, *141* (37), 14823-14842.
- (79) Sartipi, S.; Parashar, K.; Valero-Romero, M. J.; Santos, V. P.; van der Linden, B.; Makkee, M.; Kapteijn, F.; Gascon, J. *Journal of Catalysis* **2013**, *305*, 179-190.
- (80) Raichle, A.; Moser, S.; Traa, Y.; Hunger, M.; Weitkamp, J. *Catalysis Communications* **2001**, *2* (1), 23-29.
- (81) Pelmeshnikov, A.; Van Santen, R.; Janchen, J.; Meijer, E. *The Journal of Physical Chemistry* **1993**, *97* (42), 11071-11074.
- (82) Medin, A.; Borovkov, V. Y.; Kazansky, V.; Pelmentschikov, A.; Zhidomirov, G. *Zeolites* **1990**, *10* (7), 668-673.
- (83) Boronat, M.; Concepción, P.; Corma, A.; Renz, M.; Valencia, S. *Journal of Catalysis* **2005**, *234* (1), 111-118.
- (84) Schreiber, M. W.; Plaisance, C. P.; Baumgärtl, M.; Reuter, K.; Jentys, A.; Bermejo-Deval, R.; Lercher, J. A. *Journal of the American Chemical Society* **2018**, *140* (14), 4849-4859.
- (85) Phadke, N. M.; Van der Mynsbrugge, J.; Mansoor, E.; Getsoian, A. B.; Head-Gordon, M.; Bell, A. T. *ACS Catalysis* **2018**, *8* (7), 6106-6126.
- (86) Martínez-Espín, J. S.; De Wispelaere, K.; Janssens, T. V. W.; Svelle, S.; Lillerud, K. P.; Beato, P.; Van Speybroeck, V.; Olsbye, U. *ACS Catalysis* **2017**, *7* (9), 5773-5780.
- (87) Müller, S.; Liu, Y.; Kirchberger, F. M.; Tonigold, M.; Sanchez-Sanchez, M.; Lercher, J. A. *Journal of the American Chemical Society* **2016**, *138* (49), 15994-16003.
- (88) Behera, B.; Ray, S. S.; Singh, I. D., in *Studies in Surface Science and Catalysis, Vol. 166*, Elsevier, **2007**, pp. 163-200.
- (89) Yokoi, T.; Mochizuki, H.; Namba, S.; Kondo, J. N.; Tatsumi, T. *The Journal of Physical Chemistry C* **2015**, *119* (27), 15303-15315.
- (90) Yarulina, I.; Bailleul, S.; Pustovarenko, A.; Martinez, J. R.; Wispelaere, K. D.; Hajek, J.; Weckhuysen, B. M.; Houben, K.; Baldus, M.; Van Speybroeck, V. *ChemCatChem* **2016**, *8* (19), 3057-3063.
- (91) Grajciar, L.; Heard, C. J.; Bondarenko, A. A.; Polynski, M. V.; Meeprasert, J.; Pidko, E. A.; Nachtigall, P. *Chemical Society Reviews* **2018**, *47* (22), 8307-8348.
- (92) Corbett, P. T.; Sanders, J. K. M.; Otto, S. *Angewandte Chemie International Edition* **2007**, *46* (46), 8858-8861.
- (93) Pidko, E. A.; van Santen, R. A. *The Journal of Physical Chemistry C* **2009**, *113* (11), 4246-4249.
- (94) Pidko, E. A.; van Santen, R. A.; Hensen, E. J. M. *Physical Chemistry Chemical Physics* **2009**, *11* (16), 2893-2902.
- (95) Kim, S.; Park, G.; Woo, M. H.; Kwak, G.; Kim, S. K. *ACS Catalysis* **2019**, *9* (4), 2880-2892.
- (96) Reuter, K.; Stampf, C.; Scheffler, M., in *Handbook of Materials Modeling: Methods*, Springer Netherlands, Dordrecht, **2005**, pp. 149-194.
- (97) Pidko, E. A.; Kazansky, V. B.; Hensen, E. J. M.; van Santen, R. A. *Journal of Catalysis* **2006**, *240* (1), 73-84.

- (98) Pidko, E. A.; van Santen, R. A. *The Journal of Physical Chemistry C* **2007**, *111* (6), 2643-2655.
- (99) Mansoor, E.; Head-Gordon, M.; Bell, A. T. *ACS Catalysis* **2018**, *8* (7), 6146-6162.
- (100) Szécsényi, Á.; Li, G.; Gascon, J.; Pidko, E. A. *ACS Catalysis* **2018**, *8* (9), 7961-7972.
- (101) Khramenkova, E. V.; Medvedev, M. G.; Li, G.; Pidko, E. A. *The Journal of Physical Chemistry Letters* **2021**, *12* (44), 10906-10913.
- (102) Szécsényi, Á.; Khramenkova, E.; Chernyshov, I. Y.; Li, G.; Gascon, J.; Pidko, E. A. *ACS Catalysis* **2019**, *9* (10), 9276-9284.

APPENDIX D - High stability of MTA
conversion over bimetallic Ca,Ga-modified
ZSM-5

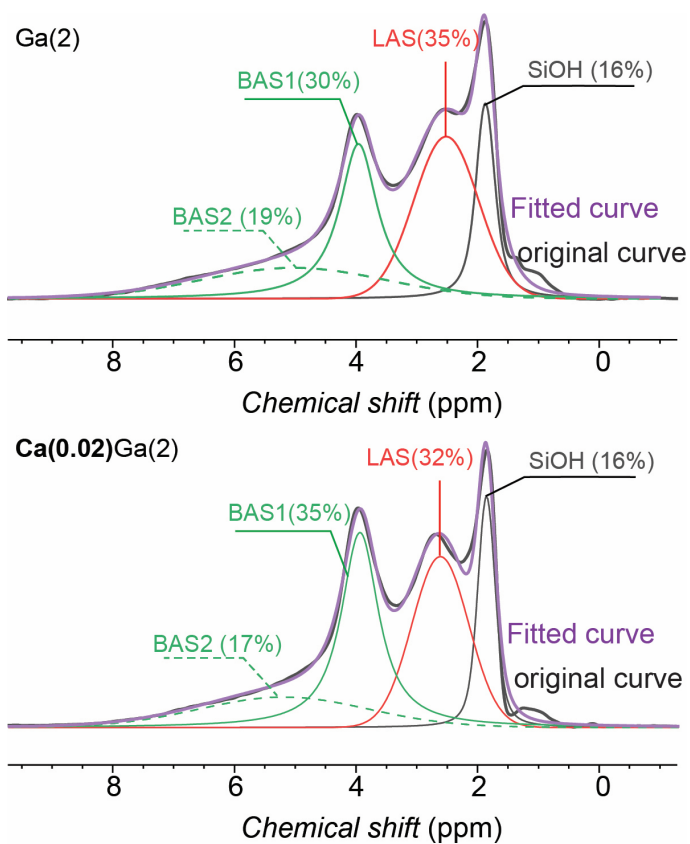


Figure D1. ^1H MAS NMR spectra and deconvolution of Ga(2) and Ca(0.02)Ga(2) under study. Following the signal assignment in the literature^[1-4], Si-OH deconvoluted (Voigt function) signal at 1.9 ppm is observed on both samples and used to normalize the peak intensity in two catalysts. Al-OH, Ga-OH, and Ca-OH groups exhibit signals between 2.6–2.5 ppm. Two signals at 5.1 and 3.9 ppm are assigned to H-bonded and isolated Si-O(H)-Al groups, respectively. Their weights relative to the entire peak area are indicated by the values in the brackets.

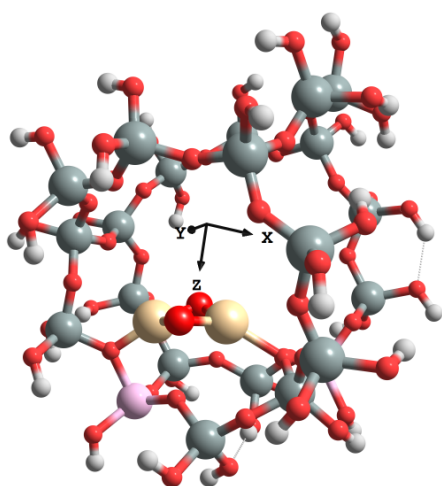
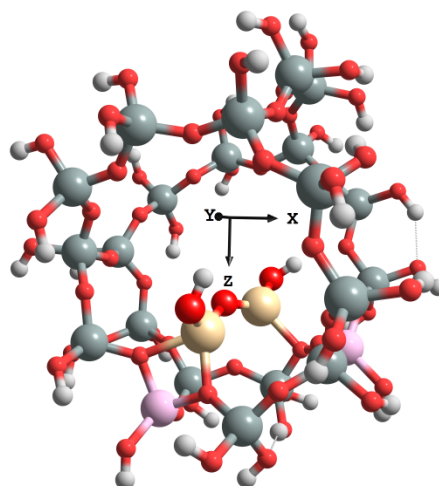
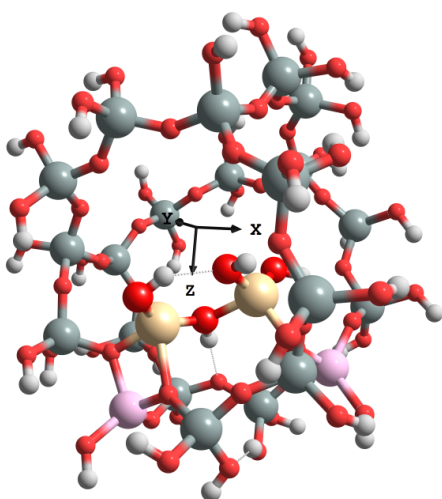
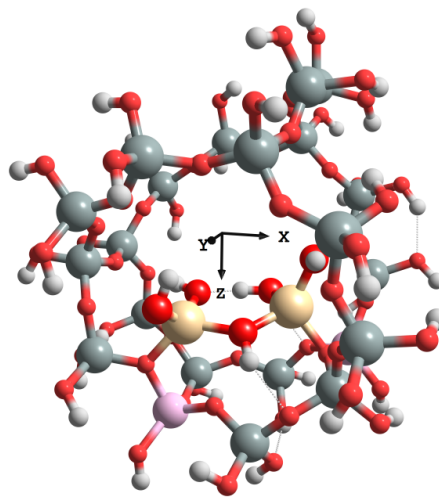
Structure $\text{Ga}_2\text{O}_2^{2+}$ in alpha site (a)Structure $\text{Ga}_2\text{O}_2(\text{H}_2\text{O})^{2+}$ in alpha site (b)Structure $\text{Ga}_2\text{O}_2(\text{H}_2\text{O})_2^{2+}$ in alpha site (c)Structure $\text{Ga}_2\text{O}_2(\text{H}_2\text{O})_3^{2+}$ in alpha site (d)

Figure D2. Global minima of the low hydrated $\text{Ga}_2\text{O}_2(\text{H}_2\text{O})_x^{2+}$ confined in the alpha site of the ZSM-5 and optimized at PBE-D3(BJ) level of theory, where $x = 0$ (a), 1(b), 2(c), 3(d). Aluminum is pink, oxygen is red, gallium is beige, silicon is grey, hydrogen is white.

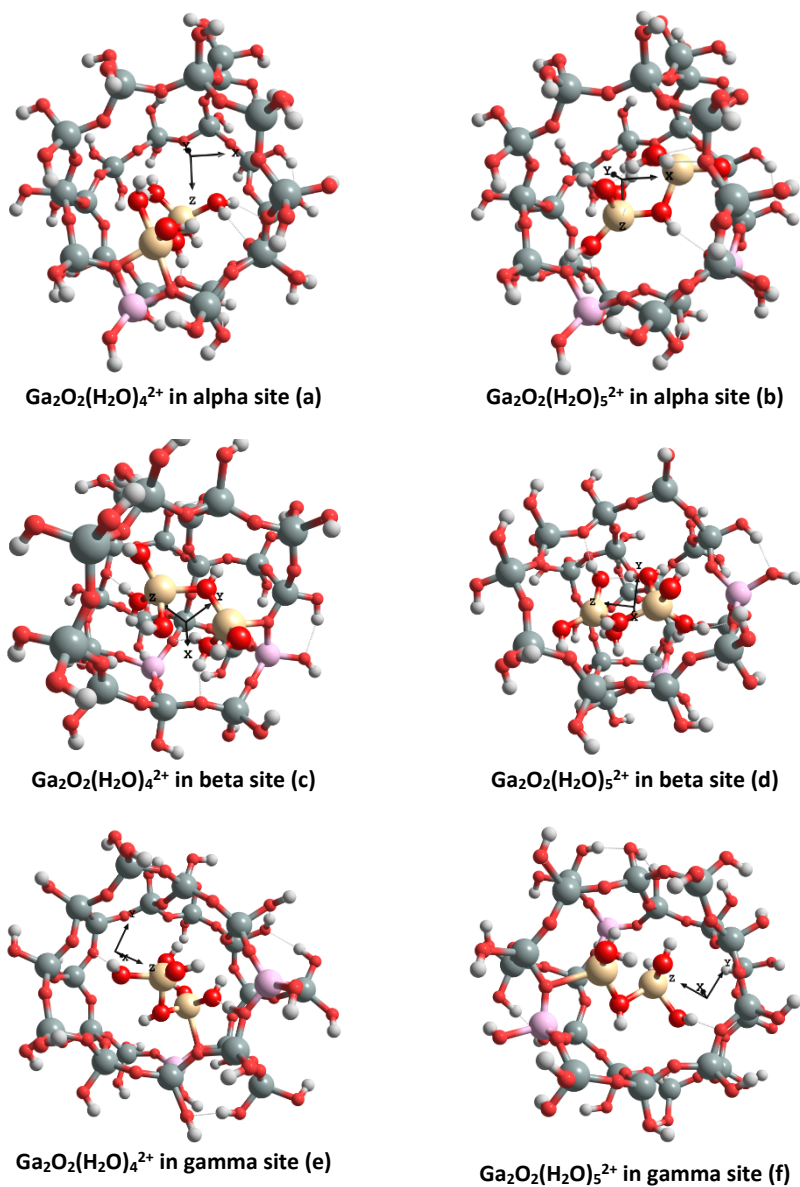


Figure D3. Global minima of $\text{Ga}_2\text{O}_2(\text{H}_2\text{O})_x^{2+}$ confined in the alpha, beta, gamma sites of the ZSM-5 and optimized at PBE-D3(BJ) level of theory, where $x = 4$ (a, c, e), 5 (b, d, f). Aluminium is pink, oxygen is red, gallium is beige, silicon is grey, hydrogen is white.

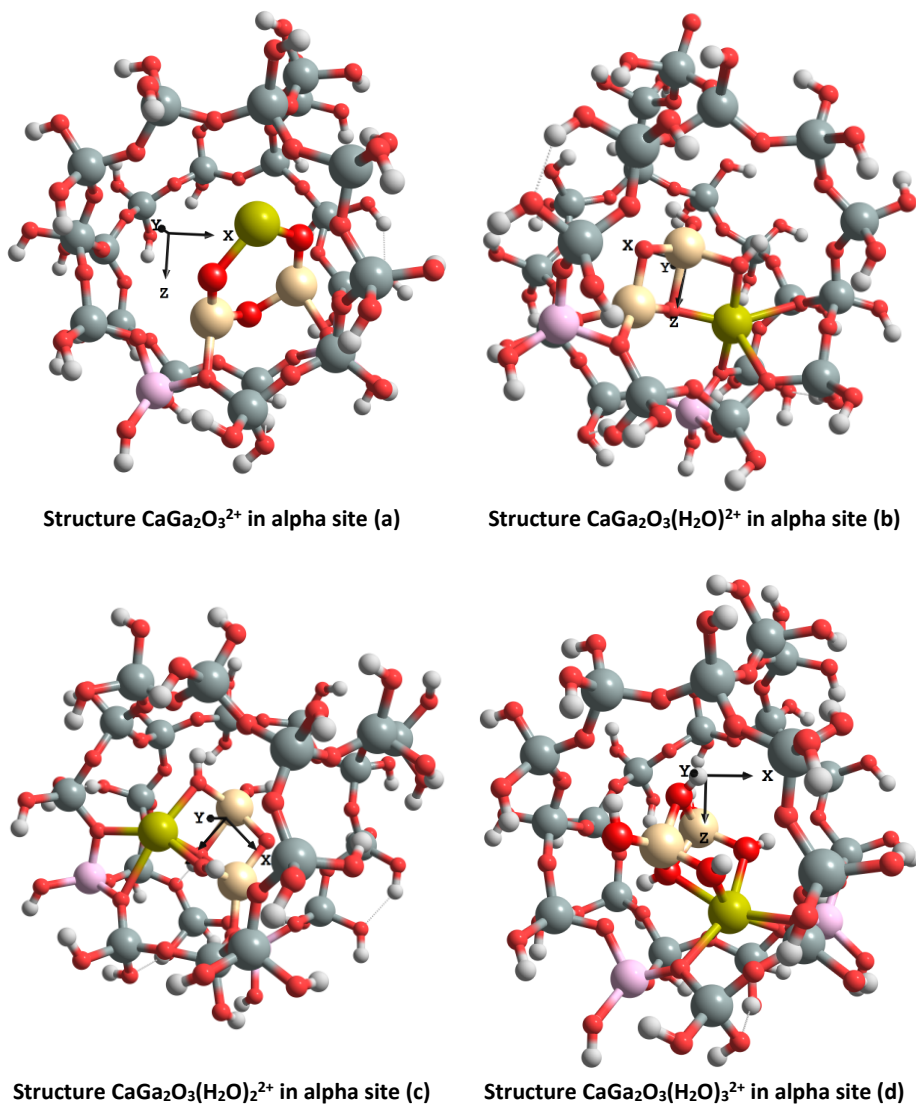


Figure D4. Global minima of the low hydrated $\text{CaGa}_2\text{O}_3(\text{H}_2\text{O})_x^{2+}$ confined in the alpha site of the ZSM-5 and optimized at PBE-D3(BJ) level of theory, where $x = 0$ (a), 1(b), 2(c), 3(d). Aluminum is pink, oxygen is red, gallium is beige, silicon is grey, hydrogen is white, calcium is yellow.

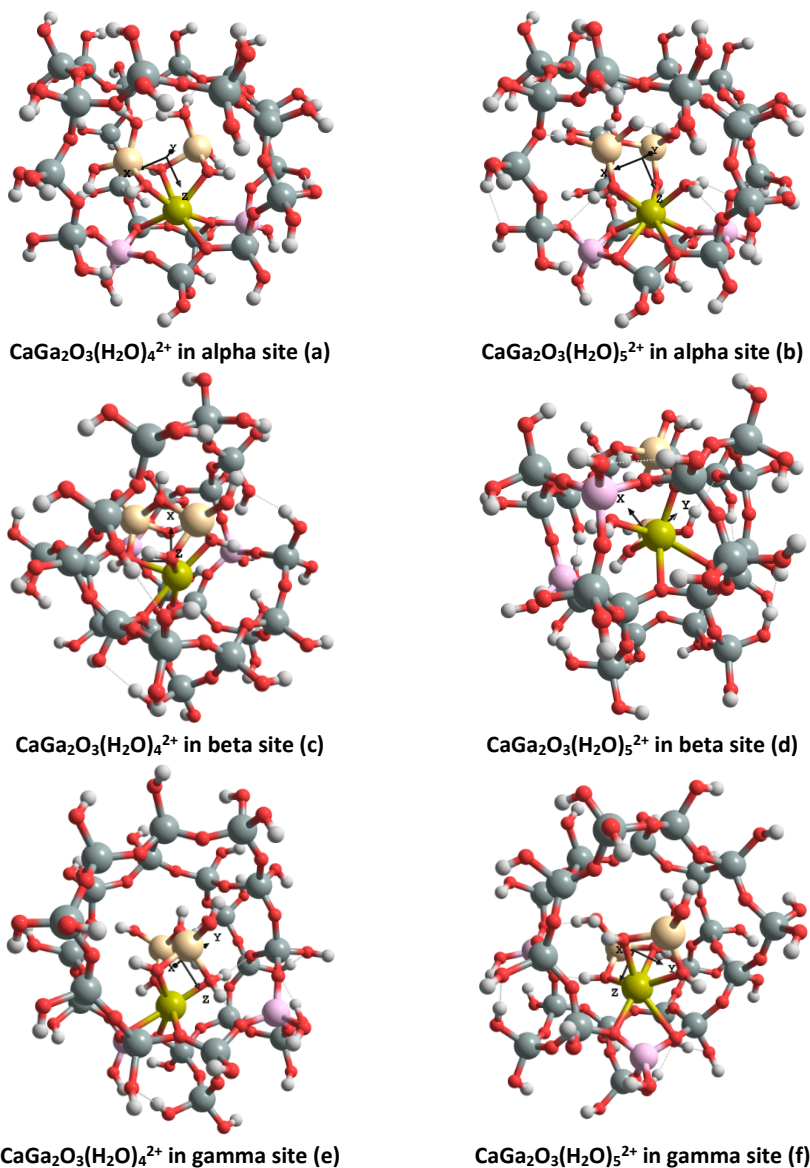


Figure D5. Global minima of $\text{CaGa}_2\text{O}_2(\text{H}_2\text{O})_x^{2+}$ confined in the alpha (a, b), beta (c, d), gamma (e, f) sites of the ZSM-5 and optimized at PBE-D3(BJ) level of theory, where $x = 4$ (a, c, e), 5 (b, d, f). Aluminium is pink, oxygen is red, gallium is beige, calcium is yellow, silicon is grey, hydrogen is white.

References

- (1) Gabrienko, A. A.; Danilova, I. G.; Arzumanov, S. S.; Pirutko, L. V.; Freude, D.; Stepanov, A. G. *The Journal of Physical Chemistry C* **2018**, *122* (44), 25386-25395.
- (2) Freude, D.; Hunger, M.; Pfeifer, H. *Zeitschrift für Physikalische Chemie* **1987**, *152* (1-2), 171-182.
- (3) Brunner, E. *Journal of Molecular Structure* **1995**, *355* (1), 61-85.
- (4) Hunger, M.; Ernst, S.; Steuernagel, S.; Weitkamp, J. *Microporous Materials* **1996**, *6* (5), 349-353.

Summary and outlook

Summary

The MTH process is recognized as one of the key ingredients of the methanol (MeOH) economy concept enabling the production of crucial hydrocarbon building blocks, such as light olefins and aromatics, starting from CO₂ as the primary carbon source. Besides the driving force of reducing reliance on fossil fuels, the highly tunable nature of this process in response to rapidly changing market demands attracts continuous process development by industry. In academia, proposing comprehensive structure-performance relationships relying on a deeper understanding of the complex reaction pathways makes MTH a perfect model reaction system for new porous material synthesis and catalyst design.

Although more than 40 years of fundamental research have achieved a number of milestones and industrialization progress (**Chapter 1**), there is still quite some room for improvement both in the mechanistic understanding and the catalyst performance, namely selectivity to target products and stability against the deactivation. This thesis book aims at providing more mechanistic and kinetic insights in the MTH process, which would guide to a more comprehensive structure-performance relationship in the MTH process. For this purpose, the following three objectives have been addressed in this thesis *i*) prove that lattice Al enriched in the straight/sinusoidal channels, as the essential parameter among other morphological and acidity features, determines the selectivity to propylene in the MTH process over a series of MFI/MEL 10-MR zeolite catalysts (**Chapter 2**); *ii*) identify two consecutive reaction pathways, *i.e.*, a fast primary product formation in the presence of MeOH, followed by a slower formation of light aromatics related to the decomposition and release of hydrocarbon pool (HCP) species and secondary reactions in absence of MeOH in the downstream part of the catalyst bed (**Chapter 3**); *iii*) provide direct experimental evidence that olefin-based cycle is kinetically favored over aromatic-based cycle reactions, with the latter undergoing a paring-type reaction route for the production of olefins and aromatics in H-ZSM-5 zeolite catalyst (**Chapter 4**); *iv*) provide a feasible approach, *i.e.*, Ca-Ga bimetallic modification, tailoring the acidic properties of H-ZSM-5 zeolite materials, to optimize the product selectivity and process stability in the MTA process (**Chapter 5**).

The extremely complex autocatalytic reaction pathway and fast kinetics make MTH research highly challenging; all reactions are rapidly completed in the micropore under industrially relevant conditions and all conceivable catalyst structural parameters and operating conditions may change the final product distribution. Nevertheless, the findings in **Chapter 2** not only help to build up comprehensive structure-performance correlations within the specific zeolites, but also calls for more kinetic investigations of the MTH mechanism. To tackle the kinetic aspects in the MTH mechanism, a transient kinetic study was conducted in **Chapters 3** and **4** using a novel fast scanning-pulse analysis (FASPA) combined with infrared spectroscopy and isotope labeling techniques. Based on obtained mechanistic and kinetic information, post-synthesis modifications on the zeolite materials are promising strategies in an attempt to tailor the targeted catalyst parameters to achieve a selective catalyst with super stability in the MTA process (**Chapter 5**).

In **Chapter 2**, an integrated approach was applied by combining a detailed analysis of the catalytic behavior and thorough material characterizations on selected medium-pore size zeolite materials including MFI, MEL and the intergrowth-type MFI/MEL. Experimental results reveal that there indeed seems to be a single key performance indicator, namely lattice Al located in the channel instead of channel intersections, predominantly explaining the product selectivity to propylene and butylenes, which are commonly accepted as the main products in the olefin cycle in the dual-cycle mechanism. In contrast with the selectivity to key products, the stability of these zeolite materials in the MTH process is rather difficult to be correlated with a single parameter. Al enrichment in the channels, crystal size, and probably other intrinsic parameters like diffusivity in the studied zeolite materials all play a role with different degrees of influence.

The complexity and the limited kinetic information on the MTH mechanism in the MFI-type H-ZSM-5 catalyst induced the transient kinetic investigation in the following chapters. In **Chapter 3** the newly developed FASPA (fast scanning-pulse analysis) approach was introduced, validated, and demonstrated to be a successful technique to characterize catalyst performance in standard equipment and to study the MTH mechanism in H-ZSM-5 zeolite catalysts. Assisted by the fine time-control between MeOH pulsing and GC sampling, the quantitative gas phase product responses in a time scale of (sub-)second are recorded upon a MeOH pulse injection. Besides providing the product distribution for a performance evaluation, the transient behavior of gas phase products and

hydrocarbon pool species probed via the *in situ* DRIFT measurements demonstrate the direct correlation between hydrocarbon pool build-up/break-down and gas phase product formation. The distinct transient behavior of aromatics compared to aliphatics points to a secondary formation process in the downstream region of the catalyst bed corresponding with a second broad release of light aromatics in the exit flow in the FASPA test.

FASPA, in combination with isotopic labeling in pulse experiments, is a powerful characterization tool for an in-depth transient kinetic investigation between MeOH and retarded HCP species, with results demonstrated in **Chapter 4**. As demonstrated by *in situ* DRIFT spectroscopy, the hydrocarbon pool is not static, but is rapidly formed in presence of MeOH followed by a rather slow desorption from the catalyst bed when the MeOH is depleted (**Chapter 3**). This dynamic feature alternatively provides the opportunity for direct probing the hydrocarbon pool mechanism by (semi-)quantitatively analyzing the isotope distribution in the gas phase aromatics and other products. Upon MeOH arriving at the reaction zone of the catalyst bed, all products are immediately formed after a rather short induction period. Water first displaces retarded aromatic HCP species still retained in the catalyst bed from the previous MeOH pulse resulting in the first fast appearance of aromatics in the exit flow. In the presence of MeOH, the remaining HCP species further react with MeOH predominantly forming aliphatics (via the cracking reactions) and aromatics via the paring route. In the end, a retarded broad peak of BTX (benzene, toluene, and xylenes) comprises the secondary formation of aromatics from decomposition and dealkylation of primary formed HCP species and retarded olefins in absence of MeOH. This fourth contribution is only observed for longer catalyst beds after full MeOH conversion. The relative contributions depend on the pulse size and injection frequency relative to the catalyst amount.

Facing the ever-increasing demand of light aromatics including benzene, toluene, and xylenes, in **Chapter 5** a strategy is presented to decouple the enhanced production of light aromatics and the fast deactivation over a bimetallic Ca,Ga-modified ZSM-5 catalyst in the MTA process. The addition of Ga into H-ZSM-5 promotes the dehydrogenation reaction rate leading to the improved selectivity to the final aromatic products, however, also causes a fast catalyst deactivation. Experimental results with detailed characterization and theoretical DFT calculations reveal that after doping less than 0.1 wt% Ca in the Ga-modified catalyst, the formed highly hydrated CaGa specimen in extraframework

Summary

positions show a lower Lewis acidity. This accordingly weakens the dehydrogenation reactions leading to a lower hydrogen formation and slightly lower selectivity to light aromatics. Eventually, the catalyst lifetime was increased by around 40% in terms of total MeOH throughput. Further increasing the Ca loading reduced the total concentration of Brønsted acid sites limiting the cracking of long chain olefins. Therefore, the lifetime decreased again. This study provides an alternative strategy for bimetallic catalyst synthesis for a selective and stable MTH process.

Outlook

The ‘Hydrogen economy’ has been much discussed recently, and our oceans represent an inexhaustible water source, water that can be split electrocatalytically into oxygen and hydrogen by using renewable electricity from solar or wind energy. Despite this, hydrogen (and also renewable electricity), as a clean energy source, is a less convenient energy storage medium. As complementary instead of competing, the ‘MeOH economy’ based on the MeOH production from hydrogen and CO₂ and its transformation into hydrocarbons expands the original hydrogen-energy concept into the field of functional material synthesis, eventually leading to a feasible CO₂-zero economy. Meanwhile, renewable MeOH can also be used as liquid fuel, which is more suitable than hydrogen in terms of storage, distribution and volumetric power density. Along with the successful scale-up and extensive commercialization, nearly 40 years’ mechanistic study, especially the recent application of advanced *in situ/operando* characterization tools in the field of MTH, have provided more insights in this host-guest chemistry including the first C–C coupling mechanism, and identity of key hydrocarbon pool intermediates.

However, in my opinion, MTH kinetic investigation combining theoretical findings and solid experimental results under industrially relevant conditions still requires more attention for a more concrete structure-performance relationship, in which structural properties can be characterized via the non-biased means while their impacts are able to explain the kinetics in the MTH mechanism, ultimately guiding the rational MTH catalyst design and process optimization strategies.

The integrated approach used in the study on MFI/MEL and intergrowth MFI/MEL model catalysts reveals that MeOH transformation in the zeolite is an extremely complex process, which is affected by multiple parameters to a different level. These parameters include but are not limited to the studied crystal size, strength of acid sites, and lattice Al distribution. Other parameters, *e.g.* the local defects within the zeolite particle, the presence of extraframework Al, the diffusivity of reactants, intermediates, key products within different zeolite frameworks cannot be ignored. It is obviously not achievable without the development of zeolite-oriented synthesis. More importantly, the quantitative correlation between these parameters with key catalytic performance and how it responds to varying operating conditions brings the other research direction, the

Samenvatting

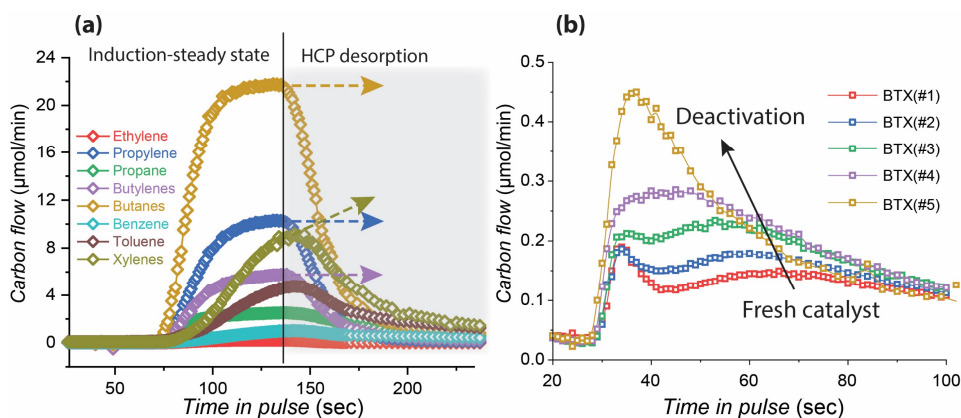


Figure 6.1. (a) Hydrocarbon responses upon pulsing excessive MeOH over parent H-ZSM-5 at 400 °C. Conditions: MeOH pulse quantity = 62.4 μmol_C per pulse, catalyst loading = 100 mg ($\sim 55 \mu\text{mol}$ Brønsted acid sites), catalyst pellet size = 150–212 μm , $P_{\text{reactor}} = 1$ bar, carrier gas He = 20 $\text{mL}_{\text{NTP}}/\text{min}$, pulse interval = 7 min; (b) BTX responses in the sequential FASPA experiments conducted at different stages of the H-ZSM-5 catalyst (#1 to #5 indicating the fresh catalyst until the deactivation in the continuous MTH test).

intrinsic kinetic investigation in the field of MTH, in which highly interweaved reactions go through a fast autocatalytic manner. These studies with concrete experimental evidence under industrially relevant conditions are rather limited due to the abovementioned lack of time-/spatial-resolved characterization tools.

FASPA, fast scanning-pulse analysis, combined with infrared spectroscopy and isotopic labeling technique used in a chromatographic reactor, has proven to be a powerful tool for conducting the transient kinetic investigation on the MTH mechanism in this thesis.

Future investigations by combining the FASPA approach and zeolite-oriented synthesis (*e.g.*, to manipulate the lattice Al distribution in the channel/intersection) will bring the current host-guest chemistry in the MTH field to another level. Many promising approaches such as hierarchical zeolite synthesis, metal (Ca, Ga, Ag, Zn, Mg, etc.) modifications, and process condition optimization (H_2 /water co-feeding) have been reported to achieve an engineered selective and stable MTA/MTO process. By applying the FASPA technique, more insight in the impact of such modifications on the MTH kinetics and mechanism would be revealed for the optimal catalytic performance.

Also FASPA is demonstrated to be a characterization tool, revealing reactions that may occur in the MTA process. An example is given by applying FASPA technique over the bimetallic Ca,Ga-modified H-ZSM-5 catalyst in the MTA process (**Chapter 5**). The disappearance of the R2 component in the aromatic responses over Ga-modified H-ZSM-5 and the increased aromatic quantity accompanied by a decrease of light olefins reveal that secondary reactions, *e.g.*, olefin aromatization via the dehydrogenation reaction route, were promoted over Ga-Lewis acid sites.

More MTH kinetic insights can be revealed by applying FASPA tests under different conditions. For example, instead of pulsing a small quantity of MeOH (**Chapter 3-5**) a long block pulse (resulting in equal amounts of MeOH and Brønsted acid sites in the catalyst bed) combined with FASPA analysis can be used to analyse the rapid transition process (0–1 min) from the induction (first C-C bond formation) to the steady-state stage in the MTH process. An example is given in **Figure 6.1(a)**. The impact of deactivation on the transient kinetic insight in the MTH process can also be studied by conducting a continuous MTH test interrupted by sequential FASPA experiments at different times-on-stream (TOS) over the catalyst. How does the inert coke deposit upstream of the catalyst bed influence the MeOH activation, hydrocarbon production and two consecutive aromatic formations? An example is given in **Figure 6.1(b)**.

Further exploring the reaction mechanism and kinetics via coupling FASPA and other transient techniques like SRE (step response experiments), SSITKA (steady-state isotopic transient kinetic analysis) over other zeolites with varying topologies (like widely used CHA-type zeolite materials in the MTO, methanol-to-olefins process) and other reaction conditions is supposed to provide more kinetic information. This novel technique can be easily extended to the kinetic study of other complex reactions like methane dehydroaromatization (MDA) and syngas/CO₂-to-hydrocarbons after careful validation.

Besides, the theoretical support from various computational tools should not be ignored. An example is given in this thesis when a genetic algorithm and *ab initio* thermodynamics were applied to predict the CaGa bimetallic structure. The reactivity of the explored CaGa structure was further tested in the dehydrogenation reactions via the DFT calculations to explain the improved stability of CaGa-modified zeolites in the MeOH-to-aromatics process. In the future, the combination of experimental study and theoretical tools will be a continuous effort to achieve a detailed understanding of the reaction mechanism.

Samenvatting

It is worth mentioning that the data-driven mechanistic investigation via machine learning might pave a new way in this field.^[1]

The application of different transient kinetic approaches for catalytic kinetic investigation would continuously contribute to the development of new and improved catalysts in C1 chemistry, such as MTH, methane activation, and CO₂/CO hydrogenation, with the goal of achieving a carbon-neutral, sustainable circular economy.

References

- (1) Koninckx, E.; Colin, J. G.; Broadbelt, L. J.; Vernuccio, S. *ACS Engineering Au* **2022**, *2* (3), 257-271.

Samenvatting en vooruitzichten

Samenvatting

Het MTH-proces wordt beschouwd als een van de belangrijkste onderdelen van het methanol (MeOH) economieconcept dat de productie mogelijk maakt van de cruciale bouwstenen voor koolwaterstoffen, zoals lichte olefinen en aromaten, uitgaande van CO₂ als primaire koolstofbron. Naast de motivatie om de afhankelijkheid van fossiele brandstoffen te verminderen, stimuleert dit proces continue procesontwikkelingen in de industrie in antwoord op de snel veranderende markt vraag. Voor de academische wereld is de MTH een perfect modelreactiesysteem voor de ontwikkeling van nieuwe poreuze materiaalsynthese en katalysatorontwerp door een beter begrip van de complexe reactieroutes en de daaraan gekoppelde uitgebreide structuur-prestatieverhouding.

Hoewel meer dan 40 jaar fundamenteel onderzoek een aantal mijlpalen en vooruitgang bij de industrialisatie heeft opgeleverd (**hoofdstuk 1**), is er nog heel wat ruimte voor verbetering, zowel wat betreft het mechanistisch inzicht in de reactie als de katalysatorprestaties, namelijk de selectiviteit voor de gewenste producten en de stabiliteit tegen deactivering. Dit proefschrift heeft tot doel meer mechanistische en kinetische inzichten te verschaffen in het MTH-proces, die kunnen leiden tot een beter begrip van de structuur-prestatieverhouding in het MTH-proces. Daartoe zijn in dit proefschrift de volgende drie doelstellingen nagestreefd *i*) aantonen dat Al in de rechte/sinusvormige kanalen van de zeolietstructuur, als meest essentiële parameter, naast andere morfologische en zuurgraadkenmerken, de selectiviteit naar propyleen bepaalt in het MTH-proces over een reeks MFI/MEL 10-MR zeolietkatalysatoren (**hoofdstuk 2**); *ii*) de identificatie van twee sequentiële reactieroutes, namelijk een snelle vorming van primaire producten in aanwezigheid van MeOH, gevolgd door een langzamere vorming van lichte aromaten gerelateerd aan de ontleding en het vrijkomen van koolwaterstofspecties (HCP) en secundaire reacties in afwezigheid van MeOH in het stroomafwaartse deel van het katalysatorbed (**hoofdstuk 3**); *iii*) het leveren van direct experimenteel bewijs dat de ‘olefinic cycle’ kinetisch wordt bevoordeeld ten opzichte van de ‘aromatic cycle’, waarbij de laatste een ‘paring-type’ reactieroute volgt voor de productie van olefinen en aromaten (**hoofdstuk 4**); *iv*) het leveren van een haalbare aanpak via Ca-Ga bimetaalmodificatie om de zure eigenschappen van zeolietmaterialen aan te passen teneinde de

productselectiviteit naar aromaten en processtabiliteit te optimaliseren (**Hoofdstuk 5**).

Het uiterst complexe autokatalytische reactieproces en de snelle kinetiek maken MTH-onderzoek zeer uitdagend; alle reacties verlopen uiterst snel in de microporiën onder industrieel relevante omstandigheden en alle denkbare katalysatorstructuurparameters en omgevingsfactoren kunnen de uiteindelijke productverdeling veranderen. Toch helpen de bevindingen in **hoofdstuk 2** niet alleen bij het opbouwen van uitgebreide structuur-prestatiecorrelaties binnen de specifieke zeolieten, maar vragen ze ook om meer kinetisch onderzoek van het MTH-mechanisme. Om de kinetische aspecten in het MTH-mechanisme aan te pakken, werd in **de hoofdstukken 3 en 4** een transiente kinetische studie uitgevoerd met behulp van een nieuwe snelle scanning-pulsanalyse (FASPA) in combinatie met infraroodspectroscopie en isotoop labelingstechnieken. Op basis van alle verkregen mechanistische en kinetische informatie zijn post-synthesemodificaties van de zeolietmaterialen veelbelovende strategieën om katalysatorparameters gericht op maat te maken zodat een selectieve katalysator met superstabiliteit in het MTH-proces verkregen kan worden (**hoofdstuk 5**).

In **hoofdstuk 2** werd een integrale onderzoeksbenadering toegepast door combinatie van een gedetailleerde analyse van het katalytische gedrag en een grondige materiaalkarakterisering van geselecteerde zeolietmaterialen met gemiddelde poriegrootte, waaronder MFI, MEL en hun intergrowth-type MFI/MEL. Experimentele resultaten laten zien dat er inderdaad één belangrijke prestatie-indicator lijkt te zijn, namelijk rooster-Al aanwezig in het zeolietkanaal in plaats van op de kanaalkruisingen, wat voornamelijk de productselectiviteit naar propyleen en butylenen verklaart, die algemeen worden beschouwd als de belangrijkste producten in de olefin cycle van het dual cycle mechanisme. In tegenstelling tot de selectiviteit voor de belangrijkste producten is de stabiliteit van deze zeolietmaterialen in het MTH-proces lastig te correleren met één enkele parameter. Al-verrijking in de kanalen, kristalgrootte, en waarschijnlijk andere intrinsieke parameters zoals diffusiviteit in de bestudeerde zeolietmaterialen spelen allemaal een rol met een verschillende mate van invloed.

De complexiteit en de beperkte kinetische informatie over het MTH-mechanisme in de H-ZSM-5-katalysator van het MFI-type vormden de aanleiding voor het transient kinetische onderzoek in de volgende hoofdstukken. In **hoofdstuk 3** werd de nieuw ontwikkelde FASPA-aanpak (fast scanning-pulse analysis) geïntroduceerd, gevalideerd en gedemonstreerd een succesvolle techniek te zijn om zowel de katalysatorprestaties in standaardapparatuur te karakteriseren en het MTH-mechanisme in H-ZSM-5 zeolietkatalysatoren te

bestuderen. Dankzij de uitgekende tijdscontrole tussen MeOH-puls en GC-bemonstering, wordt de kwantitatieve gasfase productvorming op een tijdschaal van (sub)seconden bepaald na een MeOH-pulsinjectie. Naast de productverdeling voor een prestatie-evaluatie, toont het transiënte gedrag van gasfaseproducten en de ‘hydrocarbon pool’ (HCP) componenten, die via de *in situ* DRIFT-metingen worden onderzocht, de directe correlatie aan tussen de opbouw/afbraak van de HCP en de vorming van gasfaseproducten. Het aparte transiënte gedrag van aromaten in vergelijking met alifaten wijst op een secundair vormingsproces in het benedenstroomse deel van het katalysatorbed, wat overeenkomt met een tweede brede afgifte van lichte aromaten in de productstroom bij de FASPA-test.

FASPA in combinatie met isotooplabeling in pulsexperimenten is een krachtig karakteriseringsinstrument voor een diepgaand transient kinetisch onderzoek tussen MeOH en vertraagde HCP-soorten, waarvan de resultaten worden gepresenteerd in **hoofdstuk 4**. Zoals aangetoond met *in situ* DRIFT-spectroscopie is de HCP niet statisch, maar wordt deze snel gevormd in aanwezigheid van MeOH, gevolgd door een vrij langzame desorptie uit het katalysatorbed zodra het MeOH volledig is omgezet (**hoofdstuk 3**). Deze dynamische eigenschap biedt ook de mogelijkheid om het op de HCP gebaseerde mechanisme rechtstreeks te onderzoeken via (semi-)kwantitatieve analyse van de isotopenverdeling in de aromaten en andere gasfaseproducten. Na een vrij korte inductieperiode worden bij aankomst van MeOH in de reactiezone van het katalysatorbed alle producten onmiddellijk gevormd. Water verdringt eerst de vertraagde aromatische HCP-componenten die nog in het katalysatorbed aanwezig zijn van de vorige MeOH-puls, wat resulteert in de eerste snelle verschijning van aromaten in de uitgangsstroom. In aanwezigheid van MeOH reageren de resterende HCP-componenten verder met MeOH, waarbij voornamelijk alifaten (via de kraakreacties) en aromaten via de paringroute worden gevormd. Uiteindelijk bestaat een vertraagde brede piek van BTX (benzeen, toluen en xylenen) uit de secundaire vorming van aromaten door ontleding/desorptie van primair gevormde HCP-componenten en vertraagde olefinen in afwezigheid van MeOH. Deze vierde bijdrage wordt alleen waargenomen bij langere katalysatorbedden na volledige MeOH-conversie. De relatieve bijdragen zijn afhankelijk van de pulsgrootte en de injectiefrequentie ten opzichte van de katalysatorhoeveelheid.

Met het oog op de steeds toenemende vraag naar lichte aromaten, waaronder benzeen, toluen en xylenen, wordt in **hoofdstuk 5** een strategie gepresenteerd om de verbeterde productie van lichte aromaten en de snelle deactivering over een bimetaal Ca,Ga-gemodificeerde ZSM-5 katalysator in het methanol-naar-

aromatenproces (MTA) te ontkoppelen. De toevoeging van Ga aan H-ZSM-5 bevordert de reactiesnelheid van dehydrogenering wat leidt tot een verbeterde selectiviteit voor de aromatische eindproducten, maar veroorzaakt ook een snelle deactivering van de katalysator. Experimentele resultaten met gedetailleerde karakterisering en theoretische DFT-berekeningen tonen aan dat na dotering van minder dan 0,1 wt% Ca in de Ga-gemodificeerde katalysator, de gevormde sterk gehydrateerde CaGa specimen in extraframework posities een minder Lewis zuur-karakter vertonen. Dit verzwakt de dehydrogeneringsreacties wat leidt tot een lagere waterstofvorming en een iets lagere selectiviteit voor lichte aromaten. Uiteindelijk werd de levensduur van de katalysator verlengd met ongeveer 40% betrokken op totale MeOH-doorzet. Een verdere verhoging van de Ca concentratie verminderde de totale concentratie van Brønsted-zure plaatsen waarmee het kraken van olefinen met lange ketens beperkt werd. Daardoor nam de levensduur weer af. Dit onderzoek biedt een alternatieve strategie voor bimetaalkatalysatorsynthese voor een selectief en stabiel MTH-proces.

Vooruitblik

De ‘Hydrogen economy’ is de afgelopen tijd veel bediscussieerd. Onze oceanen vormen een onuitputtelijke bron van water, water dat electrokatalytisch kan worden gesplitst in zuurstof en waterstof gebruikmakend van hernieuwbare electriciteit uit zon en wind. Alhoewel deze waterstof (en ook hernieuwbare elektriciteit) een schone energiebron vormt, het is minder makkelijk op te slaan. De ‘MeOH economy’, gebaseerd op MeOH productie uit waterstof en CO₂ en de omzetting naar koolwaterstoffen, is eerder complementair dan competitief aan het ‘hydrogen economy’ concept, en breidt het uit naar het gebied van functionele materiaalsynthese, uiteindelijk leidend tot een haalbare zero-CO₂ economie. Hernieuwbaar MeOH kan daarnaast gebruikt worden als vloeibare brandstof, en is geschikter dan waterstof in termen van opslag, distributie en vermogensdichtheid. Naast de succesvolle en uitgebreide commerciële opschaling, heeft de bijna 40-jarige studie naar het MTH mechanisme, in het bijzonder met de recente toepassing van geavanceerde *situ/operando* karakteriseringstechnieken, verder inzicht verschaft in de ‘host-guest’ chemie, waaronder het vormingsmechanisme van de eerste C-C binding en de identificatie van belangrijke HCP intermediären.

Echter, naar mijn mening is meer aandacht nodig voor kinetisch MTH onderzoek op basis van gecombineerd theoretisch en experimenteel werk onder industrieel relevante condities teneinde concretere structuur-prestatie relaties te verkrijgen, waarbij de structureigenschappen op onbevooroordeelde wijze zijn bepaald en de MTH reactiekinetiek kan worden begrepen, met als uiteindelijk doel te komen tot een rationeel MTH-katalysatorontwerp en processoptimalisatiestrategie.

De geïntegreerde aanpak die is gebruikt in het onderzoek naar MFI, MEL en MFI/MEL modelkatalysatoren laat zien dat MeOH-omzetting in de zeoliet een uiterst complex proces is, dat door meerdere parameters op verschillende niveaus wordt beïnvloed. Deze parameters omvatten, maar niet beperkt tot, de bestudeerde kristal grootte, de sterkte van de zure plaatsen en de verdeling van Al in het zeolietrooster. Andere parameters, zoals lokale defecten in het zeolietdeeltje, de aanwezigheid van ‘extraframework’ Al, de diffusiviteit van reactanten, tussenproducten en sleutelproducten binnen verschillende zeolietstructuren kunnen niet worden genegeerd. Dit is uiteraard niet haalbaar zonder de verdere ontwikkeling van zeoliet synthese. Belangrijker nog is dat de kwantitatieve correlatie tussen deze parameters en de belangrijkste katalytische

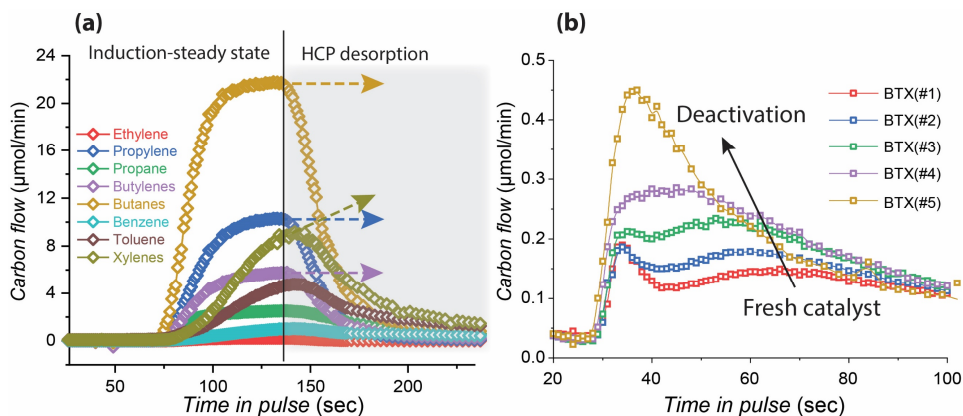
prestaties en hoe deze reageren op wisselende omgevingsfactoren de andere onderzoeksrichting aan het licht brengt, het intrinsiek kinetisch onderzoek van MTH, waarin sterk verweven reacties op een snelle autokatalytische wijze verlopen. Deze studies met concreet experimenteel bewijs onder industrieel relevante omstandigheden zijn nogal beperkt door het bovengenoemde gebrek aan tijd-/ruimte-opgeloste karakteriseringsinstrumenten.

FASPA, snelle scanning-pulsanalyse, gecombineerd met infraroodspectroscopie en isotoop labeling toegepast in een chromatografische reactor, is een krachtig instrument gebleken voor transient kinetisch onderzoek naar het MTH-mechanisme in dit proefschrift.

Toekomstig onderzoek door het combineren van de FASPA-benadering en zeoliet-georiënteerde synthese (*bijv.* om de roosterdistributie van Al in het kanaal en de kanaalkruisingen te manipuleren) zal de huidige host-guest MTH-chemie naar een ander niveau brengen. Vele veelbelovende benaderingen zoals hiërarchische zeoliet-synthese, wijzigingen van metalen (Ca, Ga, Ag, Zn, Mg, enz.) en optimalisering van de procesomstandigheden (H_2 /watertoevoer) zijn gerapporteerd als methodes om een selectief en stabiel MTA/MTO-procesontwerp te bereiken. Door toepassing van de FASPA-techniek zou meer inzicht worden verkregen in het effect van dergelijke modificaties op de MTH-kinetiek en het mechanisme voor optimale katalytische prestaties.

Ook wordt aangetoond dat FASPA een karakteriseringsinstrument is dat reacties onthult die in het MTA-proces kunnen optreden. Een voorbeeld wordt gegeven door toepassing van de FASPA-techniek op de bimetaal Ca,Ga-gemodificeerde H-ZSM-5 katalysator in het MTA-proces (**hoofdstuk 5**). Het verdwijnen van de R2-component in de aromatische respons over Ga-gemodificeerd H-ZSM-5 en de toegenomen aromatische hoeveelheid in combinatie met een afname van lichte olefinen tonen aan dat secundaire reacties, zoals aromatisering van olefinen via dehydrogenering, werden bevorderd over Ga-Lewis-zure plaatsen.

Meer MTH-kinetische inzichten kunnen worden verkregen door FASPA-tests onder verschillende omstandigheden toe te passen. Bijvoorbeeld, in plaats van het pulseren van een kleine hoeveelheid MeOH (**hoofdstuk 3-5**) kan een lange blokpuls (resultierend in gelijke hoeveelheden MeOH en Brønsted-zure plaatsen in het katalysatorbed) in combinatie met FASPA-analyse worden gebruikt om het snelle overgangsproces (0–1 min) vanaf de inductie (eerste C–C binding) naar de stationaire fase in het MTH-proces te volgen. Een voorbeeld is gegeven in **figuur 6.1(a)**. Het effect van deactivering op het transiënte kinetische



Figuur 6.1. (a) Hydrocarbon responses upon pulsing excessive MeOH over parent H-ZSM-5 at 400 °C. Conditions: MeOH pulse quantity = 62.4 μmol_C per pulse, catalyst loading = 100 mg (~55 μmol Brønsted acid sites), catalyst pellet size = 150–212 μm , $P_{\text{reactor}} = 1$ bar, carrier gas He = 20 $\text{mL}_{\text{NTP}}/\text{min}$, pulse interval = 7 min; (b) BTX responses in the sequential FASPA experiments conducted at different stages of the H-ZSM-5 catalyst (#1 to #5 indicating the fresh catalyst until the deactivation in the continuous MTH test).

gedrag van het MTH-proces kan ook worden bestudeerd door een MTH-test met continue MeOH voeding uit te voeren die wordt onderbroken door sequentiële FASPA-experimenten na verschillende operatietijden (‘time-on-stream’) over de katalysator. Hoe beïnvloedt de inerte ‘coke’ die zich stroomopwaarts in het katalysatorbed af heeft gezet de MeOH-activering, de koolwaterstofproductie en de twee opeenvolgende aromaatformingsprocessen? Een voorbeeld wordt gegeven in **figuur 6.1(b)**.

Verdere verkenning van het reactiemechanisme en de kinetiek via koppeling van FASPA en andere transiënte technieken zoals SRE (step response experiments), SSITKA (steady-state isotopic transient kinetic analysis) over andere zeolieten met verschillende topologieën (zoals veel gebruikte zeolietmaterialen van het CHA-type in het MTO-proces, methanol-naar-olefinen) en andere reactieomstandigheden moet meer kinetische informatie opleveren. Deze nieuwe techniek kan, na zorgvuldige validatie, gemakkelijk worden uitgebreid tot de kinetische studie van andere complexe reacties zoals methaan-dehydroaromatisering (MDA) en syngas/ CO_2 -tot-koolwaterstoffen.

Bovendien mag de theoretische ondersteuning van verschillende rekentechnieken niet worden genegeerd. In dit proefschrift wordt een voorbeeld gegeven waarbij een genetisch algoritme en *ab initio* thermodynamica werden

toegepast om de bimetaalstructuur van CaGa te voorspellen. De activiteit van de onderzochte CaGa-structuur werd verder getest in dehydrogeneringsreacties via DFT-berekeningen om de verbeterde stabiliteit van CaGa-gemodificeerde zeolieten in het MTA-proces te verklaren. In de toekomst zal de combinatie van experimenteel onderzoek en theoretische instrumenten continu aangewend worden om het reactiemechanisme in detail te begrijpen. Vermeldenswaardig is dat het data-gedreven mechanistische onderzoek op basis van ‘machine-learning’ een nieuwe weg zou kunnen inslaan op dit gebied.^[1]

De toepassing van verschillende transient kinetiekbenaderingen voor katalytisch kinetisch onderzoek zal voortdurend bijdragen tot de ontwikkeling van nieuwe en verbeterde katalysatoren in de C1-chemie, zoals MTH, methaanactivering, en CO₂/CO-hydrogenering, met als doel het bereiken van een koolstofneutrale, duurzame circulaire economie.

Referenties

- (1) Koninckx, E.; Colin, J. G.; Broadbelt, L. J.; Vernuccio, S. *ACS Engineering Au* **2022**, 2 (3), 257-271.

Acknowledgements

Now it goes to the last but most important section, which would probably grab the first glance of the reader after picking up this book. This project would not have been possible without the support of many people. And here I address my 'thank you' to every one of you.

My first appreciation must go to Prof. Evgeny Pidko and Prof. Freek Kapteijn, my promoters, for providing this opportunity for me to grow professionally. I actually wondered for a long time which one of you is my supervisor and which one is my promotor. But here I will express my gratitude based on the sequence of the names' appearance in the PhD contract. Thank you Freek for the excellent scientific discussion throughout this thesis. Your research enthusiasm, critical attitude on my experimental results, and extreme patience on numerous revisions of my manuscripts greatly helped me out of the confusion and sort out the storyline. You are always kind and calm, and patiently teach me how to conduct research step by step. I learned so much from you both professionally and personally. It is definitely an honor to be your last doctoral student.

Thank you very much, Evgeny. Sorry I mistook you as Freek's secretary during my online interview. At that moment, I had no idea that I was going to work with a scientist full of talent. I am always impressed by your quick thinking and your ability of extracting the key message from my results. Thank you for your wisdom and your priceless support for allowing me to choose my research topic as freely as possible. Besides your professional supervision, I also benefited from the ISE group where you house so many experts.

Evgeny Uslamin, my daily supervisor and co-promotor, thank you for throwing so many great ideas to me, who knew nothing about the MTH process at the beginning. It's a pity that only a few of them are realized in this thesis. You are the best and most reliable mentor who is always available and ready to answer any questions. Robert Franz, thank you for the career advice and for helping me check my presentation for the conference. Hope the boat of our friendship will not capsizize this time. Robbert van Putten, thank you for helping me design the Labview program. I will never forget your pranks on my desk, the coffee chats, and teaching me wired English words (here credits to Evgeny Uslamin and Robert Franz too). Elena, thank you for the collaboration and contribution to the CaGa

Acknowledgements

project. Wenjun, thank you for helping me pick up my lunch and for all the fine memories of basketball games in X, BBQs in the yard and all the lunch chats. Good luck with your defense in two days. Annika, Ali, Jittima, Vivek, thank you for sharing excellent research in the group meetings and the fine memory in the group dinner and outdoor activities. Adarshje, my officemate and the ISE new blood, thank you for correcting my dutch summary, as well as for our office/coffee chats. You are such a brilliant guy who is doing something that I have no idea about. But I am sure that you will enjoy your PhD journey to success. Georgy, thank you for sharing your knowledge and the oysters (and many other delicacies). Wish you good luck with your career in 3ME. Christophe, thank you for the lunch talk and for being in the ally supporting meat. Dapeng and Guanna, thank you for the inspiring talk and for inviting me to parties at your house many times. Lucas, Sienna, Mariangela, Ali, Enrico, and Harshini, thank you all for your hard work on your master projects. It is my pleasure to work with you and I wish all of you success in your future career.

Thank you, Liliana for helping me solve lab issues and order everything I need. If time starts over again, I am sure I will have fewer troubles on my GC. Bart, thanks for all your technical support in the lab throughout the entire project. You are not only a top-level engineer and researcher but also a successful manager who has ensured the big CE lab safely and productively running for so many years. Willy, thank you for still allowing me to work in your lab after warning me about my unapproved operations on weekends during my first year. Everyone working in CE labs should not ignore your contribution to keeping the chemicals well organized and safe in the lab servant system. Harrie, thank you for helping with the measurements in the industrial catalysis lab. Thank you, Els and Karin for helping me go through all the administrative processes and for organizing the regular group meetings and activities. I also appreciate the assistance from Caroline, Bart, Duco, Ben, Swapna, and Xiaohui.

I am grateful to CE people and my friends in the department, although some of them have left already. Xuerui, Xinlei, Meixia, Riming, and Xiaohui, thank you all for welcoming me to the CE group and showing me the Chinese-type work-and-life boundary. Ina, thank you for guiding me into the fascinating (but exhausting) IR-pyridine measurement and for sharing your knowledge in zeolite synthesis. Thank you Nat, for sharing your code and for teaching me the MCR analysis approach. Wish you good luck with your defense! Donato and José, thank you for the discussion. You don't know how many times I am drooling over

your experimental platform with portable characterization probes. It is such a pity that I cannot make our collaboration come true. Min and Sorin, thanks for sharing your brilliant projects by converting NO_x into fertilizer. Best wishes to the scale-up into the business. Davide, Srinidhi, and Han, thanks for the fine memory of sharing the lab and office before my move. Guotai, I will not forget our lunch talks and all the entertainment we had. Let's finalize the doctoral defense together and keep in touch in the future. Mengran and Nikki, Your enthusiasm for hosting parties and preparing delicious meals has really impressed me. I wish you well with your work and life in Australia.

Special thanks to people in the ARC-CBBC consortium. Sophie and Bert (UU), Robert, Lukasz, Andrei, and Trees (BASF), I enjoyed our inspiring discussions and received much feedback and support making this project on track and successful. Thank you Irina (BASF). Your thesis opened the MTH world to me and gave me much inspiration. Your suggestions during our bi-weekly discussion helped me a lot. Although I've never submitted our manuscript/presentation for clearance on time, you were still able to proceed quickly and ensure that I can disclose our results to the outside world. I am also thankful to Hannah, who organized so many wonderful workshops, summer schools, and those annual symposiums helping me be shaped both professionally and personally.

I also want to express my gratitude to the members of the PhD committee, prof.dr.ir. Atsushi Urakawa, prof.dr. Unni Olsbye, prof.dr.ir. Leon Lefferts, prof.dr.ir. J. Ruud van Ommen, and prof.dr. A.J. Houtepen. Thanks for taking time to evaluate my thesis and attend the defense ceremony. Especially I am indebted to prof.dr.ir. Atsushi Urakawa for the hospitality of using the CE lab facilities realizing my research project.

Now it goes to the names in my deep heart, my family. Na, you are the best sister all over the world. You are the perfect figure as the big sister in our family, and I followed in your footsteps in research in Europe. Thanks for your inspiration, encouragement and financial/mental support in my study. 希望你跟姐夫在挪威幸福的相守一生. Dad and mom, you are the heroes. Simply because you believe that education is the only way to get out of the village, you devote your entire life to teaching and supporting Na and me throughout our studies. I hope now you are proud of your daughter and your son.

Acknowledgements

Xiaoqun, my love, my dear wife! You deserve a full thesis and a poem next to it for all the sacrifices that you made for me and for all support that you've provided. Unfortunately, due to the space limitation, I have to crystallize all my gratitude, love and dedication to you in this final, very special paragraph. Thank you for staying with me through this four-year journey and supporting me unconditionally in all the troubles and stresses that I went through. Many things happen, good and bad. We initially made a sound-like-acceptable plan for this remote relationship, but the corona ruined everything. And I am sorry to leave you alone facing the wind and rains in this period. Although you are so confused about why I am always screwing and tubing in front of a buzzing machine, your unwavering support and deep conviction in our future provide me with the motivation to strive through all of the lows in my research. I can't wait to reunite and share the rest of my life with you. 百年修得同船渡，千年修得共枕眠。我会用我的余生带你看完这一世的风花雪月。

The last appreciation goes to those whom I forget to mention, and of course to all readers who reach here, I hope you enjoy reading this book!

List of publications

Publications within the scope of this thesis:

Liu, C., Uslamin, E.A., van Vreeswijk, S.H., Yarulina, I., Ganapathy, S., Weckhuysen, B.M., Kapteijn, F. and Pidko, E.A., An integrated approach to the key parameters in methanol-to-olefins reaction catalyzed by MFI/MEL zeolite materials. *Chinese Journal of Catalysis*, **2022**, 43(7), pp.1879-1893.

Liu, C., Uslamin, E.A., Khramenkova, E., Sireci, E., Ouwehand, L.T., Ganapathy, S., Kapteijn, F. and Pidko, E.A., High Stability of Methanol to Aromatic Conversion over Bimetallic Ca, Ga-Modified ZSM-5. *ACS catalysis*, **2022**, 12(5), pp.3189-3200.

Liu, C., Uslamin, E.A., Pidko, E.A. and Kapteijn, F., Direct discerning reaction pathways in methanol-to-hydrocarbons by transient operation – FASPA, *under review*.

Liu, C., Uslamin, E.A., Pidko, E.A. and Kapteijn, F., Revealing main reaction paths to olefins and aromatics in the MTH process over H-ZSM-5, in preparation.

Publications outside the scope of this thesis:

He, S., Kramer, T.S., Klein, F.G.H., Chandel, A., Tegudeer, Z., Heeres, A., Liu, C., Pidko, E.A. and Heeres, H.J., 2022. Improved catalyst formulations for the conversion of glycerol to bio-based aromatics. *Applied Catalysis A: General*, **2020**, 629, p.118393.

He, S., Zuur, K., Santosa, D.S., Heeres, A., Liu, C., Pidko, E.A. and Heeres, H.J., Catalytic conversion of pure glycerol over an un-modified H-ZSM-5 zeolite to bio-based aromatics. *Applied Catalysis B: Environmental*, **2021**, 281, p.119467.

List of publications

He, S., Goldhoorn, H.R., Tegudeer, Z., Chandel, A., Heeres, A., Liu, C., Pidko, E.A. and Heeres, H.J., Catalytic conversion of glycerol to bio-based aromatics using H-ZSM-5 in combination with various binders. *Fuel Processing Technology*, **2021**, 221, p.106944.

Oral presentations:

Liu, C., Uslamin, E.A., Yarulina, I., Pidko, E.A. and Kapteijn, F., MTO conversion over MFI, MEL and MFI/MEL intergrowth zeolite catalysts: interplay of topology, acidity and catalytic performance. NCCC 2020, 2 March 2020, Noordwijkerhout, the Netherlands.

Liu, C., Uslamin, E.A., Pidko, E.A. and Kapteijn, F., Direct discerning reaction pathways in methanol-to-hydrocarbons (MTH) process via transient operation. ARC-CBBC symposium 2022, 12 April 2022, Groningen, the Netherlands

Liu, C., Uslamin, E.A., Khramenkova, E., Pidko, E.A. and Kapteijn, F., High-Stability Methanol-To-Aromatics Conversion over [Ca,Ga]/H-ZSM-5. the International Chemical Congress of Pacific Basin Societies 2021, 19 Dec 2021, Hawaii (virtual), the United States.

Liu, C., Uslamin, E.A., Pidko, E.A. and Kapteijn, F., Direct discerning reaction pathways in methanol-to-hydrocarbons (MTH) process via transient operation: FASPA. 20th International Zeolite Conference, 03 July 2022, Valencia, Italy.

Curriculum Vitae

Chuncheng Liu was born on 5th July 1991 in Yantai, China. After obtaining his bachelor degree from Chongqing University, Chongqing, China in 2014, he studied energy engineering at Politecnico di Milano, Italy. Besides his studies in energy engineering courses (energy conversion, heat & mass transfer, oil and gas engineering, *etc.*), he was working on his master thesis at the Lab of Catalysis and Catalytic Process under the supervision of prof.



Enrico Tronconi and prof. Isabella Nova. In December 2016 he received his master diploma from the Energy Engineering department of Politecnico di Milano with a thesis entitled “Diesel exhaust urea NH₃-SCR aftertreatment technology: experimental investigation and kinetic modeling of a Fe-ZSM-5 based catalyst”. After the graduation, he began working as a researcher in the group of prof. Luca Lietti in the Lab of Catalysis and Catalytic Process, Politecnico di Milano, where he continued his catalytic research on NO_x removal techniques for automotive applications in collaboration with industrial partner Toyota. In May 2018, he joined the Catalysis Engineering group and Inorganic Systems Engineering group at Delft University of Technology where he started his PhD project. Under supervision of prof. dr. Freek Kapteijn, prof. dr. Evgeny A. Pidko and dr. Evgeny A. Uslamin, he was studying the reaction mechanism underlying methanol transformations into hydrocarbons including olefins and aromatics over zeolite catalysts, in close collaboration with academic partner Utrecht University and industrial partner BASF within the framework of ARC-CBBC consortium. The main findings of his work are presented in this dissertation.